Characterizing blood protein surface interactions for the development of thromboresistant fluoropolymer coatings

Sherry Liu

A dissertation
submitted in partial fulfillment of the
requirements for the degree of

Doctor of Philosophy

University of Washington
2023

Reading Committee:
Buddy D. Ratner, Chair
Lara J. Gamble
Wendy E. Thomas

Program Authorized to Offer Degree:
Bioengineering

University of Washington

Abstract

Characterizing blood protein surface interactions for the development of thromboresistant fluoropolymer coatings

Sherry Liu

Chair of the Supervisory Committee:
Buddy D. Ratner
Department of Bioengineering

Patients with long term blood-contacting medical devices will continue to require risky systemic anticoagulant administration until the effects of device thrombogenicity can be adequately addressed. Adsorption of the protein, fibrinogen, to biomaterials is broadly acknowledged as the primary mediator of platelet adhesion and aggregation, yet fibrinogen in its native soluble form is inactive and circulates harmoniously with platelets in the bloodstream. Therefore, the adsorption process induces a structural change to the protein that exposes platelet-binding epitopes. Complete elimination of protein adsorption on biomaterial surfaces for extended durations has proven a significant challenge, and even ultralow levels of surface fibrinogen can initiate full platelet activation and thromboembolism formation. However, a body of evidence suggests that platelet membranes themselves are inert against continued exposure to blood after initial degranulation. Thus, perhaps a more realistic approach to developing long-term blood contacting materials is to engineer surfaces that adsorb fibrinogen in a layer that rapidly promotes uniform platelet adhesion and spreading to form a smooth passivating layer against further activation by circulating blood components. Separately, fluoropolymers hold a long history of delivering favorable outcomes for blood-contacting applications. Our group

possesses expertise in glow-discharge plasma polymerized fluorocarbons, which have historically demonstrated exceptionally high patency rates, high blood flow, and low embolization rates in *in vitro* studies and *ex vivo* primate shunt models compared to other materials of their class. However, the mechanism behind their favorable adsorption of blood protein constituents or conformations to resist long-term activation of blood cellular components deserves more investigation to properly characterize their mode of action. In this dissertation, we present several studies of blood protein interactions on a custom plasma-polymerized fluorocarbon (ppC_3F_6) developed in our research group in comparison with standard commercial fluoropolymer counterparts to further explore the platelet membrane passivation mechanism. We begin with an overview of the historical challenges in addressing hemocompatibility and the viability of engineered fluoropolymers to fulfill long-term blood contacting needs (**Chapter 1**). We then delve into preparation and characterization of a small selection of fluoropolymers (**Chapter 2**), followed by assessments on differential total protein adsorption using quartz crystal microbalance with dissipation (**Chapter 3**). Given that the origins of thrombus formation depend on adsorption-induced structural changes of fibrinogen in addition to total adsorption, we pursued a series of studies investigating these changes across our fluoropolymer materials (**Chapter 4**). We then discuss our effort to better understand structurally sensitive regions in the fibrinogen platelet-binding domain that give rise to bleeding disorders including thrombosis through molecular dynamics simulations (**Chapter 5**). Finally, we assess platelet adhesion and activation in relation to our fluoropolymers preadsorbed with fibrinogen to identify relationships between fluoropolymer surface chemistry, adsorbed blood protein surface composition and structural bioactivity, and cellular response (**Chapter 6**), concluding with proposed mechanisms of improved blood compatibility and remarks on future directions for the application of plasma-polymerized fluoropolymers in blood-contacting devices (**Chapter 7**).

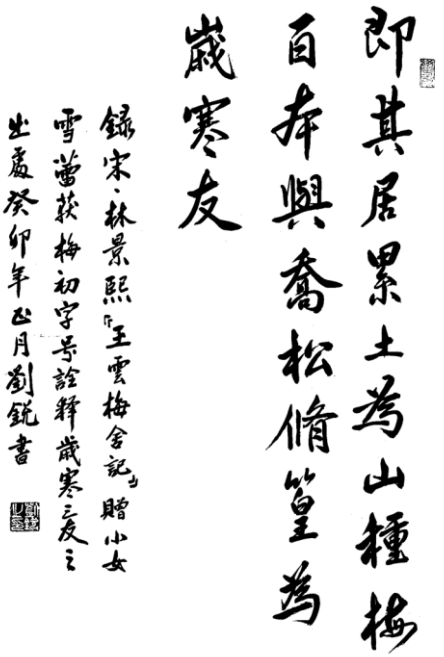

For his residence, earth was piled to form a hill
and a hundred plum trees, which, along with
lofty pines and tall bamboo comprise the friends
of winter, were planted.

-Lin Jingxi
Record of the King-Cloud Plum Cottage
Song Dynasty

Presented to the youngest daughter, Xuelei,
upon receiving the courtesy name, Meichu,
interpreting the origin of the phrase
'Three Friends of Winter.'

Calligraphy by Rei Liu
First Month of the Guimao Lunar Year

For my mother, Nan (周南); father, Rei (刘锐); and sister, Tina (刘遥)—
from whom I have learned steadfastness, resilience, and integrity,
virtues which I strive to embody every day.

&

For Jeroen, and De Kluphaus we will build
where the three will grow strong.

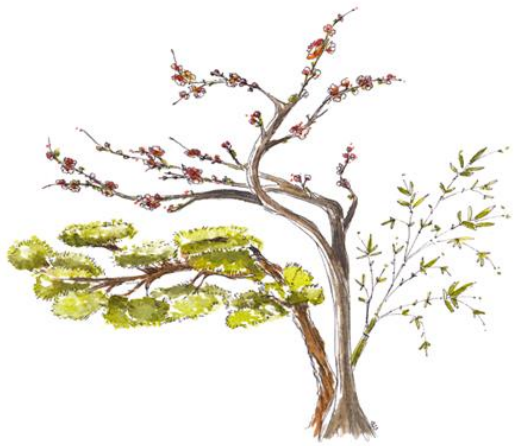

This work was supported by a grant from Northwest Kidney Centers (NKC) to the Center for Dialysis Innovation (CDI). All acknowledgments relevant to individual works are included following their respective chapters.

I am forever grateful to **Buddy Ratner** for being a wellspring of inspiration whose lifelong work in biomaterials drew me to pursue graduate studies at the University of Washington. Your tenacious dedication to this field, breadth of knowledge, and trailblazing spirit gave me the drive to become an independent researcher, and I am all the stronger for it. Thank you for giving me the opportunity to join your research group—I am proud to be a part of your academic family and hope this manuscript contributes in some small way to illuminating the great enigma that is blood compatibility.

I would also like to thank my supervisory committee—**Lara Gamble**, **Wendy Thomas**, and my GSR **Bill Mahoney**—for your insights, feedback, and advice on a research topic that often feels overwhelming and unsolvable. Your broad perspectives have helped me greatly in these final stages as I attempt to make sense of it all- thank you for further honing my critical thinking and expanding my scientific vision.

There are many people I have known throughout the years who have helped me arrive at this stage, all of whom I could not possibly thank in this document. Please know that I do remember and that I am thankful for your influence and support. I am especially and deeply grateful for:

My labmates, past and present: **Dr. Le Zhen**, **Dr. Julia King**, **Dr. Prabhleen Kaur**, **Dr. Lars Crawford**, **Irini Sotiri**, **Guoyao Chen**, **Louis Chen**, and others for the collegial environment that extends from the lab to the mountains and lakes. Science isn't as fun if you can't talk about it on an inflatable boat or while grilling over an open campfire. I am grateful for our mutual pursuit and discussion of biocompatible materials, whether plein air or under HVAC, and I am excited to see where we all go next.

Sharon Creason and **Winston Ciridon**: you have both been critical lab staff who have kept the ship afloat. Sharon, thank you for keeping this lab running and ensuring smooth operations in every possible crisis. Winston, your unending patience in teaching the intricacies of plasma deposition are forever appreciated. And if I can thank an inanimate object: thank you to the Benson 309 RFGD vacuum pump. We thought you were on your last legs since the beginning of grad school, yet you still hang on and manage to produce ever more samples for us.

The BioEngage team: **Abby Nagle**, **Soraya Bailey**, **Wes Fabyan**, and **Bella Reichardt**. If my research was making no headway, I could always count on forward momentum from all of you. I truly enjoyed working on our small team

and contributing to our department through building relationships between our student body, faculty, and biotech/medtech industry connections.

My brothers-in-arms: **Kyung-Hoon Kim** and **Dr. Kan Wu**—the graveyard is (still) alive, especially after 11:00 PM. Both of you have been instrumental in making me the scientist that I am, and I have you to thank for making me a true night owl. I will never forget our late-night discussions about science, life, philosophy, and so much more, as well as our many adventures and excursions that are too numerous to list. I could not have finished this PhD without either of you.

Kevin Hallagan: your friendship during this time of my life has been an anchor and lifesaver all in one. Thank you for your reliability, inquisitiveness, honesty, and warmth—my life is so much more enriched with your presence.

My sister, **Tina**, and brother-in-law, **Andrew**: I now never underestimate the bolstering support of food. Jokes aside, thank you for sustaining me and caring for me throughout the years, and always taking in this stray on any holiday or in-between holidays. I always know I have a safe place to turn, and a delicious meal to share!

Jeroen Vollenbroek: your love, trust, and support defy all spatiotemporal limits. The time without and the distance between are reduced to trivialities with no units. Who could have guessed that 350 years later, you and I would finally prove the existence of phlogistons? I am looking forward to sharing the many great discoveries to come in De Kluphaus [*sic*], because we'd always rather be left than right.

My mother, **Nan**, and father, **Rei**: thank you for your unconditional love and support. I am my own harshest critic, and so I thank you for knowing when to let things run their course or when to talk me down and remind me of my worth. You have both instilled in me a love for learning and I will forever hold the values you taught me throughout my life.

Contents

List of Figures

List of Tables

Chapter 1

Historical challenges in addressing blood compatibility

1.1 Hemodialysis and the unmet need for safe long-term blood-contacting biomaterials

Chronic Kidney Disease (CKD) encompasses any condition presenting with reduced kidney function over an extended period of time and can develop into end-stage renal disease (ESRD) or incite further systemic complications like hypertension, anemia, and cardiovascular disease [1,2]. As of 2016, the CDC estimates that 10% of the US population and 500 million adults worldwide have CKD, which has consistently ranked in the nation's top ten leading causes of death [3]. With average transplant waitlist times in the US upwards of 3 years, the majority of ESRD patients must rely on hemodialysis (HD) to artificially filter their blood of excess fluids and waste products.

HD is an *ex vivo* process: blood is circulated out of the body, infused with heparin to prevent clotting, and pumped through a dialyzer, where a semi-permeable membrane comprised of miniscule fibers resides [4]. Within the dialyzer compartment, fresh dialysate is flowed countercurrent to the blood and

serves as a solute sink to promote a concentration gradient for waste movement across the membrane and out of the patient's blood. Cleaned blood is then passed through an air trap and returned to the patient. HD is most often performed at a dialysis center or hospital and is required 3 times a week for up to 5 hour-long sessions at a time. As such, HD can place a significant burden on quality of life, but remains as the most efficient form of treatment for ESRD patients aside from kidney transplant.

However, this life-saving treatment remains prohibitive and inaccessible to millions in the global ESRD patient population, while those fortunate enough to receive HD must endure frequent and lengthy dialysis sessions that are restrictive, debilitating, and require careful administration and monitoring of systemic anticoagulants that places them at high hemorrhagic risk. Even still, hemodialyzers and associated blood-contacting devices continue to fail due to biofilm formation and clotting, necessitating revision procedures or inducing adverse and potentially fatal events, including septic shock and thromboembolism [5-7]. As such, HD only prolongs life for ESRD patients for an average of 3 years, with poor quality of life and exorbitant financial burdens. Medicare spending for treatment of all CKD patients over 65 years surpassed $50 billion and constituted 20% of all Medicare spending in this age category [2]. CKD is clearly an economic and public health concern, yet dialysis innovation has stagnated for decades with low governmental or industry prioritization for progress. Advancements in this field are inhibited in part by the elusiveness of synthetic materials capable of mimicking the non-fouling and antithrombotic properties of native endothelium. Without these attributes, blood-contacting devices will inevitably fail or induce blood injury and therefore cannot safely support long-term usage without systemic anticoagulation or antiplatelet therapies.

1.2 Founding of the Center for Dialysis Innovation (CDI)

The University of Washington in Seattle is the birthplace of long-term hemodialysis treatment. In 1960, UW School of Medicine nephrologist, Belding Scribner, MD, and UW biomechanical engineer and inventor, Wayne Quinton, developed the first shunt, made of Teflon™ (PTFE), as a synthetic extension of peripheral vasculature to permit repeated blood access for dialysis [8]. Together with UW chemical engineering professor Albert (Lester) Babb, PhD, they pioneered an efficient and automated long-term hemodialysis device so that ESRD could shift from a terminal illness with short life expectancy to a more manageable chronic health condition. The first outpatient hemodialysis center was the Seattle Artificial Kidney Center (SAKC) founded in 1962 and located in the basement of Swedish Hospital.

While the breakthrough invention of dialysis in the 1960s enabled patients with ESRD to survive, dialysis technology has not significantly evolved since then. The Center for Dialysis Innovation (CDI) was formed in 2017 as another partnership between UW and SAKC (now a nonprofit dialysis provider called Northwest Kidney Centers) in a renewed effort to improve the health, independence, and quality of life of dialysis patients. The CDI's mission is to develop the Ambulatory Kidney to Improve Vitality (AKTIV) device, envisioned as a wearable, miniaturized dialysis system that is low-cost, energy- and water-efficient, offers simplistic blood access, and requires minimal anticoagulation.

To enable this technology, the founding core research thrusts of the CDI are uremic toxin removal, vascular access, and blood compatibility. The work described in this dissertation belongs to the last group, and represents one of three original sub-projects pursued under this branch. The goal of the blood compatibility team is to develop methods of accurately assessing biomaterial thrombogenicity, establish criteria for blood compatibility, and provide

recommendations and/or material candidates to coat the blood-contacting surfaces of the AKTIV device. The scope of this work covers the effects of blood protein fouling, specifically albumin and fibrinogen, on a small selection of fluoropolymers, along with their characterization and downstream effects on platelet adhesion and activation. This class of materials was nominated for initial study as potential candidates based on a compendium of academic reports and clinical usages demonstrating their low thrombogenicity, high patency rates when coated on small diameter vascular grafts, and favorable materials properties like chemical inertness, lubricity, and durability [9-11]. Zwitterionic polymers, in addition to fluoropolymers, and their effect on the intrinsic coagulation pathway (clotting time, FXII activation, etc.), complement activation, and platelet activation under arterial vs. venous flow, among other topics, are under investigation by colleagues and will not be covered in this work.

Finally, while the research described in this dissertation was funded by and pursued under the stewardship of the CDI for the purpose of identifying viable biomaterials for improved blood compatible hemodialyzer surfaces, the studies performed here are fundamental in nature and relevant to the understanding of blood protein-biomaterial interactions for other long-term cardiovascular devices and applications as well.

1.3 Blood protein adsorption and the Vroman Effect

Long term blood-contacting medical devices have classically suffered from nonspecific endogenous protein adsorption that can initiate coagulation, immune, and inflammation pathways, often leading to serious or even fatal thromboembolic complications like pulmonary embolisms, myocardial infarctions, and stroke [12]. Clinical records provide a broad array of evidence showing the material incompatibility of numerous cardiovascular devices: rapid loss of patency for

medium (4-6 mm) vascular grafts [13], complete occlusion in coronary stents within weeks [14], emboli formation from catheters [15] and prosthetic heart valves [16], and even clot formation during surgical procedures like cardiopulmonary bypass [13]. Evidently, this phenomenon of rapid protein adsorption can lead to failure for blood-contacting devices and, counter to our interests, stands as a major barrier to achieving fully portable, long-lasting continuous dialysis without the need for constant anti-thrombotic pharmacological interventions.

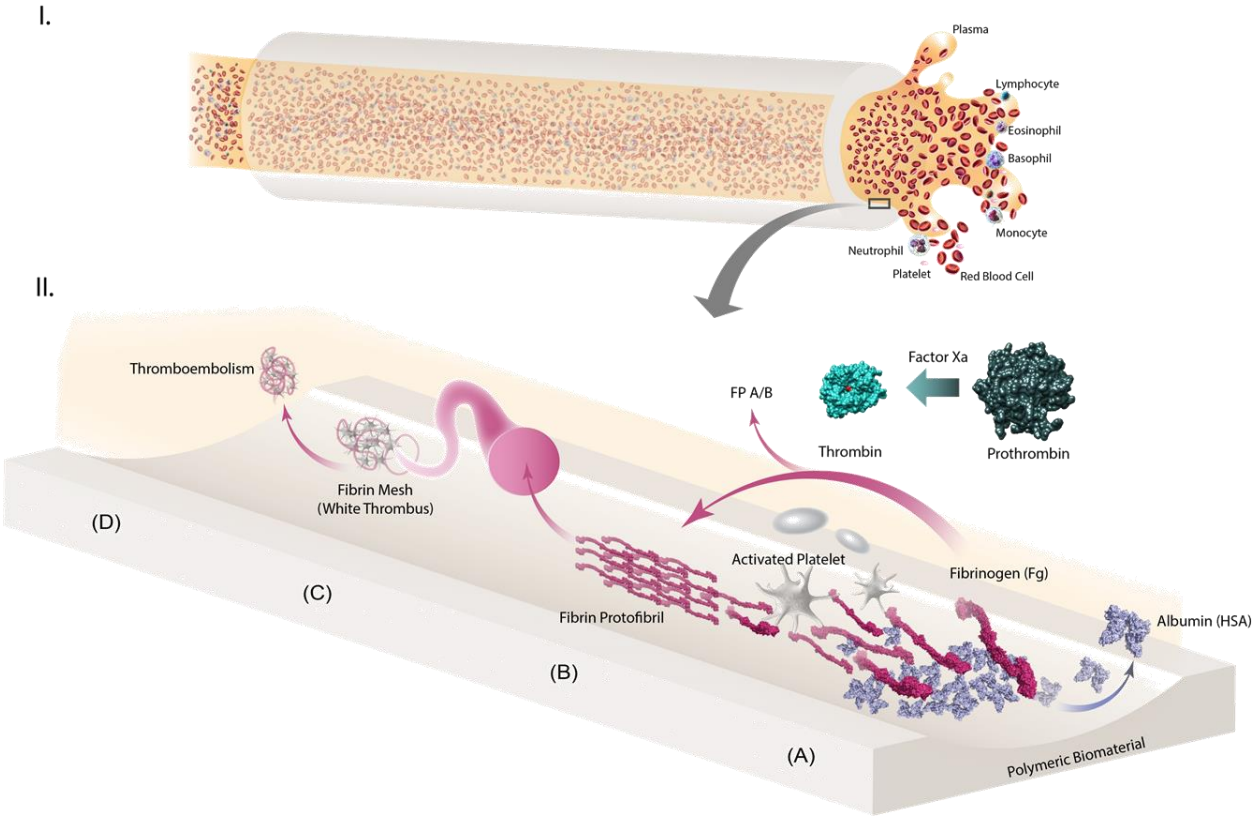

Figure 1.1. Schematic of the Vroman Effect. (I) A segment of polymeric medical tubing is depicted with blood flow through the inner lumen. **(II)** A magnified view of the luminal surface depicts **(A)** rapid albumin (HSA) diffusion and adsorption to the surface, followed closely by fibrinogen (Fg) displacement of the adsorbed HSA. Adsorbed Fg can either directly bind platelets, or undergo conversion to fibrin (Fn) through thrombin-mediated enzymatic cleavage of its fibrinopeptides (FP A/B). Unlike Fg, Fn is insoluble and can **(B)** form long fibers that enmesh platelets to **(C)** form a white thrombus. This white thrombus presents a high risk of dislodgement from the biomaterial surface as a **(D)** thromboembolism, which can lead to serious complications like a pulmonary embolism, stroke, or myocardial infarction.

The interaction of blood with a foreign material is immediately followed by a series of competitive protein adsorption events, termed the Vroman Effect (**Figure 1.1**), was first observed by Leo Vroman in 1969 [17-18]. The temporal turnover of adsorbed blood plasma proteins forms the basis for materials-induced thrombosis, and is initiated by surface deposition of the most abundant plasma protein (~60%), human serum albumin (HSA) (35-54 g/L) [19]. Due to its high plasma concentration and small rod-like hydrodynamic size of approximately 8x4 nm (68 kDa), HSA adsorption to the biomaterial surface is kinetically driven to form a preliminary passivating layer against cell adhesion since HSA is chemically and immunogenically inert [20-21]. However, this state is transient—the Vroman Effect describes the temporally-dependent, thermodynamically-favorable displacement of HSA by fibrinogen (Fg), a larger rod-like adhesion glycoprotein approximately 55x10 nm in size (340 kDa; 5 times the molecular weight of HSA) with greater surface affinity and higher transition energy (3 g/L) [22]. Fg is a major mediator of integrin receptor-based cell adhesion, leading to platelet degranulation and activation of the coagulation cascade that ultimately results in downstream fibrin clot formation. While several other plasma proteins are also observed to adsorb to biomaterial surfaces—fibronectin, vitronectin, immunoglobulins, Factor XI and XII, von Willebrand Factor (vWF), high molecular weight kininogen (HMWK), and prekallikrein (PK)—the surface protein composition generally does not reflect plasma compositions [74-75]. In other words, biomaterial surfaces selectively fractionate plasma, with certain proteins—particularly fibrinogen—consistently overrepresented on the surface compared to their plasma concentrations [76]. Meanwhile, HSA, which constitutes ~55-60% of blood plasma protein concentration, is vastly underrepresented on most surfaces [77].

The mechanism of protein deposition and turnover is still poorly understood, but its elucidation is critical to developing effective strategies against downstream prothrombotic events. Under dynamic shear flow of HSA protein solutions, Brash

& Samak showed that sequential introduction of distinct radioiodinated HSA populations (^{125}I, then ^{131}I) exhibited a gradual turnover of the HSA surface composition under steady-state conditions, thus demonstrating the ability of proteins to displace identical proteins and continuously refresh the surface adlayer [73]. With the advent of better surface analysis techniques, Bilek and colleagues recently provided strong support for the formation of a transient biomolecular complex during protein surface exchange, initially proposed by Huetz et al. in 1995 to limited reception, in contrast to the popular but oversimplified desorption/adsorption exchange model [23-27]. Using a combination of Time of Flight Secondary Ion Mass Spectroscopy (TOF-SIMS), solution-based mass spectroscopy, and Quartz Crystal Microbalance with Dissipation (QCM-D), they demonstrated through compositional changes that this exchange, first structurally described by Heinrich et al., occurs in three phases: 1) the competing protein (Fg) embeds itself into the primary adsorbed protein layer (HSA), 2) the complex overturns and forms a taller and diffuser structure that exposes the bottom protein (HSA) to solution, and 3) the bottom protein (HSA) desorbs into solution [27-28]. This network interaction implies that a degree of initial protein saturation on the material surface must first be obtained before subsequent displacement occurs.

Because the coagulation cascade is exceptionally complex with multiple activation/deactivation feedback loops and interdependencies, identifying and applying pressure to the proper bottlenecks in the process are critical to effecting the greatest inhibitory action. To date, a plethora of approaches have been taken to modify the biomaterial surface in a manner that deters protein and platelet adhesion/activation, including hydrophobic polymer deposition (fluoropolymer spin-coating), physicochemical processing (plasma/ion beam functionalization), and covalent binding of zwitterionic synthetic or biological polymers (PEG or chitosan grafting, self-assembled monolayers) [29-31]. These methods all aim to prevent nonspecific adsorption of proteins known to promote further platelet

adhesion, chief among which is Fg. The platelet adhesion receptor, glycoprotein IIb-IIIa (GPIIb-IIIa) (also called integrin αIIbβ3), belongs to the integrin family and is the most active and abundant receptor that interacts directly with Fg's RGD*X* motifs in two of its α-chain sequences (Aα95-98: RGDF; Aα572-575: RGDS) and a non-RGD dodecapeptide sequence in the COOH-terminus of its γ-chain (γC400-411: HHLGGAKQAGDV), thus providing three primary platelet binding sites (**Figure 1.2**) [32-33, 77]. This interaction then mediates platelet adhesion, spreading, and activation—even low surface-bound Fg levels are capable of launching a full-scale coagulation cascade, indicating the high sensitivity and recognition of platelets to adsorbed Fg signaling [34]. However, it should be noted that while integrins bind broadly to proteins or peptides containing RGD*X*, the Fg γC dodecapeptide binds exclusively to αIIbβ3 and is demonstrated to support platelet binding even in the presence of RGD blockers [78-80].

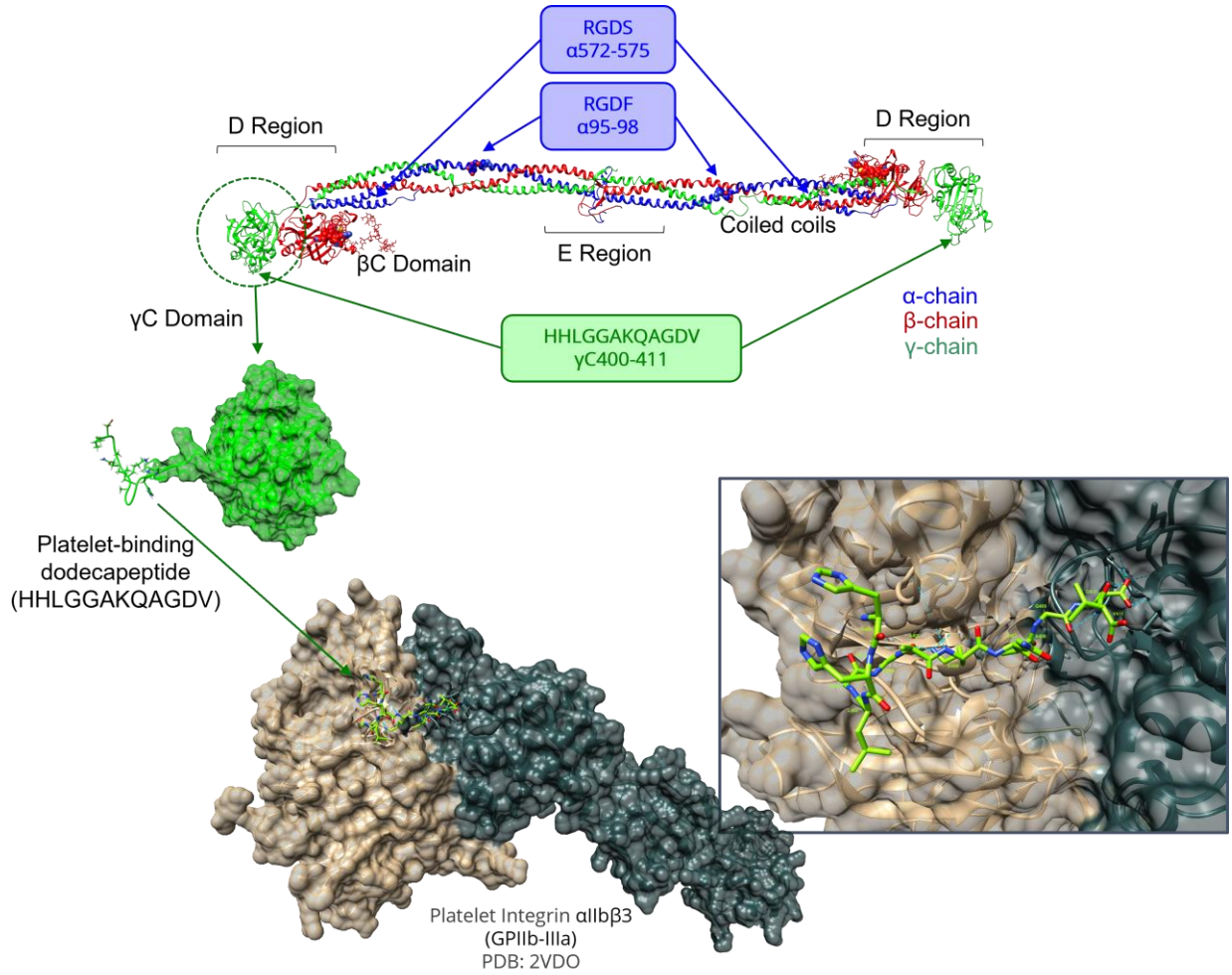

Figure 1.2. Molecular Structure of Fg and its binding sites to platelet integrin αIIbβ3 (GPIIb-IIIa). The three primary platelet binding sites are depicted: Aα95-98 (RGDF), Aα572-575 (RGDS) and the non-RGD dodecapeptide sequence at γC400-411 (HHLGGAKQAGDV). The γC domain is magnified, depicting the unordered platelet-binding dodecapeptide and its binding pocket within the platelet integrin αIIbβ3 (GPIIb-IIIa). (*Figures rendered in UCSF Chimera using PDB structures 3ghg for Fg and 2vdo for GPIIb-IIIa*)

While knowledge of Fg deposition's integral role in inciting a host response is well-accepted in the field of hemocompatibility, the molecular-level interactions that occur at the biomaterial interface have historically not been well characterized and remain a topic of contention. However, research within the last decade in this area has made great strides in unveiling the mystery behind Fg deposition and generated increasing interest in how changes in its adsorbed orientation or conformation can affect its molecular potency and subsequent

platelet recruitment [35]. Established reports have shown that Fg's adsorption-induced conformation change plays a direct role in platelet adhesion and activation through the display of platelet binding epitopes, primarily at the γC dodecapeptide [36-37]. This is corroborated by the finding that unstimulated platelets bind exclusively to immobilized Fg at this sequence, but not to soluble Fg [38]. Further investigation reveals that once adsorbed, Fg's α-helices are converted to random chains that are predominantly located on the C-terminal region of the Bβ and γ chains, which are now exposed and available for platelet interaction [39-41]. Therefore, maintaining the secondary structure of the adsorbed Fg to that of the native structure may lower the resultant surface thrombogenicity. Santore and colleagues also demonstrated that denaturation and/or reorientation of adsorbed Fg/HSA is driven by hydrophobic interactions with the interface, and that this molecular relaxation and spreading occurs at faster kinetic rates for HSA, thus making it increasingly difficult for Fg to adsorb with longer HSA residence time [23]. Furthermore, greater surface concentration of HSA over Fg demonstrates an overall reduction in platelet adhesion, and those that do adhere exhibit greater discoid platelet morphology and diminished spreading kinetics, indicating a retardation of platelet adhesion [42]. However, covalent immobilization of HSA on surfaces has proven to be a nonviable approach to ensuring long-term surface passivation. Latour and coworkers demonstrated that although an irreversibly adsorbed HSA layer that retained its native structure greatly resisted platelet adhesion in the short term, a 6-month aging process in physiological saline resulted in a significant degree of unfolding [71]. This unfolding created a denatured and oxidized form of HSA that became recognizable to platelets at the GPIIb-IIIa receptor. This is especially remarkable, considering HSA in its native form has no known GPIIb-IIIa binding sites, thus indicating that adsorption-induced structural changes in HSA elicit platelet adhesion by significantly altering the protein conformation and chemical nature. From this, it is inferred that native protein structure on surfaces is likely difficult to retain for

extended durations, and that irreversibly adsorbed proteins that are initially nonthrombogenic can become so with continued blood exposure and degradation over time. Therefore, to inhibit surface aging conformational changes that could incite delayed thrombogenic activity, proteins should remain reversibly adsorbed such that they can continuously exchange with fresh proteins in a time window before denaturation occurs [71-72].

1.4 Fluoropolymers as promising blood-contacting biomaterials

Fluoropolymers are a class of hydrophobic materials possessing a range of desirable features for biomedical coatings, including biological inertness, chemical resistance, lubricity, durability, and stability. They have seen widespread use as blood-contacting biomaterials in academic research, clinical applications, and commercial products for several decades due to their reported low platelet adhesion and activation compared to other material types [43-48]. Polyurethane (PU) surfaces modified with fluorinated macromolecules yielded a 5x decrease in platelet adhesion compared to unmodified controls, although the amount of adsorbed Fg was not significantly different [43]. Similar effects were observed for plasma-induced graft polymerization of vinylidene fluoride on polyethylene (PE) substrates compared to nongrafted PE [44]. The effect of fluorocarbon chemistries on platelet adhesion and activation extends beyond simply surface coating as well— direct modification of the bulk material, for example, through blending of polyacrylonitrile membranes with 27% poly(vinylidene difluoride) (PVDF) resulted in a marked decrease in platelet aggregation and thrombus formation compared to pure polyacrylonitrile membranes [45]. Abbott Vascular's XIENCE V® Drug Eluting Stent (DES) has seen promising results and low blood activation in a large scale clinical study through coating with poly(vinylidene fluoride-*co*-hexafluoropropylene) (PVDF-HFP) [48]. These are only a handful of

examples demonstrating the utility and versatility of fluoropolymers in blood-contacting applications, but they evidently serve as an excellent starting point for developing and characterizing our panel of coating candidates for the AKTIV device.

Despite these improved outcomes, certain biomedical applications remain intractable and difficult to design appropriate materials for. Currently, expanded polytetrafluoroethylene (ePTFE) vascular grafts for vessel transplants are the commercial and clinical standard for medium-sized vessels ≥5 mm in diameter; however, small diameter vascular grafts (<5 mm in diameter) occlude rapidly and acutely, even with co-administration of potent systemic anticoagulants. Design for these high-shear systems is further complicated when hemodynamics is introduced as an additional factor, where different blood flow regimes in relation to material surfaces initiate the blood coagulation cascade via different pathways. A simplistic view of this divides blood flow into two regimes: arterial (3.0-26 mL/min) and venous (1.2-4.8 mL/min) [70]. In arterial flow regimes, the extrinsic and common coagulation pathways dominate, where platelet adhesion and aggregation occur through Fg binding [64-65] and the shear-dependent exposure of von Willebrand factor (vWF) adhesion motifs to the platelet receptor, GPIb [66]. In venous flow regimes, the intrinsic pathway and contact protein fouling (Factor XII, high molecular weight kininogen (HMWK), prekallikrein (PKK), Factor XI) are the predominant methods for biomaterial-induced coagulation [67]. This also leads to platelet adhesion where the coagulation pathways merge into the common pathway, and as the platelets become activated, they release thrombin which amplifies both platelet and protein-mediated thrombosis in a positive feedback loop [68-69].

While hydrophilic and zwitterionic materials appear to adsorb substantially less protein than hydrophobic materials through the interference of a hydration layer at the material interface, this snapshot view within the timeframe of an *in vitro* static experiment (1-2 hours) does not scale to clinically relevant times of

days to weeks. In fact, such materials like hydrogels are not thrombo-adhesive when exposed to platelets in the short term, but are shown to support platelet aggregation—and worse, embolization—for longer durations, suggesting that platelets become activated through non-adhesive encounters with the biomaterial surface and either form unstable thrombi that shed from the surface or aggregate directly in bloodstream [62-63, 85]. Thus, low-fouling protein-resistant materials may be appropriate for short-term applications (temporary catheters, blood oxygenators, etc.), but are possibly less suitable for long-term indications (stents, vascular prostheses, etc.).

Taken together, when viewing blood-biomaterial interactions from a holistic perspective, attempting to inhibit adverse thromboembolic events by completely abolishing protein adsorption may be too idealistic, and simply reducing protein adsorption without fully eliminating it does not satisfactorily inhibit thrombi/emboli formation in the long-term. Proteomic methods have isolated thousands of distinct proteins from blood plasma [61], and the likelihood of deterring nonspecific protein adsorption from this rich bulk solution—regardless of the protein's relevance to blood coagulation— may prove to be an insurmountable task. The continuous onslaught of this protein mixture found in circulating bloodstream is a challenge that could be better met through an alternative strategy of selective passive adsorption and retention of non-platelet activating proteins like HSA.

Generally, it is well documented that hydrophobic surfaces adsorb higher amounts of protein compared to hydrophilic or zwitterionic counterparts [9, 58]. In aqueous conditions, protein folding is driven by hydrophobic core packing to adopt a native (soluble) conformation. In the presence of a hydrophobic surface, nonspecific protein adsorption is then initiated by the hydrophobic effect, where unpacking of the hydrophobic protein core to associate with the surface is entropically favored to shield the surface from the aqueous bulk medium. As a result, proteins tend to denature more from their native soluble states when

introduced to hydrophobic surfaces at low concentrations where diffusion to the surface is rate-limited, thus permitting protein relaxation and reorientation on the surface before neighboring substrate sites become occupied [23, 59]. However, at high concentration, the total adsorbed amount of protein is strongly dependent on the rate of arrival at the surface (i.e. protein mobility, which is directly related to protein size and surface affinity), and this can directly dictate which proteins are favorably adsorbed/retained, their orientation and surface packing, and final surface concentration and conformation.

This mechanism can then be harnessed in relation to plasma proteins like HSA and Fg while exploiting the natural progression of protein displacement as described by the Vroman Effect. Given the strong structure-function relationship of Fg—namely, its elongated form and the positioning of the platelet-binding γC dodecapeptide at the distal ends of the molecule that enable platelet crosslinking—it is logical to presume the exceptional importance of the structure and orientation it adopts when adsorbed on a given biomaterial surface to its ability to mediate platelet adhesion. Proteins in solution can approach surfaces in a variety of three-dimensional orientations, which affects the adsorption process of those with high aspect ratios (e.g. Fg) considerably more than those with globular structures (HSA). HSA is the earliest-arrival protein with the highest plasma concentration, and we hypothesize that materials which preferentially adsorb and retain large proportions of HSA immediately upon blood exposure leave smaller and fewer available surface sites for subsequent proteins like Fg to adsorb (**Figure 1.3**). Therefore, as a protein ~5x larger than HSA, Fg molecules in the peri-surface bulk protein ensemble with the highest likelihood of adsorbing to the biomaterial surface are those oriented in an end-on position because they approach the surface with a smaller footprint than a molecule in a side-on orientation. Thus, high initial HSA surface concentration indirectly preselects the structure and orientation of subsequently adsorbed Fg.

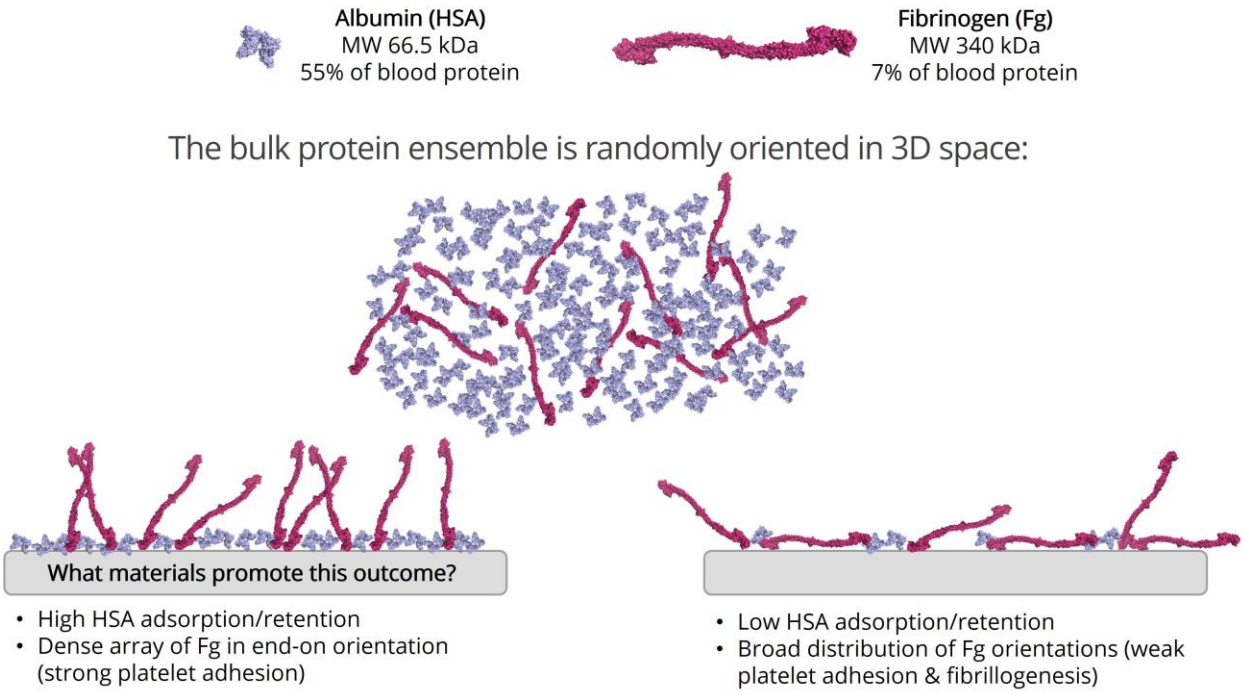

Figure 1.3. HSA is a nonreactive early-arrival protein that can crowd surface sites to bias the adsorption of Fg in favor of orientations that occupy the smallest footprint. We hypothesize that materials which preferentially adsorb and retain large proportions of HSA immediately upon blood exposure leave smaller and fewer available surface sites for subsequent proteins like Fg to adsorb, thus encouraging adsorption in the smallest surface-occupying orientation (i.e. end-on). This orientation yields one γC-domain anchored to the surface and the other γC-domain free for abundant platelet GPIIb-IIIa binding. Conversely, materials that fail to retain substantial quantities of HSA leave large regions of surface sites vacant for Fg adsorption in a variety of orientations (side-on and end-on). Some are able to support platelet adhesion via the γC dodecapeptide while others are associated with the surface or in an orientation that promotes fibrillogenesis (lateral organization into fibrin fibers). The overall effect yields weak platelet adhesion subject to dendritic-type morphologies and detachment from the biomaterial surface as thromboemboli.

Our current understanding of hemocompatibility is complex and without consensus, but evidence supports that materials selecting HSA over Fg adsorption in binary solutions exhibit reduced long-term thrombogenicity, with HSA being especially preferred by hydrophobic substrates [60]. To this end, glow discharge fluoropolymer (plasma-polymerized) films have consistently demonstrated exceptionally high retention of HSA [49-50] and low thrombogenicity in *in vitro* studies and in *ex vivo* models compared to non-hydrophobic controls, and even to

other standard fluoropolymers [51-54]. For example, plasma-polymerized tetrafluoroethylene (C_2H_4, TFE) deposited on woven Dacron vascular prostheses significantly improved graft patency in an *ex vivo* baboon femoral shunt model, with high blood flow rates as well as reduced embolization rates compared to untreated controls [11, 55]. Plasma polymerized fluoropolymers have been extensively studied in our group and among campus collaborators, with roots tracing back to the mid 1980s. Also called radio frequency glow discharge (RFGD) treatment, these films are attractive in that they offer a facile way to coat complex geometries with a smooth, robust, and highly crosslinked CF_3-enriched layer without changing bulk material properties to yield highly hydrophobic surfaces [55-57]. The mechanism of action for these materials in relation to blood is not currently well understood—only that *ex vivo* outcomes in several non-human primate studies were exceptionally favorable. Some *in vitro* studies in relation to glow-discharge plasma-polymerized fluorocarbons have demonstrated the formation of a flattened monolayer of platelet membranes via SEM imaging that were nonreactive upon continued blood exposure, with the proposal that the membranes effectively passivate the substrate and conceal it from further interaction with blood components to arrest prolonged platelet activation [81-84]. While this was not reported in the *ex vivo* baboon shunt studies, it is possible that a thin monolayer of inert platelet membranes coated the materials upon extraction and was simply not observed at the time. Therefore, it is perhaps favorable for long-term blood-contacting biomaterials to exhibit an early acute phase of uniform surface thrombus coverage that can be managed pharmacologically in the short-term to ultimately endow the surface with an inert monolayer of the patient's own platelet membranes.

Our research group possesses a well-characterized library of fluoropolymers, of which a subset (all previously mentioned)—plasma-polymerized C_3F_6 (ppC_3F_6), polyvinylidene difluoride (PVDF), and polyvinylidene difluoride-*co*-hexafluoropropylene (PVDF-HFP)—will be studied for differential protein

adsorption (HSA vs. Fg) and Fg surface structure/orientation. Through this work, we hope to shed more light on the interplay of highly hydrophobic surface chemistry with its effect on protein adsorption and downstream mediation of platelet adhesion, and pursue the hypothesis of the platelet passivation mechanism on plasma-polymerized fluoropolymers further.

1.5 Contribution of this dissertation

The goal of this project is to investigate the adsorption mechanism and structural/orientational properties of the blood coagulation protein, fibrinogen (Fg), on hydrophobic fluoropolymers for the development of thromboresistant hemodialyzer surfaces. Adsorbed Fg on blood-contacting surfaces has long been associated with platelet binding and aggregation, yet soluble Fg remains unbound by circulating platelets in native bloodstream. This suggests that contact with synthetic biomaterials induces an activated conformational state of Fg that exposes its platelet-recognition domains and promotes platelet adhesion. While platelet adhesion is considered a hallmark of thrombosis to be avoided in the development of blood-contacting materials, this view is possibly reductive and deserves reconsideration. Certain reports have shown that platelet membranes themselves after degranulation of activating compounds are nonthrombogenic upon continued exposure to fresh blood [81-84]. Therefore, a surface that can rapidly adhere platelets and promote even spreading to achieve a stable and uniform monolayer of passivating platelet membranes may ultimately prove more hemocompatible in the long-term.

Fluoropolymer coatings, particularly those deposited via radiofrequency glow discharge (RFGD) (i.e. plasma polymerization), have demonstrated reduced thrombogenicity compared to other commercial polymeric counterparts for extended indications, but the mechanism remains to be characterized. The passivating effect of an early platelet membrane monolayer has been suggested for

the plasma-polymerized fluorocarbon films, but a molecular understanding of how blood proteins interact with these surfaces to achieve this effect will enable us to accurately develop criteria for long-term thromboresistant biomaterials. We hypothesize that high initial adsorption and retention of the globular and platelet-inert HSA inhibits random orientations of the elongated Fg from adsorbing by limiting the available surface sites for binding, thus giving favor to Fg molecules approaching the surface in the end-on orientation (which possesses a smaller surface footprint) to adsorb. While HSA coverage may eventually be fully lost over longer durations, by slowing down the rate of Fg adsorption due to high HSA retention and surface crowding, randomly oriented Fg molecules are effectively excluded from the surface, permitting the formation of an organized Fg layer predominantly in the end-on orientation (**Figure 1.3**). Given that the platelet-binding dodecapeptide of Fg is situated on the distal ends of the protein, this end-on oriented layer ultimately yields a dense carpet of platelet-binding contact points, permitting rapid platelet adhesion and spreading such that membranes spread uniformly and reach surface confluence when platelets mechanosense their nearest neighbors. This hypothesis is illustrated in **Figure 1.4**.

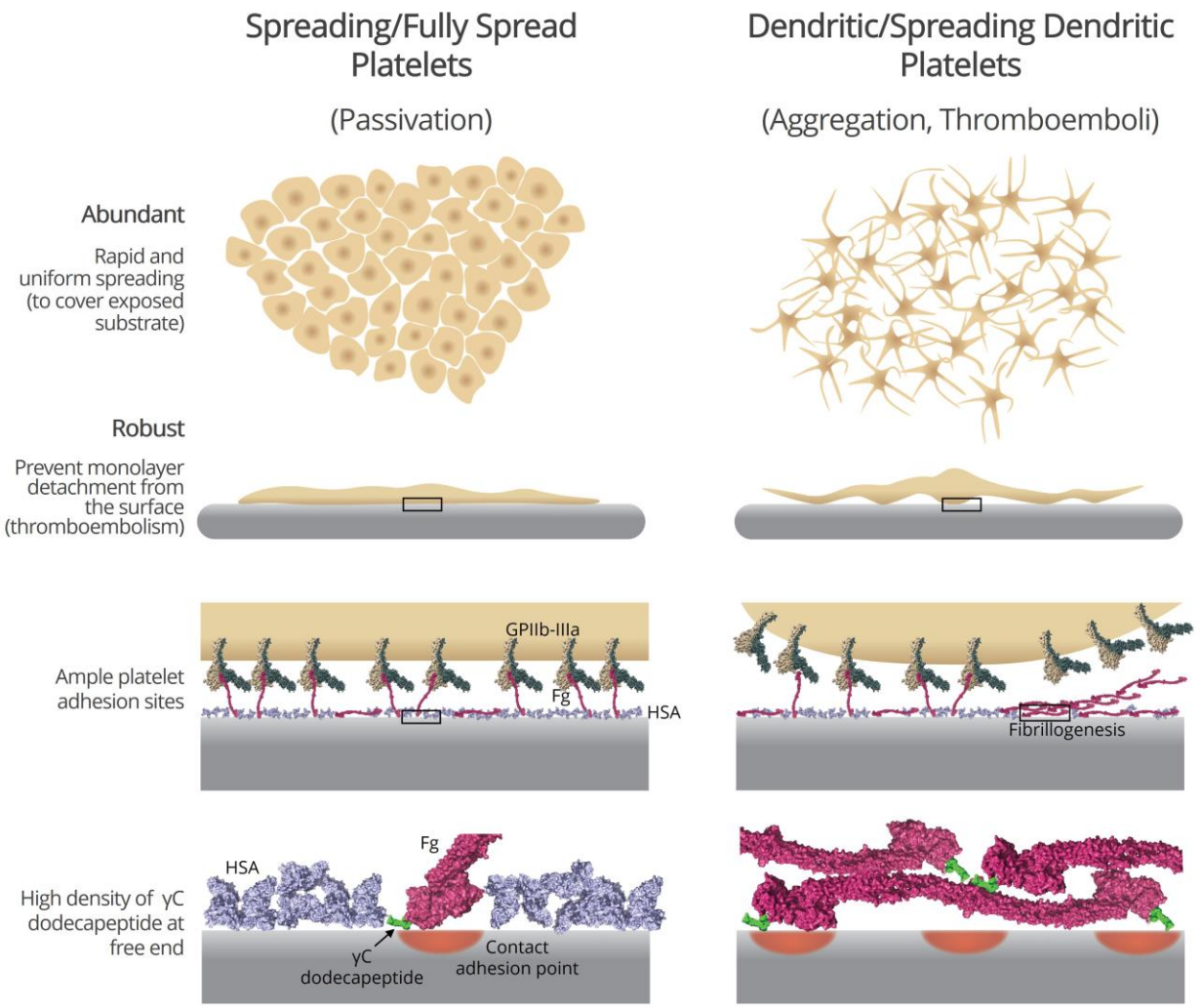

Figure 1.4. The platelet passivation strategy depends on the initial composition and formation of the adsorbed protein layer. (Left) Surface crowding of non-platelet reactive, early-arrival proteins like HSA reduces the amount of available binding sites for platelet-binding, later-arrival proteins like Fg. Therefore, surfaces that adsorb and retain large quantities of HSA bias the adsorption of Fg in favor of orientations that occupy the smallest footprint, i.e. end-on. This results in one hydrophobic Fg γC-domain (containing the γC platelet-binding dodecapeptide) anchored to the surface with the other free end available for binding to the platelet GPIIb-IIIa receptor. Greater proportions of Fg oriented in this way provide ample platelet adhesion sites to facilitate robust binding to the surface, as well as uniform spreading to rapidly cover any exposed biomaterial substrate. **(Right)** Surfaces with low HSA retention leave abundant surface sites for Fg to adsorb in random orientations that provide weak platelet adhesion. This results in more dendritic/spreading dendritic platelet morphologies that are poorly adhered to the surface and leave large regions of exposed biomaterial substrate, prolonging the duration of materials-induced blood activation and increasing risk for thromboembolism. Furthermore, side-on adsorbed Fg exposes the fibrinopeptides A/B for thrombin-mediated cleavage and fibrillogenesis to form fibrin fibers that entrap platelets (aggregation).

In this dissertation, we investigated differential HSA:Fg binding affinity to three fluoropolymer surfaces (ppC_3F_6, PVDF, and PVDF-HFP) using QCM-D to identify optimal surface modifications that demonstrate the greatest HSA adsorption. QCM-D will also inform us of adsorption kinetics, degree of HSA retention when followed by sequential Fg exposure, and film mechanics for a holistic *in situ* understanding of the Vroman Effect. Immunoassays employing monoclonal antibodies directed against fibrinogen's platelet-binding epitopes will quantitate available binding sites of Fg adsorbed on different FPs, as well as coarsely interpret surface orientation. Surface structure and orientation will also be interrogated using atomic force microscopy (AFM), adsorbed-state circular dichroism (CD), and electron spectroscopy for chemical analysis (ESCA). MD simulations will provide an atomistic explanation of structurally sensitive regions of Fg that are affected in clinically recorded mutations presenting with pro-thrombotic phenotypes. Finally, the ultimate effect of surface-induced changes in Fg based on materials surface chemistry will be assessed by incubation with platelet-rich plasma (PRP) to compare differences in platelet adhesion and activation. Altogether, this project seeks to shape our criteria for long-term hemocompatible coatings by characterizing the adsorption interactions between Fg and fluoropolymers that inhibit their propensity for prolonged platelet activation. Design of such materials based on these criteria will lengthen the lifespan of blood-contacting medical devices and reduce the risk of patients experiencing catastrophic thromboembolic events. Ideally, it would also obviate the need for continuous heparinization and antiplatelet administration that place patients at hemorrhagic risk, possibly requiring only a mild nonsteroidal anti-inflammatory drug (NSAID) like aspirin per day.

1.6 References

1. "Kidney Disease Statistics for the United States." *National Institute of Diabetes and Digestive and Kidney Diseases*, U.S. Department of Health and Human Services, 1 Dec. 2016, www.niddk.nih.gov/health-information/health-statistics/kidney-disease.
2. Sharma, S., & Sarnak, M. J. (2017). Epidemiology: The global burden of reduced GFR: ESRD, CVD and mortality. *Nature Reviews Nephrology*, **13**(8), 447–448.
3. 2016 USRDS Annual Data Report. "Chronic Kidney Disease (CKD) Surveillance System." *Centers for Disease Control and Prevention*, 31 Dec. 2016, nccd.cdc.gov/CKD/detail.aspx?Qnum=Q67.
4. Murdeshwar, H.N. & Anjum F. Hemodialysis. 2022 Nov 20. In: StatPearls [Internet]. Treasure Island (FL): StatPearls Publishing; 2022 Jan–. PMID: 33085443.
5. Fisher, M., Golestaneh, L., Allon, M., Abreo, K. & Mokrzycki, M.H. Prevention of Bloodstream Infections in Patients Undergoing Hemodialysis. *Clin J Am Soc Nephrol.***15**(1):132-151 (2020).
6. Murea, M., Geary, R.L., Davis, R.P. & Moossavi S. Vascular access for hemodialysis: A perpetual challenge. *Semin Dial.* **32**(6):527-534 (2019).
7. Schwanke, A.A., Danski, M.T.R., Pontes, L., Kusma, S.Z. & Lind, J. Central venous catheter for hemodialysis: incidence of infection and risk factors. *Rev Bras Enferm.* **71**(3),1115-1121 (2018).
8. Quinton, W., Dillard, D. & Scribner, B.H. Cannulation of blood vessels for prolonged hemodialysis. *Trans Am Soc Artif Intern Organs.* **6**, 104-113 (1960).
9. Ratner, B.D. Biomaterials Science: An Introduction to Materials in Medicine. 3rd ed. Academic Press (2013).
10. Kamberi, M., Pinson, D., Pacetti, S., Perkins, L.E.L., Hossainy, S., Mori, H. et al. Evaluation of chemical stability of polymers of XIENCE everolimus-eluting coronary stents *in vivo* by pyrolysis-gas chromatography/mass spectrometry. *J Biomed Mater Res Part B Appl Biomater.* **106**(5),1721–9 (2018).
11. Garfinkle, A.M., Hoffman, A.S., Ratner, B.D., Reynolds, L.O. & Hanson, S.R. Effects of a tetrafluoroethylene glow discharge on patency of small diameter dacron vascular grafts. *Trans Am Soc Artif Intern Organs.* **30,** 432-439

(1984).

12. Gorbet, M.B. & Sefton, M.V. Biomaterial-associated thrombosis: roles of coagulation factors, complement, platelets and leukocytes. *Biomaterials*. **26**, 5681-703 (2004).
13. Clagett, G.P. & Eberhart, R.C. "Artificial devices in clinical practice." *Hemostasis and thrombosis: basic principles and clinical practice* **3**, 1486-505 (1994).
14. Bittl, J.A. Coronary stent occlusion: thrombus horribilis. *J Am Coll Cardiol.* **28**, 368-370 (1996).
15. Eberhart, R.C. & Clagett, C.P. Catheter coatings, blood flow, and biocompatibility. *Semin Hematol.* **28**, 42-48 (1991).
16. Geiser, T., Sturzenegger, M., Genewein, U., Haeberli, A., & Beer, J. H. Mechanisms of cerebrovascular events as assessed by procoagulant activity, cerebral microemboli, and platelet microparticles in patients with prosthetic heart valves. *Stroke*, **29**(9), 1770-1777 (1998).
17. Vroman, L., & Adams, A.L. Findings with the recording ellipsometer suggesting rapid exchange of specific plasma proteins at liquid/solid interfaces. *Surface Science*, **16**, 438-446 (1969).
18. Vroman, L., & Adams, A.L. Identification of rapid changes at plasma–solid interfaces. *Journal of biomedical materials research*, **3**(1), 43-67 (1969).
19. Wulf, K., Tschierschky, U., Eickner, T., Grabow, N., & Mundkowski, R. G. Studies on the interaction of polylactid-based planar and nanoparticular biomaterials with serum albumin and fibrinogen. *Colloids and Surfaces B: Biointerfaces*, **159**, 1–6 (2017).
20. Vroman, L., Adams, A.L. Adsorption of Proteins out of Plasma and Solutions in Narrow Spaces. *J. Colloid Interface Sci.* 111(2):391-402 (1986).
21. Jung, S.Y., Lim, S.M., Albertorio, F., Kim, G.,Gurau, M.C., Yang, R.D., Holden, M.A., Cremer, P.S. The Vroman Effect: A molecular Level Description of Fibrinogen Displacement. *J. Am. Chem. Soc.* 125(42):12782:12786 (2003).
22. Grunkemeier, J. M., Tsai, W. B., Mcfarland, C. D., & Horbett, T. A. The Effect of Adsorbed Fibrinogen, Fibronectin, von Willebrand Factor, and Vitronectin on the Procoagulant State of Adherent Platelets. *Biomaterials*, **21**, 2243–2252 (2000).
23. Wertz, C. F., & Santore, M. M. Adsorption and relaxation kinetics of albumin and fibrinogen on hydrophobic surfaces: Single-species and competitive behavior. *Langmuir*, **15**(26), 8884–8894 (1999).
24. Ball, V. Mechanism of Interfacial Exchange Phenomena for Proteins Adsorbed at Solid-Liquid Interfaces, in: M. Malmsten (ed.), *Biopolymers at*

Interfaces, vol. 110, Marcel Dekker, New York, 2003, pp. 295-320.

25. Huetz, P., Ball, V., Voegel, J.C., Schaaf, P. Exchange Kinetics for a Heterogeneous Protein System on a Solid-Surface. *Langmuir*. **11,** 3145-3152 (1995).
26. Hirsh, S.L., Bilek, M.M.M., Nosworthy, N.J., Kondyurin, A., dos Remedios, C.G., McKenzie, D.R. A Comparison of Covalent Immobilization and Physical Adsorption of a Cellulase Enzyme Mixture. *Langmuir*. **12,** 4857-4865 (2010).
27. Hirsh, S.L., McKenzie, D.R., Nosworthy, N.J., Denman, J.A., Sezerman, O.U., Bilek M.M.M. The Vroman Effect: Competitive Protein Exchange with Dynamic Multilayer Protein Aggregates. *Colloids Surf. B.* **103,** 395-404 (2013).
28. Heinrich, L., Mann, E.K., Voegel, J.C., Koper, G.J.M., Schaaf, P. Scanning Angle Reflectometry Study of the Structure of Antigen-Antibody Layers Adsorbed on Silica Surfaces. *Langmuir*. **11,** 4008-4012 (1996).
29. Sen Gupta, A., Wang, S., Link, E., Anderson, E.H., Hofmann, C., Lewandowski, J., Kottke-Marchant, K., Marchant, R.E. Glycocalyx-mimetic Dextran-Modified Poly(Vinyl Amine) Surfactant Coating Reduces Platelet Adhesion on Medical-Grade Polycarbonate Surface. *Biomaterials*, **27**(16), 3084-3095 (2006).
30. Xu, H., Kaar, J.L., Russell, A.J., Wagner, W.R. Characterizing the Modification of Surface Proteins with Poly(Ethylene Glycol) to Interrupt Platelet Adhesion. *Biomaterials*, **27**(16), 3125-3135 (2006).
31. Yu, S.H., Mi, F.L., Shyu, S.S., Tsai, C.H., Peng, C.K., Lai, J.Y. Miscibility, Mechanical Characteristic, and Platelet Adhesion of 6-O-Carboxymethylchitosan/polyurethane Semi-IPN Membranes. *J. Memb. Sci.* **276**(1-2), 68-80 (2006).
32. Shattil, S.J., Hoxie, J.A., Cunningham, M., Brass, L.F. Changes in the Platelet Membrane Glycoprotein IIb.IIIa Complex During Platelet Activation. *J. Biol. Chem.* **260**, 11107 (1985).
33. D'Souza, S.E., Ginsberg, M.H., Matsueda, G.R., Plow, E.F. A Discrete Sequence in a Platelet Integrin is Involved in Ligand Recognition. *Nature*. **350**, 66-68 (1991).
34. Tsai, W.B., Grunkemeier, J.M., McFarland, C.D., Horbett, T.A. Platelet Adhesion to PS-Based Surfaces Preadsorbed with Plasmas Selectively Depleted in Fibrinogen, Fibronectin, Vitronectin, or von Willebrand's Factor. *J Biomed Mater Res.* **60**(3), 348-359 (2002).
35. van Damme, H.S., Feijen, J. Modern Aspects of Protein Adsorption on Biomaterials. Missirlis, Y.F., Ed. *Kluver Academic:* Lemm (1991).

36. Clarke, M.L., Wang, J., Chen, Z. Conformational Changes of Fibrinogen After Adsorption. *J. Phys. Chem. B.* **109**(46),22027-22035 (2005).

37. Hylton, D.M., Shalaby, S.W., Latour, R.A. Direct Correlation Between Adsorption-Induced Changes in Protein Structure and Platelet Adhesion. *J. Biomed. Mater. Res. B.* **73A**(3):349-358 (2005).

38. Savage, B., Ruggeri, Z.M. Selective Recognition of Adhesive Sites in Surface-Bound Fibrinogen by Glycoprotein IIb-IIIa on Nonactivated Platelets. *J. Biol. Chem.* **266**(17), 11227-33 (1991).

39. Spraggon, G., Everse, S.J., Doolittle, R.F. Crystal Structures of Fragment D from Human Fibrinogen and its Crosslinked Counterpart from Fibrin. *Nature*. **389**, 455-462 (1997).

40. Hawiger, J., Timmons, S., Kloczewiak, M., Strong, D.D., Doolittle, R.F. Gamma and Alpha Chains of Human Fibrinogen Possess Sites Reactive with Human Platelet Receptors. *Proc. Natl. Acad. Sci.* **79**(6), 2068-2071 (1982).

41. Chiumiento, A., Lamponi, S., & Barbucci, R. Role of fibrinogen conformation in platelet activation. *Biomacromolecules*, **8**(2), 523–531 (2007).

42. Park, K., Mao, F. W., & Park, H. Morphological characterization of surface-induced platelet activation. *Biomaterials*, **11**(1), 24–31 (1990).

43. Massa, T.M., McClung, W.G., Yang, M.L., Ho, J.Y.C., Brash, J.L. & Santerre J.P. Fibrinogen adsorption and platelet lysis characterization of fluorinated surface-modified polyetherurethanes. *J Biomed Mater Res A* **81A**(1), 178-185 (2006).

44. Lin, J.C., Tiong, S.L. & Chen, C.Y. Surface characterization and platelet adhesion studies on fluorocarbons prepared by plasma-induced graft polymerization. *J Biomed Sci Polym Ed,* **11**(7), 701-714 (2000).

45. Liu, T.Y., Lin, W.C., Huang, L.Y., Chen, S.Y. & Yang, M.C. Surface characteristics and hemocompatibility of PAN/PVDF blend membranes. Polym. Adv. Technol. **16**(5), 413-419 (2005).

46. Paton, D.M., Ashton, T.R. & Roshan, M. Fluorinating polymer surfaces. US patent 5356668 (Oct 18, 1994).

47. Lilenfeld, R., Popadiuk, N.M., Steinheuser, P. & Menezes, E. Surgical filaments from vinylidene fluoride copolymers. US patent 4564013 (Jan 14 1986)

48. Grube *et al.* The SPIRIT V study: A clinical evaluation of the XIENCE V everolimus-eluting coronary stent system in the treatment of patients with de novo coronary artery lesions. *JACC: Cardiovasc. Interventions,* **4**(2), 168-175 (2011).

49. Bohnert, J.L., Fowler, B.C., Horbett, T.A. & Hoffman, A.S. Plasma gas

discharge deposited fluorocarbon polymers exhibit reduced elutability of adsorbed albumin and fibrinogen. *J Biomater Sci Polym Ed.* **1**(4), 279-297 (1990).

50. Kiaei, D., Hoffman, A.S. & Horbett, T.A. Tight binding of albumin to glow discharge treated polymers. *J Biomater Sci Polym Ed.* **4**(1), 35-44 (1992).
51. Yeh, Y.S., Iriyama, Y., Matsuzawa, Y., Hanson, S.R. & Yasuda, H. Blood compatibility of surfaces modified by plasma polymerization. *J Biomed Mater Res* **22**(9), 795-818 (1988).
52. Kiaei, D., Hoffman, A.S., Horbett, T.A. & Lew, K.R. Platelet and monoclonal antibody binding to fibrinogen adsorbed on glow-discharge-deposited polymers. *J Biomed Mater Res.* **29**(6), 729-39 (1995).
53. Kiaei, D., Hoffman, A.S. & Hanson, S.R. Ex vivo and in vitro platelet adhesion on RFGD deposited polymers. *J Biomed Mater Res.* **26**(3), 357-72 (1992).
54. Kiaei, D., Hoffman, A.S., Ratner, B.D., Horbett, T.A. & Reynolds, L.O. Blood interaction with gas discharge treated vascular grafts. *ACS Polym. Mat. Sci. Eng.* **56**, 710-714 (1987).
55. Hoffman, A.S. *et al.* The small diameter vascular graft — a challenging biomaterials problem. *Mat. Res. Soc. Symp. Proc.* **55**, 3-15 (1986).
56. Garrison, M. D., Luginbühl, R., Overney, R. M., Ratner, B. D. Glow discharge plasma deposited hexafluoropropylene films: surface chemistry and interfacial materials properties. *Thin Solid Films* **352**, 13-21 (1999).
57. Luginbühl, R. e*t al.* Comprehensive surface analysis of hydrophobically functionalized SFM tips. *Ultramicroscopy* **82**(1–4), 171-179 (2000).
58. Brash, J.L., Sharma, C.P. & Szycher, M. (Eds.). Blood compatible materials and devices, *Technomic Publishing Company*, Lancaster, 3-24 (1991).
59. Santore, M.M. & Wertz, C.F. Protein spreading kinetics at liquid-solid interfaces via an adsorption probe method. *Langmuir*, **21**, 10172-78 (2005).
60. Nonckreman, C.J., Fleith, S., Rouxhet, P.G. & Dupont-Gillain, C.C. Competitive adsorption of fibrinogen and albumin and blood platelet adhesion on surfaces modified with nanoparticles and/or PEO. *Colloids Surf. B*, **77**, 139-149 (2010).
61. Pieper, R. e*t al.* The human serum proteome: display of nearly 3700 chromatographically separated protein spots on two-dimensional electrophoresis gels and identification of 325 distinct proteins. *Proteomics,* **3**(7), 1345-64 (2003).
62. Cholakis, C.H., Zingg, W. & Sefton, M.V. Effect of heparin-pva hydrogel on platelets in a chronic canine arterio-venous shunt. *J Biomed Mater Res.*

23(4), 417-441 (1989).

63. Hanson, S.R., Harker, L.A., Ratner, B.D. & Hoffman, A.S. In vivo evaluation of artificial surfaces with a nonhuman primate model of arterial thrombosis. *J Lab Clin Med*, **95**(2), 289-304 (1980).

64. Tsai, W.B., Grunkemeier, J.M. & Horbett, T.A. Variations in the ability of adsorbed fibrinogen to mediate platelet adhesion to polystyrene-based materials: a multivariate statistical analysis of antibody binding to the platelet binding sites of fibrinogen. *J Biomed Mater Res.* **67A**(4), 1255-1268 (2003).

65. Soman, P., Rice, Z. & Siedlecki, C.A. Measuring the time-dependent functional activity of adsorbed fibrinogen by atomic force microscopy. *Langmuir*, **24**(16), 8801-8806 (2008).

66. Schneider, S.W. *et al.* Shear-induced unfolding triggers adhesion of von Willebrand factor fibers. *PNAS*, **104**(19), 7899-7903 (2007).

67. Spijker, H.T., Graaf, R., Boonstra, P.W., Busscher, H.J. & van Oeveren, W. On the influence of flow conditions and wettability on blood material interactions. *Biomaterials,* **24**(26), 4717-4727 (2003).

68. Sperling, C., Fischer, M., Maitz, M.F. & Werner, C. Blood coagulation on biomaterial requires the combination of distinct activation processes. *Biomaterials*, **30**(27), 4447-4456 (2009).

69. Okamura, Y. e*t al.* A few immobilized thrombins are sufficient for platelet spreading. *Biophys J.* **100**(8), 1855-1863 (2011).

70. Klarhöfer, M., Csapo, B., Balassy, Cs., Szeles, J.C. & Moser, E. High-resolution blood flow velocity measurements in the human finger. *Magnetic Resonance in Medicine*, **45**(4), 716-719 (2001).

71. Sivaraman, B. & Latour, R.A. Time-dependent conformational changes in adsorbed albumin and its effect on platelet adhesion. *Langmuir*, **28**, 2745-2752 (2012).

72. Leonard, E.F. & Vroman, L. Is the Vroman effect of importance in the interaction of blood with artificial materials? *J Biomater Sci Polym Ed.* **3**, 95-107 (1991).

73. Brash, J.L. & Samak, Q.M. Dynamics of interactions between human albumin and polyethylene surface. *J. Colloid Interface Sci.* **65**(3), 495-504 (1978).

74. Ballet, T., Boulange, L., Brechet, Y., Bruckert, F., and Weidenhaupt, M. Protein conformational changes induced by adsorption onto material surfaces: an important issue for biomedical applications of material science. *Bull. Pol. Acad. Sci. Tech. Sci.* **58**, 303–313 (2010).

75. Long, A. T., Kenne, E., Jung, R., Fuchs, T. A., and Renné, T. Contact system

revisited: an interface between inflammation, coagulation, and innate immunity. *J. Thromb. Haemost*. **14**, 427–437 (2016).

76. Cornelius, R.M., Archambault, J.G., Berry, L., Chan, A. & Brash, J.L. Adsorption of proteins from infant and adult plasma to biomaterial surfaces. *J Biomed Mater Res.* **60**, 622-632 (2002).

77. Salsmann, A., Schaffner-Reckinger, E., Kabile, F., Plancon, S. & Kieffer, N. A new functional role of the fibrinogen RGD motif as the molecular switch that selectively triggers integrin αIIbβ3-dependent RhoA activation during cell spreading. *J Biol Chem.* **280**(39), 33610—33619 (2005).

78. Bennett, J.S. Platelet-fibrinogen interactions. *Ann N Y Acad Sci.* **936**, 340-354 (2001).

79. Springer, T.A., Zhu, J. & Xiao, T. Structural basis for distinctive recognition of fibrinogen γC peptide by the platelet integrin αIIbβ3. *J Cell Biol.* ***182***(4), 791-800 (2008).

80. Sivaraman, B. & Latour, R.A. The relationship between platelet adhesion on surfaces and the structure versus the amount of adsorbed fibrinogen. *Biomaterials*, **31**, 832-839 (2010).

81. Riederer, M.A., Ginsberg, M.H. & Steiner, B. Blockade of platelet GPIIB-IIIA (integrin alphaII(b)beta(3)) in flowing human blood leads to passivation of prothrombotic surfaces. *Thromb Haemost*. **88**(5), 858-64 (2002).

82. Haycox, C. & Ratner, B.D. *In vitro* platelet interactions in whole human blood exposed to biomaterial surfaces: insights on blood compatibility. *J Biomed Mater Res.* **27**, 1181-1193 (1993).

83. Dion, I., Baquey, C., Candelon, B. & Monties, J.R. Hemocompatibility of titanium nitride. *Int J Artif Organs.* **15**, 617 (1992).

84. Szott, L.M., Irvin, C.A., Trollsas, M., Hossainy, S. & Ratner, B.D. Blood compatibility assessment of polymers used in drug eluting stent coatings. *Biointerphases*, **11**, 029806 (2016).

85. Mehta, R. I., Mehta R. I., Solis, O. E., Jahan, R., Salamon, N., Tobis, J. M., Yong, W. H., Vinters, H. V., Fishbein, M. C. Hydrophilic Polymer Emboli: An Under-Recognized Iatrogenic Cause of Ischemia and Infarct. *Modern Pathology*. **23**, 921-930 (2010).

Chapter 2

Materials preparation & characterization

2.1 Abstract

The core of this dissertation work relies on understanding the effects of surface chemistry on biomolecular interfacial events and characterizing these interactions on different length scales, from atomic at the biomaterial surface level, to molecular at the protein/surface interface, to cellular at the platelet/protein interface. As such, to begin, this chapter will fully detail how each relevant fluoropolymer surface is produced and then characterized for surface elemental and chemical composition (ESCA/XPS), roughness (AFM), thickness (profilometry), and surface energy (water contact angle). These parameters are instrumental in building a body of evidence for the relationship between hydrophobic fluoropolymer biomaterial surfaces to proteins and platelets in our effort to better characterize and identify the optimal coating for blood-contacting applications.

2.2 Methods

2.2.1 Preparation of radio frequency glow discharge (RFGD) plasma-polymerized C_3F_6 (ppC_3F_6)

Plasma polymerization is a powerful method of depositing pinhole-free, high bond strength, and highly crosslinked fluoropolymer coatings that cannot be achieved through conventional techniques [1-4, 31]. The primary advantages of plasma polymerization, particularly for biomedical applications, lay in its obviation of solvents, etchants, initiators, additives, and high temperature processing; conversely, plasma polymerization can be operated at ambient temperature with neutral monomer species in a low pressure (vacuum) environment. The plasma polymerization of perfluorinated monomers including tetrafluoroethylene (TFE, C_2F_4), hexafluoroethane (HFE, C_2F_6), and perfluoropropane (C_3F_8, PFP) has been explored in depth as biomaterials for blood-contacting applications due to their demonstrated low thrombogenicity and ability to selectively tight-bind blood proteins, resist platelet aggregation and activation [5-7, 30].

Our fluoropolymer coating—termed plasma-polymerized C_3F_6 (ppC_3F_6)—is a physicochemical surface modification produced via radio frequency glow discharge (RFGD) deposition, and is a well-documented process amenable to a variety of monomers and substrate types/geometries. The Ratner lab possesses a home-built plasma reactor (**Figure 2.1**) fitted with externally positioned capacitively coupled electrodes spaced 10 cm apart and a 13.56 MHz radio frequency generator to induce plasma that is maintained via a Tegal matching network. The gaseous perfluorinated monomer precursor, hexafluoropropylene (HFP, C_3F_6) (CAS No. 116-15-4, SynQuest Laboratories Inc., Alachua, FL) is injected at low pressure into the plasma reactor chamber under vacuum per previously

described methods [8-9] and subjected to the capacitively coupled electric discharge, causing monomer fragmentation into active species (ions, electrons, atoms, radicals) that react with each other and covalently bind to the substrate. The final polymer film is a random rearrangement of CF, CF_2, and CF_3 species, but with reproducible total compositions of each species when deposition duration, monomer pressure and feed rate, plasma power supply, and substrate positioning within the reactor are maintained. Substrates were reacted in-the-glow (ITG) between the coupled electrodes with the parameters summarized in **Table 2.1**. Briefly, substrate surfaces are first activated via 5 minutes of argon etching, followed by a 5-minute methane (CH_4) gas adhesion layer (G1949112 Ultra High Purity, Matheson, Irving, TX) to prevent C_3F_6 delamination [10]. The HFP monomer precursor is then injected into the chamber at 10 sccm for 1 minute at an elevated power of 60 W for initial adhesion into the CH_4 layer, followed by 20 minutes at a reduced power of 20 W for film deposition. The film was then quenched with 5 minutes of monomer flow sans application of power, then slowly returned to atmospheric pressure under argon.

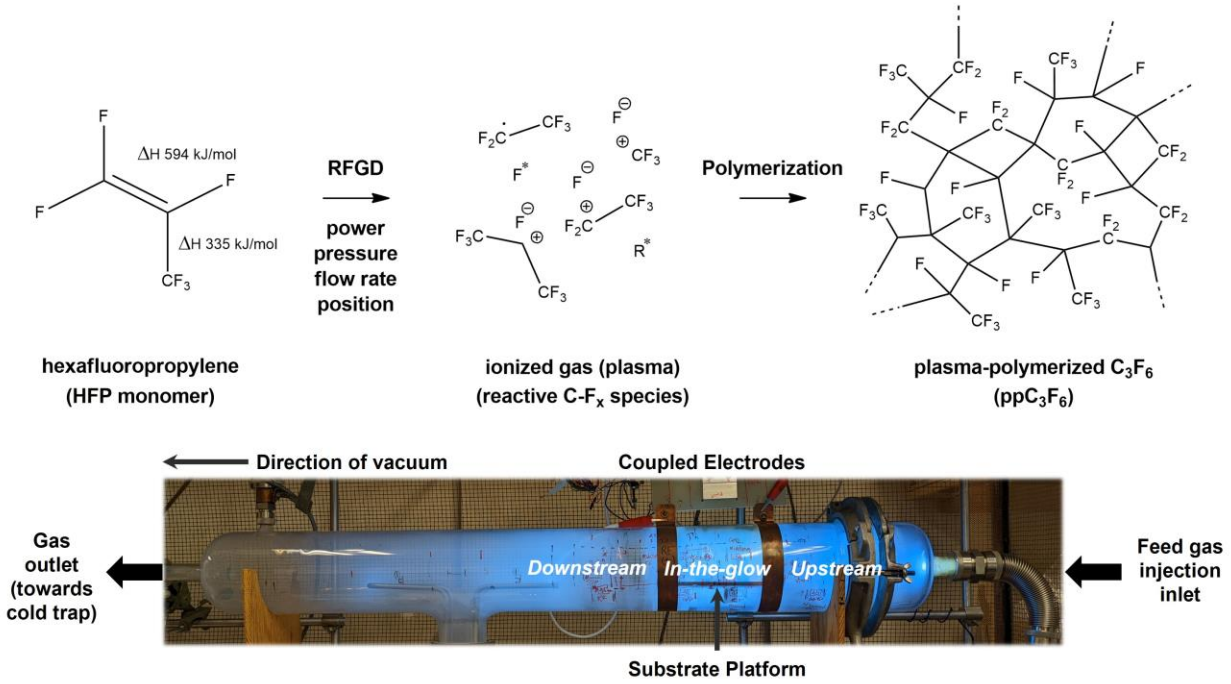

Figure 2.1. In-House Plasma Reactor Chamber. Our fluoropolymer coating—termed

plasma-polymerized C_3F_6 (ppC_3F_6)—is a physicochemical surface modification produced via radio frequency glow discharge (RFGD) deposition. The gaseous perfluorinated monomer precursor, hexafluoropropylene (HFP, C_3F_6) is injected at low pressure into the plasma reactor chamber under vacuum and subjected to the capacitively coupled electric discharge, causing monomer fragmentation into active species that react with each other and covalently bind to the substrate. The final polymer film is a random rearrangement of CF, CF_2, and CF_3 species, but with reproducible total compositions of each species when deposition duration, monomer pressure and feed rate, plasma power supply, and substrate positioning within the reactor are maintained.

Table 2.1. Plasma Deposition Parameters. Standard parameters for producing ppC_3F_6 films.

	Pressure (mTorr)	Power (W)	Flow Rate (sccm)	Duration (min)
Ar Surface Etch	200	40	62.1	5
CH_4 Adhesion Layer	150	80	1.5	5
C_3F_6 Adhesion Layer	150	60	10	1
C_3F_6 Deposition Layer	150	20	10	20
C_3F_6 Monomer Quench	150	0	10	5
Return samples to atmospheric pressure under argon.				

2.2.2 Preparation of spin-coated fluoropolymers

Poly(vinylidene-fluoride) (PVDF) (Cat. No. 427152, Sigma-Aldrich, St. Louis, MO) and poly(vinylidene fluoride-*co*-hexafluoropropylene) (PVDF-HFP) (Cat. No. 427160, Sigma-Aldrich, St. Louis, MO) pellets were dissolved in dimethylformamide (DMF) in a 65 °C oven for 1 hour to final concentrations of 2.7 w/w% and 2.3 w/w%, respectively. Depending on the intended usage and unless otherwise mentioned, the PVDF and PVDF-HFP fluoropolymer solutions were spin-coated (P6700 Programmable Tabletop Spin Coater, Specialty Coating Systems Inc., Indianapolis, IN) onto a variety of substrates: RCA SC1-cleaned Au-coated quartz sensors for QCM-D studies (Chapter 3.3), silicon chips for AFM imaging (Chapter 4.3.1.2), or 15 mm clean glass coverslips for platelet studies (Chapter 6.3). Spin-coating was performed using pre-optimized settings developed

by lab alumna, Irini Sotiri. Briefly, the spin coater chamber was backfilled with nitrogen to reduce humidity and a nitrogen nozzle was positioned 1 inch directly above the vacuum-mounted substrate during spin coating supplying fresh N_2 gas at 50 kPa. 85-120 µL of the polymer solution was pipetted onto 12-15 mm diameter substrates, ensuring total coverage of the substrate before spinning. Substrates are spun for 2 minutes at 2000 rpm with 5 second ramp-up and ramp-down times, then annealed overnight at 65 °C to prevent vapor-induced phase separation. For glass coverslip substrates, an additional ethylmethacrylate-silane (EMA-silane) layer was spin-coated directly onto the glass to provide better adhesion for the PVDF or PVDF-HFP coating on top. Delamination testing was performed to ensure coating stability in liquid media and was performed by submerging coated substrates in deionized water overnight on an orbital shaker, drying, and comparing ESCA/XPS spectra to that of a non-washed coated control. All substrates processed this way passed delamination testing.

2.2.3 Electron spectroscopy for chemical analysis (ESCA)

Evaluation of substrate coverage and confirmation of elemental composition and surface chemistries was determined using electron spectroscopy for chemical analysis (ESCA) (also known as x-ray photoemission spectroscopy, XPS) on a Kratos AXIS Ultra DLD XPS instrument (Kratos Analytical Ltd., Manchester, UK) at the National ESCA and Surface Analysis Center for Biomedical Problems (NESAC/BIO, University of Washington, Seattle, WA). A monochromatic Al K_α x-ray source was used with a hemispherical electron energy analyzer at a take-off angle (i.e. angle between substrate surface normal and analyzer axis) of 0° corresponding to a surface penetration depth of ~100 Å, and surface charging on the non-conductive fluoropolymer films was compensated for by a 5 eV electron flood gun. Compositional survey scans (0-1200 eV; 1 eV step size; 160 eV pass

energy) and high-resolution C1s scans (280-300 eV; 0.1 eV step size; 20 eV pass energy) were collected with a 700 x 300 μm x-ray spot size, and pressure in the analytical chamber during acquisition was maintained at $<10^{-8}$ Torr. Spectral binding energies were referenced to the standard aliphatic hydrocarbon (C-H) peak at 285.0 eV for PVDF and PVDF-HFP [11], and the CF_2 peak at 292.0 eV for the ppC_3F_6 C1s envelope [8, 12, 29]. All peak identification and area calculations from survey scans for elemental analysis were performed in the Kratos Vision2 software (Kratos Analytical, Manchester, UK). High-resolution C1s envelope spectra were resolved into Gaussian peaks with matching constrained FWHMs using least-squares fitting and subtracted by a Shirley background for peak area quantification (CasaXPS software, Ltd.). Compositions are reported as atomic percent and represent the average of n=3 spots (elemental, survey scans) or n=2 spots (carbon chemical environment, high-resolution C1s) per material type.

2.2.4 Atomic force microscopy (AFM)

Surface morphology and topography of fluoropolymer films was imaged using a Dimension ICON with ScanAsyst atomic force microscope (AFM) in tapping mode (Bruker Corporation, Billerica, MA) using 70 kHz silicon nitride cantilever probes (SCANASYST-AIR, Bruker Corporation, Billerica, MA). Scans were acquired on the NanoScope 8.15 software and post-acquisition data analysis was performed using Gwyddion 2.51. Root mean square (RMS) surface roughness was determined for each material type (n=3).

2.2.5 Profilometry

Film thicknesses were determined using a Bruker OM-DektakXT profilometer (Bruker Corporation, Billerica, MA) with a 2 μm radius diamond stylus. Three scratches were created across each surface type using a razor blade, and thickness

was measured using the hill-and-valley profile acquisition setting and reported in nm (n=3).

2.2.6 Water contact angle & surface free energy

Water contact angle (WCA) was measured on a Krüss Drop Shape Analyzer goniometer (DSA100L, Krüss GmbH, Hamburg, Germany). A total of n=7 WCA sessile drop measurements were taken per two 2.0 µL droplets on each substrate (n=14), and this was performed for triplicate substrates of each material type. Droplets were made using Krüss ADVANCE 1.7.2.1 software and fit with an ellipse shape fitting method and automated baseline generation for WCA measurement. The same process was repeated with diiodomethane as a nonpolar probe solvent in order to determine surface free energy (SFE, mN/m) using the Owens-Wendt-Rabel-Kaelble (OWRK) Model.

2.3 Results

2.3.1 ESCA (Chemical Composition)

ESCA/XPS survey scans were used to confirm chemical compositions of fluoropolymer films and their integrity following delamination testing. Elemental percentages are summarized in **Table 2.2**, with representative high-resolution C1s spectra presented in **Figure 2.2**. PVDF and PVDF-HFP showed only presence of carbon and fluorine before and after delamination testing, indicating robust spin-coated layers with no remnants of DMF solvent in the final coating. Silicon peaks from the underlying glass substrate are not present in the survey scans either, indicating a coating thickness of at least 10 nm. The PVDF coating shows 49.6 ± 1.0% C and 50.4 ± 1.0% F which is in agreement with the theoretically expected 1:1 C:F ratio. The high-resolution C1s scan also depicts 49.3 ± 0.2% C-H

bonds to 50.7 ± 0.1% C-F_2, which matches the 1:1 CH:CF_2 chemical structure of PVDF. Similarly, the PVDF-HFP coating shows good congruency with expected elemental compositions: 46.0 ± 0.6% C to 54.0 ± 0.6% F, with high-resolution C1s peaks corresponding to the proper carbon chemical bonds of C-H (44.9 ± 0.4%), C-F (2.4 ± 0.9), C-F_2 (48.2 ± 0.3), and C-F_3 (4.5 ± 0.2), which matches similar reports in the literature [13]. From these peak percentages, it is evident that PVDF-HFP is a copolymer comprised predominantly of PVDF with only <5% HFP composition.

PpC_3F_6 survey scans showed trace amounts of oxygen incorporation into the polymerized film (<1%) but were otherwise pure carbon and fluorine. From the high resolution C1s scans, the presence of a distinguishable C-CF_x peak indicates successful polymerization of the HFP monomer, which does not possess this chemical bond, and the conversion of the unsaturated C=C double bond to the saturated polymer form. The CF_3 and CF_2 peaks are clearly defined at 293.9 and 292.0 eV, respectively, while the C-F/C=CF_x and C-CF_x peaks are slightly broader at 289.9 and 287.8 eV, respectively (**Table 2.2**). While a substantial portion of monomer compositional structure is retained in the final film (CF_3:CF_2:CF ~1:1:1), there is a 25% reduction in the total F:C ratio down to 1.5 compared to the HFP (C_3F_6) monomer, which has F:C ratio of 2. In other words, there is a distinct loss in fluorine that corresponds to an average of 1-2 fluorine atoms extracted per monomer unit during polymerization, in agreement with reported values [4, 8]. Experimentally, this was physically manifested as the collection of a small quantity of yellow condensate in the cold trap positioned after the reactor chamber outlet and before the vacuum pump, as well as a growing yellow coating on the interior of the reactor chamber that required periodic air etch cleanings between depositions.

Table 2.2. ESCA Elemental and Carbon Envelope Compositions. Summary of surface elemental compositions of PVDF, PVDF-HFP, and ppC_3F_6 surface coatings determined from ESCA survey scans (n=3). High-resolution C1s spectra were resolved into Gaussian peaks using a least-squares fitting method in Hawk Analysis 7.0 software, and peak areas are

reported as percent composition (n=2). Following 24-hour delamination testing, compositions and the high-resolution C1s envelope remained unchanged with only trace amounts of oxygen contaminants detected (<1%), indicating robustness of the deposited coatings.

Survey Spectra					
	F1s		**C1s**		**O1s**
Binding Energy (eV)	**684.9**		**285.0**		**530.1**
Pre-Delamination Test (atomic %)					
PVDF	50.4 ± 1.0		49.6 ± 1.0		-
PVDF-HFP	54.0 ± 0.6		46.0 ± 0.6		-
ppC_3F_6	59.6 ± 0.1		39.8 ± 0.1		0.6 ± 0.0
Post-Delamination Test (atomic %)					
PVDF	49.0 ± 0.2		51.0 ± 0.2		-
PVDF-HFP	52.5 ± 0.8		47.5 ± 0.8		-
ppC_3F_6	59.3 ± 0.1		39.8 ± 0.0		0.9 ± 0.1
High Resolution C1s Spectra					
	C-H	**C-CF_x**	**C-F, C=CF_x**	**C-F_2**	**C-F_3**
Binding Energy (eV)	**285.0**	**287.8**	**289.8**	**292.0**	**293.9**
Pre-Delamination Test (atomic %)					
PVDF	49.3 ± 0.2	-	-	50.7 ± 0.1	-
PVDF-HFP	44.9 ± 0.4	-	2.4 ± 0.9	48.2 ± 0.3	4.5 ± 0.2
ppC_3F_6	-	25.0 ± 0.2	25.7 ± 0.5	25.8 ± 0.2	23.5 ± 0.3
($FWHM_{ppC3F6}$)	-	(1.75)	(1.67)	(1.19)	(1.16)
Post-Delamination Test (atomic %)					
PVDF	50.3 ± 0.5	-	-	49.7 ± 0.2	-
PVDF-HFP	45.9 ± 0.2	-	2.7 ± 0.3	47.0 ± 0.2	4.4 ± 0.6
ppC_3F_6	-	25.4 ± 0.2	24.3 ± 0.4	27.2 ± 0.1	23.1 ± 0.4
($FWHM_{ppC3F6}$)	-	(1.70)	(1.66)	(1.26)	(1.25)

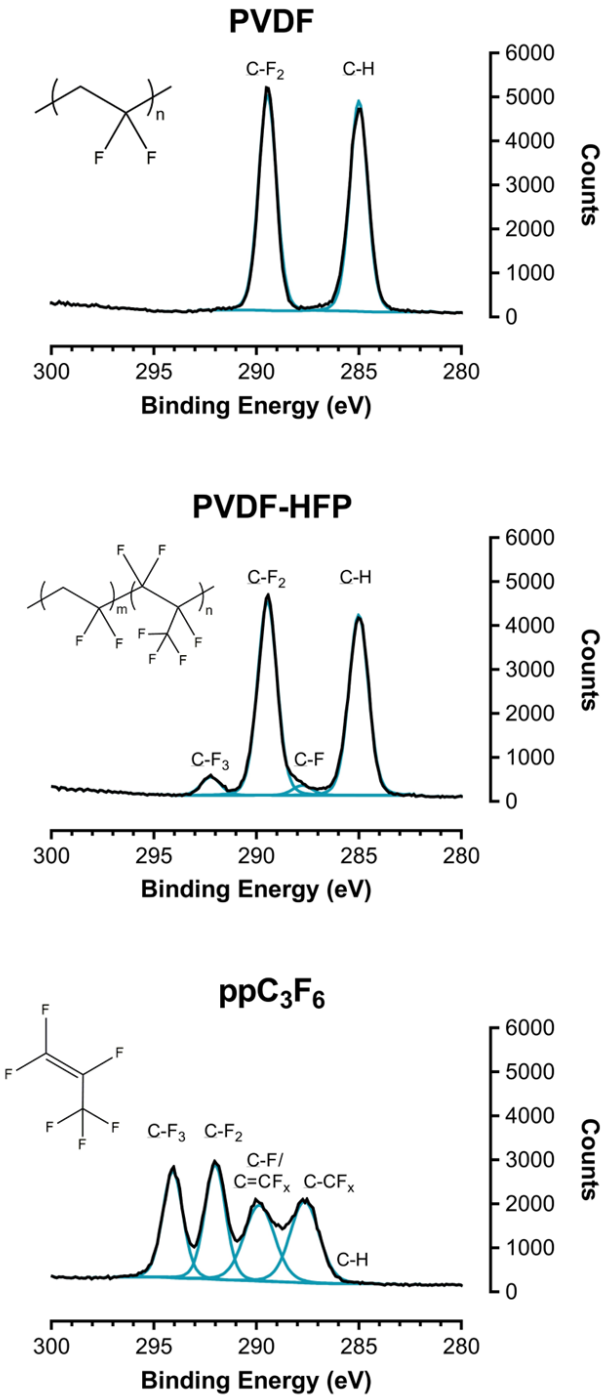

Figure 2.2. Representative high-resolution C1s spectra of PVDF, PVDF-HFP, and ppC_3F_6. The C1s peak (black envelope) is depicted with fitted peaks corresponding to unique carbon bonding environments for each chemical structure (inset: PVDF and PVDF-HFP with respective polymer structures; ppC_3F_6 with hexafluoropropylene monomer structure).

2.3.2 AFM (Surface Roughness and Morphology)

PVDF displays a semi-crystalline morphology with presence of micron and submicron-sized spherulites and mean surface roughness of S_a = 10.7 nm. PVDF-HFP and ppC_3F_6 were considerably smoother, with mean surface roughnesses of S_a = 0.8 nm and S_a = 0.7 nm, respectively. A one-way ANOVA with Tukey HSD post-hoc multiple comparisons test revealed that there was a statistically significant ($p<0.0001$) difference in RMS surface roughness between PVDF and the PVDF-HFP/ppC_3F_6 (n=3). A summary of results is presented in **Figure 2.3**.

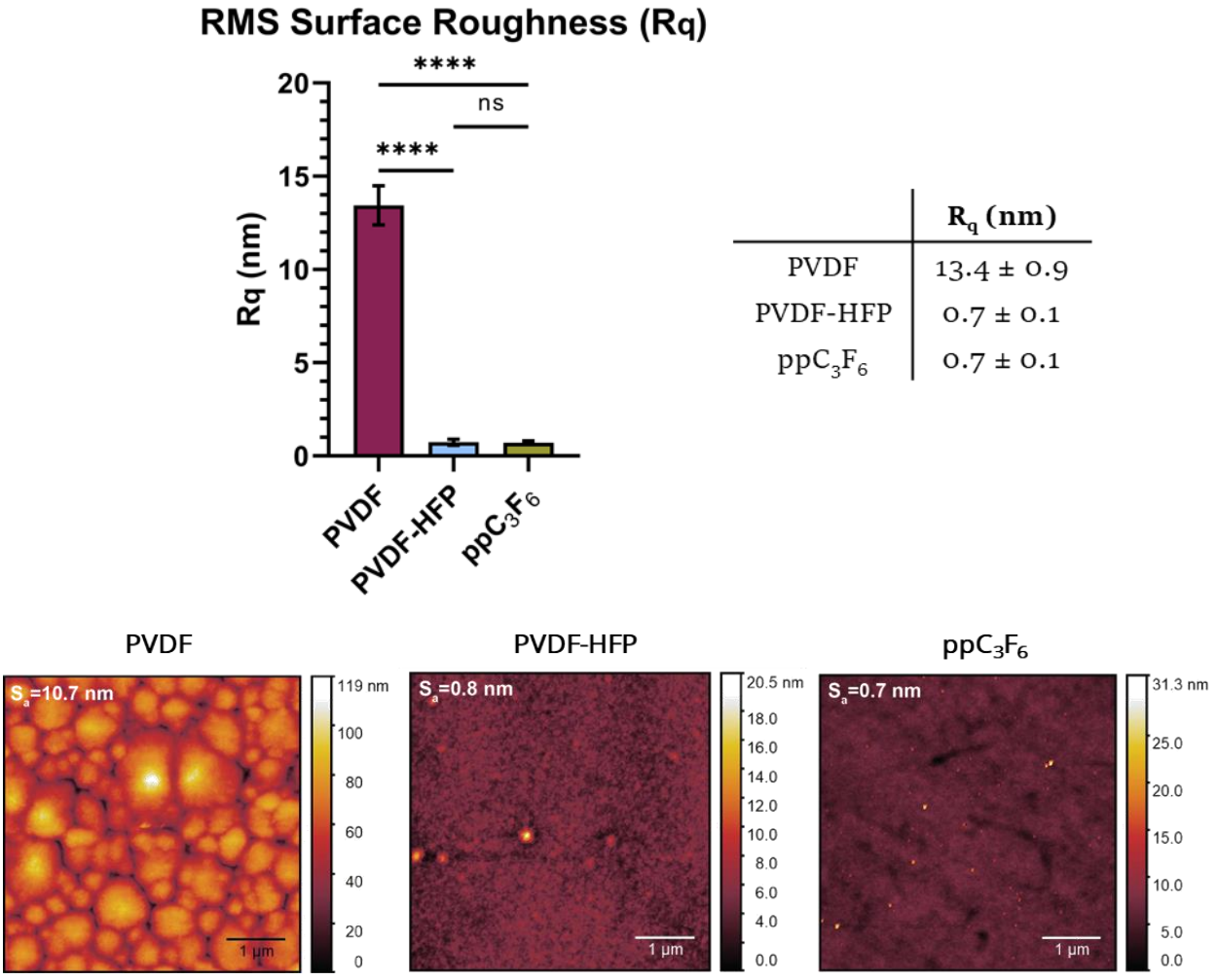

	R_q (nm)
PVDF	13.4 ± 0.9
PVDF-HFP	0.7 ± 0.1
ppC_3F_6	0.7 ± 0.1

Figure 2.3. Surface roughness of PVDF, PVDF-HFP, and ppC_3F_6 as determined via atomic force microscopy (AFM). (Top) RMS surface roughness (R_q) of PVDF is significantly greater than that observed for PVDF-HFP and ppC_3F_6 due to its

semi-crystalline structure ($p<0.0001$, $n=3$). (Bottom) Representative images for each coating are depicted, with PVDF β-phase spherulite structures visible compared to the smoother morphologies of PVDF-HFP and ppC_3F_6. The mean surface roughness (S_a) is provided in the upper left corner of each image, and scale bar is 1 μm.

2.3.3 Profilometry (Coating Thickness)

PVDF and PVDF-HFP both yielded film thicknesses of ~70 nm and were not significantly different between them ($p>0.05$), demonstrating the uniformity and reproducibility of the spin-coating parameters developed to deposit them. The ppC_3F_6 film is 5x the thickness of the spin-coated films at ~370 nm. This is a direct outcome of the plasma deposition duration (20 min), and is a parameter that can be adjusted to vary film thickness without changing overall surface composition down to a minimum of a 5 min deposition. A summary of film thicknesses are reported in **Figure 2.4** (n=3).

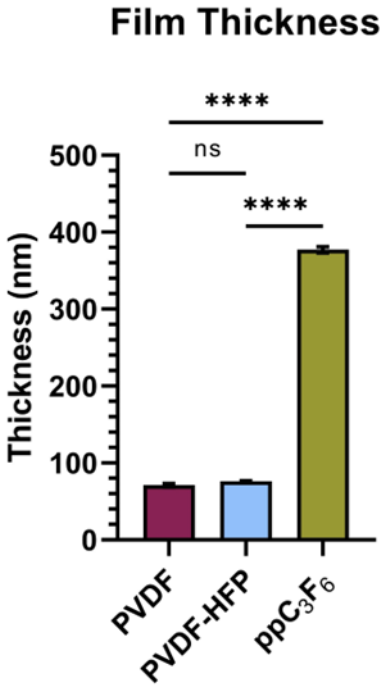

	Thickness (nm)
PVDF	70.9 ± 2.0
PVDF-HFP	75.9 ± 0.7
ppC_3F_6	377.2 ± 3.1

Figure 2.4. Coating Thicknesses of PVDF, PVDF-HFP, and ppC_3F_6 as determined via profilometry. Film thickness for the spin-coated PVDF and PVDF-HFP (~70 nm) are not significantly different ($p>0.05$), while the ppC_3F_6 film thickness, which is directly related

to the plasma deposition duration (20 min), is ~5x thicker at ~370 nm. All thicknesses are reported in nm (n=3).

2.3.4 Water Contact Angle (Surface Energy)

Water contact angle (WCA) is an indirect measurement for approximating a material's surface energy, which is a common predictor of interactions between biomolecules in an aqueous phase at a solid interface. This is especially relevant for studying blood protein adsorption on biomaterials, as proteins must first engage with the local water structure before approaching the foreign surface. WCA is also influenced by a combination of surface roughness (i.e. Cassie-Baxter state) and chemistry (e.g. fluorination), therefore the effects of both of these parameters, which are respectively measured in the AFM and ESCA data reported above, are captured in these measurements.

Static WCA measurements provided in **Figure 2.5** depict materials ordered in increasing -CF_3 content as an unofficial metric of increased hydrophobicity (and therefore anticipated increasing WCA). Conventionally, materials with contact angles <90° are considered hydrophilic, >90° hydrophobic [14], and >150° superhydrophobic [15], the latter being achieved through microstructured surfaces that entrap gases under the droplet (lotus effect) [16]. Here, we include uncoated glass as a hydrophilic control (46°) and polytetrafluoroethylene (PTFE, $(C_2F_4)_n$) as a common hydrophobic control (~105°). Despite containing fluorocarbon groups, PVDF (50% CH, 50% CF_2) and PVDF-HFP (45% CH, 2.5% CF, 48% CF_2, 4.5% CF_3) both exhibited lower WCAs than PTFE (100% CF_2) due to their high CH content. The small percentage of CF_3 groups in PVDF-HFP was not enough hydrophobic characteristic to endow the surface with a greater WCA than the CF_2-saturated PTFE film. However, our ppC_3F_6 material exhibited the highest WCA at ~108° with a unique combination of multiple fluorocarbon chemistries.

Combining water contact angles with that of a nonpolar solvent probe

(diiodomethane) enables the determination of surface free energy with the application of the OWRK theory, which divides interfacial interactions into polar and dispersive [17-19]. Increasingly hydrophobic surfaces generally correspond to lower surface energy and reduced wettability. Here, we observe decreasing surface energy in the following order: glass, PVDF, PVDF-HFP, PTFE, and ppC_3F_6, with the lowest surface energy at ~14.5 mN/m. A one-way ANOVA with Tukey HSD post-hoc multiple comparisons test revealed that there was a statistically significant ($p<0.0001$) difference in SFE between ppC_3F_6 and both PVDF and PVDF-HFP (n=42).

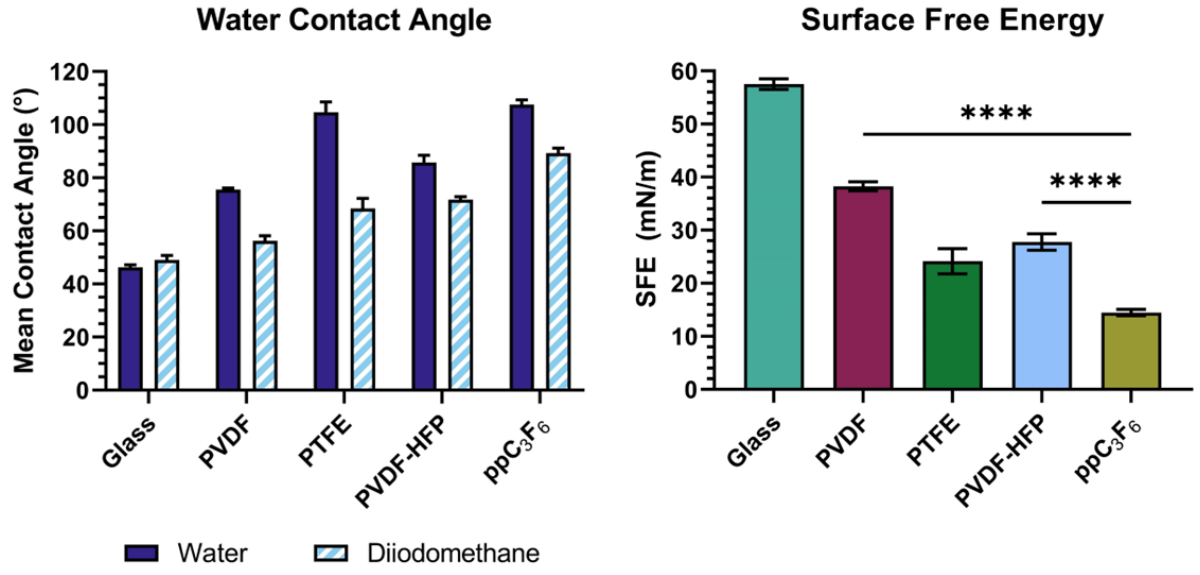

	Contact Angle (Water) *(°)*	Contact Angle (Diiodomethane) *(°)*	Surface Free Energy *(mN/m)*
Glass	46.2 ± 0.8	49.0 ± 1.4	57.5 ± 0.8
PVDF	75.6 ± 0.5	56.2 ± 1.6	38.3 ± 0.7
PTFE	104.6 ± 3.2	68.5 ± 3.1	24.2 ± 1.9
PVDF-HFP	85.7 ± 2.2	71.8 ± 0.9	27.8 ± 1.3
ppC_3F_6	107.6 ± 1.4	89.3 ± 1.6	14.5 ± 0.5

Figure 2.5. Water contact angle (WCA) and surface free energy (SFE) of PVDF, PVDF-HFP, and ppC_3F_6 as determined via an automated drop shape analyzer.

Materials are listed in order of increasing -CF_3 content from left to right for the plots and top to bottom in the table. ppC_3F_6 exhibits the highest WCA and lowest SFE ($p < 0.0001$) out of all tested materials, demonstrating high hydrophobicity and low wettability. Measurements are reported as the average of n=7 automated contact angle measurements taken on n=2 droplets of water or diiodomethane per substrate, with triplicates (n=3) of each substrate type (total n=42).

2.4 Discussion

The spectral broadening observed for the C-F/C=CF_x (1.67) and C-CF_x (1.75) peaks (compared to CF_2 1.19 and CF_3 1.16) of the high-resolution C1s ppC_3F_6 scan is in agreement with observations from literature suggesting the influence of nearest neighbor binding environments and double bonds on the primary carbon, which contribute to secondary peak shifts [8, 20, 32]. Extensive reports have determined the relative shifts of C-F_x species when probed via ESCA, which are confirmed in the work presented here as well. **Figure 2.6** shows the chemical structure of the theoretical HFP polymer with the relevant unique carbon species numbered. With respect to the adventitious hydrocarbon (C-H) peak at 285.0 eV, the C-F peak with 7 nearest neighbors (7βF) is shifted 4.8 eV to 289.8 eV, the C-F_2 peak with 2 nearest neighbors (2βF) is shifted 6.8 eV to 291.8 eV, and the C-F_3 peak with 1 nearest neighbor (1βF) is shifted 8.9 eV to 293.9 eV in the unsaturated repeating polymer structure. Additionally, the presence of a distinct fourth peak at 287.8 eV is attributed to the presence of C-CF_x, which does not exist in the HFP monomer form, and is indicative of a highly polymerized film.

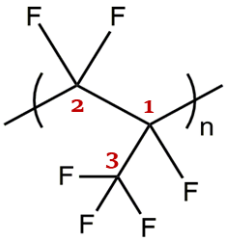

[1]CF + 7βF
[2]CF_2 + 2βF
[3]CF_3 + 1βF

Species	Environment	Binding Energy	Relative Shift
C	C-H	285	0
C	2βF	285.7	0.7
C	4βF	286.4	1.4
C	4βF	286.8	1.8
C-F	C-H	287.9	2.9
C-F	7βF	289.8	4.8
C-F2	C-H	290.9	5.9
C-F2	C-H	291.2	6.2
C-F2	2βF	291.8	6.8
C-F2	4βF	292.5	7.5
C-F3	1βF	293.9	8.9

Figure 2.6. ppC_3F_6 carbon nearest neighbor binding environments and corresponding C1s ESCA peak shifts. Peak shift values are adapted from Beamson & Briggs (1992) [21].

The extraction of fluorine in the final polymer film that produces a final F:C composition of 1.5 instead of 2 is attributed to the random fragmentation of the HFP monomer in a monomer-starved reaction to produce reactive species that participate in etching (i.e. atomic F) rather than polymerization (i.e. CF_x fragments) [22, 4]. Chen, Gorelik & Silverstein capture the kinetics of HFP plasma polymerization with the description:

$$R_d = R_p - R_e$$

where R_d is the rate of deposition, R_p the rate of polymerization, and R_e the rate of etching. R_p increases with increasing power (W) supplied to the plasma, but plateaus when the monomer feed rate into the reaction chamber is surpassed. In this way, the plasma state is converted from energy-starved to monomer-starved while the R_e continues to increase. Thus, the R_d increases and reaches a maximum for constant supplied W before decreasing again, during which active species in the plasma have a higher likelihood of colliding with nonreactive (i.e. polymerized) species on the substrate rather than other active

species in the plasma and, therefore, drive the deposition vs. etching equilibrium towards the etching regime. For ppC_3F_6, it was determined that a monomer-starved plasma produced below 50 W was more energy efficient and could sustain R_d linearly with increasing monomer feed rate and pressure [4]. Our ppC_3F_6 deposited at 20 W with a modest monomer feed rate of 10 sccm is thus able to polymerize on the substrate without significant co-etching, while also retaining much of the original monomer structure. Thus, we observe high incorporation of CF_3 groups at low power without converting the CF_3^+ ion into a physical etchant [2].

The F:C ratio achieved for ppC_3F_6 (1.5) is also reported as the optimal range for maximum protein retention, along with high incorporation of CF_3 species [9]. The ~23.5% CF_3 content achieved in ppC_3F_6, compared to 4.5% in PVDF-HFP, demonstrates the high utility of plasma polymerization as a process for generating CF_3-enriched surfaces. When assessing bond energetics, the C—C bond between the CF and CF_3 moieties possesses the lowest bond energy at ΔH=335 kJ/mol, while the C=C double bond is nearly twice as energetically costly at ΔH=594 kJ/mol [22]. Therefore, scission of the C—CF_3 bond is energetically preferred at lower powers, creating active CF_3 fragments that randomly re-insert into the growing polymer film. Studies have shown that RF glow discharge polymerized fluorocarbons produced in-the-glow (ITG) yield highly disordered films with high degrees of crosslinking and random branching [23]. Our results support this observation with strong C1s peak signatures for C-F/C=CF_x and C-CF_x peaks, with the C-F (i.e. $\underline{C}$F-CF_x) peak indicating polymer branch sites [8]. Although the overlap between the C=CF_x double bond peak (also a chain propagating species) obfuscates precise calculation of the degree of branching, simply taking the peak area percentage suggests that 25% of the carbon atoms in the film are involved in crosslinking. Therefore, if branching is assumed to be randomly distributed throughout the film, on average, a linear polymer segment would be ~4 carbons long.

Delamination testing showed that all coatings were robust and remained

adhered to the substrate following full submersion in water overnight under gentle shear conditions. Carbon and fluorine peaks from ESCA survey scans as well as the high resolution C1s envelope remained unchanged, and the incorporation of adventitious contaminants like oxygen into the film was only detected in trace amounts (<1%). For the ppC_3F_6 coating, the underlying plasma-polymerized methane (PPM) layer is critical in providing substrate adhesiveness for low surface energy films like hydrophobic fluoropolymers by creating a hydrocarbon enriched surface for improved film wettability and bond strength [10]. Sharma & Yasuda observed that lower monomer feed rates for PPM adhered best to glass substrates, with no polymer film lifting following a combinatorial boiling and saline soaking test that was estimated to be commensurate with three years in aqueous conditions at physiological temperature (37 °C) [10]. Low monomer feed rates for plasma polymers were also found to yield more highly crosslinked polymer films that remained chemically intact at temperatures >800 °C under inert conditions.

As expected for the solvent-based coating process, PVDF displays a semi-crystalline morphology of predominantly β-phase crystals with presence of spherulites [24]. Surface roughness is reported to play a role in hemolysis [25] and overall thrombogenicity [26], although a deeper understanding of its effect on blood protein adsorption and downstream platelet adhesion beyond empirical observations deserves exploration. Additionally, Ma & coworkers found that copolymerization with asymmetrical units of HFP (i.e. PVDF-HFP) inhibited crystallization, and our smooth PVDF-HFP spin-coated films are consistent with this observation [24]. PVDF-HFP is commercially employed in FDA-approved blood-contacting devices like Abbott Vascular's XIENCE™ Drug Eluting Stent and is reported to exhibit low-fouling properties, though clinical usage of these devices still requires systemic antiplatelet and anticoagulant administration [27].

Early reports of the use of plasma polymerization on HFP employed reaction parameters that resulted in a combination of gas-phase and surface

polymerization [4, 28]. However, films produced in this manner exhibited micron-sized spheroid agglomerates that are generated during gas-phase polymerization and undergo further polymerization when deposited on the substrate surface to form a heterogeneous film structure. This undesirable morphology was corrected for in later studies with adjusted plasma parameters to promote surface-polymerization that yielded smooth and defect-free films, with RMS roughness values of 4.5 Å [8]. Our ppC_3F_6 demonstrates similar smoothness with a RMS roughness of 8 Å.

Through profilometry, we observe that the spin coating process is capable of producing uniformly thin surfaces (<100 nm). Our standard recipe for producing ppC_3F_6 employs a plasma deposition time of 20 minutes with an underlying 5 minute methane layer. This ultimately yields a layer nearly 5x as thick as the spin-coated fluoropolymers. However, if needed, the deposition time can be varied to achieve the desired film thickness. As expected, water contact angle (WCA) measurements followed by surface free energy calculations showed that ppC_3F_6 had the lowest surface energy and was therefore the most hydrophobic material ($p < 0.0001$). This correlates well with the high-resolution C1s ESCA data confirming its CF_3-enriched surface and high degree of crosslinking within the film, and is purported to account for much of the material's unique properties as observed in past *in vitro* and *ex vivo* studies.

2.5 Summary

In this chapter, all the test materials (PVDF, PVDF-HFP, and ppC_3F_6) are prepared and characterized. We employed electron spectroscopy for chemical analysis (ESCA) to verify chemical composition, atomic force microscopy (AFM) for surface roughness, profilometry for coating thickness, and water contact angle (WCA) measurements for surface energy. We confirmed that the ppC_3F_6 coating is a CF_3-enriched surface with a high degree of crosslinking within the film, and is

purported to account for much of the material's unique properties as observed in past *in vitro* and *ex vivo* studies. It was also highly smooth, thick (though thickness is easily adjustable via change in deposition time), and possessed a significantly lower surface free energy compared to the other polymers. PVDF and PVDF-HFP also exhibited the expected chemical compositions, and were significantly thinner than the ppC_3F_6 coating from the spincoating process. PVDF also demonstrated a rougher texture than the other two materials owing to its semi-crystallinity.

2.6 Acknowledgments

The authors would like to thank the following staff members and users at the National ESCA and Surface Analysis Center for Biomedical Problems (NESAC/BIO) and Molecular Analysis Facility (MAF) at the University of Washington: Gerry Hammer and Dr. Samantha Young for their assistance and expertise in acquiring and analyzing ESCA/XPS spectra; Dr. Micah Glaz for assistance with AFM image acquisition; and Dr. Prabhleen Kaur for assistance with profilometry measurements. The authors are grateful for the usage of the Krüss Drop Shape Analyzer goniometer located at the Washington Clean Energy Testbeds (WCET) for water contact angle measurements.

2.7 References

1. Yasuda, H. Plasma polymerization, *Academic Press*, New York (1985).
2. Biederman, H. & Osada, Y. Plasma polymerization processes, *Elsevier Science Publishers*, New York (1992).
3. Boenig, H.V. Fundamentals of plasma chemistry and technology, *Technomic Publishing*, Lancaster, PA (1988).
4. Chen, R., Gorelik, V. & Silverstein, M. S. Plasma polymerization of hexafluoropropylene: Film deposition and structure. *J. App. Polym. Sci.* **56**(5), 615–623 (1995).
5. Kiaei, D., Hoffman, A.S. & Horbett, T.A. Tight binding of albumin to glow

discharge treated polymers. *J Biomater Sci Polym Ed.* **4**(1), 35-44 (1992).

6. Kiaei, D., Hoffman, A.S. & Hanson, S.R. Ex vivo and in vitro platelet adhesion on RFGD deposited polymers. *J Biomed Mater Res.* **26**(3), 357-72 (1992).
7. Kiaei, D., Hoffman, A.S., Ratner, B.D., Horbett, T.A. & Reynolds, L.O. Blood interaction with gas discharge treated vascular grafts. *ACS Polym. Mat. Sci. Eng.* **56**, 710-714 (1987).
8. Garrison, M. D., Luginbühl, R., Overney, R. M., Ratner, B. D. Glow discharge plasma deposited hexafluoropropylene films: surface chemistry and interfacial materials properties. *Thin Solid Films* **352**, 13-21 (1999).
9. Favia, P., Pérez-Luna, V., Boland, T., Castner, D. & Ratner, B.D. Surface chemical composition and fibrinogen adsorption-retention of fluoropolymer films deposited from an RF glow discharge. *Plasma Pol.* **1**(4), 299-326 (1996).
10. Sharma, A., Yasuda, H. Polymerization of methane. *J. App. Polym. Sci.* **38**(4), 741-754 (1989).
11. Wagner, C.D., Riggs, W.M., Davis, L.E., Moulder, J.F. & Mulienberg, G.E. Handbook of X-Ray Photoelectron Spectroscopy, Perkin Elmer, Eden Prairie, 1979.
12. Dilks, A. Characterisation of Polymers by ESCA. *Applied Science*, Essex, UK (1986).
13. Hinckley, A.C. *et al.* Investigation of a solution-processable, nonspecific surface modifier for low cost, high work function electrodes. *ACS Appl. Mater. Interfaces.* **8**(30), 19658-64 (2016).
14. Zisman, W.A. Contact Angle, wettability, and adhesion. *ACS (F. Fowkes ed.)*, pg. 1-51 (1964).
15. Wang, S. & Jiang, L. Definition of superhydrophobic states. *Adv. Mater.* **19**(21), 3423-3424 (2007).
16. Lafuma, A. & Quere, D. Superhydrophobic states. *Nat. Mater.* **2**(7), 457-460 (2003).
17. Kaelble, D.H. Dispersion-polar surface tension properties of organic solids. *J. Adhesion* **2,** 66-81 (1970).
18. Owens, D. & Wendt, R. Estimation of the surface free energy of polymers. *J. Appl. Polym. Sci* **13,** 1741-1747 (1969).
19. Rabel, W. Einige Aspekte der Benetzungstheorie und ihre Anwendung auf die Untersuchung und Veränderung der Oberflächeneigenschaften von Polymeren. *Farbe und Lack* **77**(10), 997-1005 (1971).

20. Dilks, A. In: Brundle, C.R. & Baker, A.D. Electron spectroscopy theory, techniques, and applications. *Academic Press*, New York, pg. 277 (1981).

21. Beamson, G. & Briggs, D. High resolution XPS of organic polymers: the Scienta ESCA300 database. *Wiley*, New York, NY (1992).

22. D'Agostino, R., Cramarossa, F., Fracassi, F. & Illuzzi F. Plasma deposition, treatment, and etching of polymers. R. D'Agostino, Ed., *Academic Press*, New York, pg. 95 (1990).

23. Castner, D., Lewis, K., Fischer, D., Ratner, B.D. & Gland, J. Determination of surface structure and orientation of polymerized tetrafluoroethylene films by near-edge x-ray absorption fine structure, x-ray photoelectron spectroscopy, and static secondary ion mass spectrometry. *Langmuir*, **9**, 537-542 (1993).

24. Ma, W., Zhang, J., Chen, S. & Wang, X. Crystalline phase formation of poly(vinylidene fluoride) from tetrahydrofuran/N,N-dimethylformamide mixed solutions. *J. Macromol. Sci. B.* **3**, 434-449 (2008).

25. Wielogorski, J.W., Davy, T.J. & Regan, R.J. The influence of surface rugosity on haemolysis occurring in tubing. *Biomed. Eng.* **11**(3):91–94 (1976).

26. Hecker, J.F. & Scandrett, L.A. Roughness and thrombogenicity of the outer surfaces of intravascular catheters. *J Biomed Mater Res.* **19**(4):381–95 (1985).

27. Szott, L.M., Irvin, C.A., Trollsas, M., Hossainy, S. & Ratner, B.D. Blood compatibility assessment of polymers used in drug eluting stent coatings. *Biointerphases*, **11**, 029806 (2016).

28. Silverstein, M.S., Chen, R. & Kesler, O. Hexafluoropropylene plasmas: polymerization rate-reaction parameter relationships. *Polym. Eng. Sci.* **36**(20), 2542-2549 (1996).

29. Pender, M.R., Shen, M., Bell, A.T. & Millard, M. ESCA characterization of plasma-polymerized fluorocarbons. *Plasma Polymerization, ACS Symposium Series*, 147-162 (1979).

30. Kiaei D, Hoffman AS, Horbett TA, Lew KR. Platelet and monoclonal antibody binding to fibrinogen adsorbed on glow-discharge-deposited polymers. J Biomed Mater Res. 1995 Jun;29(6):729-39. doi: 10.1002/jbm.820290609. PMID: 7593010.

31. Shard, A. Plasma assisted thin film formation. *Durham theses,* Durham University (1992).

32. Dilks, A. In: Brundle, C.R. & Baker, A.D. Electron spectroscopy theory, techniques, and applications. *Academic Press*, New York, pg. 277 (1981).

Chapter 3

Quartz crystal microbalance with dissipation (QCM-D) characterization of blood protein adsorption on thromboresistant fluoropolymers

Liu, S., Kim, K.H. & Ratner, B.D. Quartz crystal microbalance with dissipation (QCM-D) characterization of albumin and fibrinogen adsorption to fluoropolymers for blood-contacting applications. In preparation.

Initiated by Sherry Liu (SL) as a part of, and funded by, the Center for Dialysis Innovation (CDI) for Co-Director and Principal Investigator Dr. Buddy D. Ratner (BDR) under the Blood Compatibility research project. SL motivated and conceptualized the work, designed and executed the experiments, performed all analyses, and wrote the manuscript. KHK will provide additional experimental data that will be detailed in their dissertation. Barring revisions or edits suggested by committee members, the following text will serve as the draft for a journal submission.

3.1 Abstract

Blood-contacting medical devices are subjected to endogenous protein adsorption that initiates coagulation and inflammation pathways, often leading to fatal thromboembolic complications. The temporal turnover of adsorbed plasma proteins forms the basis for materials-induced thrombosis: human serum albumin (HSA), a platelet-inert and mobile protein, forms an initial passivating layer but is rapidly displaced by fibrinogen (Fg), which is surface-activated to mediate platelet recruitment and initiate fibrin clot formation. In this chapter, we employ quartz crystal microbalance with dissipation (QCM-D) to monitor competitive HSA:Fg adsorption on our selected panel of hydrophobic low-fouling fluoropolymers (FPs): poly(vinylidene difluoride) (PVDF), poly(vinylidene difluoride)-*co*-poly(hexafluoropropylene) (PVDF-HFP), and our custom plasma-polymerized C_3F_6 (ppC_3F_6). Across all FPs, ppC_3F_6 demonstrates the greatest HSA:Fg adsorption affinity ratio. Comparing Sauerbrey vs. Voigt mass uptake models, ppC_3F_6 exhibits an uncharacteristic viscoelasticity for the HSA adlayer attributed to hydrophobic-induced reorganization and partial coupling of the hydration layer at the protein-bulk fluid interface. Additionally, binary protein exposure reduced the equilibrium areal mass (R_{max}) compared to the pure Fg condition across all FPs, indicating that HSA competes with Fg for nonspecific binding spots and is retained on the surface at different equilibrium coverages for prolonged periods. Finally, longer HSA residence time on the surface reduces total Fg adsorption upon sequential exposure, suggesting that time-dependent denaturation and packing of HSA on a surface following adsorption increases resistance to Fg displacement. Ultimately, our observations for ppC_3F_6 are attributed to its unique fluoro-chemistry and hydrophobic properties created through the plasma polymerization process, while the hydration shells are subject to further study due to existing evidence that they deter cellular adhesion. With QCM-D-enabled characterization of protein adlayers, we seek to identify the optimal fluoropolymer

surface modifications that encourage favorable protein surface compositions and mitigate downstream thrombus formation.

3.2 Background

Quartz crystal microbalance with dissipation (QCM-D) is a real-time, *in situ* acoustic-sensing technique capable of detecting minute mass and structural changes and useful for investigating interfacial phenomena, including protein adsorption kinetics and adsorbate materials properties on various substrates [1-5, 28-32]. The QCM-D functions through the reverse piezoelectric properties of an AT-cut quartz sensor disk sandwiched between two metal (e.g. Au) electrodes. With the application of an alternating current, piezoelectric materials expand and contract at their resonant frequencies (f_0), and this resonance is directly dependent on the total crystal mass, which varies as a result of surface molecular adsorption and is therefore highly mass sensitive (**Figure 3.1**). The raw data generated are odd-integer harmonic overtones (n=1, 3, 5, etc.) of frequency change (Δf, Hz), where overtone number is inversely related to penetration depth to enable multilayer profiling. The addition of mass (Δm) to the sensor surface results in a simultaneous decrease in frequency described by the Sauerbrey relation [6]:

$$\Delta m = -C \cdot \frac{\Delta f}{n}$$

Where the constant C is a materials constant and n is the harmonic overtone number. For a standard quartz sensor with fundamental frequency (n=1) of 5 MHz, the constant C is equal to 17.7 ng/(cm^2·Hz). However, this relation must fulfill the following three conditions: the adsorbed layer (adlayer) is thin (<2% thickness of the crystal sensor), homogeneously distributed, and rigid. If the adlayer is thick, nonuniform, or subject to slip or deformation, the relation is invalid and will underestimate the mass by failing to account for energy losses due

to frictional dissipation. It is generally accepted that the Sauerbrey relation can be used when the dissipation change is <5% Δf, or when all the f overtones overlap.

To accommodate mass estimation in aqueous systems better suited for studying nonrigid molecules like polymers and proteins as well as the compounding effects of coupled or entrapped solvent molecules, energy dissipation (D) signals are induced by rapidly cutting the driver to the oscillating sensor as frequently as 200 ON/OFF cycles per second, which allows the sensor to relax as the amplitude decays. This decay voltage is recorded and fitted to a model to yield a dimensionless dissipation parameter (D, 10^{-6}) that accounts for energy loss from the system. Rigid adlayers demonstrate close vibrational coupling to the oscillating quartz sensor to perpetuate a long-lived vibrational decay with overlapping harmonic overtones. Conversely, the motion of nonrigid adlayers is decoupled from that of the crystal, and this stimuli-response hysteresis results in rapid vibrational decay and non-overlapping harmonics. In other words, the propagating wave peaks occur out of synchrony with each other at different depths. Here, the frequency response is not just a function of added mass, but also influenced by film characteristics like viscosity and shear modulus. Thus, adlayers with nonrigid properties can exhibit characteristic dissipation signatures that must be analyzed using Voigt viscoelastic modeling software [7, 16-18].

Herein, we employ QCM-D to investigate differential HSA and Fg binding affinity for fluoropolymer surfaces (PVDF, ppC_3F_6, PVDF-HFP) to identify optimal surface modifications that demonstrate the greatest HSA retention and resistance to Fg adsorption under flow conditions. QCM-D will also inform us of adsorption kinetics, degree of HSA retention when followed by sequential Fg exposure, and film mechanics for a holistic *in situ* understanding of the Vroman Effect [8-10]. With QCM-D-enabled characterization of protein adlayers, we hope to identify the optimal fluoropolymer surface modifications that encourage favorable protein compositions and mitigate downstream thrombus formation.

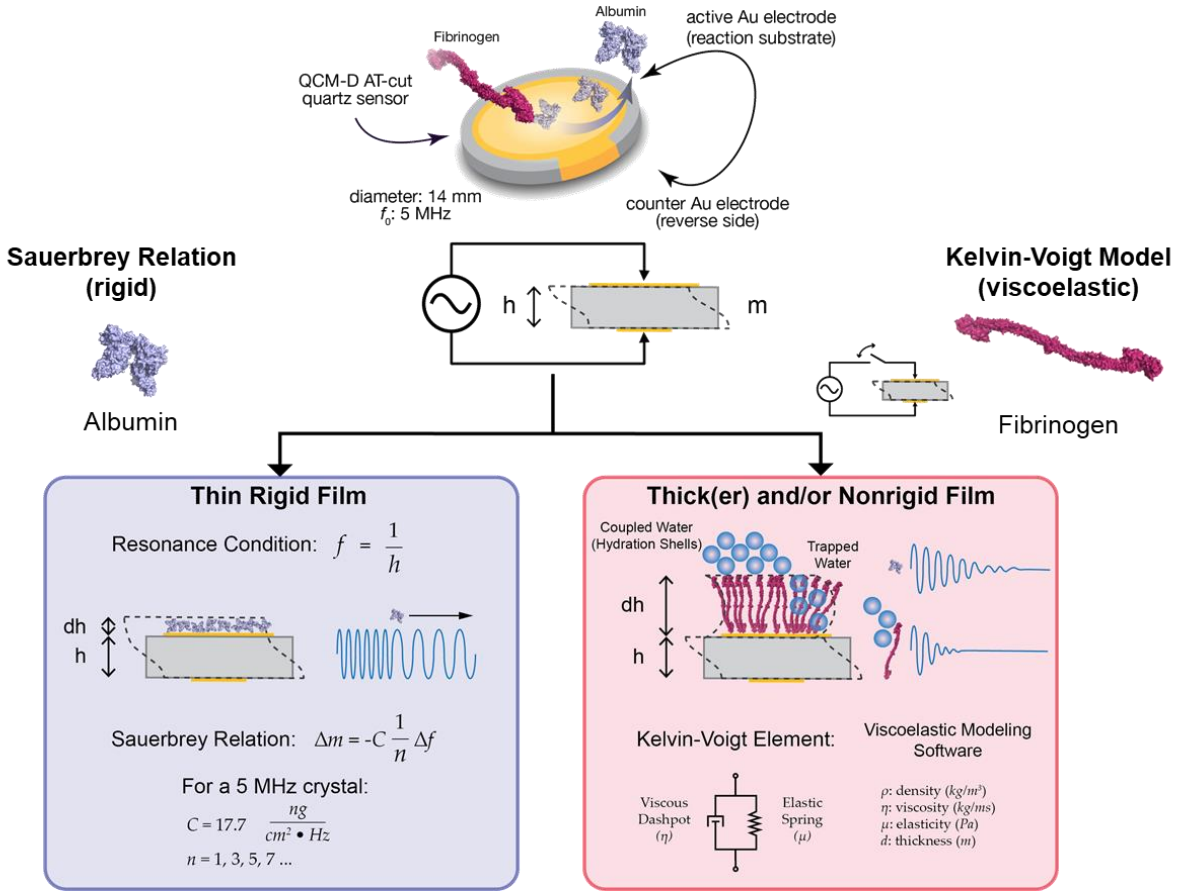

Figure 3.1. QCM-D theory and the Sauerbrey vs. Voigt mass models. The QCM-D functions through the reverse piezoelectric properties of a quartz sensor sandwiched between two metal electrodes that oscillate at a resonant frequency (f_0) under the application of an alternating current. (left) For small, rigid, and uniform adsorbates, the adlayer mass can be directly calculated from Δf via the Sauerbrey relation. (right) For elongated, nonrigid, and nonuniform adsorbates, application of the Sauerbrey relation fails to account for energy loss in the system due to vibrational decay and will therefore underestimate the added mass. Rapid on/off cycling of the sensor driver permits recording and fitting of a dimensionless dissipation factor (ΔD). The Voigt visoelastic modeling software can then be applied to fit resulting Δf and ΔD values and determine mass addition.

3.3 Materials & Methods

QCM-D sensors (QSensor QSX 301 Au, Nanoscience Instruments, Phoenix, AZ) were surface treated with PVDF, PVDF-HFP, and ppC_3F_6 through methods described in Chapter 2. HSA (Human Serum Albumin, Sigma-Aldrich A8763) and Fg (Human Plasma Fibrinogen, Sigma-Aldrich F3879) buffers were prepared the

day of QCM-D experimentation by dissolving in 1X filtered phosphate buffered saline to final concentrations of 300 μg/mL and 30 μg/mL, respectively, to approximately mimic the physiological 10:1 HSA:Fg plasma proportions at a 1% plasma concentration. All buffers were degassed for 30 minutes prior to use in the QCM-D and maintained at ambient temperature. All QCM-D studies were performed on the Q-Sense E4 instrument (Biolin Scientific AB, Stockholm, SE) using the in-house provided QSoft401 acquisition software (maximum time resolution: 300 data points per second, where each data point represents one f and D value collected per harmonic overtone) and QTools analysis software. Sensors were mounted in QCM-D flow modules containing serpentine temperature stabilization inlet channels docked on the chamber platform set at 22°C, and connected to a peristaltic pump set to continuous flow mode at a flow rate of 200 μL/min. Flow modules containing one of each fluoropolymer-coated sensor were run in parallel for each experiment and used the same protein stock solutions prepared fresh the day of experimentation. Because QCM-D is a time-resolved technique with a maximum of 4 flow modules in parallel, and replicate studies could not all be run within the same day while the protein stock solutions remained fresh, each experiment was repeated 3 times on different days to ensure adsorption trends between the fluoropolymer coatings were consistent and reproducible. Because there are always slight variations in protein concentration with each fresh protein stock, and due to the high mass sensitivity of the QCM-D instrument, the absolute adsorbed protein measured for each experimental replicate varies slightly, but all trends within each experiment were consistent. Therefore, time-resolved data reported in this work are representative of these trends observed n=3 times.

A variety of protein buffer flow conditions were used to assess HSA and Fg adsorption interactions with each fluoropolymer. Concentration isotherms using 1:2 serial dilutions of HSA (150, 300, 600, 1200 μg/mL) or Fg (15, 30, 60, 120 μg/mL) solutions at 1% plasma concentration were developed to provide a kinetic

analysis and determine maximum areal mass (R_{max}) and affinity constant (K_A) of both proteins on each fluoropolymer. Each protein buffer concentration was run to surface saturation for 1 hour and the average value of the final 1-minute interval (~n=30) was taken as the equilibrium areal mass. Based on the Langmuir model, adsorption kinetics were determined by normalizing each protein concentration to the equilibrium areal mass and fitting a linear regression from which R_{max} and K_A were calculated from the slope and intercept, respectively (see **Appendix 8.1** for full derivation). Additionally, protein adsorption on each type of fluoropolymer-modified sensor was studied with QCM-D in the following protein buffer variations: pure HSA (300 μg/mL), pure Fg (30 μg/mL), binary 10:1 HSA:Fg (300:30 μg/mL), and sequential HSA (300 μg/mL) to Fg (30 μg/mL). Finally, we probed the effect of HSA residence time on resistance to sequential Fg displacement by varying the duration of HSA pre-adsorption before Fg introduction (1, 5, 30, 60 minutes).

The Sauerbrey relation and viscoelastic Voigt modeling were applied to raw frequency and dissipation data (Δf, ΔD) for mass estimation of rigid vs. soft adlayers, respectively. The Sauerbrey relation was adequate for converting frequency measurements for HSA to areal mass due to its small (65 kDa) globular structure, which adheres rigidly to the surface with minimal deformation or slip [11]. This was also confirmed by ensuring $\Delta D < 5\% \Delta f$. Conversely, the Voigt viscoelastic modeling system within the QTools software was used to fit and convert the frequency measurements for Fg into areal mass ($\Delta D > 5\% \Delta f$) due to Fg's large (340 kDa) elongated structure, which deforms with the sensor's piezoelectric-induced oscillations [12-15]. Therefore, the Sauerbrey relation condition of a rigidly adhered adsorbate layer is not fulfilled, and applying the relation to this system would underestimate the mass by not accounting for kinetic energy loss in the layer due to adsorbate viscoelastic dissipation. Areal mass conversions for HSA were performed using the Sauerbrey relation (n=7), while those for Fg were performed using Voigt viscoelastic modeling (n=3, 5, 7, 9, 11).

3.4 Results

Results presented in this section have been converted to mass using either the Sauerbrey relation or Voigt viscoelastic modeling. Raw Δf and ΔD data are shared in **Appendix 8.2**.

3.4.1 Sauerbrey vs. Voigt modeling for HSA and Fg monolayers

We applied both the Sauerbrey and Voigt mass uptake models to raw Δf and ΔD values obtained for HSA and Fg single protein solutions to verify the validity of each mass conversion method in relation to the protein adsorbate's material properties. Expectations based on each protein's molecular structure alone suggest that the Sauerbrey relation is appropriate for HSA mass modeling (small, globular, rigidly adhered) while Voigt viscoelastic modeling is more suitable for Fg mass modeling (large, elongated, deforms). However, differences in mass profiles obtained from the raw $\Delta f/\Delta D$ values can provide insight into unanticipated surface effects. Theoretically, applying the Voigt model to a rigid adlayer would yield the same mass estimation as seen for the Sauerbrey relation because additional rheological parameters (i.e. fluid density, viscosity, etc.) would not need to be represented in the system to account for dissipative energy loss. However, applying the Sauerbrey relation to an adsorbate system that does exhibit a dissipative element would underestimate the true hydrated mass. Hybrid-type films—for example, where the solid adsorbate is small and rigidly adhered but highly hydrated to form a coupled water network—could therefore be inaccurately represented by the Sauerbrey relation. This concept is schematically represented in **Figure 3.2**.

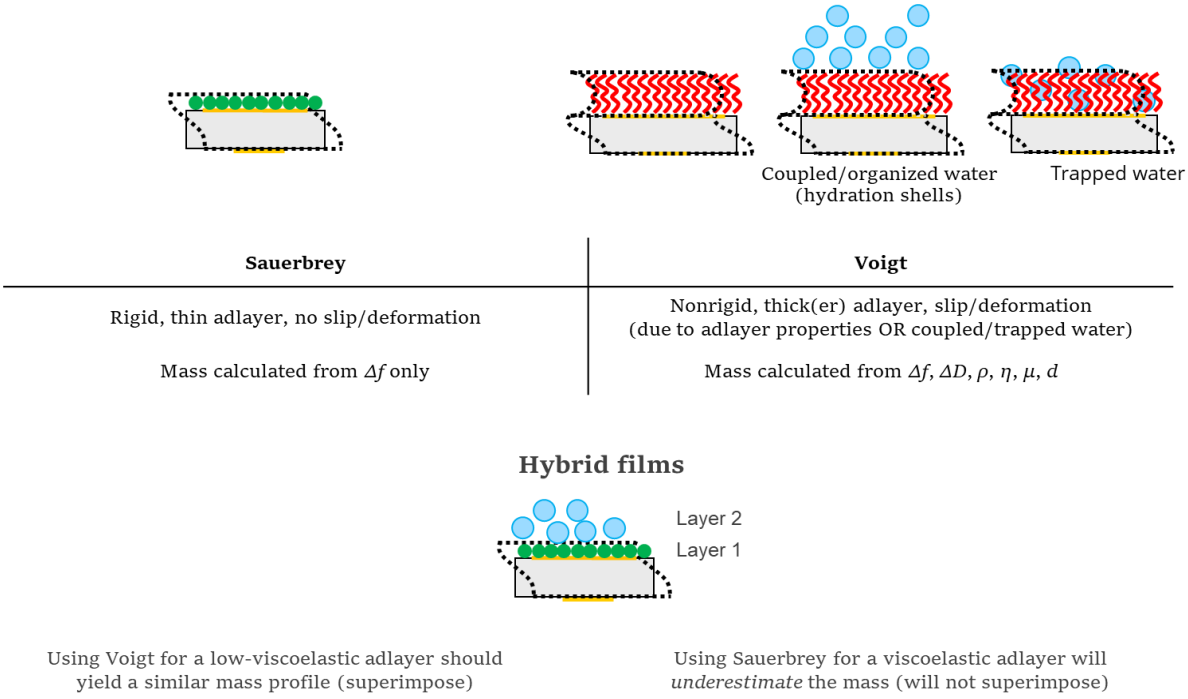

Figure 3.2. Cross-referencing Sauerbrey and Voigt mass models scheme. Applying both Sauerbrey and Voigt mass models to raw f and D measurements can aid in predicting adsorbate materials properties like viscoelasticity.

Upon dual application of the Sauerbrey (n=7) and Voigt (n=3, 5, 7, 9, 11) mass models to HSA adsorbed to each fluoropolymer (**Figure 3.3, left**), we observed equivalent mass profiles for PVDF and PVDF-HFP indicating the rigidity of their adsorbed HSA layers, consistent with expectations (equilibrium areal mass ~130 ng/cm^2 for both fluoropolymers using both models). However, a significant increase in Voigt mass estimation (912 ng/cm^2) is seen for HSA adsorbed to ppC_3F_6 compared to that determined via Sauerbrey relation (300 ng/cm^2), suggesting that an additional dissipative characteristic was detected by the QCM-D sensor. We suspect that this ~600 ng/cm^2 differential in mass estimation is caused by a partially coupled water network over top the ppC_3F_6-adsorbed HSA that causes motion with the sensor's oscillations, thereby inducing a dissipation signal that is accounted for in the Voigt mass modeling process.

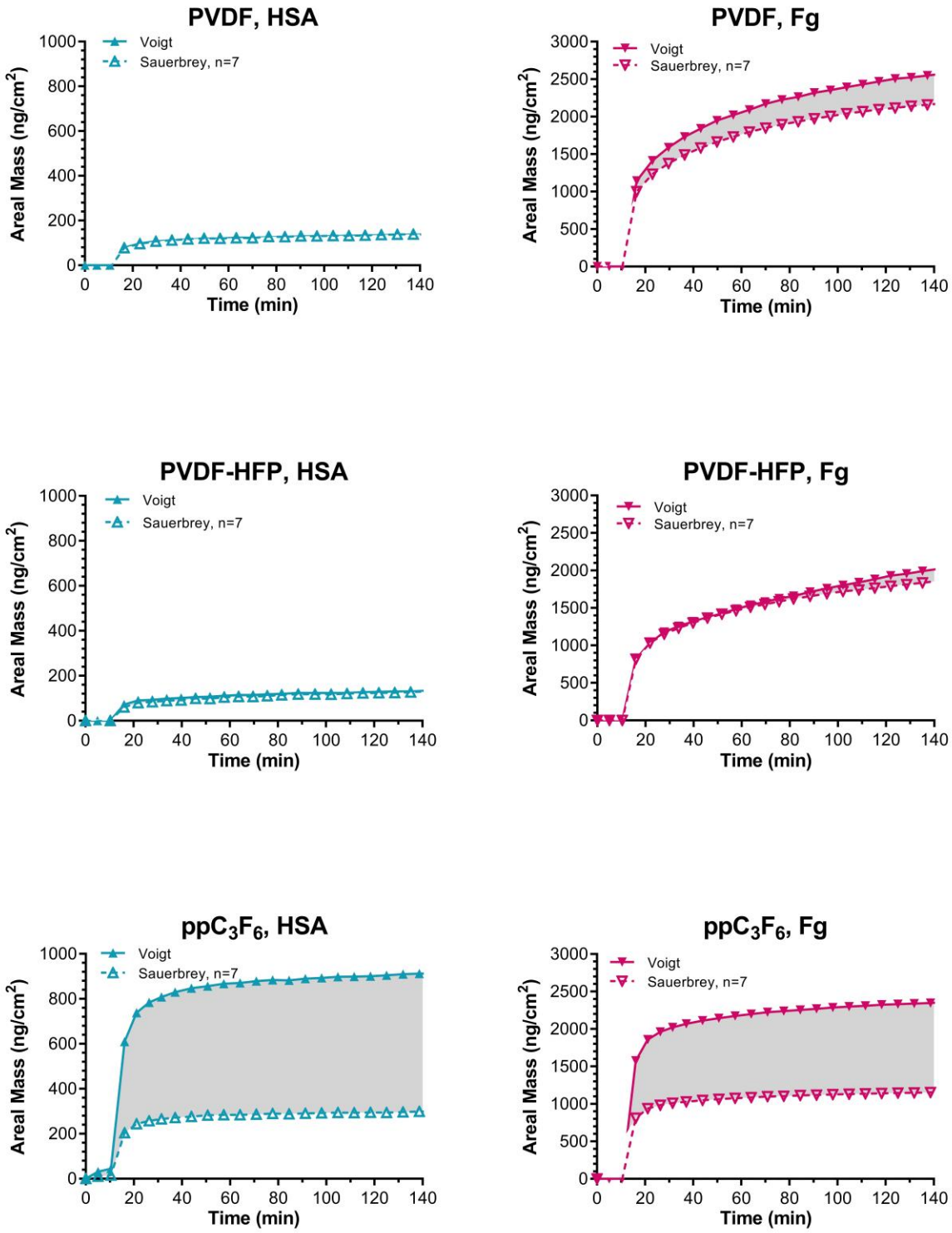

Figure 3.3. Sauerbrey and Voigt mass models applied to HSA and Fg adsorbed on PVDF, PVDF-HFP, and ppC_3F_6. Concentrations used were 0.3 mg/mL for HSA and 0.03 mg/mL for Fg to replicate the 10:1 HSA:Fg ratio of physiological concentrations. **(Left, blue)** HSA as an adsorbate is expected to yield a rigidly adhered layer with an areal mass

that is adequately represented by the Sauerbrey relation. Applying the Voigt model for this particular layer should then yield no difference from the Sauerbrey relation, as no dissipation is detected. This is observed to be true for PVDF and PVDF-HFP, but does not hold for ppC_3F_6, which yields a significantly greater mass estimation when modeled with the Voigt system compared to the Sauerbrey relation. This indicates that a dissipation signal is detected for HSA adsorbed to ppC_3F_6, which we attribute to a partially coupled water network. **(Right, magenta)** Fg adsorbed to all fluoropolymers yielded a difference in Sauerbrey vs. Voigt mass uptake models but is most pronounced for ppC_3F_6. While a differential was expected for Fg due to its elongated structure, the extent of Sauerbrey mass underestimation observed for Fg on ppC_3F_6 could suggest a surface preference for end-on adsorption of the protein on this material compared to PVDF and PVDF-HFP, which depict more similar mass estimations and therefore less viscoelastic dissipation (e.g. side-on adsorption).

As expected, differences in Sauerbrey vs. Voigt mass uptake modeling are observed for Fg adsorbed on all three fluoropolymers (PVDF, PVDF-HFP, and ppC_3F_6), though this effect is most pronounced for ppC_3F_6 (**Figure 3.3, right**). The resultant viscoelasticity detected for Fg adlayers can be attributed to a combination of Fg's inherent elongated structure as well as coupled water molecules, and the extent of the Sauerbrey vs. Voigt mass estimation differential can provide hints at the surface orientation of Fg. In other words, a smaller estimated mass difference can suggest a more rigid, side-on adsorbed Fg layer, while a larger estimated mass difference can suggest a more viscoelastic, end-on adsorbed Fg layer.

Based on the results obtained here and for simplicity, subsequent studies employed Sauerbrey mass modeling for HSA single protein conditions and Voigt mass modeling for all other protein conditions (Fg single protein, HSA/Fg binary). However, the unusually high dissipative content of HSA-on- ppC_3F_6 is noted and attributed to associated water molecules.

3.4.2 HSA and Fg concentration isotherms and kinetic analysis

The average areal mass of the final 1-minute interval for each protein concentration (Fg: 15, 30, 60, 120 μg/mL; HSA: 150, 300, 600, 1200 μg/mL) run to

saturation was taken as the equilibrium areal mass (M_{eq}) and plotted as concentration curves (**Figure 3.4**). Each data point represents a flow module housing a coated sensor of that particular fluoropolymer and exposed to that particular protein concentration, and each curve was 4 flow modules run in parallel. Areal mass numbers reported represent the sum of the mass of the protein and retained water (Sauerbrey model), or these contributions plus additional viscoelastic effects at the surface (Voigt model).

Based on the Langmuir model of the adsorption isotherm, a derivation employing temporal boundary conditions to solve the rate equation ultimately yields a linear form where the maximum response (in our case, areal mass M_{max}) and affinity constant K_A of each protein to each fluoropolymer can be determined (see **Appendix 8.2** for full derivation).

Adsorption curves for all FPs reveal that ppC_3F_6 achieves the greatest equilibrium HSA coverage across multiple concentrations. The corresponding kinetic analysis through a linear regression fit of the normalized equilibrium areal mass values confirms that ppC_3F_6 demonstrates the highest M_{max} (~420 ng/cm^2) for HSA. Similarly, ppC_3F_6 yielded the greatest HSA affinity constant (K_A=[AS]/[A][S]), indicating that at equilibrium, the surface-adsorbed HSA ([AS]), exists in higher concentrations than the free form protein ([A]) and the free surface ([S]). Conversely, ppC_3F_6 demonstrates the lowest M_{max} for Fg (~1860 ng/cm^2), indicating low surface adsorption of Fg. Together, this data suggests that ppC_3F_6 has the greatest surface preference for adsorbing HSA over Fg compared to PVDF and PVDF-HFP, and may be a more blood-compatible biomaterial with favorable protein adsorbate compositions that deter platelet adhesion and activation.

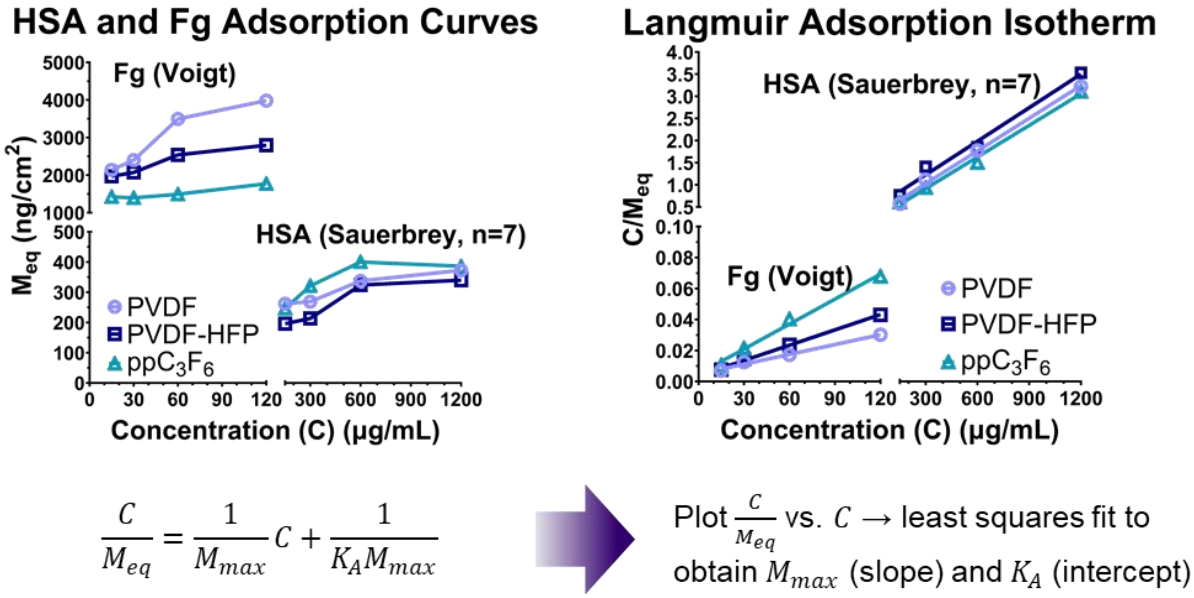

	Maximum Areal Mass, M_{max} (10^2 ng/cm^2)			Affinity Constant, K_A (10^{-2} cm^2/ng)	
Species	**Fg**	**HSA**	**HSA:Fg**	**Fg**	**HSA**
PVDF	47.4	4.06	0.086	4.39	0.856
PVDF-HFP	30.3	3.96	0.131	9.08	0.542
ppC_3F_6	18.6	4.20	0.226	11.1	1.21

Figure 3.4. QCM-D adsorption curves and Langmuir concentration isotherms. Developing concentration curves for HSA and Fg on each fluoropolymer surface permits the determination of the theoretical maximum areal mass (M_{max}) and affinity constant (K_A) through application of the Langmuir model and linearization of the adsorption rate equation. Four 1:2 serial dilutions of both HSA and Fg were run to saturation, and the final equilibrium areal mass (M_{eq}) was taken for each concentration (C). By plotting C/M_{eq} vs. C, we determine the adsorption kinetic parameters, M_{max} and K_A.

3.4.3 HSA vs. Fg total adsorption from single-protein solutions

To visualize and assess each fluoropolymer's surface affinity for HSA vs. Fg, each protein solution was run independently with each material type to surface

saturation or near-saturation (**Figure 3.5**). After an initial 10-minute PBS equilibration, 300 µg/mL of HSA or 30 µg/mL of Fg were introduced to the flow modules. Both PVDF and PVDF-HFP demonstrated near-identical mass profiles, with final HSA surface concentrations of ~140 and 130 ng/cm², respectively, and final Fg surface concentrations of ~3600 ng/cm². Conversely, ppC_3F_6 adsorbed more than twice the surface mass of HSA (~300 ng/cm²) and less than half that of Fg (~1600 ng/cm²). These data suggest a selective surface preference of ppC_3F_6 for HSA adsorption and resistance to Fg adsorption compared to other standard fluoropolymers.

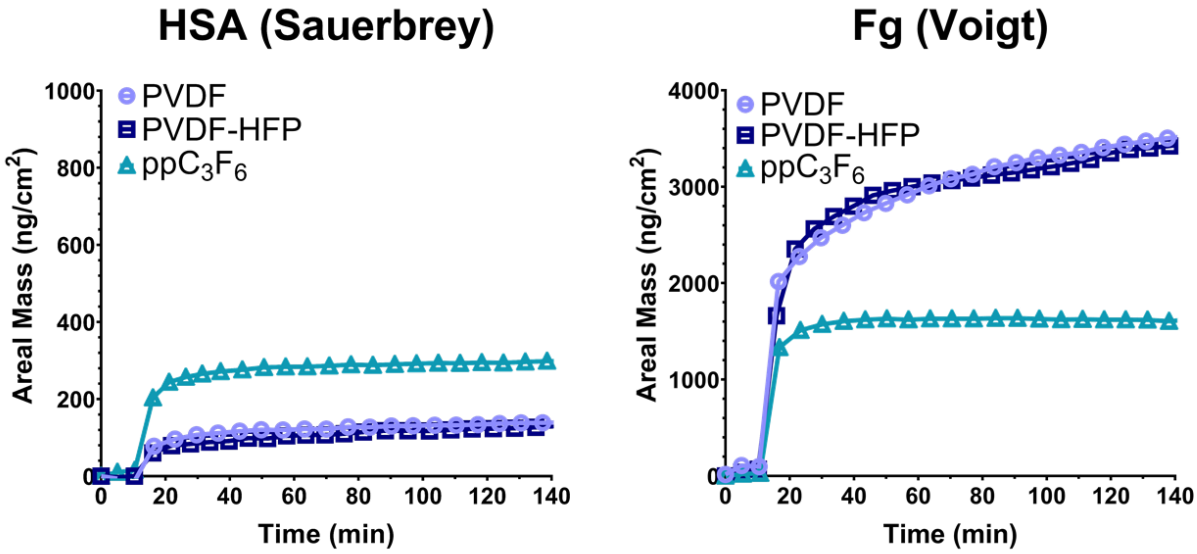

	Areal Mass (ng/cm²)
PVDF	141.7 ± 1.0
PVDF-HFP	129.6 ± 1.3
ppC_3F_6	296.9 ± 1.2

	Areal Mass (ng/cm²)
PVDF	3593.4 ± 10.6
PVDF-HFP	3587.3 ± 1.9
ppC_3F_6	1605.6 ± 5.8

Figure 3.5. HSA vs. Fg single protein solution adsorption on PVDF, PVDF-HFP, and ppC_3F_6. ppC_3F_6 demonstrates the greatest HSA and least Fg adsorption from single protein solutions, suggesting a selective preference for HSA adsorption and resistance to Fg adsorption compared to PVDF and PVDF-HFP. Table values represent the average areal mass values of the last 1-minute interval of each QCM-D trace (n=30).

3.4.4 Protein sequence: exploring the Vroman Effect

The effects of sequential protein exposure to the fluoropolymer surfaces was also investigated to observe the Vroman Effect (Chapter 1.3) on a measurable timescale. A 10-minute PBS wash step was inserted between protein steps to remove any loosely bound protein from the surface. When following the regular adsorption sequence based on inherent protein surface affinity and mobility (i.e. HSA followed by Fg), preadsorption with 300 μg/mL HSA for 1 hour followed by subsequent 30 μg/mL Fg exposure exhibits a marked increase in surface mass as the Fg occupies available surface binding sites and/or displaces non-tightly adsorbed HSA (**Figure 3.6, left**). This effect is significantly reduced for ppC_3F_6, which is explored with greater granularity in the following sections. The HSA layer areal mass was determined via the Sauerbrey relation (n=7), while the Fg regime was determined via Voigt modeling using n=3, 5, 7, 9, and 11.

To test the unidirectionality of the Vroman Effect—specifically, that Fg can displace HSA but not vice versa—the sequential protein solution order was reversed on all fluoropolymers (i.e. Fg followed by HSA) (**Figure 3.6, right**). The initial mass gain due to Fg adsorption is greater on all coatings than that observed for the secondary Fg sequence in the standard Vroman Effect experiment, but rapidly saturates the surface. After ~80 minutes and a 10-minute PBS wash, HSA was introduced. No mass change was observed for ppC_3F_6, and a minimal increase was temporarily observed for PVDF and PVDF-HFP before returning to the same concentration pre-HSA exposure. The small mass gain is attributed to transient interactions of the HSA with the adsorbed Fg layer before being washed away. For the reverse Vroman Effect, Voigt viscoelastic modeling was applied to the secondary HSA adsorption regime due to the preadsorbed dissipative Fg underlayer to more accurately measure mass change.

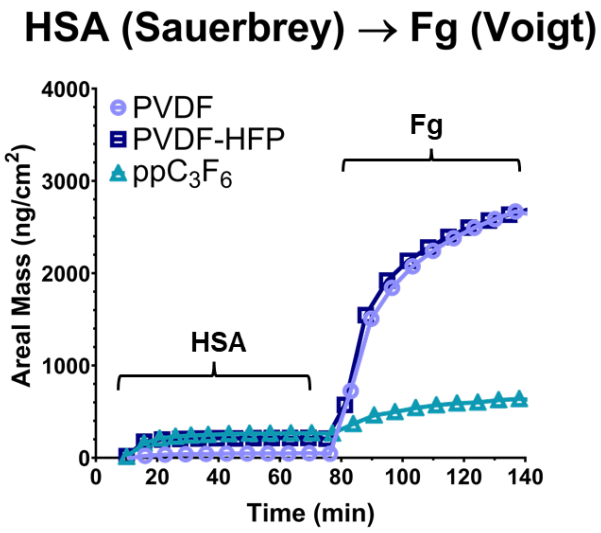

	Areal Mass (ng/cm²)	
	After HSA	After Fg
PVDF	43.3 ± 0.9	2620.2 ± 5.8
PVDF-HFP	212.4 ± 2.5	2647.7 ± 5.0
ppC_3F_6	265.9 ± 1.2	639.0 ± 4.6

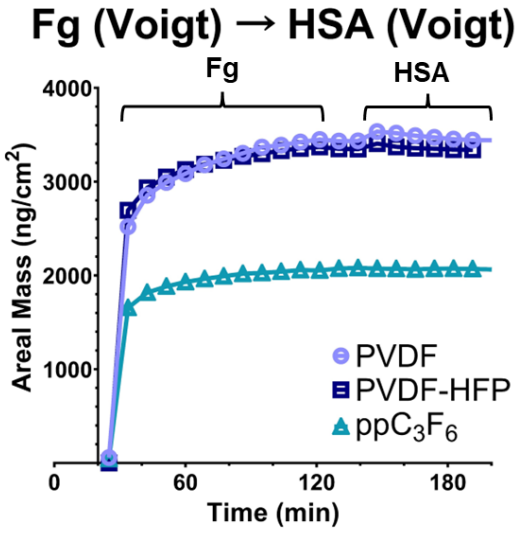

	Areal Mass (ng/cm²)	
	After Fg	After HSA
PVDF	3432.8 ± 2.0	3438.3 ± 2.1
PVDF-HFP	3350.8 ± 2.8	3330.3 ± 3.1
ppC_3F_6	2067.4 ± 5.8	2067.1 ± 2.4

Figure 3.6. The Vroman Effect is assessed by alternating HSA/Fg sequential flow adsorption on PVDF, PVDF-HFP, and ppC_3F_6. We verify that Fg can displace preadsorbed HSA but HSA cannot displace preadsorbed Fg on all fluoropolymers. Table values represent the average areal mass values of the last 1-minute interval of each QCM-D trace (n=30).

3.4.5 HSA and Fg protein solution variations

The following studies sought to investigate differential protein binding to the fluoropolymer surfaces under various protein composition and/or exposure conditions: pure HSA (300 µg/mL) for 2 hours, pure Fg (30 µg/mL) for 2 hours, binary 10:1 HSA:Fg (300:30 µg/mL) for 2 hours, and sequential HSA (300 µg/mL) to Fg (30 µg/mL) for 1 hour each (2 hours total). The 10:1 concentration ratio of HSA:Fg is intended to recapitulate physiological ratios of these two blood proteins at a 1% plasma concentration to fall within the detection range of QCM-D. Trends for each protein condition were consistent within each material type, though absolute values differed between fluoropolymers (**Figure 3.7**).

Pure HSA and pure Fg formed lower and upper bounds, respectively, for total adsorbate areal mass. The HSA protein layer was rigidly adhered with equilibrium surface coverage ~300 ng/cm^2 while Fg yielded a nonrigid layer with significant dissipation measurements across all fluoropolymers (~3500 ng/cm^2 for PVDF and PVDF-HFP; ~2360 ng/cm^2 for ppC_3F_6). Compared to the pure Fg condition, the co-introduction of HSA at a 10:1 HSA:Fg concentration in the binary solution was expected to result in competitive protein adsorption of HSA with Fg for surface binding sites and delay/deter total Fg surface coverage. Indeed, co-exposure of HSA and Fg reduces the equilibrium areal mass for all surface coatings by about ~1100-1500 ng/cm^2 for PVDF and PVDF-HFP. Given ppC_3F_6 adsorbed less Fg overall from the pure Fg single solution, the overall decrease in mass addition was less dramatic for the binary condition, but a marked decrease by ~770 ng/cm^2 was still observed.

When HSA was given an hour to pre-adsorb to the fluoropolymer-coated sensors in the sequential exposure condition, subsequent Fg adsorption was significantly reduced for ppC_3F_6 by 60% (-980 ng/cm^2) compared to the binary condition. This effect was not observed for PVDF or PVDF-HFP, which both exhibited a secondary Fg mass profile trace that approximately matched the final equilibrium areal mass of the binary condition (~2500 and 1960 ng/cm^2, respectively), suggesting that retention of HSA vs. Fg to these surfaces is independent of adsorption kinetics and surface residence time. Moreover, these data indicate that ppC_3F_6 has a unique ability to tight-bind and retain a significant portion of preadsorbed HSA and resist subsequent Fg displacement, while PVDF and PVDF-HFP experience protein turnover from HSA to Fg to a common final surface composition regardless of when HSA is introduced to the system (i.e. prior to or concurrently with Fg). The concept of HSA preadsorption in a noncompetitive environment and its effect on downstream Fg displacement was explored further in a dedicated HSA residence time study.

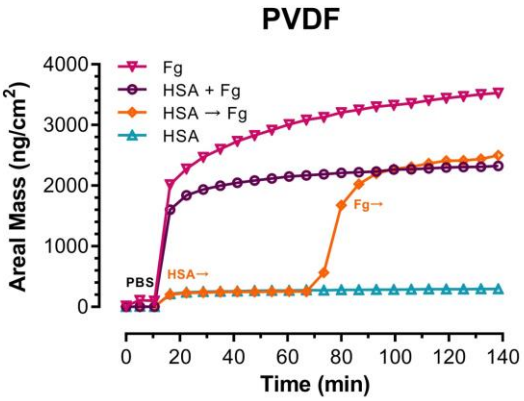

	Eqbm. Areal Mass (ng/cm²)
Fg	3547.9 ± 7.3
HSA + Fg	2334.1 ± 3.6
HSA → Fg	2496.5 ± 13.2
HSA	297.1 ± 1.4

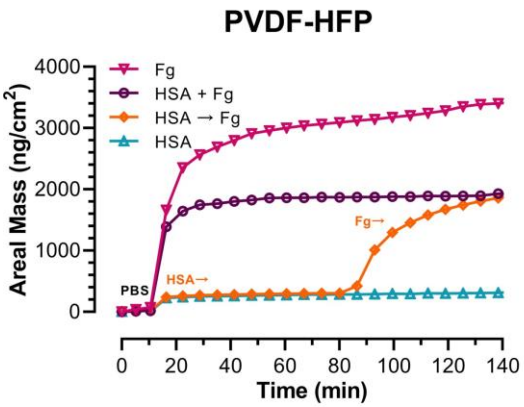

	Eqbm. Areal Mass (ng/cm²)
Fg	3451.0 ± 3.0
HSA + Fg	1924.7 ± 4.8
HSA → Fg	1960.3 ± 3.0
HSA	330.6 ± 1.2

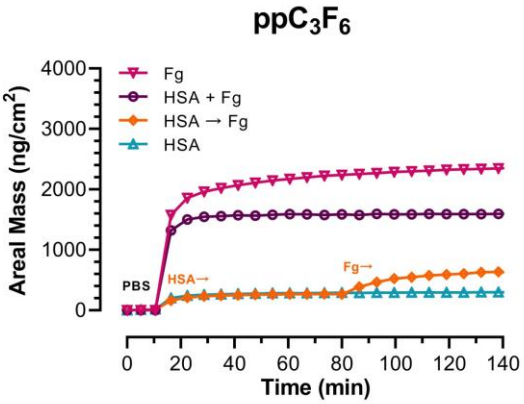

	Eqbm. Areal Mass (ng/cm²)
Fg	2362.1 ± 1.7
HSA + Fg	1587.3 ± 9.0
HSA → Fg	609.2 ± 5.2
HSA	297.0 ± 1.1

Figure 3.7. Four protein solution conditions (pure HSA, pure Fg, competitive binary HSA+Fg, and noncompetitive sequential HSA →Fg) are tested on PVDF, PVDF-HFP, and ppC$_3$F$_6$. All fluoropolymers demonstrated consistent trends across the 4 protein buffer conditions. Pure HSA and pure Fg formed lower and upper bounds, respectively, for total adsorbate areal mass. Competitive binary exposure of HSA+Fg reduces total adsorbate mass compared to that of pure Fg, while prolonged pre-adsorption with HSA in a noncompetitive environment followed by sequential Fg exposure reduces this value even more. Table values represent the average areal mass values of the last 1-minute interval of each QCM-D trace (n=30). (Concentrations used: 0.3 mg/mL HSA and 0.03 mg/mL Fg, to replicate 10:1 HSA:Fg physiological ratios)

3.4.6 HSA residence time on sequential Fg adsorption

Santore and colleagues demonstrated that denaturation and/or reorientation of adsorbed Fg/HSA is driven by hydrophobic interactions with the interface, and that this molecular relaxation and spreading occurs at faster kinetic rates for HSA, thus making it increasingly difficult for Fg to adsorb with longer HSA surface aging durations [9]. This process was investigated with the QCM-D on ppC_3F_6-coated sensors using sequential HSA to Fg buffer exchange with multiple HSA flow durations. We observed corroborative evidence indicating that longer HSA residence time on the surface reduces total Fg adsorption upon sequential exposure (**Figure 3.8**). Final protein adsorption was reduced by 50% for the ppC_3F_6 surface that received 60 minutes of HSA preadsorption compared to only 1 minute, with the most significant decrease in Fg displacement and adsorption kinetics occurring within the first 30 minutes. This suggests that time-dependent spreading and packing of HSA following adsorption increases resistance to Fg displacement.

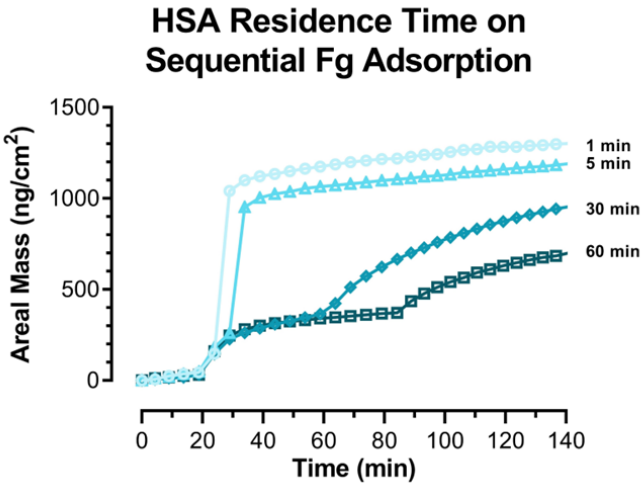

HSA Residence Time (min)	Fg Eqbm. Areal Mass (ng/cm²)
1	1303.5 ± 1.1
5	1188.6 ± 2.2
30	954.7 ± 1.3
60	697.1 ± 2.7

Figure 3.8. Effect of HSA Residence Time on Fg Displacement. Increasing the duration of HSA preadsorption on ppC_3F_6 reduces subsequent Fg adsorption.

3.4.7 D vs. F plots

Plotting dissipation (D) as a function of frequency (f) is a qualitative interpretation of QCM-D data that yields a time-independent relation. Because data points are temporally equi-spaced, increased distance between points indicates faster adsorption kinetics. Each D vs. f plot represents an adsorption 'fingerprint' unique for each protein (HSA or Fg) interaction with each fluoropolymer coating, in which multiple phases can be observed. A change to a steeper slope indicates a more viscoelastic overlayer, while a flatter slope suggests a change to a more rigid layer. These observations can be interpreted to suggest a change in protein orientation or degree of hydration that alters the adsorbate layer's detected viscoelasticity.

Here, we visualize the D vs. f plots for HSA and Fg single solutions, as well as sequential (HSA → Fg) and binary (HSA + Fg) exposure on PVDF, PVDF-HFP, and ppC_3F_6 (**Figure 3.9**). HSA adsorption shows data clusters for PVDF and PVDF-HFP at low Δf and ΔD in line with expectations for HSA's small globular structure—both adsorbed less HSA than ppC_3F_6 with fairly rigid adlayers (D < 0.5). Moreover, PVDF-HFP exhibits nearly no dissipation in its HSA layer and near-perfect coupling of the protein to the coating on the oscillating QCM-D sensor. Conversely, ppC_3F_6 demonstrates markedly higher Δf, with large steps between 0 to -10 Hz indicating rapid HSA adsorption to the layer, with an unusually high ΔD. This finding is in agreement with the large mass underestimation observed when the Sauerbrey relation was applied to HSA adsorbed on ppC_3F_6 (**Figure 3.3**, bottom left), suggesting a large dissipative element represented on the surface that is not attributed to the protein alone. Fg adsorption for ppC_3F_6 is distinctively lower ($|\Delta f|$ 70 Hz) compared to PVDF and PVDF-HFP ($|\Delta f|$ > 100 Hz) but exhibits parallel viscoelastic traces with both. Interestingly, PVDF-HFP demonstrates a marked increase in slope at $|\Delta f|$ 80 Hz while PVDF remains constant, suggesting a change to a more viscoelastic characteristic for the adsorbate layer beyond a

certain point of surface saturation. Sequential flow of HSA to Fg exhibits distinct biphasic traces for PVDF-HFP and ppC_3F_6 with the transition between proteins, though both phases remain viscoelastically consistent as they adsorb (linear slope). The PVDF coating adsorbed very little HSA such that a dissipation signature is essentially nonexistent, then exhibited rapid adsorption of Fg in the second phase that catches up to that observed for PVDF-HFP. In comparison, exposure to the binary HSA+Fg protein solution does not exhibit a clear viscoelastic phase transition for any of the surfaces, though with increasing mass addition (i.e. greater Δf), a slow transition to an increased slope (higher viscoelasticity) is observed, most prominently for PVDF-HFP. This is interpreted to signify the simultaneous gradual turnover of the protein adlayer from predominantly HSA to predominantly Fg without reaching full saturation for either protein, and thereby maintaining an intermediate characteristic of both.

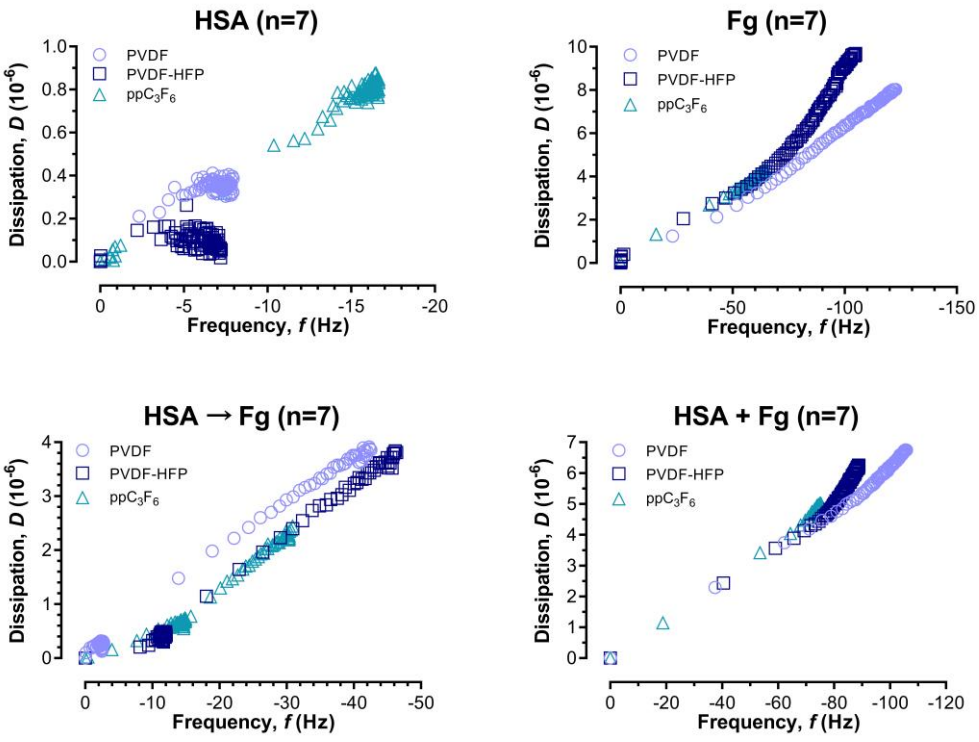

Figure 3.9. QCM-D dissipation vs. frequency plots of each protein condition. An increase in slope indicates a change to a more viscoelastic adlayer, while a decrease in slope indicates a change to a more rigid adlayer.

When viewing D vs. f plots of each protein condition in direct comparison across each fluoropolymer type, the adsorption of HSA on the surface often has clear effects on the subsequent adsorption of Fg (**Figure 3.10**). For PVDF, HSA co-introduced with Fg (binary exposure) demonstrates no difference in viscoelastic characteristic compared to the pure Fg condition, indicating that HSA does not display high surface affinity for this material and is not competitive with Fg for surface binding sites. However, HSA pre-adsorption in the sequential condition produces a more viscoelastic Fg overlayer (steeper slope), in addition to significantly reduced overall Fg adsorption ($|\Delta f|$ ~40 Hz vs. ~120 Hz for binary and pure Fg). Approximately similar trends for the sequential condition are seen for PVDF-HFP, although the pure Fg and binary conditions exhibit a higher dissipative characteristic with a steeper slope change at $|\Delta f|$ 70 Hz. PpC_3F_6 demonstrates minimal viscoelastic changes in overlayer across all protein exposure conditions, with fairly superimposed dissipation traces across the entire Δf range (mass addition to the coated sensor surface).

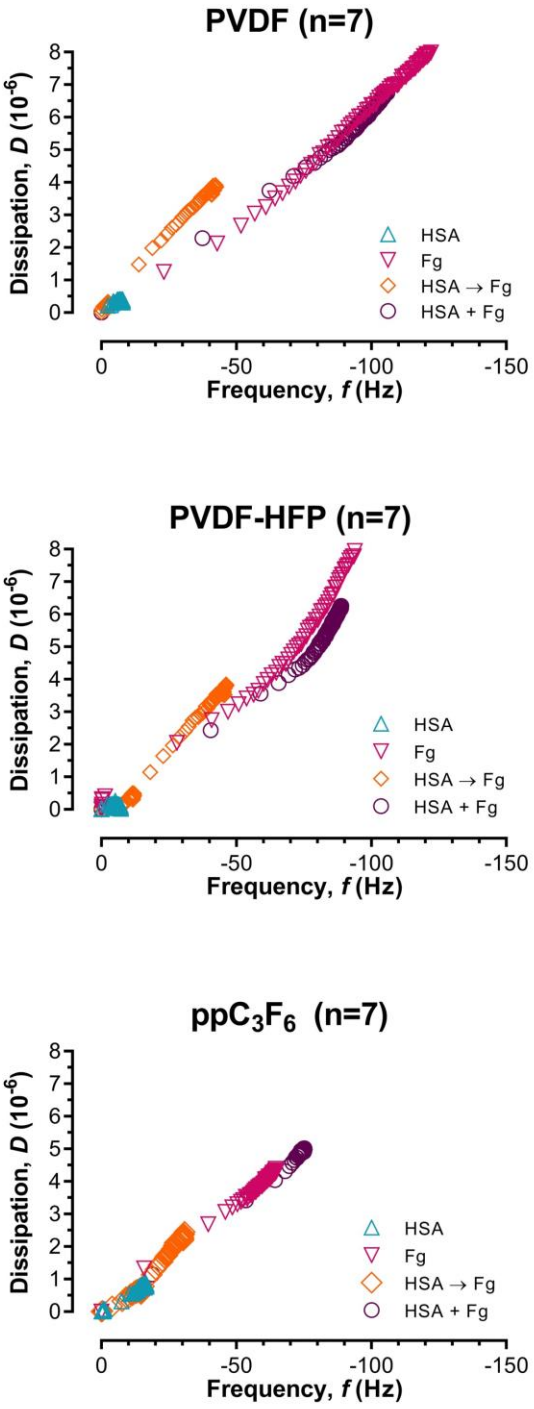

Figure 3.10. Summary QCM-D dissipation vs. frequency plots for PVDF, PVDF-HFP, and ppC_3F_6. Both PVDF and PVDF-HFP demonstrate variable dissipation signatures across the different protein conditions. PpC_3F_6 shows similar *f*:*D* values across all protein conditions.

3.5 Discussion

A combination of QCM-D studies has enabled the multiplex examination of HSA and Fg interaction with three fluoropolymer coatings. Concentration isotherms based on the Langmuir model were developed for each protein to yield a theoretical maximum surface concentration (or areal mass, M_{max}) on each material type. The ppC_3F_6 coating demonstrated the highest M_{max} for HSA and greatest affinity constant, as well as the lowest M_{max} for Fg. This material exhibits an inherent surface preference for adsorbing HSA over Fg compared to PVDF and PVDF-HFP. It should be noted that although commonly employed for characterizing protein adsorption behavior, the Langmuir model faces criticism as an oversimplified portrayal of the complex interaction of proteins on surfaces [19]. The Langmuir model, originally developed for modeling gaseous adsorbates under ideal isothermic conditions, requires the assumption of many conditions that are not satisfied by protein-surface interactions. These requirements are summarized as: equivalent adsorption sites, each adsorption site binds one adsorbate molecule, binding is fully reversible and reaches a dynamic equilibrium, and adsorbed molecules do not interact with each other. In contrast, proteins often denature and spread on surfaces—particularly hydrophobic surfaces that destabilize the native solution structure—which increases their occupancy of surface binding sites (footprint) and greatly reduces the likelihood of desorption. In addition, non-globular proteins undergo surface reorientation, which can be affected by both the core stability of the protein as well as proximity of neighboring proteins as surface crowding effects become relevant. More complex adsorption models, such as the random sequential adsorption (RSA) process developed by Ramsden and coworkers, may better capture the nuances of protein adsorption and their tendency for cooperativity and aggregation on surfaces [20-23]. In summary, while these non-ideal conditions should be taken into consideration, the final surface concentrations measured for each protein at each

solution concentration are still valid and demonstrate the high surface adsorption of HSA and low surface adsorption of Fg to ppC_3F_6, independent of the calculated M_{max} and K_A.

The unidirectionality of the Vroman Effect based on protein surface affinity was also examined and verified. Fg was able to permanently displace preadsorbed HSA on all fluoropolymers, albeit to a significantly lesser extent on ppC_3F_6, but HSA was not able to permanently displace preadsorbed Fg on any of the fluoropolymers. In this latter case, minimal to no protein deposition was observed, verifying that protein adsorption is unidirectional and non-aggregative (only monolayers form). This is consistent with reported observations that proteins do not tend to nonspecifically adsorb to each other [24-26].

Introduction of a variety of protein conditions demonstrates the competitive binding environment of dual protein solutions for surface adsorption sites. Binary exposure of HSA+Fg (10:1) reduces the equilibrium areal mass of total protein adsorption compared to the pure Fg condition for all fluoropolymers. This indicates that HSA does rapidly arrive at and adsorb on the surface while exhibiting some resistance to Fg displacement (as observed through the decrease in total equilibrium areal mass at saturation compared to the pure Fg solution condition), although the lack of a bimodal adsorption profile suggests that HSA-to-Fg turnover in a binary competitive environment is extremely rapid such that a surface monolayer of HSA is either never achieved or not resolvable on the timescales analyzed via QCM-D. Additionally, the overall reduction in areal mass suggests that some HSA remains on the surface for a prolonged period, i.e. the surface tight-binds HSA. This was verified further with the sequential addition of HSA followed by Fg, which showed that surface aging of HSA for 1 hour in a noncompetitive environment permitted protein spreading over the fluoropolymer coating that further resisted subsequent Fg displacement. This effect was most pronounced for ppC_3F_6, which exhibited minimal mass addition with the secondary Fg exposure, indicating the surface's ability to tightly bind and retain HSA even

when faced with a higher surface affinity protein like Fg.

HSA adsorption on ppC_3F_6 exhibits a large discrepancy between Sauerbrey and Voigt mass profiles compared to the superimposed profiles seen for PVDF and PVDF-HFP, indicating an uncharacteristic viscoelasticity for the ppC_3F_6-adsorbed HSA layer. This observation is consistent with the large dissipation signature seen for this condition in the D vs. f plot [27]. Given HSA's small and globular native conformation, a rigid adlayer was expected. Thus, this viscoelastic behavior is suggested to represent reorganization of water molecules at the protein-fluid interface that is partially coupled to, and therefore detected, by the oscillating QCM-D sensor. A possible explanation is that the highly crosslinked and CF_3-enriched ppC_3F_6 coating entropically drives rapid and abundant adsorption of HSA to the surface through the hydrophobic effect, which causes the HSA molecules to spread and unpack their hydrophobic cores towards the surface and reduce the free energy at the interface [33-34]. As a result, this conformational transformation strongly orients the hydrophilic residues of HSA towards the interfacial water network, which induces increased hydrogen bonding with the peri-surface water molecules to form hydration shells that delay Fg adsorption.

3.6 Summary

Through surface characterization and subsequent QCM-D studies, we have shown that ppC_3F_6 demonstrates the highest and lowest surface affinities for HSA and Fg, respectively, with the overall greatest preference for HSA:Fg adsorption. We have also verified some basic principles regarding competitive protein adsorption on hydrophobic fluoropolymers using various protein buffer conditions to compare the effects of binary competitive adsorption and sequential non-competitive adsorption against HSA or Fg single protein solutions. The hypothesis that HSA unpacks and spreads upon prolonged surface exposure—particularly to ppC_3F_6—to yield greater resistance to Fg displacement

was confirmed. Finally, the unique fluoro-chemistries and highly hydrophobic properties created by the plasma polymerization process for ppC_3F_6 are suspected to entropically drive rapid adsorption of HSA and free the energetically unfavorable association of surface-adjacent water molecules back into the bulk continuum. This causes a conformational change in the HSA to strongly associate hydrophobic residues with the surface while reorienting hydrophilic residues to the bulk aqueous phase, thereby creating a partially coupled interfacial water network above the adsorbed protein layer that delays Fg adsorption.

Employing multiple analytical techniques enables us to draw better-informed conclusions on surface-level molecular events. The QCM-D provides excellent information on time-resolved adsorption kinetics and adlayer properties, but does not elucidate the final protein layer composition (HSA:Fg). These will be quantitively investigated with existing radiolabeling methods used within our lab in the dissertation work of a colleague (Kyung-Hoon Kim) and will therefore not be presented in this dissertation.

In summary:

- ppC_3F_6 demonstrates the highest HSA adsorption, highest HSA retention upon subsequent Fg exposure, and highest HSA & Fg binding affinity
- Both HSA and Fg adsorption on ppC_3F_6 are highly dissipative, suggesting strong water association in the case of HSA and a population of end-on adsorbed molecules in the case of Fg
- Protein displacement is unidirectional and multilayers do not form
- Fg adsorption can be attenuated through rapid surface aging of early-arrival proteins (HSA)

3.7 Acknowledgments

The authors gratefully acknowledge the assistance of Dr. John Sumida for his assistance in setup, training, and maintenance of the QCM-D instrument located in

the Analytical Biopharmacy Core (ABC) at the Molecular Analysis Facility (MAF), University of Washington.

3.8 References

1. Tonda-turo, C., Carmagnola, I. & Ciardelli, G. Quartz Crystal Microbalance With Dissipation Monitoring : A Powerful Method to Predict the in vivo Behavior of Bioengineered Surfaces. **6**, 1–7 (2018).
2. Mosley, R. J., Talarico, M. V. & Byrne, M. E. Recent applications of QCM-D for the design, synthesis, and characterization of bioactive materials. *J. Bioact. Compat. Polym.* **36**, 261–275 (2021).
3. Easley, A. D. *et al.* A practical guide to quartz crystal microbalance with dissipation monitoring of thin polymer films. *J. Polym. Sci.* **60**, 1090–1107 (2022).
4. Murakami, D. *et al.* Hydration Mechanism in Blood-Compatible Polymers Undergoing Phase Separation. *Langmuir* **38**, 1090–1098 (2022).
5. Berglin, M. *et al.* Fibrinogen Adsorption and Conformational Change on Model Polymers : Novel Aspects of Mutual Molecular Rearrangement. **25**, 5602–5608 (2009).
6. Sauerbrey, G. Use of quartz crystals for weighing thin films and microweighing. *Z. Physik* **155**, 206–222 (1959).
7. Voinova, M.V., Rodahl, M., Jonson, M. & Kasemo, B. Viscoelastic acoustic response of layered polymer films at fluid-solid interfaces: continuum mechanics approach. *Phys. Scr.* **59**(5), 391 (1999).
8. Vroman, L., Adams, A.L. Adsorption of Proteins out of Plasma and Solutions in Narrow Spaces. *J. Colloid Interface Sci.* **111**(2), 391-402 (1986).
9. Wertz, C. F., & Santore, M. M. Adsorption and relaxation kinetics of albumin and fibrinogen on hydrophobic surfaces: Single-species and competitive behavior. *Langmuir*, **15**(26), 8884–8894 (1999).
10. Norde, W. My voyage of discovery to proteins in flatland ...and beyond. *Colloids Surf B Biointerfaces.* **61**(1), 1-9 (2008).
11. Phan, H. T. M., Bartelt-Hunt, S., Rodenhausen, K. B., Schubert, M. & Bartz, J. C. Investigation of bovine serum albumin (BSA) attachment onto self-assembled monolayers (SAMs) using combinatorial quartz crystal microbalance with dissipation (QCM-D) and spectroscopic ellipsometry (SE). *PLoS One* **10**, (2015).

12. Weber, N., Wendel, H. P. & Kohn, J. Formation of viscoelastic protein layers on polymeric surfaces relevant to platelet adhesion. *J. Biomed. Mater. Res. - Part A* **72**, 420–427 (2005).

13. Weber, N., Pesnell, A., Bolikal, D., Zeltinger, J. & Kohn, J. Viscoelastic properties of fibrinogen adsorbed to the surface of biomaterials used in blood-contacting medical devices. *Langmuir* **23**, 3298–3304 (2007).

14. Kubiak, K., Adamczyk, Z. & Wasilewska, M. Mechanisms of fibrinogen adsorption at the silica substrate determined by QCM-D measurements. *J. Colloid Interface Sci.* **457**, 378–387 (2015).

15. Doliška, A., Ribitsch, V., Stana Kleinschek, K. & Strnad, S. Viscoelastic properties of fibrinogen adsorbed onto poly(ethylene terephthalate) surfaces by QCM-D. *Carbohydr. Polym.* **93**, 246–255 (2013).

16. Voinova, M. V., Rodahl, M., Jonson, M. & Kasemo, B. Viscoelastic acoustic response of layered polymer films at fluid-solid interfaces: Continuum mechanics approach. **59**, (1998).

17. Höök, F., Rodahl, M., Brzezinski, P. & Kasemo, B. Energy Dissipation Kinetics for Protein and Antibody - Antigen Adsorption under Shear Oscillation on a Quartz Crystal Microbalance. *Langmuir* **14**, 729–734 (1998).

18. Höök, F. & Kasemo, B. Variations in coupled water, viscoelastic properties, and film thickness of a Mefp-1 protein film during adsorption and cross-linking: A quartz crystal microbalance with dissipation monitoring, ellipsometry, and surface plasmon resonance study. *Anal. Chem.* **73**, 5796–5804 (2001).

19. Latour, R.A. The Langmuir isotherm: a commonly applied but misleading approach for the analysis of protein adsorption behavior. *J. Biomed. Mater. Res. Part A.* **103**, 949-958 (2015).

20. Ramsden, J.J. Concentration scaling of protein deposition kinetics. *Phys Rev Lett.* **71**, 295–298 (1993).

21. Ramsden, J.J. Review of new experimental-techniques for investi- gating random sequential adsorption. *J Stat Phys* **73**, 853– 877 (1993).

22. Van Tassel, P.R., Guemouri, L., Ramsden, J.J., Tarjus, G., Viot, P. & Talbot, J. A particle-level model of irreversible protein adsorption with a postadsorption transition. *J Colloids Interface Sci* **207**, 317– 323 (1998).

23. Van Tassel, P.R., Viot, P., Tarjus, G., Ramsden, J.J. & Talbot, J. Enhanced saturation coverages in adsorption-desorption processes. *J Chem Phys* **112**, 1483–1488 (2000).

24. Horbett, T.A., Brash, J.L. & Norde, W. Proteins at interfaces III, state of the art. *ACS Symposium Series*. American Chemical Society, Washington, DC,

869 (2012).

25. Brash, J.L. & Horbett, T.A. Proteins at interfaces: physicochemical and biochemical studies. *ACS Symposium Series*, American Chemical Society, Washington, DC, 706 (1987).
26. Horbett, T.A & Brash, J.L. Proteins at interfaces II: fundamentals and applications. *ACS Symposium Series*. Washington, DC, 561 (1995).
27. Rodahl, M. *et al.* Simultaneous frequency and dissipation factor QCM measurements of biomolecular adsorption and cell adhesion. *Faraday Discuss.* **107**, 229–246 (1997).
28. Hussain, M., Northoff, H. & Gehring, F. K. QCM-D providing new horizon in the domain of sensitivity range and information for haemostasis of human plasma. *Biosensors and Bioelectronics* **66**, 579–584 (2015).
29. Irwin, E. F., Ho, J. E., Kane, S. R. & Healy, K. E. Analysis of interpenetrating polymer networks via quartz crystal microbalance with dissipation monitoring. *Langmuir* **21**, 5529–5536 (2005).
30. Kanazawa, K. & Cho, N. J. Quartz crystal microbalance as a sensor to characterize macromolecular assembly dynamics. *J. Sensors* **2009**, (2009).
31. Luan, Y. *et al.* 125I-radiolabeling, surface plasmon resonance, and quartz crystal microbalance with dissipation: Three tools to compare protein adsorption on surfaces of different wettability. *Langmuir* **30**, 1029–1035 (2014).
32. Lakshmanan, R. S., Efremov, V., Cullen, S. M. & Killard, A. J. Measurement of the evolution of rigid and viscoelastic mass contributions from fibrin network formation during plasma coagulation using quartz crystal microbalance. *Sensors Actuators, B Chem.* **192**, 23–28 (2014).
33. Latour, R.A. Biomaterials: protein-surface interactions, in: G.E. Wnek, G.L. Bowlin (Eds.), The Encyclopedia of Biomaterials and Bioengineering, second ed., Informa Healthcare, New York, NY, 2008, 270-284.
34. Ratner, B.D. Role of water in biomaterials, in: B.D. Ratner, A.S. Hoffman, F.J. Schoen, J.E. Lemons (Eds.), Biomaterials Science: An Introduction to Materials in Medicine, third ed., *Academic Press*, Waltham, MA, 2013, 55-59.

Chapter 4

Investigation of fibrinogen surface structure and bioactivity

Liu, S., Kim, K.H. & Ratner, B.D. Surface-induced changes in fibrinogen bioactivity on a radiofrequency glow-discharge fluoropolymer mediate platelet adhesion in a surface passivation strategy for long-term blood compatibility. In preparation.

Initiated by Sherry Liu (SL) as a part of, and funded by, the Center for Dialysis Innovation (CDI) for Co-Director and Principal Investigator Dr. Buddy D. Ratner (BDR) under the Blood Compatibility research project. SL motivated and conceptualized the work, designed and executed the experiments, performed all analyses, and wrote the manuscript. Barring revisions or edits suggested by committee members, the following text, combined with work described in Chapter 6 (to which KHK contributed), will serve as the draft for a journal submission.

4.1 Abstract

Although total fibrinogen (Fg) adsorption on biomaterial surfaces is an accepted measure of thrombogenicity, a wholly non-fouling artificial biomaterial surface remains—and may forever be—elusive. Therefore, given the low-fouling fluoropolymers developed at present, selecting surfaces within this materials class

that adsorb Fg in a non-platelet activating conformation or orientation may be a more realistic and actionable strategy. In this chapter, bioactivity of fibrinogen (Fg) will be explored using a series of immunoassays employing structurally sensitive antibody probes to investigate how proteins activate and deactivate depending on adsorption-induced structural changes. These surface-denatured Fg will be compared to thermally denatured Fg to determine if loss in bioactive sites is similar across denaturation mechanisms. In addition, we employ atomic force microscopy (AFM), quartz crystal microbalance with dissipation (QCM-D), and electron spectroscopy for chemical analysis (ESCA) to determine Fg surface orientation and adsorbate layer thickness. We hope to understand how the bioactive states of Fg correspond to differential protein interactions with various material substrates, with the aim to develop surface-based strategies that block or prevent their exposure to circulating platelets.

4.2 Background

Efforts to develop materials that resist protein adsorption have traditionally focused on reducing the total amount of protein adsorption, yet even ultralow surface amounts of Fg are capable of supporting full-scale platelet activation [1-2]. A substantial body of evidence now supports that adsorption-induced conformational changes in Fg structure—and not the total surface quantity—determines the degree of platelet adhesion through the exposure of platelet-binding epitopes [3-7]. Latour & coworkers found that platelet adhesion and activation are largely attenuated when the fibrinogen retained its near-native structure, but increased as much as 5x as the protein unfolded [5].

Fg is an elongated molecule comprised of dimerized symmetric protomers each consisting of an Aα (FGA), Bβ (FGB), and γ (FGG) polypeptide chain that emanate from their N-termini as disordered coiled-coils (central E region) to their C-termini as two globular domains (D region) [8-9]. The dodecapeptide at the

γ-chain carboxyl-terminus (γC dodecapeptide HHLGGAKQAGDV: γ400-411) serves as a direct ligand for residues 294-314 of the platelet adhesion receptor GPIIb-IIIa, which belongs to the integrin family and is the most active and abundant surface receptor [10-12]. Zhang et al. demonstrated that the hydrophobic D regions strongly adsorb to hydrophobic surfaces and repel the αC region, creating a deflected tri-nodular structure where both ends of the molecule are engaged with the surface to form a monomeric Fg layer [13]. When stained with an antibody targeting the platelet-binding γC dodecapeptide, the Fg monolayer adsorbed to a hydrophobic polystyrene (PS) surface showed almost no fluorescence, while that adsorbed to a hydrophilic poly(4-vinylpyridine) (P4VP) surface displayed uniform staining across the surface irrespective of the concentration of the Fg bulk solution used to deposit the adlayer (<10% plasma concentration of 0.1 mg/mL to physiological concentration at 4 mg/mL) [13].

The dominant effects of surface conformation are further corroborated by the fact that unstimulated platelets bind exclusively to immobilized Fg at the γC sequence but not to soluble Fg, emphasizing the significance of adsorbed γC in mediating platelet adhesion [14-16]. Once adsorbed, Fg's α-helices in the carboxy-terminal region of the Bβ and γ chains are converted to random chains, leaving the γC dodecapeptide structurally unprotected and exposed for platelet interaction [17]. Two additional binding sites are located in the Aα chain at α95-98 (RGDF) and α572-575 (RGDS), though these have been shown to hold a secondary role to mediating platelet adhesion and activation [18-21]. Sivaraman & Latour showed RGD-blocking of platelet integrins reduces platelet adhesion and activation, while polyclonal antibody-Fg treatment completely inhibits it, indicating the critical involvement of non-RGD binding platelet receptors during adhesion [18]. Therefore, preserving the secondary structure of the adsorbed Fg to that of the native soluble structure appears to lower the resultant surface thrombogenicity at the acute stage. However, the sustainability of this approach is debated— certain research groups have proposed that hydrophobic surfaces that

encourage rapid platelet adhesion and spreading over the surface drive passivation of the bare substrate with a uniform layer of platelet membranes after releasing their activated components [22-23]. Hydrophobic C18-enriched surfaces have shown evidence of highly spread platelet monolayers after rapid release of lactate dehydrogenase (LDH) [24], and formation of these adherent and uniform thrombi exhibit non-thrombogenic behavior upon continued exposure to flowing whole blood [25-26]. Thus, though potentially counterintuitive, a surface that promotes rapid platelet adhesion to form a stable thrombus during an initial phase of acute reactivity may have better long-term outcomes, by inhibiting prolonged platelet activation and aggregation at a bare biomaterial surface that would continuously form unstable multilayers prone to shedding.

4.3 Methods

4.3.1 Fg surface orientation

The initial orientation of adsorbed proteins do not necessarily translate to their final equilibrium orientation state, if this state is ever attained. The dependency of biomolecule surface orientation on bulk solution concentration, mass transport, and protein-protein interactions on the surface have all been reported at length [4-5, 13, 18, 27]. Given the elongated structure of Fg, we investigate changes in its surface orientation in dry and hydrated states through concentration-dependent immunoassays, atomic force microscopy (AFM), quartz-crystal microbalance with dissipation (QCM-D), and electron spectroscopy for chemical analysis (ESCA).

4.3.1.1 Globular vs. elongated protein structural immunoassays

To test the surface reorientation of ellipsoid proteins like Fg from side-on to end-on adsorption with increasing bulk concentration, concentration ranges of the

following proteins were coated onto four 96-well polystyrene microplates: 1:2 serial dilutions of Fg (human plasma fibrinogen, F3879, Sigma-Aldrich, St. Louis, MO) from 1920-0 μg/mL (on two plates), 1:2 serial dilutions of Fn (human plasma fibronectin, Cat. No. 341635, Sigma-Aldrich, St. Louis, MO) from 1000-0 μg/mL, and 1:2 serial dilutions of HSA (human serum albumin, Cat. No. A8763, Sigma-Aldrich, St. Louis, MO). Fibronectin (Fn) was included as an alternate elongated protein control with comparable molecular weight and dimensions (440 kDa dimer and 133 nm long [28-29]) to that of Fg (340 kDa and 9 x 47.5 x 6 nm [30]). HSA was included as a negative control representing a globular-shaped protein with no distinctive aspect ratio (and therefore no expected surface orientation preference). Plates were then incubated overnight at 4°C to allow the proteins to preadsorb and adopt their equilibrium conformation. The following day, plates were washed x3 in 0.1% PBS-T, blocked with Pierce® protein-free blocking buffer (Cat. No. 37584, Thermo Scientific, Waltham, MA), and incubated for 1 hour at ambient temperature with the following primary monoclonal antibodies: mouse anti-human Fg α-chain (FGA) ([UC45], ab19079, Abcam, Cambridge, MA), mouse anti-human Fg γ-chain (FGG) ([5A6], ab119948, Abcam, Cambridge, MA), mouse anti-human fibronectin ([BC-1], ab154210, Abcam, Cambridge, MA), and mouse anti-human serum albumin ([15C7], ab10241, Abcam, Cambridge, MA). Following primary mAb incubation, plates were washed x3 in 0.1% PBS-T and incubated for 1 hour with the secondary antibody (goat anti-mouse IgG H&L (HRP), ab205719, Abcam, Cambridge, MA). Binding was detected with 1-Step™ Ultra TMB substrate (Cat. No. 34028, Thermo Scientific, Waltham, MA) and stopped with 1N H_2SO_4, followed by absorbance measurements at 450 nm with 540 nm background readings (BioTek Synergy Multi Mode Reader, Agilent Technologies, Santa Clara, CA), with each serial dilution on each plate carried out in duplicate and subtracted by the blank well measurements.

4.3.1.2 Atomic force microscopy (AFM) imaging of unfolded Fg

Atomic force microscopy (AFM) is a powerful tool that can probe protein surface conformation *in situ* at the single-molecule level. When adsorbed at sub-monolayer concentrations, individual molecules can be resolved and visualized for changes in structure and sometimes orientation. For AFM study of Fg on ppC_3F_6 under ambient conditions, Si substrates were ultrasonically cleaned in methanol for 10 minutes and dried with N_2 prior to in-the-glow plasma deposition as described in (Chapter 2.2.1).

To adsorb Fg onto the surface, 100 µL of a 300 ng/mL Fg solution (10% plasma concentration) (human plasma fibrinogen, F3879, Sigma-Aldrich, St. Louis, MO) in DI water was drop-cast onto the coated substrate and allowed to evaporate overnight. Imaging was performed in air on a Cypher VRS AFM (Asylum Research, Santa Barbara, CA) operated in tapping mode using Si tips on a SiN cantilever with a spring constant of 0.12 N/m and nominal tip radius of 2 nm (SNL-10B, Bruker, Billerica, MA). Images were analyzed using Gwyddion SPM data analysis software.

4.3.1.3 ESCA determination of Fg adlayer thickness and orientation

Electron spectroscopy for chemical analysis (ESCA) can indirectly estimate surface orientation of elongated proteins like Fg based on sampling depth. Following surface adsorption of a protein on a film, detection of unique film elements not present in the protein (e.g. fluorine, in our case) at known take-off angles indicates a protein adlayer that is less than the thickness of the corresponding sampling depth, assuming monolayer coverage. For example, the standard take-off angle for ESCA is taken at 0 °C with a surface penetration of ~10 nm. Specifically for Fg, with a molecular size of approximately 45 nm x 9 nm, the theoretical thickness of a side-on adsorbed monolayer would be ~6-10 nm thick at a surface concentration of 0.14 µg/cm², while a packed end-on adsorbed

monolayer would be ~45-50 nm thick at a surface concentration of 0.89 μg/cm² [31].

For increased surface sensitivity, angle-dependent ESCA can be performed on the Kratos AXIS Ultra DLD XPS instrument (Kratos Analytical Ltd., Manchester, UK) by conducting acquisition in hybrid mode. In addition to the nominal photoelectron take-off angle of 0 °C (~10 nm sampling depth), two additional angles can be measured: 55 °C (~5 nm sampling depth) and 75 °C (~1 nm sampling depth). Three concentrations of Fg (human plasma fibrinogen, F3879, Sigma-Aldrich) solvated in ultrapure water—0.03, 0.3, and 3 mg/mL, corresponding to 1%, 10%, and 100% plasma concentration—were prepared, and a 100 μL droplet of each was deposited on ppC_3F_6-coated silicon substrates and allowed to adsorb for 1 hour at ambient temperature in a humid chamber to prevent evaporation. The droplets were then rinsed off with fresh ultrapure water and dried with a nitrogen stream. Standard and angle-dependent ESCA were performed for compositional assessment only (i.e. survey scans) and analyzed as previously described (Chapter 2.2.3). To indirectly verify the surface orientation of the adsorbed Fg at each of the three concentrations, the fluorine and nitrogen content were evaluated for n=3 spots at each take-off angle. Loss in fluorine content indicated a Fg layer thicker than 10 nm and presumably in a packed end-on adsorption orientation, while an increase in nitrogen content (which exists in abundance in the peptide bonds of proteins) was used to confirm the increase of Fg on the surface.

4.3.2 FGA/FGG monoclonal antibody binding to Fg on fluoropolymers

The accessibility of platelet-binding epitopes on Fg is an important marker of its adsorbed-state bioactivity [18, 32]. To evaluate changes in Fg surface orientation and/or conformation as a result of adsorption to fluoropolymer

surfaces, enzyme-linked immunosorbent assays (ELISAs) employing two monoclonal antibodies (mAbs) targeting the α-chain (mouse anti-human FGA antibody [UC45], ab19079, Abcam, Cambridge, MA) and γ-chain (mouse anti-human FGG antibody, ab119948 [5A6], Abcam, Cambridge, MA) of Fg were developed and optimized for working dilutions through checkerboard titrations in a microplate format. The binding target for the FGA mAb is located on the α-helical strand in the central region of the α-chain and includes RGD binding sites at the N-terminal, which are suggested to mediate Fg polymerization into fibrin in the presence of thrombin [13, 21]. The binding target for the FGG mAb corresponds to residues 210-437 located on the C-terminus of the γ-chain, and importantly includes the platelet-binding dodecapeptide 400-411. Thus, response signals from these two mAbs are intended to coarsely represent the Fg molecule adsorbed side-on (greater FGA signal) or end-on (greater FGG signal), as well as assist in evaluating the exposure of the critical platelet-binding epitope on the γ-chain carboxy-terminus of the protein.

To prepare the 96-well microplates, 200 µL of 2.7% PVDF and 2.3% PVDF-HFP solutions dissolved in DMF were pipetted into each well and incubated for 1 hour in a chemical fume hood before aspirating off any remaining solution. The plates were then placed in a 65 °C oven overnight to fully remove any remaining DMF solvent and anneal the polymer coatings. PpC_3F_6 was directly deposited onto clean polystyrene high-binding 96-well microplates reacted in-the-glow of the plasma reactor according to previously described methods (Chapter 2.2.1). The plate was rotated 180° after 10 minutes of deposition to ensure wells received even coverage within the plasma glow. The three fluoropolymer-coated plates (ppC_3F_6, PVDF, and PVDF-HFP) were then incubated overnight at 4°C with 1:2 serial dilutions of human Fg (human plasma fibrinogen, F3879, Sigma-Aldrich) in sodium carbonate buffer (pH 9.6) from 3840 µg/mL (physiological concentration) down to 0.916 µg/mL to allow the protein to preadsorb and adopt its equilibrium conformation on each surface coating type. The following day, plates were blocked in Pierce®

protein-free blocking buffer (Cat. No. 37584, Thermo Scientific, Waltham, MA), incubated for 1 hour at ambient temperature with the primary mAbs, then 1 hour with the secondary antibody (goat anti-mouse IgG H&L (HRP), ab205719, Abcam, Cambridge, MA). All incubation steps included a x3 0.1% PBS-T wash step inserted before. Binding was detected with 1-Step™ Ultra TMB substrate (Cat. No. 34028, Thermo Scientific, Waltham, MA) and stopped with 1N H_2SO_4, followed by absorbance measurements at 450 nm with 540 nm background readings (BioTek Synergy Multi Mode Reader, Agilent Technologies, Santa Clara, CA), with each serial dilution per FP type carried out in duplicate and subtracted by the blank well measurements.

4.3.3 Fg thermal denaturation and effects on FGA/FGG monoclonal antibody binding

While the effects of surface-induced denaturation on Fg are variable due to the diverse nature of surface types (surface energy, roughness, surface charge, etc.), thermal denaturation of proteins in aqueous solution (native state) has long been shown to irreversibly alter protein secondary structure in predictable ways that directly influence their bioactivity. Fg in the absence of Ca^{2+} (a stabilizing coordinating ion) is reported to have a melting temperature (T_m) of 54.0±0.1 °C [33], while precipitation occurs above 56 °C [34-37]. The thermal denaturation of Fg at 54 °C was confirmed with circular dichroism (CD) on a Jasco J-720 spectropolarimeter (JASCO Inc., Easton, MD) flushed with nitrogen gas. Fg (human plasma fibrinogen, F3879, Sigma-Aldrich) was dissolved in 10 mM phosphate buffer (PB, pH 7.0) to a final concentration of 1 μM for three separate conditions: nondenatured (kept on ice at ~4 °C), thermally denatured (1 hour in a 54 °C water bath), and a third condition to test the irreversibility of the thermal cycle with a 1 hour 54 °C incubation followed by 2 hours at 4 °C. CD spectra were collected in a 1 mm path length cuvette (Cat. No. 110-1-40, Hellma Analytics, Müllheim, Baden

Württemberg, Germany) with an accumulation of n=8 in the far-UV range from 250 to 200 nm. All data were corrected with blank buffer measurements and processed through a FFT filter to reduce noise in the accompanying spectra analysis software. The mean residual ellipticity (MRE) was calculated by first subtracting the protein signal with the blank signal and zeroing the curve against the value at 270 nm, then correcting for the protein solution concentration and number of peptide bonds.

With the thermal denaturation of Fg verified, we sought to compare the epitope binding availability of nondenatured Fg (ND-Fg) with thermally denatured Fg (TD-Fg) after adsorption to our selected fluoropolymers by employing the same conformational immunoassay described in the previous section (Chapter 4.3.2) with a few modifications. For the TD-Fg microplate, a stock concentration of 3840 µg/mL Fg in sodium carbonate buffer (pH 9.6) was heated to 54 °C for 1 hour in a water bath and allowed to cool to ambient temperature before 1:2 serial dilutions from 3840 µg/mL (physiological concentration) down to 0.916 µg/mL in the 96-well microplate, followed by overnight incubation at 4 °C with the ND-Fg microplate. The remainder of the assay was performed in parallel with the ND-Fg microplate.

We also investigated the effects of thermal denaturation on FGA and FGG MAb binding with higher granularity by creating mixtures of the following percentage ratios of ND-Fg to TD-Fg (54 °C): 100:0, 75:25, 50:50, 25:75, and 0:100. To create the mixtures, two 3840 µg/mL stock solutions were created, and one was heated to 54 °C for 1 hour in a water bath and allowed to cool to ambient temperature before mixing with the appropriate volume of ND-Fg. Five 96-well polystyrene microplates (one per mixture type) were then coated with 1:2 serial dilutions of 3840 µg/mL down to 0.916 µg/mL of ND-Fg:TD-Fg overnight at 4 °C. The five plates were then run in parallel according to the same protocol described previously (Chapter 4.3.2).

4.3.4 Adsorbed-state circular dichroism of Fg on ppC3F6

The methods for this section were developed at the Biomaterials Engineering and Testing (BET) Core at Clemson University, Clemson, SC under the scientific supervision and directorship of Dr. Robert Latour. Their methods are comprehensively detailed in other reports [18, 27, 38] and will only be briefly summarized here. Experimental development and data acquisition for Fg adsorption on our specific fluoropolymer coating (ppC_3F_6) was performed and analyzed by Dr. Guzeliya Korneva, PhD.

Developing experimental methods for directly characterizing secondary and tertiary structure of surface-adsorbed proteins in hydrated systems remains a challenge with few options to pursue. Well-established techniques exist for empirically assessing protein structure in solution such as circular dichroism spectroscopy (CD), nuclear magnetic resonance (NMR), or cryogenic electron microscopy (cryo-EM), or in a crystalline state using x-ray diffraction (XRD), but those for precisely monitoring secondary structural changes of biomolecules at the liquid-solid interface are far more limited with current technology [39].

In response to this, Latour and coworkers have developed a custom system for applying circular dichroism to characterize the adsorption-induced changes in protein secondary structure on a variety of coatings [38]. Briefly, a Jasco J-810 spectrophotometer (Jasco, Inc., Easton, MD) is used for solution- and adsorption-state measurements and calibrated over the spectral range of 190-320 nm. Scan settings are determined case by case depending on the total absorbance of the test sample to ensure that the high-tension voltage (HTV) applied to the photomultiplier does not exceed 600 V, after which the signal-to-noise ratio is too low. An in-house cuvette assembly setup was developed, which consists of six fused quartz slides (9.4 mm x 1.43 mm x 41.2 mm, Chemglass Life Sciences, Newfield, NJ) stacked together and interleaved with 7 polymeric spacers. The test

protein solution is pipetted into the spaces between each slide and allowed to adsorb, through which the incident beam passes and CD spectra are recorded from 190-300 nm at a scan rate of 10-100 nm/min with response time of 0.25-2 seconds (depending on % transmission of light output of the test system; %T >5 is scanned at the higher rate) and bandwidth of 0.5 nm. The stack of surface-modified slides with both sides exposed to the test protein solution permits protein signal buildup to compensate for losses in light transmission as the beam passes through each substrate, thereby maximizing the signal-to-noise ratio and reducing the path length of the buffer that the beam travels through. The final CD spectrum is an accumulation of n=6 scans, and a scaling system is applied to accommodate the path length and molar concentration of the test protein to yield molar elliptical units ([θ], deg·cm^2/dmol). To quantify the percentages of each secondary structure, the final CD spectrum is treated as the sum of fractional multiples of the CD spectrum of each pure structural component (α-helix, β-sheet, etc.) and deconvoluted using existing mathematical software like CONTIN-LL and DichroWeb to fit the test spectrum with the spectra of reference datasets.

Latour and coworkers provided us with the custom cut quartz slides (n=12), to which we deposited our ppC_3F_6 fluoropolymer on both sides and returned for testing. Initially, our ppC_3F_6-treated slides yielded excessively high absorbance values, with HTV >600 V. However, through a series of troubleshooting steps, several processing adjustments for the plasma polymerization were made: the CH_4 adhesion layer was omitted, the Ar etching time to activate the surface was doubled from 5 to 10 minutes to compensate for the removal of the CH_4 adhesion layer, and the overall ppC_3F_6 deposition time was decreased from 20 minutes down to 5 minutes. The full details and characterization of these adjustments, along with evidence that the final surface composition was still that of ppC_3F_6 and passed delamination testing, are provided in **Appendix 8.3**.

An outline of the methods employed following this initial troubleshooting step are described below:

1. Standard solution-state CD was first performed for Fg (human fibrinogen, Pg/vWF/Fn depleted, FIB3, lot #5710P, Enzyme Research Laboratories, South Bend, IN) in 5 mM potassium phosphate buffer (PPB) at 0.1 mg/mL to check its solution-state native structure before proceeding to the adsorption experiments.
2. CD measurements were taken for the unmodified (i.e., plain quartz) slides in 5 mM PPB in a 1.0 cm cuvette before and after Fg adsorption as a control system to verify that the CD instrument was performing properly. Fg adsorption was performed with the slides first immersed in 10 mM PPB, after which Fg was added to the buffer solution to obtain a final concentration of 3.0 mg/mL Fg (physiological concentration). After three hours adsorption time, the adsorption wells were infinitely diluted by multiple dilutions with 10 mM PPB buffer, and then with 5 mM buffer to remove the Fg from solution. Slides were left in 5 mM buffer for their turn to be measured on the CD spectropolarimeter. Slides were measured in 5 mM PPB in the same sets as before the adsorption procedure, in the same order as they were scanned before the adsorption.
3. For the CD analysis, the CD spectra of the baselines (i.e., unmodified and ppC_3F_6-coated slides before Fg adsorption) were subtracted from the CD spectra of the corresponding slides after Fg adsorption (in the same sets), with the difference in the spectra representing the CD response of the adsorbed layer of protein by itself.
4. The CD spectra of native Fg (FIB3) in 5 mM PPB in a 1.0 mm quartz cuvette over a range of concentrations were measured against the same buffer solution without Fg to determine the extinction coefficient, which is needed for surface density calculations.
5. To determine % secondary structure of native Fg structure in solution as well as secondary structures of adsorbed Fg on ppC_3F_6-coated and unmodified quartz slides, two separate CD software programs were used:

DichroWeb (open-source; http://dichroweb.cryst.bbk.ac.uk/html/home.shtml) and the CD analysis software package that was provided with the CD instrument (CD Pro) [40-43]. Each of these CD analysis software programs uses four separate analysis methods, which are based on separate sets of protein libraries with known CD spectral responses: Contin-LL [44-45] and CDSSTR [46-48], using library sets #4 and #7.

6. Comparisons of secondary structure percentages between solution-state Fg and ppC_3F_6-adsorbed Fg, as well as surface density calculations between Fg adsorbed to unmodified quartz slides vs. PpC_3F_6-coated slides, are analyzed via unpaired, two-tailed Student's t-tests in GraphPad Prism 8.0.

4.4 Results

4.4.1 Fg surface orientation

4.4.1.1 Globular vs. elongated protein structural immunoassays

The effects of surface crowding on orientation of elongated proteins like Fg can be readily observed from these studies: with increasing concentration, both FGA and FGG mAb responses achieve a peak at ~30 μg/mL bulk protein solution concentration (1% plasma concentration), but instead of plateauing to form the typical dose-dependent sigmoidal curve, as concentration is further increased towards native concentrations, the signal response decreases nearly to baseline. In comparison, HSA detection using a murine anti-HSA antibody yielded a typical sigmoidal response curve with surface saturation achieved at ~1 μg/mL solution concentration, characteristic of small globular proteins that do not exhibit preferential adsorption orientations (**Figure 4.1**). Results demonstrate the

importance of surface orientation on bioactivity of adsorbed proteins by facilitating or inhibiting access to binding epitopes. This concept is illustrated in the cartoon in **Figure 4.1**, where elongated proteins initially adsorb in a side-on orientation below a threshold bulk protein concentration until a monolayer is attained (surface saturation). For elongated proteins of similar size and shape to fibrinogen and fibronectin, the threshold bulk protein concentration before molecules shift from a side-on to end-on adsorption orientation is ~30 μg/mL (1% plasma concentration). As the solution concentration of Fg is increased towards the physiological bulk Fg blood concentration range of 1500-4000 μg/mL for healthy adults (green band) [49], a greater diversity in orientations is adopted at the surface with a mixture of side-on and end-on adsorbed molecules. At the highest tested bulk solution concentration representative of physiological plasma concentrations (1920 μg/mL), molecules are adsorbed primarily in the end-on orientation to permit better surface packing, which in turn increases steric hindrance of mAb binding to their targeted epitopes and reduces overall binding signal. Over these same concentration ranges, small globular proteins like HSA demonstrate no change in binding signal from 0.0025% to the 100% plasma concentration range of 35-50 mg/mL (purple band) [64], indicating that maximum surface concentration has been achieved regardless of increasing solution concentration.

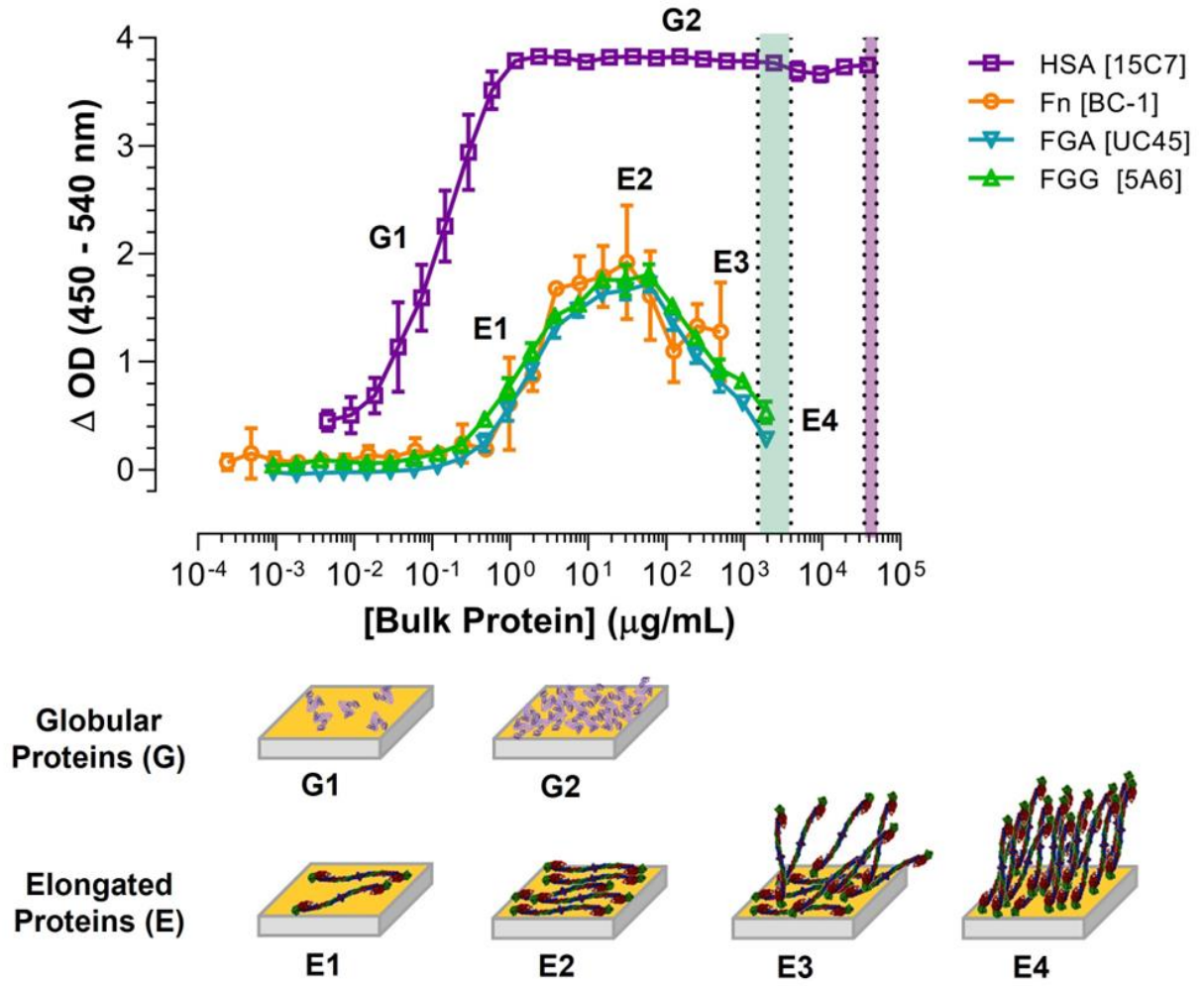

Figure 4.1. Differential changes in mAb binding based on protein shape and concentration-dependent surface orientation and packing. Globular proteins like HSA exhibit signal saturation beyond a threshold solution concentration, indicating maximum surface coverage. Elongated proteins display a peak at intermediate solution concentrations—~30 μg/mL in the case of Fg and Fn—before decreasing in signal again with increasing solution concentration. This behavior is attributed to changes in surface orientation with different bulk protein concentrations from side-on to end-on adsorption, which permits improved surface packing. The green band represents physiological concentration of Fg (1.5-4 mg/mL) and the purple band represents physiological concentration of HSA (35-50 mg/mL).

4.4.1.2 Atomic force microscopy (AFM) imaging of unfolded Fg

AFM imaging of the pristine ppC_3F_6 layer yielded an average surface roughness (S_a) of ~400 pm, which is sufficiently smooth enough to visualize a submonolayer

of Fg adsorbed on top: at a size of approximately 9 x 47.5 x 6 nm [30], a native Fg molecule at its smallest dimension (i.e. the diameter, adsorbed side-on) is ~15 times taller in the z-direction from the background texture. Individual Fg molecules were resolved on the ppC_3F_6 as mostly flat adsorbates void of the distinctive trinodular morphology of native Fg (**Figure 4.2**). This finding is in agreement with studies of Fg adsorbed on other hydrophobic materials like highly-oriented pyrolytic graphite (HOPG) at low concentration, where Fg denaturation occurs in the sub-second timescale after adsorption [51-53]. Other studies have shown that the molecular footprint of Fg on hydrophobic materials increases fivefold after 30 minutes of adsorption compared to only a 0.6 increase for a hydrophilic surface after 112 minutes [54-55]. Altogether, Fg undergoes rapid relaxation on ppC_3F_6 when adsorbed from a solution concentration of 300 ng/mL (0.01% plasma concentration) to form a surface structure significantly different from its native soluble form.

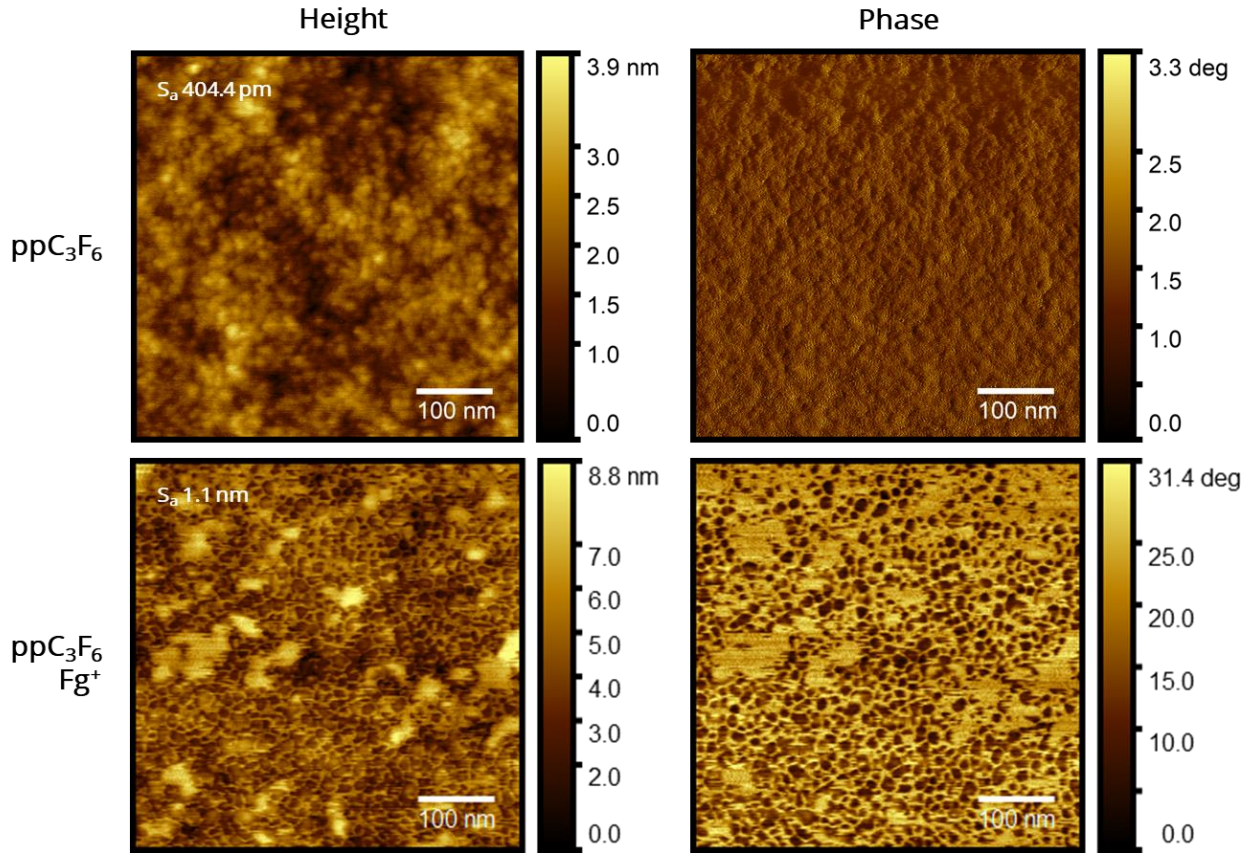

Figure 4.2. Representative AFM images (topography, left; phase, right) show that Fg adsorbed to ppC_3F_6 at 10% plasma concentration (submonolayer coverage) exhibits surface-induced spreading and denaturation. (Top) Pristine ppC_3F_6 with average surface roughness (S_a) ~404.4 pm. (Bottom) ppC_3F_6 adsorbed with 300 ng/mL Fg (0.01% plasma concentration) depicts individual Fg molecules without the distinctive trinodular structure of native Fg. Instead, Fg molecules appear as flat adsorbates with noticeable degrees of spreading over the surface.

4.4.1.3 ESCA determination of Fg adlayer thickness and orientation

Fluorine atomic percentage from angle-dependent ESCA survey scans was used to evaluate adlayer thickness and orientation of Fg adsorbed on ppC_3F_6 at 1%, 10%, and 100% plasma concentrations as a measure of surface crowding effects. Given that the molecular dimensions of Fg are 9 x 47.5 x 6 nm [30], a surface monolayer of Fg adsorbed side-on would have a layer thickness of 6-10 nm and yield a strong fluorine signal at a take-off angle of 0 °C (~10 nm sampling depth) from the underlying ppC_3F_6 similar to pristine ppC_3F_6 (~60% F). Conversely, a surface monolayer of Fg adsorbed end-on would have a layer height of 40-50 nm thick which exceeds the sampling depth limits of the instrument, therefore detecting zero to minimal fluorine content.

Based on the QCM-D concentration isotherm developed in Chapter 3.4.1, all bulk Fg concentrations employed in this study yield surface concentrations above what is required for surface monolayer coverage; the lowest tested Fg solution concentration (0.03 mg/mL) corresponds to a hydrated surface concentration of 2.4 μg/cm² (Voigt mass model; note that mass of coupled water is included in this value, but the Sauerbrey model that eliminates viscoelastic mass accommodation still yields a surface concentration well above monolayer coverage (data not shown)). For 1% plasma concentration of Fg (0.03 mg/mL), there is significantly elevated detection of fluorine at all sampling depths, from 15-33% descending from 1 nm to 10 nm into the surface (**Figure 4.3, top**). Considering the maximum fluorine content of pristine ppC_3F_6 is 59.6±0.1% based on ESCA spectra analysis (Chapter 2.3.1), the Fg layer adsorbed from a 1% plasma concentration yields a

mixture of Fg molecules in side-on and end-on orientations. There is no difference in fluorine content observed between 0.3 and 3 mg/mL Fg adlayers (10% and 100% physiological plasma concentration), suggesting that the final surface orientations are identical and there is no major change in adsorption mechanism in all the intervening bulk Fg concentrations. Both are significantly attenuated compared to 0.03 mg/mL Fg, with ~6% fluorine signature at the deepest sampling depth and 1-2% at the most surface-sensitive depths (<5 nm). This data suggests a Fg adlayer that is densely packed and predominantly adsorbed in the end-on orientation such that fluorine in the underlying film is not detectable. To confirm the increase of Fg on the surface, the nitrogen content was also measured (**Figure 4.3, bottom**). Again, for 0.03 mg/mL we observe markedly lower nitrogen percentages compared to Fg layers adsorbed from 0.3 and 3 mg/mL bulk solutions, but it does show a distinct increase in nitrogen content moving up towards the surface (10 to 5 to 1 nm sampling depth), suggesting a thin layer of side-on adsorbed Fg. The 0.3 and 3 mg/mL nitrogen signatures are not significantly different, confirming the same trend seen from the fluorine signature and likely representing the predominant end-on adsorption orientation. Interestingly for both, the intermediate sampling depth of 5 nm yielded an average nitrogen composition slightly higher than that detected at 1 or 10 nm sampling depth. This is consistent with expectations for an end-on adlayer of Fg molecules that are not perfectly close-packed, where some space between molecules permits gyrational motion in the untethered tail. The peptide bond-rich βC and γC domain heads in the D-region of the free end then collapse in the dehydrated state when ESCA scans are taken to yield a slightly nonuniform protein layer with an intermediate density of peptide chains.

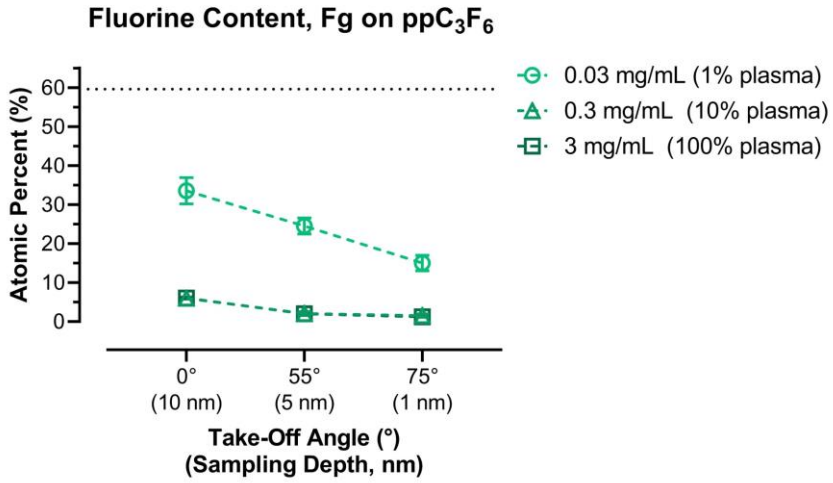

Fluorine Atomic %

[Bulk Fg]	0° (10 nm)	55° (5 nm)	75° (1 nm)
0.03	33.6 ± 2.8	24.5 ± 1.7	15.0 ± 1.6
0.3	6.0 ± 0.5	2.1 ± 0.4	1.5 ± 0.4
3	6.1 ± 0.2	2.0 ± 0.3	1.2 ± 0.1
Pristine ppC_3F_6	59.6 ± 0.1 (>300 nm thick)		

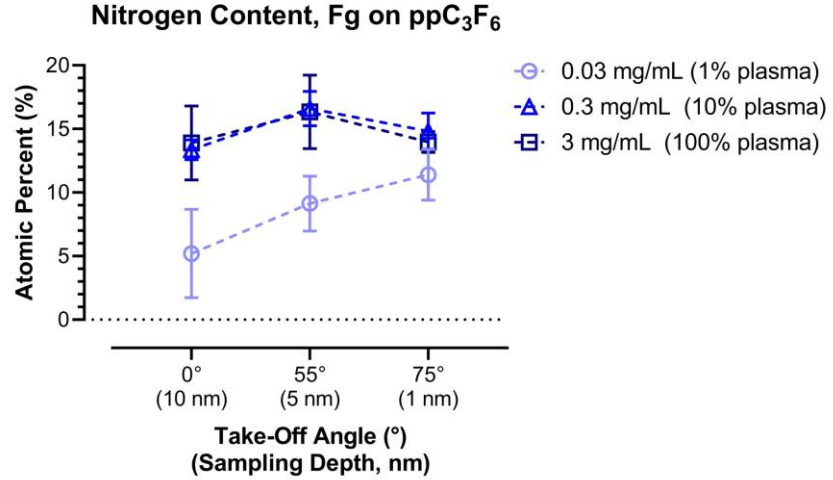

Nitrogen Atomic %

[Bulk Fg]	0° (10 nm)	55° (5 nm)	75° (1 nm)
0.03	5.2 ± 2.8	9.1 ± 1.8	11.4 ± 1.6
0.3	13.4 ± 0.5	16.3 ± 1.1	14.8 ± 1.2
3	13.8 ± 2.1	16.3 ± 2.4	14.0 ± 0.7
Pristine ppC_3F_6	0 ± 0.0		

Figure 4.3. Changes in fluorine and nitrogen content inform on Fg layer thickness and molecular orientation at monolayer coverage on ppC_3F_6. (Top) Fluorine content is strongly present in the 0.03 mg/mL (1% plasma concentration) Fg adlayer, suggesting side-on adsorption to form a thin monolayer <10 nm in thickness detectable by a 0 °C

ESCA take-off angle (10 nm sampling depth). Both the 0.3 and 3 mg/mL (10 and 100% plasma concentration, respectively) showed minimal fluorine content, particularly at <5 nm sampling depths, suggesting predominantly end-on adsorption of the Fg film. The horizontal dotted line at 59.6% represents the average fluorine content of a pristine ppC_3F_6 film. Therefore, all three concentrations do show presence of a protein layer with the attenuation of fluorine signal, but fluorine content is nearly completely abolished at 0.3 and 3 mg/mL Fg bulk solution concentrations. (Bottom) Nitrogen content shows the reverse of the fluorine signatures to demonstrate the presence of protein peptide bonds. Again, the 0.03 mg/mL Fg adlayer displays reduced nitrogen content compared to 0.3 mg/mL and 3 mg/mL, indicating a thin layer of Fg adsorbed in a side-on orientation. Nitrogen signatures for 0.3 and 3 mg/mL samples are near identical at all sampling depth levels and interestingly display a slight reduction in nitrogen content at the most surface-level sampling depth (~1 nm), which is attributed to partial packing of end-on adsorbed Fg molecules that collapse upon drying for ESCA analysis. The horizontal dotted line at 0% represents the absence of nitrogen in the pristine ppC_3F_6 film; therefore, all samples show clear adsorption of Fg to their surfaces.

4.4.2 FGA/FGG monoclonal antibody binding to Fg on fluoropolymers

Three iterations of the conformational immunoassays were carried out for each FP type, and trends were consistent across all (only one iteration depicted, **Figure 4.4**). FGA mAb binding to Fg adsorbed on ppC_3F_6 is significantly reduced across the entire tested concentration range, with half the binding signal (~1.8 OD) observed for the maximum values seen for PVDF and PVDF-HFP (~3.5 OD at 30 µg/mL). Interestingly, beyond the FGA MAb binding maximum at 30 µg/mL, PVDF-HFP thereafter exhibits a typical signal plateau while PVDF steadily decreases with increasing concentration down to 77% of the maximum at the physiological bulk Fg blood concentration range of 1500-4000 µg/mL [49] (between the dotted lines). Based on the QCM-D concentration isotherm developed in Chapter 3.4.1, this bulk Fg concentration corresponds to a hydrated surface concentration of 2.4 µg/cm² (Voigt mass model; note that mass of coupled water is included in this value). PVDF-HFP FGA MAb binding plateaus beyond 15 µg/mL bulk Fg concentration (corresponding to a hydrated surface concentration of 2.0 µg/cm²).

FGG binding on ppC_3F_6 is significantly elevated and remains consistently that way with increasing bulk Fg concentration after 3 μg/mL (0.1% plasma concentration). PVDF and PVDF-HFP show similar responses to each other, with a small increase in FGG mAb binding availability between 7.5-15 μg/mL, but overall low FGG recognition compared to ppC_3F_6, especially at physiological concentration.

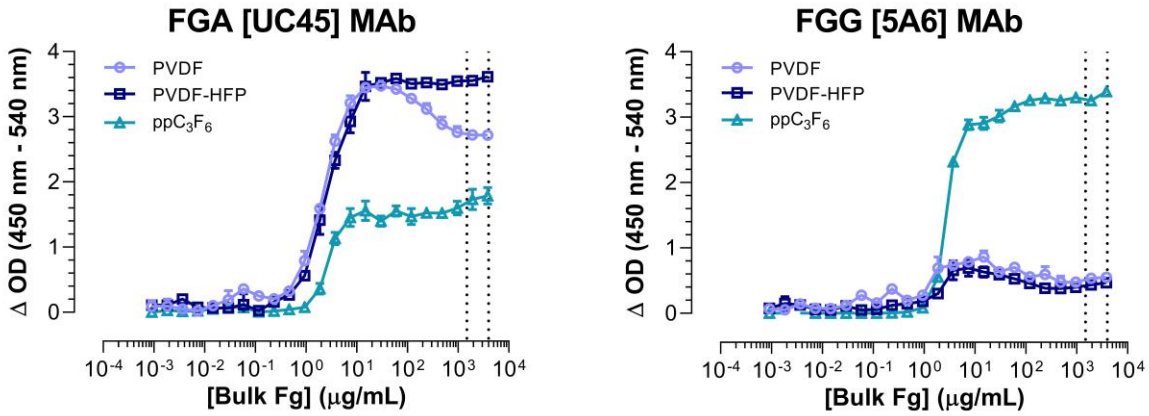

Figure 4.4. FGA and FGG mAb binding to Fg adsorbed to PVDF, PVDF-HFP, and ppC_3F_6. (Left) FGA binding is significantly suppressed for Fg adsorbed to ppC_3F_6 than to PVDF and PVDF-HFP across the entire concentration range. Binding reaches saturation for PVDF-HFP and ppC_3F_6, but decreases beyond 30 μg/mL for PVDF, with a binding signal halfway between that of PVDF-HFP and ppC_3F_6 at physiological Fg blood plasma concentration range (1500-4000 μg/mL; between the dotted lines). (Right) FGG binding is significantly elevated for ppC_3F_6 compared to the other fluoropolymers and plateaus after 3 μg/mL all the way to physiological concentration. Conversely, PVDF and PVDF-HFP show minimal FGG mAb recognition overall, with a modest increase between 7.5-15 μg/mL that decreases again with higher bulk Fg concentration to a small amount a little above baseline.

4.4.3 Fg thermal denaturation and effects on FGA/FGG monoclonal antibody binding

Circular dichroism (CD) spectra were collected for nondenatured (4 °C) and thermally denatured (54 °C) Fg to confirm loss in secondary structure (**Figure 4.5**). The ND-Fg profile displays prominent α-helicity in the 208 and 222 nm

troughs to form the classic 'w' shape, as well as antiparallel β-sheet structures at the 218 nm trough [56-57]. Disordered regions show low ellipticity over 210 nm, constituting the steep return to baseline below this wavelength. The estimated percentages of secondary structures for the native solution state Fg are 35% α-helix, 16% β-sheet, 20% β-turn, and 30% random coils [58]. After thermal denaturation at 54 °C for 1 hour, significant loss in all secondary structures is observed with a loss in ellipticity, and CD features are not recovered when Fg is returned to 4 °C for 2 hours, indicating irreversibility of the protein unfolding.

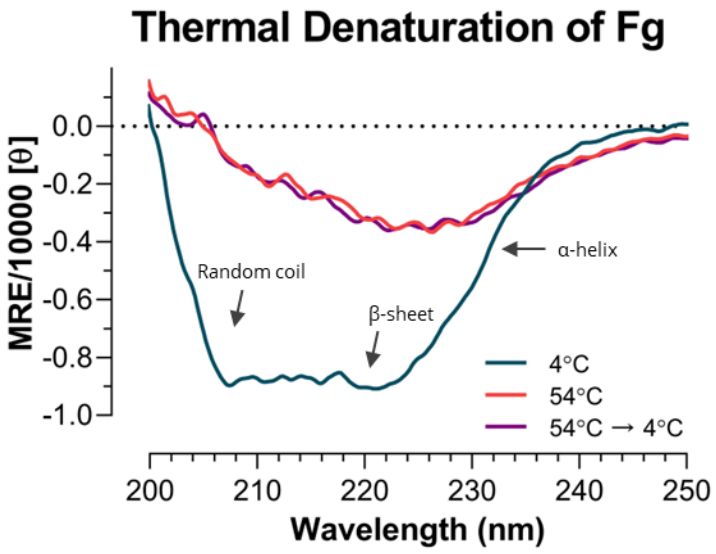

Figure 4.5. Circular dichroism (CD) spectra of nondenatured (ND-Fg) and thermally (TD-Fg) denatured Fg. The ND-Fg (1 μM in 10 mM phosphate buffer, pH 7.0) exhibits clear evidence of secondary structural elements, including α-helices, β-sheets, and disordered regions (blue trace). One hour at 54 °C was sufficient in eliminating most of these structures (red trace), and returning the Fg solution to 4 °C was not capable of recovering them (purple trace), demonstrating the thermal treatment's irreversibility. Spectra are represented as mean residual ellipticity (MRE, θ) and were collected as the average of n=8 scans.

The TD-Fg was then tested with the FGA/FGG mAbs to determine accessibility of these binding epitopes in relation to the ND-Fg (Chapter 4.4.2) (**Figure 4.6**). FGA mAb binding to TD-Fg is elevated across all FPs compared to ND-Fg but most dramatically for ppC_3F_6, which plateaus at 30 μg/mL. PVDF and PVDF-HFP both

appear to reach saturation at ~77% that of the binding signal for ppC_3F_6, but unusually begin to increase again at 240 μg/mL and higher. A possible explanation for this behavior is that adsorption kinetics of Fg on PVDF and PVDF-HFP are slower than that observed on ppC_3F_6 (as determined in the QCM-D adsorption kinetic studies from Chapter 3.4.1), therefore below the threshold Fg bulk concentration of 240 μg/mL, adsorption to the surface is diffusion limited such that the denatured molecules have time to further unfold and spread on the surface before new molecules can adsorb onto neighboring surface sites. This would yield an intermediate maximum surface coverage of thermally denatured and (further surface-denatured) Fg molecules. However, above this threshold, the number of TD-Fg molecules in bulk solution is no longer diffusion limited and adsorb onto the surface in a more packed formation, therefore demonstrating a second increase in FGA mAb binding. At the high end of physiological Fg blood plasma concentration range (i.e. 3840 μg/mL) though, there is no significant difference in FGA mAb binding to TD-Fg on any of the fluoropolymers.

For FGG mAb binding to TD-Fg, PVDF and PVDF-HFP show significantly elevated signal across the entire concentration range compared to that on ND-Fg. Binding of FGG mAb to TD-Fg or ND-Fg on ppC_3F_6 appears similar, though the clear difference in FGA binding between ND-Fg vs. TD-Fg ppC_3F_6 suggests that the epitope recognition mechanism (while high for both) are achieved through different means (orientation vs. conformational, respectively). Altogether, FGG mAb recognition to TD-Fg appears to be equivalent across all fluoropolymers. Given that the FGG mAb binding target is the γC globular domain in the distal D regions of Fg, we observe that the loss of secondary structure in this domain due to thermal denaturation largely eliminates orientational preferences of Fg adsorption to any of the fluoropolymer surfaces, in stark contrast to the ND-Fg assays. The platelet-binding dodecapeptide (γ400-411) is included within the recognition site of the FGG mAb, and as a natively unstructured segment of residues at the carboxyl-terminus of the γ-chain in the γC nodule, loss in

structural integrity of this nodule frees the dodecapeptide for maximal binding recognition. Interestingly, after the sustained signal plateau from ~30 – 960 μg/mL (1% to 32% plasma concentration), there is a slight reduction in FGG mAb binding signal as the bulk Fg concentration enters physiological range. We attribute this behavior to surface crowding effects and slight masking of the FGG mAb binding site with increasing protein-protein interactions.

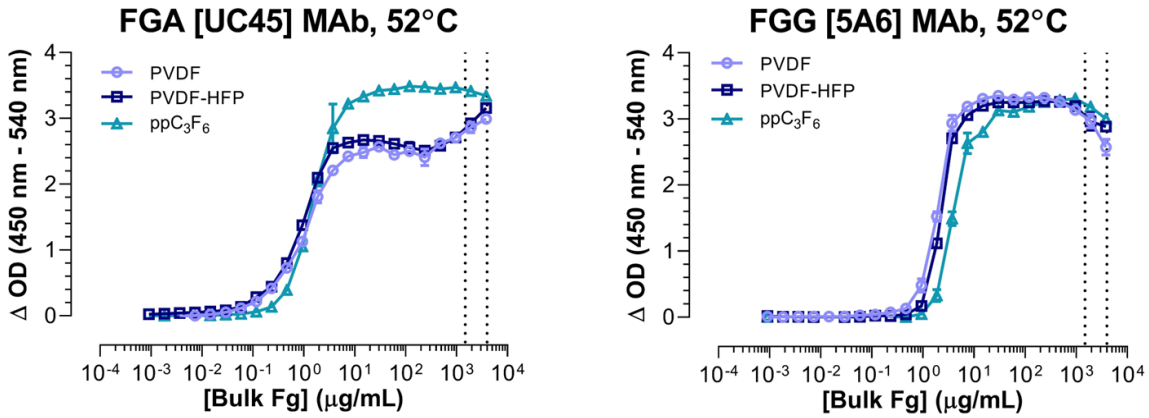

Figure 4.6. FGA and FGG mAb binding to thermally denatured Fg (TD-Fg) adsorbed on PVDF, PVDF-HFP, and ppC_3F_6. Thermal denaturation of Fg increases both FGA and FGG mAb binding across all fluoropolymers compared to the nondenatured form. The physiological bulk solution Fg concentration range is represented between the dotted lines (1500-4000 μg/mL). (Left) TD-Fg on ppC_3F_6 yields a high FGA mAb response that plateaus at high concentration, while that on both PVDF and PVDF-HFP exhibit a biphasic response, where a second signal increase is observed at 240 μg/mL to match ppC_3F_6 at the higher end of physiological concentration range (3840 μg/mL). (Right) FGG mAb binding is similar across all fluoropolymers and significantly elevated from ND-Fg for PVDF/PVDF-HFP, while fairly similar for ppC_3F_6. For the latter, we propose that the difference in signal observed for FGA on ND-Fg vs. TD-Fg suggests that the high signal observed for FGG on ND-Fg vs. TD-Fg are due to different epitope recognition mechanisms (i.e. orientational vs. conformational, respectively). Binding slightly decreases within physiological range, presumed to be a result of surface crowding that obstructs access to the binding epitope.

A more granular investigation of differences in ND-Fg vs. TD-Fg mAb binding recognition revealed adsorbed-state structural biases between the two binding sites (**Figure 4.7**). Increasing the proportion of TD-Fg steadily increases FGA mAb binding until a plateau is reached at 100% TD-Fg content. Between 25-75% TD-Fg content, FGA mAb binding appears to plateau but then exhibits an increase in

binding again at physiological concentration range that approaches that seen for 100% TD-Fg. Conversely, FGG mAb binding is largely unaffected by increasing proportions of TD-Fg, with all binding curves superimposed across compositions and displaying the typical dose-dependent response. There is a slight decrease in FGG mAb binding—particularly for mixtures containing greater ND-Fg:TD-Fg ratios—for bulk Fg concentrations >60 μg/mL, which reaches a small local minimum at the lower threshold of the physiological concentration range (1920 μg/mL) before increasing again at the higher end (3840 μg/mL) to match the 100% TD-Fg signal. Overall, FGA mAb binding is affected by thermal denaturation of the Fg prior to adsorption, but FGG mAb binding is not, suggesting that the binding epitope for this antibody is not conformationally sensitive. Therefore, with this knowledge, the orientation of the Fg molecule in its adsorbed state may play a more important role in concealing the γC platelet binding dodecapeptide than small conformational changes induced by surface chemistry.

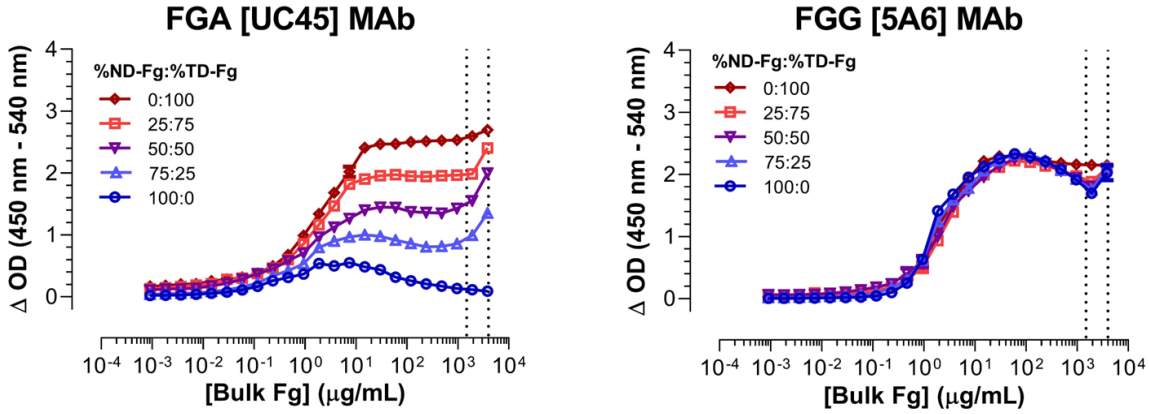

Figure 4.7. FGA and FGG mAb binding in ND-Fg:TD-Fg mixtures reveal structural biases in their respective binding targets. The FGA mAb exhibits increasing binding signal with decreasing ND-Fg:TD-Fg ratios (left), while FGG mAb binding is indifferent to ND- or TD-Fg composition in the adlayer (right). This suggests that the FGA mAb binding epitope is conformationally sensitive and cryptic in its nondenatured form, while the FGG mAb is not. The physiological bulk solution Fg concentration range is represented between the dotted lines (1500-4000 μg/mL).

4.4.4 Adsorbed-state circular dichroism of Fg on ppC3F6

By comparing results after using the two CD spectral analysis methods (DichroWeb and CD Pro), the slide sets showing consistently reliable results were determined based on their resulting differential spectra and their interpretation by the CD analysis software package. Generally, 6 protein-adsorbed slides are used for this method; however, some baseline absorbance from the ppC_3F_6 treated slides was unavoidable, even with the modifications described in Chapter 4.3.4. Therefore, the total slide number was reduced to 4, which yielded no significant difference in measured datasets from 6 slides for the unmodified quartz slides, and was also sufficient in yielding a detectable structural signature for the ppC_3F_6-adsorbed Fg (**Appendix 8.4**).

For the ppC_3F_6 treated slides, two sets of 4 slides were measured. These results were compared against the secondary structure of native Fg in solution to determine if Fg secondary structure was significantly changed upon surface adsorption (**Table 4.1**). These results showed that there was no significant difference ($p>0.05$) in any of the secondary structural elements of Fg, specifically α-helices, antiparallel β-sheets, β-turns, or unordered residues (**Figure 4.8**). Therefore, the adsorption of the Fg with ppC_3F_6-modified surfaces does not significantly alter the secondary structural composition of the Fg compared to its solution-state structure when the Fg is adsorbed from a solution concentration of 3 mg/mL for 3 hours.

Table 4.1. Comparison of secondary structure between Fg in solution vs. Fg adsorbed on ppC_3F_6-treated quartz slides. There is no significant difference ($p>0.05$) in any secondary structure elements between solution-state Fg (native) vs. ppC_3F_6-adsorbed Fg. For each set of slides, each of the utilized algorithms (DichroWeb and CD Pro) provide four independent estimates for each % content, which were averaged to provide the estimated % structural content.

	Fg in Solution				Fg on ppC_3F_6-Coated Slides				t ratio (dof = 2)	Signif-icance (p value)
Secondary Structure Elements	**CD Pro**	**Dichro Web**	**Mean**	**St Dev**	**Set 1**	**Set 2**	**Mean**	**St Dev**		
% Helix	44.7	45.4	45.0	0.51	49.0	53.7	51.4	3.38	2.652	0.118
% Sheet	14.7	10.9	12.8	2.69	14.8	10.8	12.8	2.86	0.000	>0.999
% Turns	17.0	16.9	17.0	0.07	18.1	15.2	16.7	2.02	0.207	0.855
% Unordered	23.6	26.1	24.8	1.77	18.1	20.2	19.2	1.49	3.492	0.073
Total %	99.9	99.3	99.6		100.0	100.0	100.0		**t.crit =4.303**	

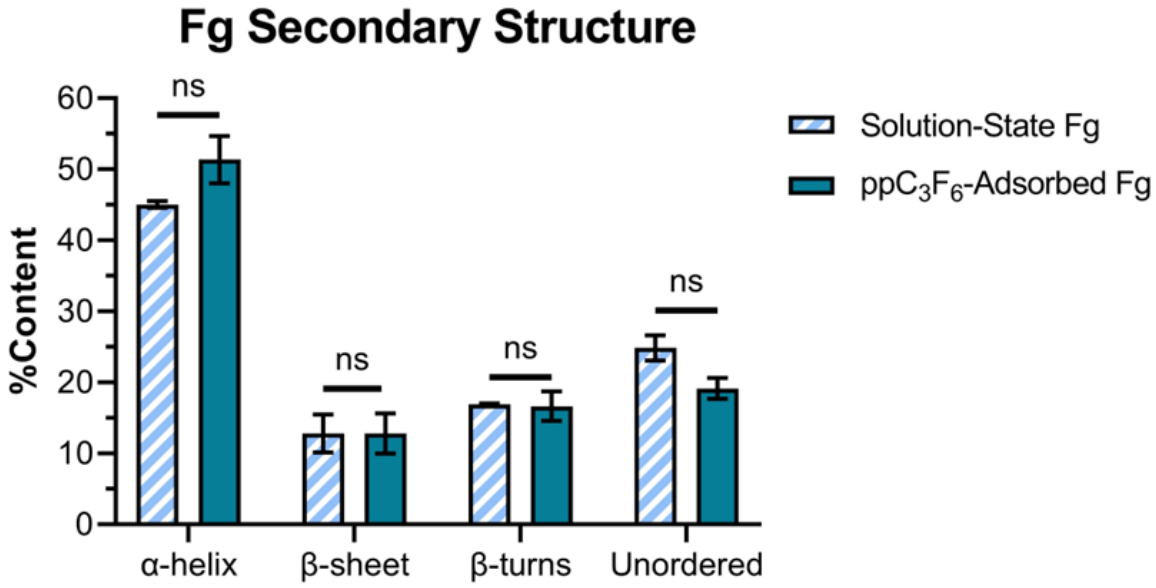

Figure 4.8. Secondary structure content between Fg in solution vs. Fg adsorbed on ppC_3F_6-treated quartz slides. There is no significant difference ($p>0.05$) in any secondary structure elements between solution-state Fg (native) vs. ppC_3F_6-adsorbed Fg, indicating that Fg adsorbed to ppC_3F_6 at physiological concentration is mostly preserved in its native structural state. (ns, not significant; assessed by unpaired, two-tailed Student's t-test)

Although the CD spectra of some sets of surface-treated slides had to be discarded for the final analyses of adsorbed-state secondary structures, the surface density of adsorbed Fg in some of these sets was still possible to estimate. Results for surface density are listed in **Table 4.2**. By Student's t-test analysis, the amount of Fg adsorbed on the surface-treated slides was significantly greater than on the plain quartz slides ($p<0.0005$), with approximately twice the surface density (**Figure 4.9**). This is within expectations, as hydrophobic materials are known for their high protein adsorption.

Table 4.2. Comparison of Fg surface density between unmodified quartz slides and ppC_3F_6-coated quartz slides. All slides were numbered and different combinations were used to calculate surface density from CD scans using the extinction coefficient of the native solution-state Fg. PpC_3F_6-coated slides adsorb significantly more Fg (~2x) than unmodified quartz slides ($p < 0.0005$).

Quartz Slides			**PpC_3F_6-Coated Slides**		
Quantity of Slides	**Slide Numbers**	**Surface Density (µg/cm²)**	**Quantity of Slides**	**Slide Numbers**	**Surface Density (µg/cm²)**
2	1, 2	0.234	2	5, 6	0.485
	3, 4	0.205	3	4, 5, 6	0.509
	5, 6	0.168	4	1, 2, 9, 21	0.243
3	1, 2, 3	0.241		3, 4, 5, 6	0.495
	4, 5, 6	0.167	5	2, 3, 4, 5, 6	0.484
4	1, 2, 3, 4	0.262			
5	1, 2, 3, 4, 5	0.257			
6	1, 2, 3, 4, 5, 6	0.292			
Mean		0.228 ± 0.045	Mean		0.443 ± 0.112

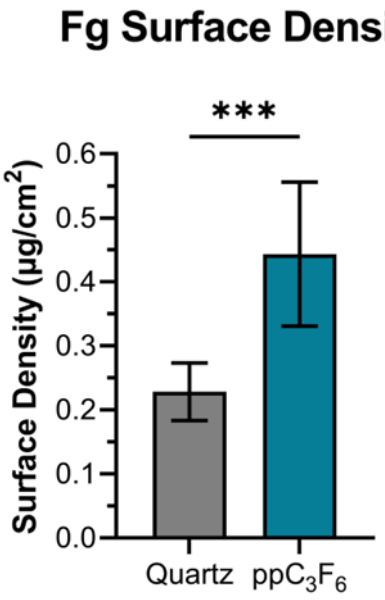

Figure 4.9. Fg surface density between unmodified quartz slides and ppC_3F_6-coated quartz slides. Surface density of Fg adsorbed from physiological concentration of 3 mg/mL on ppC_3F_6 is significantly higher than that on quartz (***$p<0.0005$; assessed by unpaired, two-tailed Student's t-test).

4.5 Discussion

Total elimination of protein adsorption on blood-contacting artificial surfaces is a perpetual challenge that may never fully replicate the non-fouling antithrombogenic and regulatory properties of the endothelium lining native vasculature. However, various studies have shown how surface chemistry of engineered biomaterials can significantly alter the bioactivity of adsorbed elongated proteins like Fg by passively controlling their preferential surface conformation and/or orientation that ultimately influence the availability of platelet-binding epitopes [3-4, 21, 32]. This metric is termed the 'molecular potency' of the adlayer, which represents the fraction of adsorbed molecules that exhibit cell adhesion abilities [21]. Therefore, to fully understand the blood compatibility performance of a biomaterial, multiple analytical techniques to probe Fg surface conformation following adsorption are needed to properly

characterize surface-induced changes in Fg conformation and orientation.

Monoclonal antibody binding to the α-chain (FGA) and γ-chain (FGG) of Fg adsorbed on PVDF, PVDF-HFP, and ppC_3F_6 reveal differences in orientation and availability of the γC platelet-binding dodecapeptide. FGA binding was used primarily as a coarse estimation of Fg surface orientation: unlike the β- and γ-chains, the α-chain does not terminate in a globular domain at its carboxyl terminus at the distal ends of the Fg molecule, and therefore mAb binding availability of this region—which targets the center of Fg—is severely limited if the molecule is not adsorbed in a flat side-on orientation. Therefore, we attribute low FGA binding at concentrations higher than surface monolayer coverage (>1% plasma concentration: ~30 μg/mL) to an end-on adsorption orientation where binding access to the α-chain is sterically obstructed. We observe that at physiological concentration of bulk Fg (between 1500-4000 μg/mL), ppC_3F_6 exhibits significantly lower FGA binding than PVDF and PVDF-HFP, signifying its preference for end-on adsorption that enables improved surface packing. A possible alternative interpretation of the suppressed FGA recognition of Fg adsorbed on ppC_3F_6 is the denaturation of the α-helices comprising this chain such that antibody recognition of the epitope is inhibited; however, this interpretation is disproved by the CD studies showing near-full preservation of Fg's native secondary structures when adsorbed to ppC_3F_6 at physiological concentration (3 mg/mL). Additionally, our thermally denatured Fg (TD-Fg) ELISA studies demonstrated that loss in secondary structure of Fg due to heat application, as verified through circular dichroism, increases FGA mAb binding. This indicates that the RGD binding sites in the α-chain are conformationally sensitive and remain cryptic in the native structure, a finding that is also reported in the literature [59]. Furthermore, the distal D domains of Fg are mostly comprised of hydrophobic residues that are entropically driven in aqueous environments to associate with hydrophobic surfaces. At non-diffusion limited, high bulk protein fluid concentrations, the near-surface Fg protein ensemble is more likely to adsorb

at one hydrophobic end than side-on with both ends engaged with the surface, as adjacent surface sites are rapidly occupied by other molecules that inhibit side-on adsorption and surface unfolding. This conclusion is consistent with the surface orientation studies performed via ESCA analysis that evaluated detectable fluorine content from the ppC_3F_6 following adsorption of Fg at 0.03, 0.3, and 3 mg/mL Fg (1%, 10%, and 100% plasma concentrations, respectively). At 3 mg/mL Fg bulk solution concentration, the adsorbed Fg layer on ppC_3F_6 completely masked any fluorine content from the fluoropolymer layer underneath down to 10 nm in depth. Given that the diameter of Fg is 6-9 nm and length is ~45-47 nm, a side-on adsorbed Fg molecular layer would most certainly yield a strong fluorine signal close to that of pristine ppC_3F_6 (~60%). Therefore, it can be deduced that the Fg adlayer is predominantly adsorbed in a packed end-on orientation with a layer thickness of ~50 nm. Surface density calculations from the adsorbed-state CD measurements indicate ppC_3F_6 adsorbs significantly more Fg on its surface compared to the uncoated quartz substrate, with nearly twice the surface density at 0.443 μg/cm². Theoretical calculations of Fg monolayer surface density assuming molecular dimensions of 45 x 9 nm and a molecular weight of 340 kDa yield a maximum of 0.14 μg/cm² for side-on adsorption and 0.89 μg/cm² for end-on adsorption. Our estimated surface density falls between this range, though it should be noted that the theoretical maximum for end-on adsorption assumes rigid protein bodies, no protein-protein interactions, and perfect close-packing. As this is an ideal state, the true maximum surface density for side-on adsorption under normal adsorption conditions is most likely considerably lower than 0.89 μg/cm², and likewise, that for side-on adsorption is most likely below 0.14 μg/cm². Therefore, our ppC_3F_6 Fg surface density of 0.443 μg/cm² is appreciably high.

Accessibility of the platelet-binding dodecapeptide at γC400-411 is another important consideration in mediating platelet adhesion and is indirectly influenced by surface concentration of the bulk protein solution through preferential orientation effects under non-diffusion limited conditions.

Immunoassays employing the FGG mAb—which targets a region on the γC domain that includes the terminal platelet-binding dodecapeptide—reveal that at full monolayer protein coverage (>3 μg/mL bulk Fg concentration), ppC_3F_6 exhibits significantly more FGG mAb binding signal than PVDF and PVDF-HFP. Given the rapid protein adsorption kinetics of Fg on ppC_3F_6 compared to the other fluoropolymers (as determined in the QCM-D adsorption kinetic studies from Chapter 3.4.1), this observation suggests high Fg adsorption to the surface in a conformation that abundantly exposes the γC domain (end-on orientation), and with a surface density that inhibits protein surface unfolding and spreading, consistent with reported studies [55]. The spreading effects of low surface density (via low bulk Fg concentrations) are demonstrated through AFM imaging, where we observed that at submonolayer coverage, individual Fg molecules adsorbed on ppC_3F_6 lose their distinct trinodular structure and become flat adsorbates (300 ng/mL, or 0.01% plasma concentration). Combining this with the findings from the FGA mAb immunoassay, we purport that the differences in FGA and FGG binding to Fg adsorbed to ppC_3F_6 vs. PVDF or PVDF-HFP are predominantly caused by differences in the final surface orientation of Fg, which is a direct result of Fg's surface affinity for each of the fluoropolymers based on their surface chemistries. This surface affinity dictates the rapidity of adsorption kinetics and initial orientation of Fg binding, which in turn determines its molecular ability to form packed end-on adlayers and mediate platelet adhesion [1]. While hydrophobic materials are generally accepted to adsorb more protein than hydrophilic or zwitterionic materials, ppC_3F_6 demonstrates this to an exceptional extent compared to other commercial fluoropolymers, with its highly crosslinked layer rich in hydrophobic CF_3 groups that favors adsorption of Fg's hydrophobic D region at the distal ends of the molecule. As a result, Fg adsorbs *en masse* to ppC_3F_6 in the end-on conformation, where one hydrophobic D region is associated with the hydrophobic surface, leaving the other available for platelet recognition. However, the high quantity of adsorbed molecules, which are confirmed via CD to

maintain their native solution-state structure, creates a packed brush-like adlayer with a high density of binding epitopes that appear 'immobilized' to platelets, thus forming a surface rich in platelet adhesion points. While at first this appears counter to our aim of reducing thrombogenicity, certain studies have proposed that hydrophobic surfaces promoting rapid platelet adhesion to a surface to form a stable passivating platelet membrane layer conceals the underlying protein and substrate layers so that they are no longer activating upon continued exposure to circulating blood [22-26]. Therefore, an initial phase of acute activation upon blood exposure to form this passivating membrane layer may ultimately prove more hemocompatible for long-term indications.

Based on past data from our group and collaborators using plasma-polymerized glow-discharge fluoropolymer films in *ex vivo* baboon and canine shunt studies, we have continuously observed high patency and low embolization rates for these materials at extended durations when in contact with fresh circulating blood [26, 60-63]. Altogether, we have strong reason to believe ppC_3F_6 surface chemistry encourages high quantities of Fg adsorption in the end-on orientation that enables surface packing and reduced ability of Fg to spread or unfold on the surface by limiting protein-surface contact points, thus preserving the protein's native structure. Ultimately, this yields a dense carpet of platelet-binding contacts to enable rapid adhesion and spreading for the formation of a stable uniform platelet membrane monolayer that passivates the surface.

4.6 Summary

In this chapter, we employed a variety of methods to assess changes in Fg conformation and orientation following adsorption to the fluoropolymers PVDF, PVDF-HFP, and ppC_3F_6. We first demonstrated the importance of bulk protein solution concentration in determining the adsorption orientation of elongated proteins, where below a threshold concentration, molecules adsorb in a side-on

orientation and are susceptible to further surface-induced spreading and unfolding; however, above this threshold when molecular diffusion to the surface is no longer limited, fewer molecules are able to adsorb in the side-on orientation due to competitive occupation of surface sites by adjacent molecules. Thus, we observe a loss in monoclonal antibody binding with further increasing bulk protein solution concentration all the way to physiological levels. Conversely, bulk protein solution concentration does not appear to affect the antibody binding recognition of small globular proteins like HSA, confirming the importance of surface orientation and packing for high aspect ratio proteins in providing access to binding epitopes. Then, through a combination of immunoassays targeting the α-chain (FGA) and γ-chain (FGG) of Fg, we determined that ppC_3F_6 encourages rapid Fg adsorption in a configuration that limits FGA binding—in agreement with the end-on adsorbed interpretation where the FGA binding epitope is packed into the center of the adlayer 'forest'—and increases FGG binding at intermediate bulk solution concentrations before decreasing again due to the binding-inhibitory effects of surface crowding. Thermally denaturing Fg prior to adsorption on the fluoropolymers increased FGA/FGG mAb for all materials, indicating that loss in structural integrity of Fg eliminates orientational preference of the protein and increases mAb binding accessibility, and by extension, platelet binding accessibility. The high-packing ability of end-on adsorbed Fg was also demonstrated through adsorbed-state circular dichroism (CD) to assist in preserving the protein's native structure by preventing surface spreading and unfolding. While it is true that the native Fg protein is non-platelet activating, we believe that the dense surface packing of Fg on ppC_3F_6 creates a carpet of end-on adsorbed Fg molecules that encourage rapid uniform platelet adhesion and spreading to form a passivating surface layer of platelet membranes after the initial phase of activation is past. This theory will be further explored in Chapter 6.

4.7 Acknowledgments

The authors thank the following individuals for their contributions to the work in this chapter: Dr. Heather Niles for assistance on the Cypher VRS atomic force microscope (AFM), Dr. Samantha Young for ESCA data acquisition on the Kratos AXIS Ultra DLD XPS instrument, and Dr. Martin Sadilek for assistance on the Jasco J-720 spectropolarimeter for solution-state circular dichroism measurements. The authors also gratefully acknowledge the invaluable generosity of Drs. Robert Latour and Guzeliya Korneva at Clemson University for providing their custom adsorbed-state circular dichroism method in the determination of Fg secondary structure on ppC_3F_6 and assisting in materials provision, data acquisition, data analysis, and scientific discussion.

4.8 References

1. Tsai, W.B., Grunkemeier, J.M., Horbett, T.A. Human plasma fibrinogen adsorption and platelet adhesion to polystyrene. *J. Biomed. Mater. Res.* **44**, 130-139 (1999).
2. Tsai, W.B., Grunkemeier, J.M., McFarland, C.D., Horbett, T.A. Platelet adhesion to PS-based surfaces preadsorbed with plasmas selectively depleted in fibrinogen, fibronectin, vitronectin, or von Willebrand's factor. *J Biomed Mater Res.* **60**(3), 348-359 (2002).
3. Clarke, M.L., Wang, J., Chen, Z. Conformational Changes of Fibrinogen After Adsorption. *J. Phys. Chem. B.* **109**(46), 22027-22035 (2005).
4. Hylton, D.M., Shalaby, W.S., Latour, R.A. Direct correlation between adsorption-induced changes in protein structure and platelet adhesion. *J. Biomed. Mater. Res.* **73A**, 349-358 (2005).
5. Sivaraman, B., Latour, R.A. The adherence of platelets to adsorbed albumin by receptor-mediated recognition of binding sites exposed by adsorption-induced unfolding. *Biomaterials*. **31**, 1036-1044 (2010).
6. Ugarova, T.P., Budzynski, A.Z., Shattil, S.J., Ruggeri, Z.M., Ginsberg, M.H., & Plow, E.F. Conformational changes in fibrinogen elicited by its interaction with platelet membrane glycoprotein GPIIb-IIIa. *J. Biol. Chem.* **268**(28), 21080-21087 (1993).

7. Tsai, W.B., Grunkemeier, J.M., Horbett, T.A. Variations in the ability of adsorbed fibrinogen to mediate platelet adhesion to polystyrene-based materials: a multivariate statistical analysis of antibody binding to the platelet binding sites of fibrinogen. *J Biomed Mater Res. A.* **67**(4), 1255-1268 (2003).

8. Kollmann, J., Pandi, L., Sawaya, M., Riley, M., Doolittle, R. Crystal structure of human fibrinogen. *Biochemistry*. **48**, 3877-3886 (2009).

9. Mosesson, M.W. Fibrinogen and fibrin structure and functions. *Thromb. Haemost.* **3**, 1894-1904 (2005).

10. D'Souza, S.E., Ginsberg, M.H., Burke, T.A., & Plow, E.F. The ligand binding site of the platelet integrin receptor GPIIb-IIIa is proximal to the second calcium binding domain of its alpha subunit. *J. Biol. Chem.* **265**(6), 3440-3446 (1990).

11. D'Souza, S.E., Ginsberg, M.H., Matsueda, G.R., Plow, E.F. A Discrete Sequence in a Platelet Integrin is Involved in Ligand Recognition. *Nature*. **350**, 66-68 (1991).

12. Shattil, S.J., Hoxie, J.A., Cunningham, M., Brass, L.F. Changes in the Platelet Membrane Glycoprotein IIb.IIIa Complex During Platelet Activation. *J. Biol. Chem.* **260**, 11107 (1985).

13. Zhang, L. e*t al.* The influence of surface chemistry on adsorbed fibrinogen conformation, orientation, fiber formation, and platelet adhesion. *Acta Biomater*. **54**, 164-174 (2017).

14. Farrell, D.H., & Thiagarajan, P. Binding of recombinant fibrinogen mutants to platelets. *J. Biol. Chem.* **269**, 226-231 (1994).

15. Savage, B., Ruggeri, Z.M. Selective Recognition of Adhesive Sites in Surface-Bound Fibrinogen by Glycoprotein IIb-IIIa on Nonactivated Platelets. *J. Biol. Chem.* **266**(17), 11227-33 (1991).

16. Weisel, J.W., Nagaswami, C., Vilaire, G., & Bennett, J.S. Examination of the platelet membrane glycoprotein IIb-IIIa complex and its interaction with fibrinogen and other ligands by electron microscopy. *J. Biol. Chem.* **267**, 16637-16643 (1992).

17. Spraggon, G., Everse, S.J., Doolittle, R.F. Crystal Structures of Fragment D from Human Fibrinogen and its Crosslinked Counterpart from Fibrin. *Nature*. **389**, 455-462 (1997).

18. Sivaraman, B. & Latour, R.A. The relationship between platelet adhesion on surfaces and the structure versus the amount of adsorbed fibrinogen. *Biomaterials*, **31**, 832-839 (2010).

19. Hawiger, J., Timmons, S., Kloczewiak, M., Strong, D.D., Doolittle, R.F.

Gamma and Alpha Chains of Human Fibrinogen Possess Sites Reactive with Human Platelet Receptors. *Proc. Natl. Acad. Sci.* **79**(6), 2068-2071 (1982).

20. Kloczewiak, M., Timmons, S., Lukas, T.J. & Hawiger, J. Platelet receptor recognition site on human fibrinogen. Synthesis and structure-function relationship of peptides corresponding to the carboxy-terminal segment of the γ-chain. *Biochemistry*, **23**(8), 1767-1774 (1984).
21. Wu, Y., Simonovsky, F.I., Ratner, B.D. & Horbett, T.A**.** The role of adsorbed fibrinogen in platelet adhesion to polyurethane surfaces: a comparison of surface hydrophobicity, protein adsorption, monoclonal antibody binding, and platelet adhesion. *J. Biomed. Mater. Res. A* **74**(4), 722-738 (2005).
22. Szott, L.M., Irvin, C.A., Trollsas, M., Hossainy, S. & Ratner, B.D. Blood compatibility assessment of polymers used in drug eluting stent coatings. *Biointerphases*, **11**, 029806 (2016).
23. Haycox, C. & Ratner, B.D. *In vitro* platelet interactions in whole human blood exposed to biomaterial surfaces: insights on blood compatibility. *J Biomed Mater Res.* **27**, 1181-1193 (1993).
24. Dion, I., Baquey, C., Candelon, B. & Monties, J.R. Hemocompatibility of titanium nitride. *Int J Artif Organs.* **15**, 617 (1992).
25. Riederer, M.A., Ginsberg, M.H. & Steiner, B. Blockade of platelet GPIIB-IIIA (integrin alphaII(b)beta(3)) in flowing human blood leads to passivation of prothrombotic surfaces. *Thromb Haemost.* **88**(5), 858-64 (2002).
26. Garfinkle, A.M., Hoffman, A.S., Ratner, B.D., Reynolds, L.O. & Hanson, S.R. Effects of a tetrafluoroethylene glow discharge on patency of small diameter dacron vascular grafts. *Trans Am Soc Artif Intern Organs*. **30,** 432-439 (1984).
27. Sivaraman, B., Fears, K.P. & Latour, R.A. Investigation of the effects of surface chemistry and solution concentration on the conformation of adsorbed proteins using an improved circular dichroism method. *Langmuir*, **25**, 3050-3056 (2009).
28. Früh, S.M., Schoen, I., Ries, J. & Vogel, V. Molecular architecture of native fibronectin fibrils. *Nat Comm.* **6**, 7275 (2015).
29. Erickson, H.P., Carrell, N. & McDonagh, J. Fibronectin molecule visualized in electron microscopy: a long, thin, flexible strand. *J Cell Biol.* **91**(3), 673-678 (1981).
30. Henschen, A., Lottspeich, F., Kehl, M. & Southan, C. Covalent structure of fibrinogen. *Ann NY Acad Sci*, **408**(1), 28-43 (1983).
31. Park, K., Mao, F.W. & Park, H. Morphological characterization of surface-induced platelet activation. *Biomaterials*, **11**, 24-31 (1990).

32. Chiumiento, A., Lamponi, S., & Barbucci, R. Role of fibrinogen conformation in platelet activation. *Biomacromolecules*, **8**(2), 523–531 (2007).

33. Crossen, J. & Diamond, S.L. Thermal shift assay to probe melting of thrombin, fibrinogen, fibrin monomer, and fibrin: Gly-Pro-Arg-Pro induces a fibrin monomer-like state in fibrinogen. *Biochim Biophys Acta*, **1865**(2), 129805 (2021).

34. Marx, G. e*t al.* Heat denaturation of fibrinogen to develop a biomedical matrix. *J Biomed Mater Res B*, **84**(1), 49-57 (2008).

35. Mihalyi, E. Clotting of fibrinogen. 1. Scanning calorimetric study of the effect of calcium. *Biochemistry,* **24**, 3434– 3443 (1985).

36. Mihalyi, E. & Donovan, J.W. Clotting of fibrinogen. 2. Calorimetry of the reversal of the effects of calcium on clotting with thrombin and with ancrod. *Biochemistry,* **24**, 3443–3448 (1985).

37. Medved, L.V., Litvinovich, S.V. & Privalov, P.L. Domain organization of the terminal parts in the fibrinogen molecule. *FEBS Lett,* **202**, 298–302 (1986).

38. Thyparambil, A.A., Wei, Y. & Latour, R.A. Experimental characterization of adsorbed protein orientation, conformation, and bioactivity. *Biointerphases* **10**(1), 019002 (2015).

39. Venyaminov, S.Y., Yang, J.T. Determination of protein secondary structure. In: Fasman, G.D. (eds) *Circular Dichroism and the Conformational Analysis of Biomolecules*. Springer, Boston, MA (1996).

40. Miles, A.J, Ramalli, S.G, & Wallace, B.A. DichroWeb, a website for calculating protein secondary structure from circular dichroism spectroscopic data. *Protein Science*: https://doi.org/10.1002/pro.4153 Pubmed (2021) .

41. Whitmore, L. & Wallace, B.A. Protein secondary structure analyses from circular dichroism spectroscopy: Methods and Reference Databases. *Biopolymers* **89,** 392-400 (2008).

42. Whitmore, L. & Wallace, B.A. DICHROWEB: an online server for protein secondary structure analyses from circular dichroism spectroscopic data. *Nucleic Acids Res* **32,** W668 - 73 (2004).

43. Lobley, A., Whitmore, L. & Wallace, B.A. DICHROWEB: an interactive website for the analysis of protein secondary structure from circular dichroism spectra. *Bioinformatics* **18,** 211-212 (2002).

44. Provencher, S.W. & Glockner, J. Estimation of globular protein secondary structure from circular dichroism. *Biochemistry* **20,** 33-37 (1981).

45. Van Stokkum, I.H.M., Spoelder, H.J.W., Bloemendal, M., Van Grondelle, R., & Groen, F.C.A. Estimation of protein secondary structure and error analysis

from CD spectra. *Anal. Biochem.* **191,** 110-118 (1990).

46. Compton, L.A. & Johnson, W.C., Jr. Analysis of protein circular dichroism spectra for secondary structure using a simple matrix multiplication. *Anal. Biochem.* **155,** 155-167 (1986).
47. Manavalan, P. & Johnson, W.C., Jr. Variable selection method improves the prediction of protein secondary structure from circular dichroism spectra. *Anal. Biochem.* **167,** 76-85 (1987).
48. Sreerama, N. & Woody, R.W. Estimation of protein secondary structure from CD spectra: Comparison of CONTIN, SELCON and CDSSTR methods with an expanded reference set. *Anal. Biochem.* **287**(2), 252-260 (2000).
49. Weisel, J.W. & Litvinov, R.I. Fibrin formation, structure and properties. *Subcell Biochem.* **82**, 405-456 (2017).
50. Moman, R.N., Gupta, N. & Varacallo, M. Physiology, Albumin. [Updated 2022 Jan 4]. In: StatPearls [Internet]. Treasure Island (FL): StatPearls Publishing (2022).
51. Barinov, N.A., Prokhorov, V.V., Dubrovin, E.V. & Klinov, D.V. AFM visualization at a single-molecule level of denaturated states of proteins on graphite. *Colloids Surf.* **146**, 777-784 (2016).
52. Dubrovin, E.V., Barinov, N.A., Schäffer, T.E. & Klinov, D.V. In situ single-molecule AFM investigation of surface-induced fibrinogen unfolding on graphite. *Langmuir.* **35**, 9732-9739 (2019).
53. Agnihotri, A. & Siedlecki, C.A. Time-dependent conformational changes in fibrinogen measured by atomic force microscopy. *Langmuir.* **20**, 8846-8852 (2004).
54. Wertz, C.F. & Santore, M.M. Effect of surface hydrophobicity on adsorption and relaxation kinetics of albumin and fibrinogen: single-species and competitive behavior. *Langmuir.* **17**, 3006-3016 (2001).
55. Santore, M.M. & Wertz, C.F. Protein spreading kinetics at liquid-solid interfaces via an adsorption probe method. *Langmuir.* **21**, 10172-10178 (2005).
56. Greenfield, N.J. Using circular dichroism spectra to estimate protein secondary structure. *Nat Prot.* **1**(6), 2876-2890 (2006).
57. Ranjbar, B. & Gill, P. Circular dichroism techniques: biomolecular and nanostructural analyses- a review. *Chem Biol Drug Des.* **74**, 101-120 (2009).
58. Sankaranarayanan, K. & Meenakshisundaram, N. Influence of ficoll on urea induced denaturation of fibrinogen. *AIP Adv.* **6**, 035130 (2016).
59. Hogg, N. Human monocytes are associated with the formation of fibrin. *J*

Exp Med. **157**(2): 473-85 (1983).

60. Yeh, Y.S., Iriyama, Y., Matsuzawa, Y., Hanson, S.R. & Yasuda, H. Blood compatibility of surfaces modified by plasma polymerization. *J Biomed Mater Res* **22**(9), 795-818 (1988).
61. Kiaei, D., Hoffman, A.S., Horbett, T.A. & Lew, K.R. Platelet and monoclonal antibody binding to fibrinogen adsorbed on glow-discharge-deposited polymers. *J Biomed Mater Res.* **29**(6), 729-39 (1995).
62. Kiaei, D., Hoffman, A.S. & Hanson, S.R. Ex vivo and in vitro platelet adhesion on RFGD deposited polymers. *J Biomed Mater Res.* **26**(3), 357-72 (1992).
63. Kiaei, D., Hoffman, A.S., Ratner, B.D., Horbett, T.A. & Reynolds, L.O. Blood interaction with gas discharge treated vascular grafts. *ACS Polym. Mat. Sci. Eng.* **56**, 710-714 (1987).
64. Adamczyk, Z. et al. Fibrinogen conformations and charge in electrolyte solutions derived from DLS and dynamic viscosity measurements. *J Colloid Interface Sci*, **385**(1), 244-257 (2012).

Chapter 5

Investigating thrombotic and hemorrhagic conformations of human fibrinogen gamma-chain variants using atomistic molecular dynamics (MD)

This work was initiated, conceptualized, executed, and written by Sherry Liu and performed under the scientific and computational guidance of Dr. Valerie Daggett (Department of Bioengineering, University of Washington). While this project is still in its nascent stages and requires longer simulation times of at least 100 nanoseconds for publishable characterization, it is, to the best of our knowledge, the foremost instance of an attempt to simultaneously simulate secondary structural instabilities of three clinically-recorded pathogenic variants of the platelet-binding γC-domain of fibrinogen that phenotypically present with thrombophilia, hemophilia, or both.

5.1 Abstract

In this chapter, we identified three pathogenic variants of the platelet-binding

γC-domain of fibrinogen obtained from clinical cases presenting with thrombotic (R275H), hemorrhagic (M310T), and combined (G292V) phenotypes. By performing molecular dynamics (MD) simulations on each of the mutants along with the wild-type structure, we sought to highlight structural differences and elucidate the molecular underpinnings that cause the different blood disorders to arise. To this end, conformations unique to thrombotic phenotypes may shape design criteria for blood compatible materials. Our results demonstrated that three critical loop regions (γ214-229, γ292-298, and γ357-362) are highly sensitive to perturbations in surrounding water organization or steric clashes that affected ensemble structural flexibility or ligand binding. Decreasing mobility in these loop regions was associated with increasingly thrombotic genotype/phenotypes. Ultimately, we purport that surfaces that adsorb fibrinogen in a conformation that preserves the flexibility of these loop regions will yield reduced thrombogenicity.

5.2 Background

Countless congenital blood disorders have been documented based on reported clinical cases presenting with such abnormalities as afibrinogenemia (fibrinogen deficiency) and dysfibrinogenemia (structurally and functionally altered fibrinogen) that can cause pathological bleeding, thrombosis, or both. Mutations can occur in any of the three genes coding for Fbg's three polypeptide chains (*FGA*, *FGB*, and *FGG* for Aα-, Bβ-, and γ-chain, respectively) and are often associated with a predisposition for venous thromboembolism (VTE) or pulmonary embolism (PE) due to defective thrombin binding or inhibited plasmin degradation of fibrin clots (Rogers, Nakashima, & Kottke-Marchant, 2018). Given the clinical manifestation of thrombophilia from certain inherited fibrinogen mutations in the γ-chain nodule (D region), an improved structural understanding of these mutant forms could serve as potential indicators for abnormal conformations adopted in

this region that invite thrombotic responses like platelet adhesion. Insight into thrombogenic structural changes in the γ-chain nodule could then inform design criteria for hemocompatible materials that avoid Fbg adsorption in its bioactive, platelet-signaling conformation.

Herein, we report the results of four molecular dynamics (MD) simulations comparing the 30 kDa carboxyl terminal fragment of human fibrinogen γ-chain to three pathogenic variants (Haifa-1: R275H, Baltimore-1: G292V, Asahi: M310T). These three mutations were selected from the Online Mendelian Inheritance in Man (OMIM) database (Entry 134850: Fibrinogen, G Gamma Polypeptide; FGG) due to multiple clinical reports of patients with history of posttraumatic or unprovoked bleeding disorders (McKusick-Nathans Institute of Genetic Medicine, 1985-2020). Case reports of fibrinogen Haifa-1 (R275H) present multiple instances of thrombotic propensity to peripheral arterial thrombosis in several unrelated patients (Brook, Tabori, Tatarski, Hashmonai, & Schramek, 1983; Reber et al., 1986; Siebenlist et al., 1989; Yamazumi, Terukina, Onohara, & Matsuda, 1988; Yoshida et al., 1992). In contrast, fibrinogen Asahi (M310T) was detected in a patient with posttraumatic hemorrhage as well as history of bleeding diathesis (Yamazumi, Shimura, Terukina, Takahashi, & Matsuda, 1989). In addition to the mutation, N308 was discovered to be N-glycosylated through the formation of a new consensus sequence (N308-G309-T310). These two modifications impair fibrin-fibrinogen crosslinking, and hyperglycosylation is predicted to reduce the clotting rate and increase tendency for hemorrhage (Cote, Lord, & Pratt,1998). Inclusion of this variant is intended to serve as a foil to the pro-thrombotic variant Haifa-1 (R275H) and uncover potential γC structural changes that facilitate pathological bleeding. Finally, the G292V mutation in fibrinogen Baltimore-1 is derived from a GGC GTC codon change and resides in a portion of the γC-nodule necessary for fibrin polymerization (Bantia, Mane, Bell, & Dang, 1990; Stucki et al., 1999). Symptoms for patients with Baltimore-1 paradoxically encompassed both thrombo- and hemophilia, suggesting that the G292 residue is essential to

maintaining hemostatic balance (Bantia, Mane, Bell, & Dang, 1990; Beck, Charache, & Jackson, 1965). By investigating these three unique pathogenic variants in relation to WT 1FID γC domain, we sought to uncover protein conformational changes underlying clinically reported symptoms. Using MD, we demonstrated that three loop structures, located on the opposite of the protein from the platelet binding epitope, are affected by changes in mobility due to the mutations. Based on this, we propose that hemocompatible surfaces must preserve the flexibility of these loop structures if platelet binding is to be avoided.

5.3 Methods

5.3.1 Model construction

The starting coordinates for the carboxyl terminal fragment of fibrinogen's γ-nodule were obtained from the 2.1 Å resolution x-ray crystal structure deposited in the Protein Data Bank (PDB) and determined by Yee et al. (PDB ID: 1FID) (Berman et al., 2000; Yee et al., 1997). The embedded Ca^{2+} ion—which catalyzes the proteolysis of fibrinogen by thrombin to form fibrin precursors necessary for clotting—was removed from 1FID to reduce complications with simulation. Additionally, the homology modeling program MODELLER was employed to determine structures for ten disordered residues that were not resolved in 1FID (i.e. V143, G403, G404, A405, K406, Q407, A408, G409, D410, V411) (Sali & Blundell, 1993). Five models were generated and the one with the lowest estimated Cα RMSD was selected for MD simulation. Residue mutations for Haifa-1 (R275H), Baltimore-1 (G292V), and Asahi (M310T) were introduced *in silico* using UCSF Chimera (Pettersen et al., 2004) combined with the Dynameomics rotamer library (Towse et al., 2016). The final rotamers were selected based on the following list of descending priorities: least number of predicted clashes with

surrounding atoms, number of hydrogen bonds introduced, and probability of rotamer occurrence in the Dynameomics database. All four structures (1FID, R275H, G292V, M310T) were modeled under neutral pH conditions to best represent the pH conditions of human blood (**Figure 5.1**).

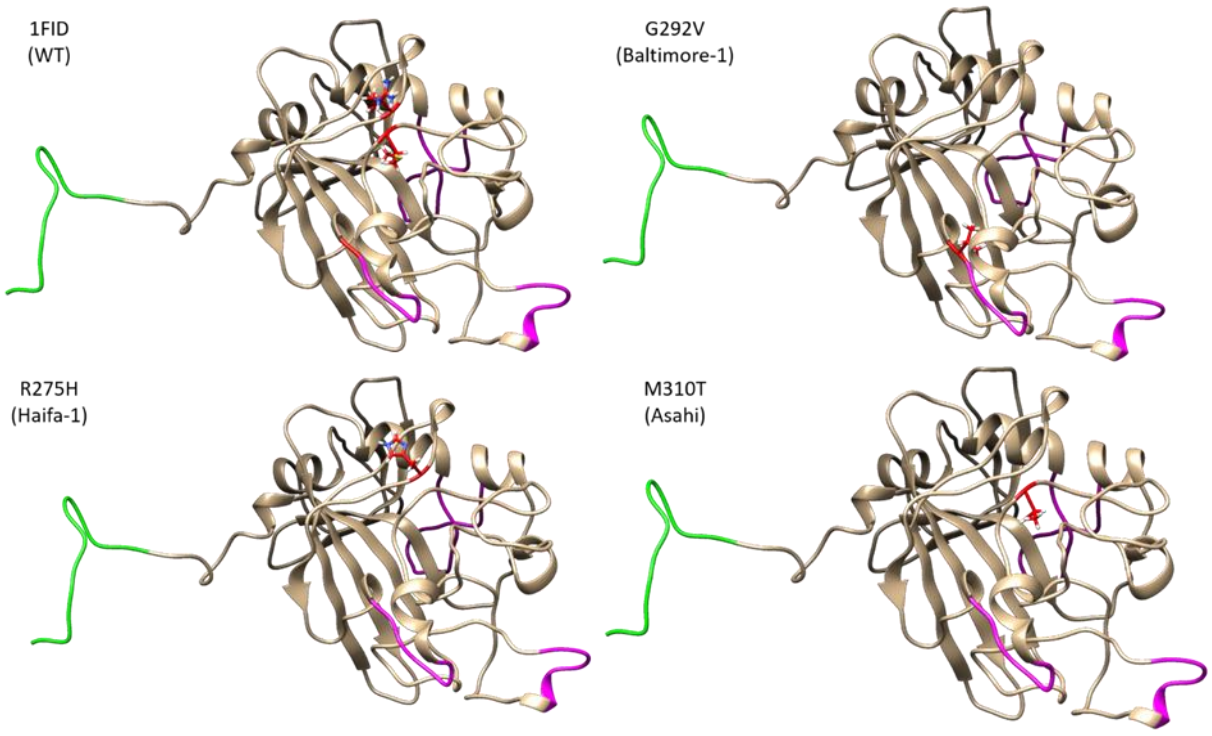

Figure 5.1. Structure of Protein Variants. PDB entry 1FID (human fibrinogen γC-terminal fragment) was used as the wild-type (WT) starting structure. The three pathogenic variants spanning thrombotic, hemorrhagic, and mixed based on clinical cases were created by mutating indvidual residues on 1FID (Haifa-1: R275H, Asahi: M310T, Baltimore-1: G292V). Native residues are shown in tan, mutations are shown in red (only the locations of the three mutations are shown on the WT 1FID structure), the three critical flexible loop structures (residues 214-229, 292-298, and 357-362) are shown in magenta, and the platelet binding active epitope (residues 400-411) is shown in green.

5.3.2 Molecular dynamics (MD) simulations

The 1FID, R275H, G292V, and M310T starting structures were prepared using the *in lucem* molecular mechanics (*il*mm) package (Beck et al., 2000-2020)

combined with the force field from Levitt et al. (Levitt et al., 1995) and the flexible three-centered water model (F3C) (Levitt et al., 1997). All PDB entries were manually verified and corrected to reflect the appropriate histidine tautomer as visualized in UCSF Chimera (HID: protonated ND1; HIE: protonated NE2; HIP: double protonation) (**Table 5.1**). Histidines without evident hydrogen bonding were left as HIE, which is the preferred tautomer in solution. Cysteines in all four structures were disulfide bonded and denoted appropriately as CYS (i.e. CYS153-CYS182; CYS326-CYS339). In *il*mm, missing hydrogen atoms were first added to the cleaned crystal structures and minimized for 500 steps. Then, all atoms were further minimized via steepest descent for 1000 steps and residues were verified for L-type chirality. Next, each structure was solvated in a water box of size 10 Å past all atoms. Solvent (water) atoms were minimized, equilibrated, then further minimized for 1000, 500, and 500 steps, respectively. All protein atoms (non-water) were minimized for an additional 500 steps afterwards. Coordinates were recorded every picosecond for analysis. All three production simulations were run in triplicate (total n=12) at 310 K (approximately body temperature) and neutral pH for a duration of 5 ns with a 2-fs integration step.

Table 5.1. Histidine tautomers selected for each starting structure.

PDB Residue Number	**Histidine Tautomer**			
	1FID (WT)	**G292V (Baltimore-1)**	**R275H (Haifa-1)**	**M310T (Asahi)**
146	HIE	HIE	HIE	HIE
217	HIE	HIE	HIE	HIE
234	HID	HID	HID	HID
275	---	---	HIE	---
307	HID	HID	HID	HID
340	HIP	HIP	HIP	HIP
343	HIE	HIE	HIE	HIE

400	HIE	HIE	HIE	HIE
401	HIE	HIE	HIE	HIE

5.3.3 Simulation analysis

Root-Mean-Square Deviations (RMSD): The C_α RMSD for each variant was determined as a function of time, as well as a time-averaged value by each residue. To obtain an ensemble mean structure, the C_α RMSD capturing coordinates of every atom in the dynamic protein was averaged across the duration of the simulation (5 ns).

Secondary Structure Detection: Secondary structure changes throughout the time course of the simulations were determined based on recurrent hydrogen bonding patterns of main-chain dihedral angles. Specifically, α-helices were defined as three consecutive residues with α_R main-chain dihedral angle motifs (Φ = -87° ± 35°, Ψ = -49° ± 35°), while β-sheets were defined as three consecutive residues with β main-chain dihedral angle motifs (Φ = -115° ± 32.5°, Ψ = 130° ± 50°).

Contact Analysis: Atomic contacts were categorized as native (existing in the starting structure) or non-native (acquired during simulation). Hydrogen bonding (protein-protein or -solvent) was defined as donor-acceptor pair distances <2.6 Å and ≤45° from linearity (McCully et al., 2013). Contact between side chains was defined as ≤5.4 Å (carbon-carbon) or ≤4.6 Å (other interactions) between a minimum of one pair of atoms from each side chain.

5.4 Results

A total of 12 MD monomeric simulations were conducted for the Fbg γC nodule under human blood-like conditions (neutral pH, 310 K). The four unique sequences simulated in triplicate included wild-type human γC nodule (1FID) and

three pathogenic variants clinically reported as thrombotic (Haifa-1: R275H), hemorrhagic (Asahi: M310T), or mixed (Baltimore-I: G292V).

5.4.1 Backbone motion

Conformational changes to all tertiary structures of the Fbg γC nodule were identified by calculating the C_α RMSD determined from MD relative to the minimized starting crystal structure. The ensemble time-averaged RMSD (Å) for each variant is as follows: 1FID (3.72 ± 0.76), R275H (3.59 ± 0.80), G292V (3.82 ± 0.82), and M310T (3.95 ± 0.87) (**Table 5.2**). Given that the individual standard deviations for the ensemble averages are all within 0.11 Å of each other (0.76 to 0.87), the mean C_α RMSD values are rendered more comparable and show a distinct decreasing trend with increasing thrombotic symptoms. Haifa-1 (R275H), which was associated with thrombophilia, demonstrates the lowest C_α RMSD while Asahi (M310T), which was associated with severe hemorrhagic tendency, yielded the highest C_α RMSD. C_α RMSD for Baltimore-1 (G292V), which was linked to mixed thrombosis and bleeding diathesis, fell between these two but was greater than that for the WT structure (1FID).When viewing the RMSD simulation time profile for each structure (n=3), the averaged result reveals a period of rapid structural change as trajectories move away from the starting crystal structure that slows appreciably after the 1 ns mark (**Figure 5.2**). As expected, re-plotting this data as a function of residue number in each variant shows that the most rigid regions were the hydrogen bond-stabilized α-helices and β-strands, while the most mobile regions with the greatest RMSD values were the loops between these strands and the flexible N- and C- termini (**Figure 5.3**). The three most prominent loop structures yielding the highest RMSD values were residues 214-229, 292-298, and 357-362, which are all located distal from the platelet-binding epitope (γC 400-411 terminus) on the opposite side of the protein fragment. Compared to WT (1FID), all three mutants demonstrated greatly reduced RMSD in residues 214-229,

increased RMSD for Haifa-1 (R275H) and Asahi (M310T) but reduced RMSD for Baltimore-1 (G292V) in residues 292-298, and comparable RMSD in residues 357-362.

Table 5.2. Average C_α RMSDs from MD simulations of human fibrinogen γC nodule.

Fbg γC Variant	Run	Cα RMSD (Å)	Ensemble Cα RMSD (Å)
1FID (WT)	1	3.59 ± 0.69	3.72 ± 0.76
	2	3.83 ± 0.90	
	3	3.73 ± 0.68	
G292V (Baltimore-1)	1	3.13 ± 0.48	3.82 ± 0.82
	2	4.23 ± 1.01	
	3	4.10 ± 0.97	
R275H (Haifa-1)	1	3.51 ± 0.80	3.59 ± 0.80
	2	4.03 ± 0.94	
	3	3.22 ± 0.65	
M310T (Asahi)	1	3.95 ± 0.89	3.95 ± 0.87
	2	3.57 ± 0.85	
	3	4.33 ± 0.88	

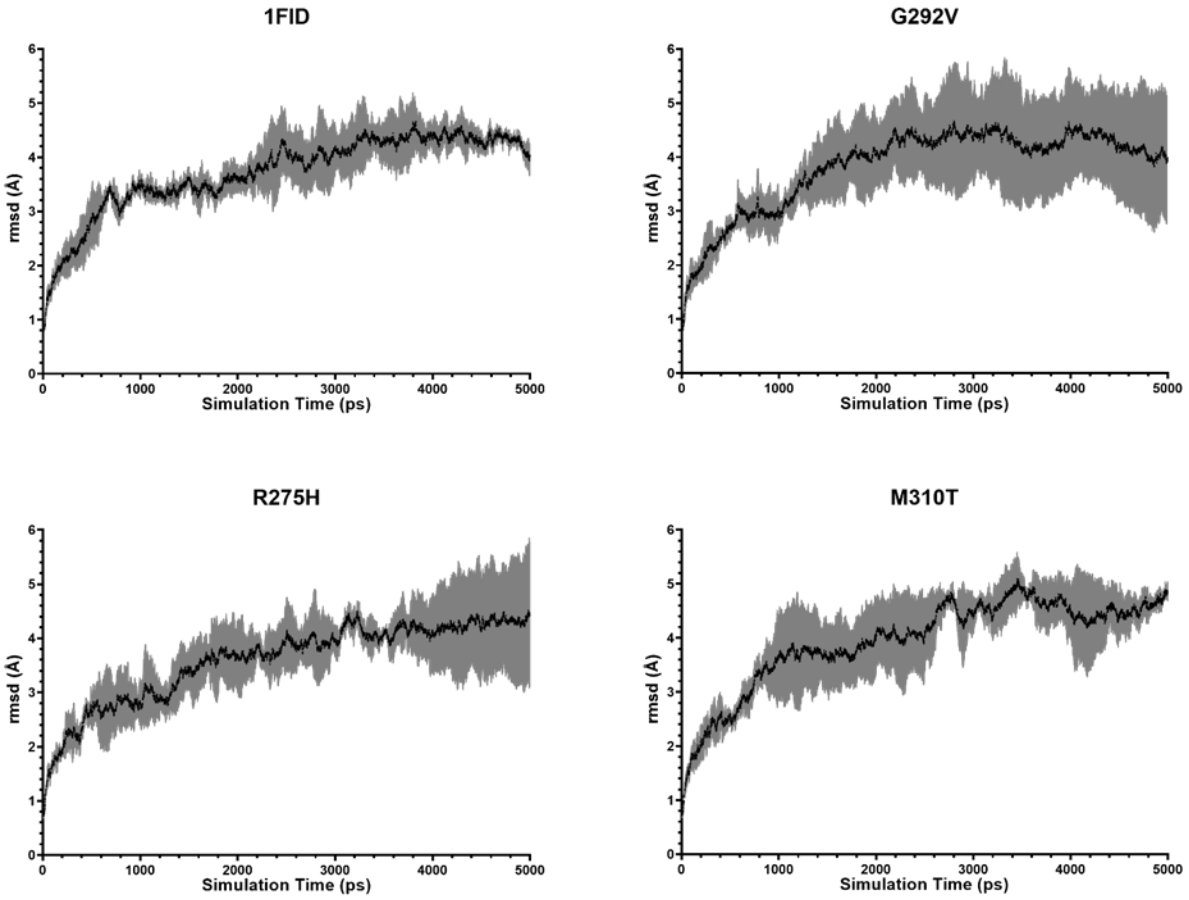

Figure 5.2. Profile of RMSD vs. simulation time (5 ns). Time-averaged rmsd for 1FID was 3.72 ± 0.76 while that for the thrombotic, mixed, and hemorrhagic variants was 3.59 ± 0.80, 3.82 ± 0.82, and 3.95 ± 0.87, respectively. Less mobile structures are associated with higher tendency for thrombogenic events, and excessively flexible structures are associated with propensity for pathological bleeding. The SD for G292V (Baltimore-1; mixed symptoms) is notably large, which reflects underlying individual runs that exhibited a cyclic sawtooth pattern.

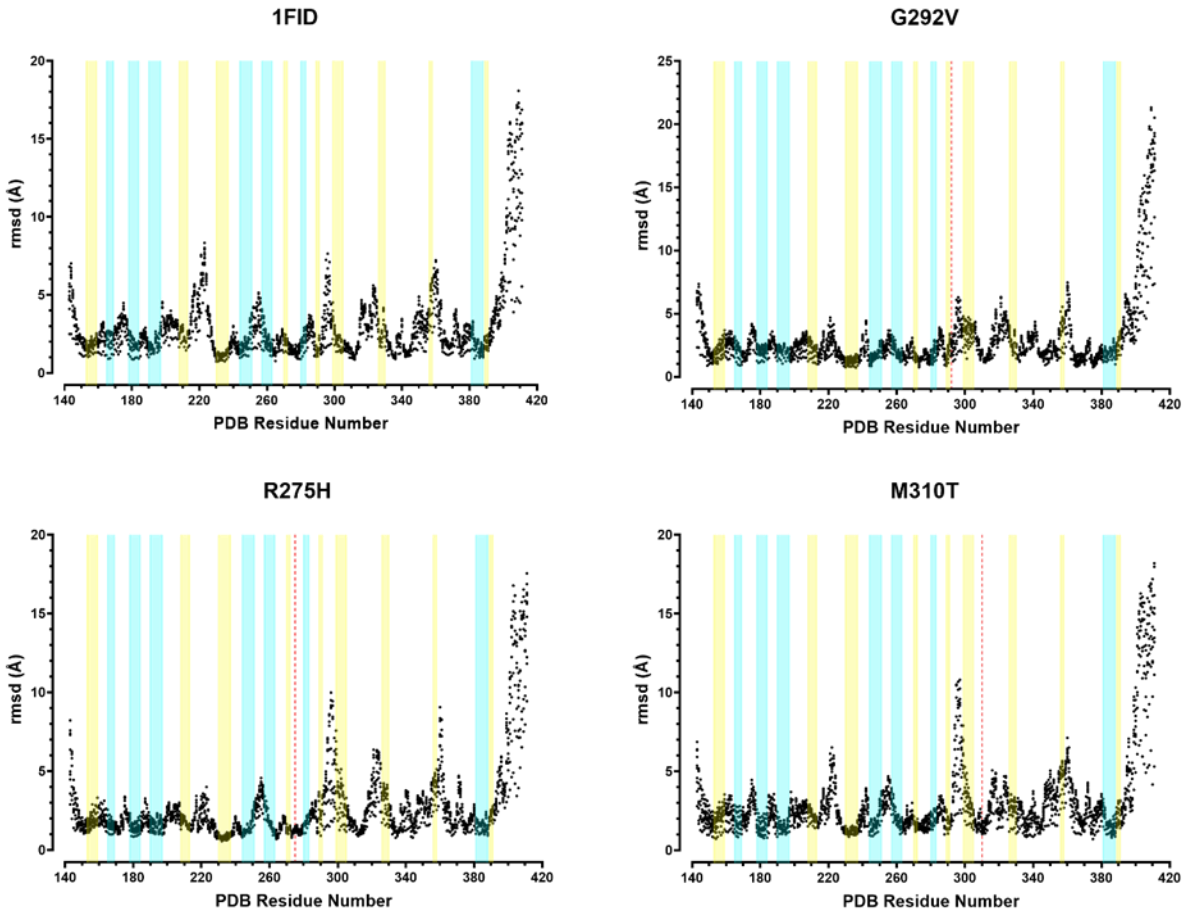

Figure 5.3. Plot of RMSD vs. residue number. As expected, residues comprising α-helices (highlighted in yellow) and β-strands (highlighted in blue) maintained relatively lower RMSD values (troughs) than the loops between them (spikes). The three most prominent peaks were considered critical loop structures (residues 214-229, 292-298, and 357-362) and were used to analyze the effects of subsequent mutations in their vicinity (mutations represented as red dotted line).

5.4.2 Define secondary structure of proteins (DSSP) plots

DSSP plots were generated based on an *il*mm script that identifies hydrogen bonding within the backbone and categorizes them into eight types of secondary structure (Kabsch & Sander, 1983) (**Figure 5.4**). The 1FID WT structure maintains all α-helices and β-strands by the end of the simulation with minimal fluctuation or loss of structure throughout. However, Haifa-1 (R275H) and Baltimore-1

(G292V) both demonstrate loss of integrity of the α-helix at residues 299-305 (PSDKFFT), which sporadically adopts 3/10 helical structure interspersed throughout the simulation (i.e. hydrogen bonds are 3 residues apart instead of the typical 4 in an α-helix). Alternatively, Haifa-1 and Asahi (M310T) both demonstrate loss of structure in the α-helix at residues 326-330 (CAEQD), which intermittently assumes pi-helical structure (i.e. hydrogen bonds are 5 residues apart). Extensive β-bridge structures are created in the expanse of loops from residues 331-380 in the three mutants, some of which are evolved from original short β-like structures and others which are completely non-native in nature. Additionally, the previously mentioned reduction in RMSD values for the three mutants observed in the α-helix-flanked loop structure for residues 214-229 are reflected in the DSSP plots, with the noticeable presence of β-sheet structure forming in the middle of the simulation that reduces the mobility of this region. In all, the ensemble effect of the mutations on the platelet-binding γC-terminus (400-411) results in fully unstructured C-termini, whereas the WT 1FID structure can form two stable β-bridges at residues 402 and 408 to yield a distinctive rounded kink.

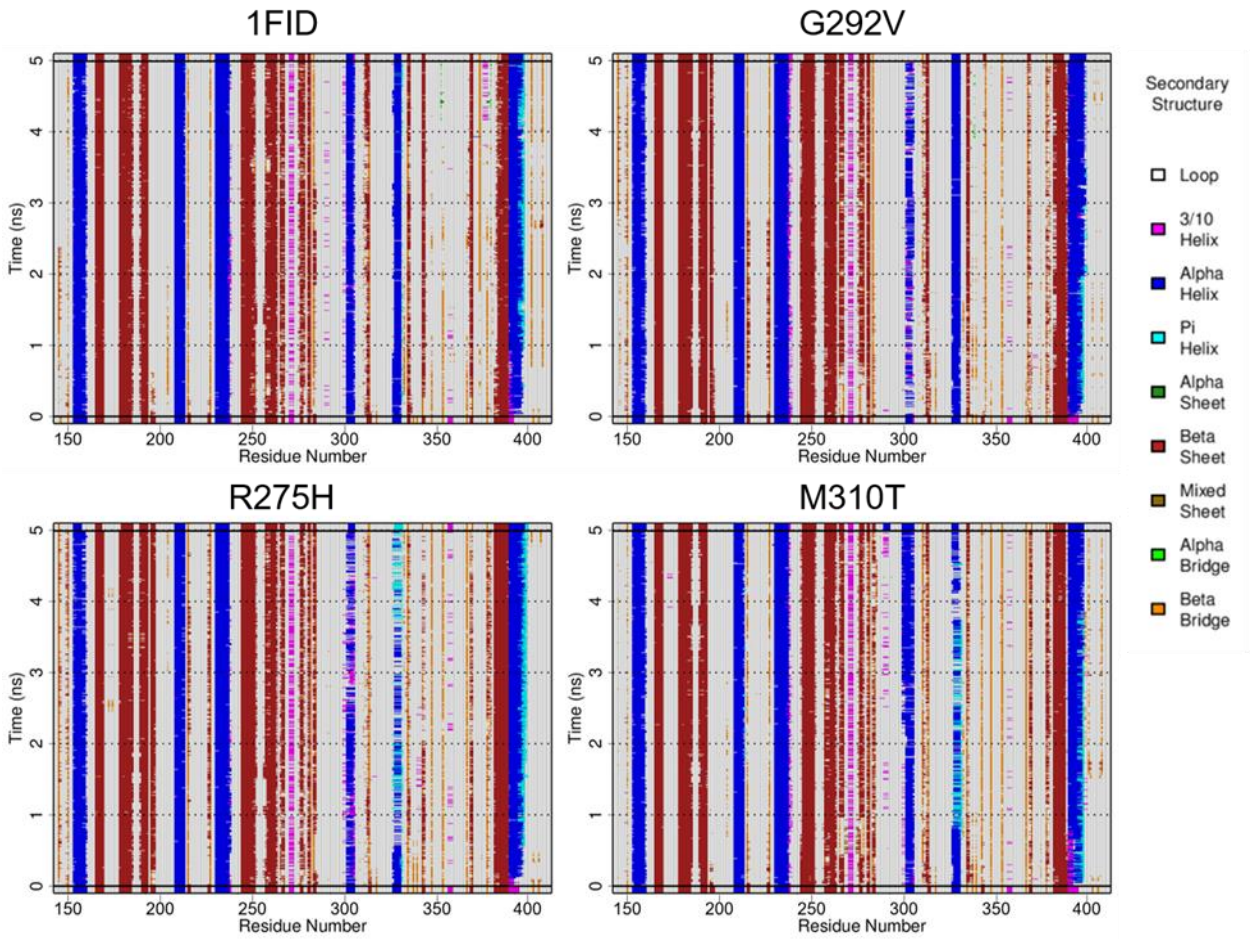

Figure 5.4. DSSP plots show changes in secondary structure throughout the simulation. The WT 1FID structure demonstrated almost full retention of the main secondary structures (α-chains and β-strands). However, Haifa-1 (R275H) and Baltimore-1 (G292V) both demonstrate conversion of α-helix to 3/10 helical structure, while Haifa-1 and Asahi (M310T) both demonstrate conversion of α-helix to pi-helical structure. Extensive β-bridge structures are created in the loops from residues 331-380 in all three mutants. The ensemble effect of the mutations on the platelet-binding γC-terminus (400-411) results in fully unstructured C-termini, whereas the WT 1FID structure can form two stable β-bridges at residues 402 and 408.

5.4.3 Contact analysis

Asymmetric contact maps depicting native (upper left) and non-native (lower right) contacts are plotted in **Figure 5.5**, with fraction of time of contact increasing from red to blue (see binary 0-1 scale on right). The left column of plots depicts the contacts observed in the starting crystal structure for all variants

(ref_tot), and comparison with the right column shows the variation in contacts seen during the simulation (asymmetric). The contacts representing the β-strands visibly protrude outwards along the diagonal of the plot while α-helices lie parallel to it in short repeated patterns that appear as small serrations. Contacts in the starting crystal structure are relatively diffuse with many occurring in isolated instances between nonlocal residues (congruous with the high degree of unstructured intermeshed loops), yet these are largely lost by the end of the simulation for all variants. However, several shorter, nonnative β-like structures are formed in agreement with previously described DSSP data (β-bridge structures). Thus, the overall structure of the γC-nodule is highly non-robust, even for the WT structure.

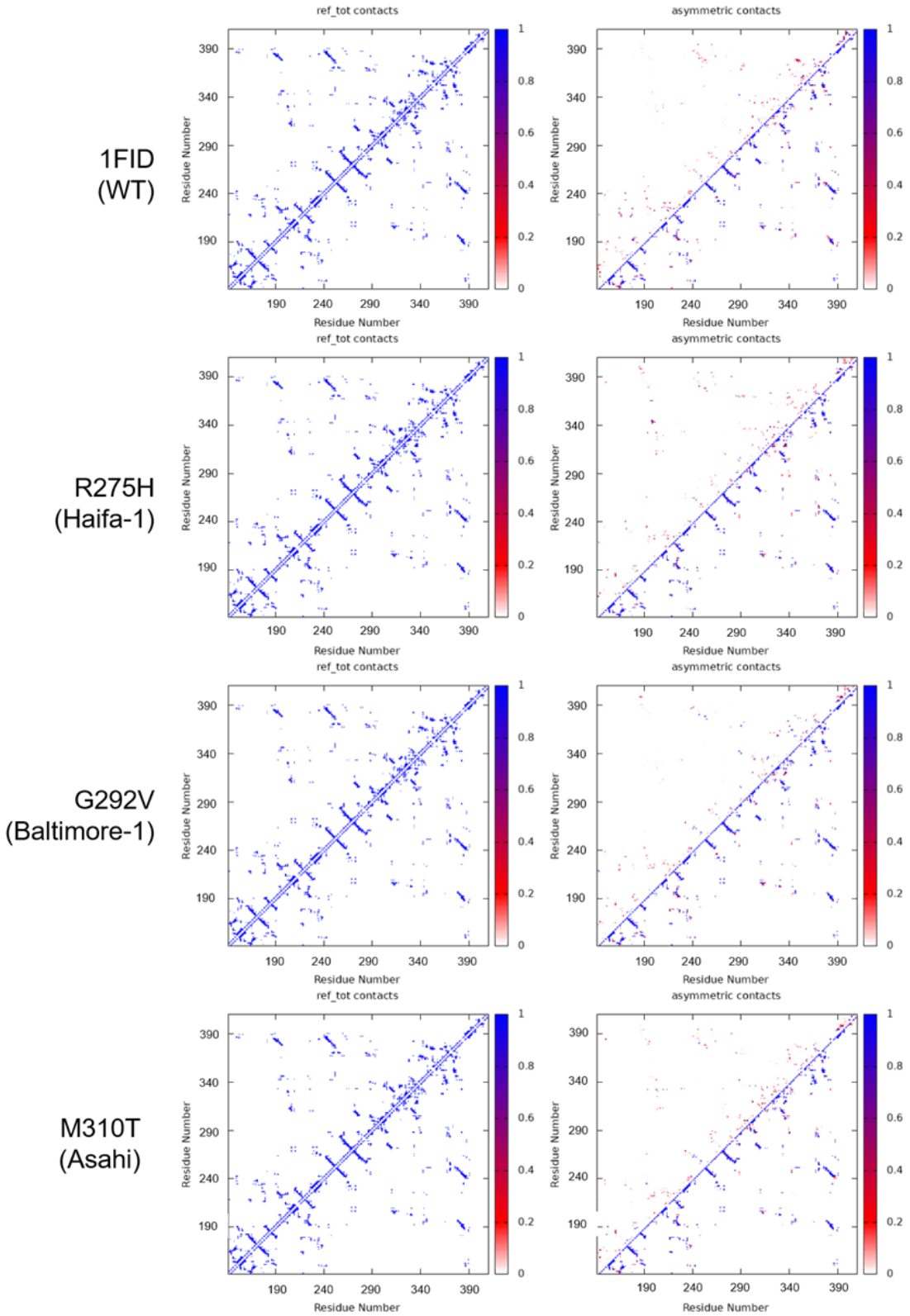

Figure 5.5. Native vs. non-native contact plots. (left) Contact plots of the starting

crystal structure prior to MD simulation (native contacts mirrored across diagonal). (right) Asymmetric contact plot of native vs. non-native contacts after MD simulation. The color bar depicts fraction of time contacts are made throughout the simulation (red=0, blue=1). β-strands are observed protruding from the diagonal. Contacts in the starting crystal structure are diffuse with many occurring between nonlocal residues in tortuous loop structures, yet these are mostly lost by the end of the simulation for all variants. However, several shorter, nonnative β-bridge structures are formed.

5.5 Discussion

The mobility of the flexible loop structures distal to the γC-terminus platelet binding epitope (400-411) appear to bear a strong influence on movement of the C-terminus itself, suggesting the importance of long-range interactions. Specifically, with increased rigidity of these loop structures (214-229, 292-298, and 357-362), we observe a marked decrease in RMSD of the overall structure and a distinct trend in clinical outcome, with the least mobile variant (Haifa-1, R275H) associated with thrombotic tendencies and the most mobile variant (Asahi, M310T) associated with hemorrhagic tendencies. The three mutations were all introduced either in the near vicinity of (R275H, G292V) or within (M310T) these loops. Haifa-1 (R275H) was assessed by Siebenlist et al. and demonstrated extended thrombin times, slower fibrin polymerization rates, and the formation of highly-branched clot matrices with thinner fiber diameters than WT fibrinogen (Siebenlist et al., 1989). However, in the presence of $CaCl_2$, the polymerization rate was mostly restored. Combined with Haifa-1's structural similarity to normal α-fibrin molecules, they hypothesized that Haifa-1 suffers from defective Ca^{2+} usage due to disruption of the β-chain carboxy-terminal, which lies directly adjacent to the γC nodule. Because of its ability to distribute negative charge due to resonance within the imidazole group, His supports proton transfer more effectively than Arg and can thus interface with surrounding water molecules more rapidly. The R275H mutation also sits near the U-turn of a hairpin-shaped loop that directly tugs on the Ca^{2+} pocket via hydrogen bonds, therefore rapid

stabilization with water molecules reduces RMSD by preventing outward flapping of the hairpin-shaped loop (**Figure 5.1**). It is possible that the loss in mobility of this "swinging arm" rigidifies the protein elsewhere like the nearby γC nodule, which primes it for platelet recognition and capture. This rigidifying effect could be a similar mechanism observed for fibrinogen adsorption to solid surfaces that ultimately result in increased platelet binding. Conversely, the M310T mutation (Asahi; hemorrhagic) resides near the Ca^{2+} ion pocket (residues 318-326: DNDKFEGNC) and appears to directly affect the shape of this ligand binding region. As Ca^{2+} is critical to catalyzing the fibrin polymerization process, structural changes within or around the pocket may significantly impair Ca^{2+} binding and clot formation, leading to pathological bleeding. The conversion of the linear nonpolar sidechain of Met to the branched polar sidechain of Thr, which sits directly across from the Ca^{2+} binding pocket, invites restructuring of surrounding water molecules with the increase in conformational entropy that may impact Ca^{2+} entry into the space, as the binding pocket is predominantly comprised of hydrophilic residues. Baltimore-1 (G292V) exhibits a mutation to a branched residue (Val) that clashes with the α-helix at residues 299-305. Although not directly involved in the helical structure, the Val sits in a tight turn right out of it on one of the highly fluctuating loop structures mentioned previously. Given the demonstrated need for mobility in these loop structures, the steric clashing of the Val with the helix in this region could give rise to main chain movement in a cyclical process. Indeed, the individual RMSD profiles for this variant demonstrated jagged, sawtooth-like patterns which could correlate with moments of clashing that periodically subsided before clashing again. This could also potentially explain the mixed symptoms of thrombosis and hemorrhage for patients with this mutation, as the clotting ability of the fibrinogen molecule undergoes periodicity.

Based on contact maps, the γC-nodule does not preserve much of its native contacts in neutral pH solution. This is not too surprising considering the protein

fragment is inherently loosely-packed: the γC domain contains an a-hole into which the A-knob from neighboring Fbg molecules bind after fibrinopeptide cleavage—a process essential to fibrin polymerization (Weisel et al., 2007). However, this means that the γC nodule is far more sensitive to forces like the entropic restructuring of water or steric interactions. Therefore, the formation (or lack thereof) of comparatively weaker β-bridge structures throughout the multitude of flexible loops can ultimately determine the conformation and rigidity of the entire γC domain and the subsequent level of platelet binding.

5.6 Summary

Herein, we have performed and analyzed the molecular dynamics for the platelet-binding subunit of fibrinogen (1FID, γC domain) along with three pathogenic variants clinically reported as thrombotic (Haifa-1, R275H), hemorrhagic (Asahi, M310T), or mixed (Baltimore-1, G292V). We have identified three key flexible loop structures (residues 214-229, 292-298, and 357-362) that demonstrated altered mobility (via RMSD) in each of the three mutants compared to the WT structure. Due to the large proportion of open loops distal to the active epitope (i.e. C-terminal dodecapeptide) compared to robust α-helices or β-sheets, we believe that Fbg's γC domain is highly sensitive to mutational changes that disrupt water organization or sterically interfere with isolated secondary structure that may be critical to downstream ligand binding (e.g. Ca^{2+}). The γC domain is most in its native soluble (and therefore inactive) state when these loops are mobile, thus adsorption mechanisms onto device surfaces should afford these regions with high flexibility. Altogether, development of hemocompatible surfaces should focus efforts on adsorbing Fbg in an orientation that avoids perturbing these delicate loop structures.

5.7 Acknowledgments

Protein images were generated using UCSF Chimera, contact plots were generated by *il*mm, and data figures were prepared using Graphpad Prism 8.0. MD simulations were performed using the Extreme Science and Engineering Discovery Environment (XSEDE) resource STAMPEDE through allocation TG-MCB160195.

5.8 References

1. Baier, R.E., Dutton, R.C. Initial events in interactions of blood with a foreign surface. *J. Biomed. Mater. Res.* **3**, 191-206 (1969).
2. Bantia, S., Mane, S.M., Bell, W.R., & Dang, C.V. Fibrinogen Baltimore I: polymerization defect associated with a gamma 292Gly----Val (GGC----GTC) mutation. *Blood.* **76**(11), 2279-2283 (1990).
3. Beck, E.A., Charache, P., & Jackson, D.P. A New Inherited Coagulation Disorder Caused by an Abnormal Fibrinogen ('Fibrinogen Baltimore'). *Nature*. **208**, 143-145 (1965).
4. Berman, H.M., Westbrook, J., Feng, Z., Gilliland, G., Bhat, T.,N., Weissig, H., Shindyalov, I.N., Bourne, P.E. The Protein Data Bank. *Nucleic Acids Res.* **28**, 235-242 (2000).
5. Brook, J.G., Tabori, S., Tatarsky, I., Hashmonai, M., & Schramek, A. Fibrinogen 'Haifa'—a new fibrinogen variant: a case report. *Haemostasis*. **13**, 277-281 (1983).
6. Chiumiento, A., Lamponi, S., & Barbucci, R. Role of fibrinogen conformation in platelet activation. *Biomacromolecules*, **8**(2), 523–531 (2007).
7. Clarke, M.L., Wang, J., Chen, Z. Conformational Changes of Fibrinogen After Adsorption. *J. Phys. Chem. B.* **109**(46), 22027-22035 (2005).
8. Cote, H.C.F., Lord, S.T., & Pratt, K.P. Gamma-chain dysfibrinogenemias: molecular structure-function relationships of naturall occurring mutations in the gamma chain of human fibrinogen. *J. Am. Soc. Hemat.* **92**, 2195-2212 (1998).
9. D'Souza, S.E., Ginsberg, M.H., Burke, T.A., & Plow, E.F. The ligand binding site of the platelet integrin receptor GPIIb-IIIa is proximal to the second calcium binding domain of its alpha subunit. *J. Biol. Chem.* **265**(6), 3440-3446 (1990).

10. D'Souza, S.E., Ginsberg, M.H., Matsueda, G.R., Plow, E.F. A Discrete Sequence in a Platelet Integrin is Involved in Ligand Recognition. *Nature*. **350**, 66-68 (1991).

11. Farrell, D.H., & Thiagarajan, P. Binding of recombinant fibrinogen mutants to platelets. *J. Biol. Chem.* **269**, 226-231 (1994).

12. Hawiger, J., Timmons, S., Kloczewiak, M., Strong, D.D., Doolittle, R.F. Gamma and Alpha Chains of Human Fibrinogen Possess Sites Reactive with Human Platelet Receptors. *Proc. Natl. Acad. Sci.* **79**(6), 2068-2071 (1982).

13. Hylton, D.M., Shalaby, W.S., Latour, R.A. Direct correlation between adsorption-induced changes in protein structure and platelet adhesion. *J. Biomed. Mater. Res.* **73A**, 349-358 (2005).

14. Kabsch, W., Sander, C. Dictionary of Protein Secondary Structure: Pattern Recognition of Hydrogen-Bonded and Geometrical Features. *Biopolymers*. **22**(12), 2577-2637 (1983).

15. Kohler, S., Schmid, F., Settanni, G. The internal dynamics of fibrinogen and its implications for coagulation and adsorption. *PLoS Comput. Biol.* **11**(9), e1004346 (2015).

16. Kollmann, J., Pandi, L., Sawaya, M., Riley, M., Doolittle, R. Crystal structure of human fibrinogen. *Biochemistry*. **48**, 3877-3886 (2009).

17. McCully, M., Beck, D., Daggett, V. Promiscuous Contacts and Heightened Dynamics Increase Thermostability in an Engineered Variant of the Engrailed Homeodomain. *Protein Engineering, Design & Selection*. **26**, 35-45 (2013).

18. Mosesson, M.W. Fibrinogen and fibrin structure and functions. *Thromb. Haemost.* **3**, 1894-1904 (2005).

19. Online Mendelian Inheritance in Man, OMIM®. Johns Hopkins University, Baltimore, MD. MIM Number: 134850. 07/15/2016. World Wide Web URL: https://omim.org/

20. Reber, P., Furlan, M., Henschen, A., Kaudewitz, H., Barbui, T., Hilgard, P., Nenci, G.G., Berettini, M., & Beck, E.A. Three abnormal fibrinogen variants with the same amino acid substitution (gamma275 arg-to-his): fibrinogens Bergamo II, Essen and Perugia. *Thromb. Haemost.* **56**, 401-406 (1986).

21. Rogers, H.J., Nakashima, M.O. & Kottke-Marchant, K. Hemostasis and Thrombosis. in *Hematopathology* (eds. Hsi, E.D.) 57-105 (Elsevier Inc. 2019).

22. Sali, A., Blundell, T. L. Comparative protein modelling by satisfaction of spatial restraints. *J. Mol. Biol.* **234**, 779-815 (1993).

23. Savage, B., Ruggeri, Z.M. Selective Recognition of Adhesive Sites in

Surface-Bound Fibrinogen by Glycoprotein IIb-IIIa on Nonactivated Platelets. *J. Biol. Chem.* **266**(17), 11227-33 (1991).

24. Shattil, S.J., Hoxie, J.A., Cunningham, M., Brass, L.F. Changes in the Platelet Membrane Glycoprotein IIb.IIIa Complex During Platelet Activation. *J. Biol. Chem.* **260**, 11107 (1985).

25. Siebenlist, K.R., Mosesson, M.W., Di Orio, J.P., Tavori, S., Tatarsky, I., & Rimon, A. The polymerization of fibrin prepared from fibrinogen Haifa (gamma-275-arg-to-his). *Thromb. Haemost.* **62**, 875-879 (1989).

26. Sivaraman, B., Latour, R.A. The adherence of platelets to adsorbed albumin by receptor-mediated recognition of binding sites exposed by adsorption-induced unfolding. *Biomaterials*. **31**, 1036-1044 (2010).

27. Spraggon, G., Everse, S.J., Doolittle, R.F. Crystal Structures of Fragment D from Human Fibrinogen and its Crosslinked Counterpart from Fibrin. *Nature*. **389**, 455-462 (1997).

28. Stucki, B., Schmutz, P., Schmid, L., Haeberli, A., Lämmle, B., & Furlan, M. Fibrinogen St. Gallen I (gamma 292 GlyVal): Evidence for Structural Alterations Causing Defective Polymierization and Fibrinogenolysis. *Thromb. Haemost.* **81**(2), 268-274 (1999).

29. Tsai, W.B., Grunkemeier, J.M., Horbett, T.A. Human plasma fibrinogen adsorption and platelet adhesion to polystyrene. *J. Biomed. Mater. Res.* **44**, 130-139 (1999).

30. Tsai, W.B., Grunkemeier, J.M., McFarland, C.D., Horbett, T.A. Platelet adhesion to PS-based surfaces preadsorbed with plasmas selectively depleted in fibrinogen, fibronectin, vitronectin, or von Willebrand's factor. *J Biomed Mater Res.* **60**(3), 348-359 (2002).

31. Ugarova, T.P., Budzynski, A.Z., Shattil, S.J., Ruggeri, Z.M., Ginsberg, M.H., & Plow, E.F. Conformational changes in fibrinogen elicited by its interaction with platelet membrane glycoprotein GPIIb-IIIa. *J. Biol. Chem.* **268**(28), 21080-21087 (1993).

32. Vilaseca, P., Dawson, K.A., Franzese, G. Understanding and modulating the competitive surface-adsorption of proteins through coarse-grained molecular dynamics simulations. *Soft Matter*. **9**, 6978-6985 (2013).

33. Weisel, J.W. Structure of fibrin: impact on clot stability. *J. Thromb. Haemost.* Suppl **1**, 116-124 (2007).

34. Weisel, J.W., Nagaswami, C., Vilaire, G., & Bennett, J.S. Examination of the platelet membrane glycoprotein IIb-IIIa complex and its interaction with fibrinogen and other ligands by electron microscopy. *J. Biol. Chem.* **267**, 16637-16643 (1992).

35. Yamazumi, K., Shimura, K., Terukina, S., Takahashi, N., & Matsuda, M. A gamma methionine-310 to threonine substitution and consequent N-glycosylation at gamma asparagine-308 identified in a congenital dysfibrinogenemia associated with posttraumatic bleeding, fibrinogen Asahi. *J. Clin. Invest.* **83**(5), 1590-1597 (1989).

36. Yamazumi, K., Terukina, S., Onohara, S., & Matsuda, M. Normal plasmic cleavage of the gamma-chain variant of 'fibrinogen Saga' with an arg275-to-his substitution. *Thromb. Haemost.* **60**, 476-480 (1988).

37. Yoshida, N., Imaoka, S., Hirata, H., Matsuda, M., & Asakura, S. Heterozygous abnormal fibrinogen Osaka III with the replacement of gamma-arginine-275 by histidine has an apparently higher molecular weight gamma-chain variant. *Thromb. Haemost.* **68**, 534-538 (1992).

38. Yee, V.C., Pratt, K.P., Cote, H.C., Trong, I.L., Chung, D.W., Davie, E.W., Stenkamp, R.E., Teller, D.C. Crystal structure of a 30 kDa C-terminal fragment from the gamma chain of human fibrinogen. *Structure*, **5**, 125-138 (1997).

Chapter 6

Fluoropolymer and adsorbed blood protein effects on platelet adhesion and activation

Liu, S., Kim, K.H. & Ratner, B.D. Surface-induced changes in fibrinogen bioactivity on a radiofrequency glow-discharge fluoropolymer mediate platelet adhesion in a surface passivation strategy for long-term blood compatibility. In preparation.

Initiated by Sherry Liu (SL) as a part of, and funded by, the Center for Dialysis Innovation (CDI) for Co-Director and Principal Investigator Dr. Buddy D. Ratner (BDR) under the Blood Compatibility research project. SL motivated and conceptualized the work and wrote the manuscript. SL and KHK jointly designed the studies, executed the experiments, and performed data analyses. This chapter is a continuation of work described in Chapter 4 and, barring revisions or edits by committee members, will serve as the draft for a journal submission.

6.1 Abstract

In Chapter 3, we employed QCM-D to evaluate differential total binding, surface adsorption kinetics, adlayer properties, and competitive displacement mechanisms of HSA and Fg to PVDF, PVDF-HFP, and ppC_3F_6. Chapter 4 focused on

the effects of PVDF, PVDF-HFP, and ppC_3F_6 surface chemistry on Fg adsorption orientation, packing, and overall structure as indicators of platelet binding ability. In this chapter, we determine the ultimate effect of fluoropolymer surface chemistry and resultant Fg surface structure on blood component interactions. Fresh platelet-rich plasma (PRP) is exposed to Fg-preadsorbed PVDF, PVDF-HFP, and ppC_3F_6 under static *in vitro* conditions to assess platelet adhesion and activation. Adhered platelets are imaged via SEM, counted, and characterized by morphology based on activation state. Outcomes from this study will create a unifying examination of the interdependent relationships between surface chemistry, plasma protein surface quantities and structures, and platelet adhesion and activation in our effort to characterize the best strategies for engineering blood-compatible materials.

6.2 Background

Platelets in native bloodstream circulate in a quiescent state with a lifetime of 7-10 days, and are prevented from adhesion, activation, and aggregation under healthy physiological conditions by a monolayer of endothelial cells lining the vasculature. The endothelium not only serves as a physical barrier between circulating blood components and underlying vessel tissues like collagen, but also continuously secretes regulatory chemicals like prostacyclin (PGI2) and nitric oxide (NO) to actively inhibit platelet activation [1-3]. The extrinsic pathway of blood coagulation describes the biological function of platelet adhesion during vascular injury, when endothelial damage exposes subendothelial collagen and triggers the release of tissue factor to rapidly mediate platelet adhesion and plug formation.

In the case of blood exposure to artificial biomaterials, platelet adhesion can also be mediated by the adsorbed protein layer to form thrombi at the surface with varying morphologies and degrees of aggregation, with some of the most serious

complications occurring from thrombotic occlusion (in the case of medical devices like small diameter vascular grafts) or poorly adherent platelet aggregates that detach from the biomaterial surface as emboli, leading to risk for stroke and myocardial infarction [23]. As covered in Chapters 3 and 4, the composition and structure of the plasma protein adlayer (which largely depends on the surface chemistry of the underlying biomaterial) determines the extent and mechanism of cellular interactions. Fg is a major mediator of platelet adhesion via specific receptor-ligand binding of its γC dodecapeptide (γC400-411: HHLGGAKQAGDV) to the platelet integrin αIIbβ3 (GPIIb-IIIa) [4-6, 24-25, 30-33], and this outside-in signaling leads to platelet activation through the release of alpha (50-80 per platelet) and dense (3-6 per platelet) granules [7]. Alpha granules contain a variety of hemostatic proteins and regulatory compounds including chemokines (platelet factor 4 (PF4) and SDF-1α), growth factors (VEGF), Factors V and IX, fibrinogen, plasminogen, vWF, β-thromboglobulin (β-TG; leukocyte recruitment) [2, 8], p-selectin (interaction with PSGL-1 on luekocytes for neutrophil activation) [9-10], and polyphosphates (intrinsic coagulation pathway initiation via Factor XII activation) [11].

Adherent platelets on biomaterial surfaces also manifest activation through morphology changes in their cytoskeletal arrangement. Platelet activation can occur as rapidly as 180 ms [21] with irreversible morphological transformations. The resting inactive state yields round (R), discoid shaped platelets similar to that observed in circulation, then become activated to dendritic (D) forms with early pseudopodia, followed by spread-dendritic (SD) with extended dendrites, to spreading (S) forms showing flattened membranes with a localized granule, and finally fully spread (FS) platelets that have been fully activated and released their contents (delocalized granule) [12]. The degree of platelet activation can thus be categorized into these five morphologies as a qualitative understanding of surface thrombogenicity [26-29]. Generally, the morphology changes from R → D → SD → S → FS on biomaterials are evaluated in a linear spectrum from inactive

(favorable) to highly activated (unfavorable), with biomaterials exhibiting high proportions of FS platelets as the most thrombogenic. While this binary assessment may be true for short durations, the long-term effects of these morphologies may not correlate with extended thrombogenicity. In fact, a handful of studies have demonstrated that rapid platelet adhesion and spreading on artificial surfaces to the FS morphology promote surface passivation with a layer of degranulated platelet membranes that are no longer reactive and effectively mask the biomaterial from further exposure to circulating platelets [13-14]. Thus, in this chapter, appropriate methods for characterizing hemocompatibility of biomaterials via the rapid surface passivation strategy will include quantification of total platelet adhesion [15], platelet morphology [16], and PF4 release [17-18].

6.3 Methods

Glass coverslips (15 mm, ProSci Corp) were cleaned via ultrasonication for 10 minutes in a 1:64 isopanasol in DI water dilution (CR Callen Corp, Seattle, WA). Coverslips were then rinsed via five ultrasonications in ultrapure water for 10 minutes before drying with a nitrogen stream. The deposited ppC_3F_6 (Chapter 2.2.1), PVDF (Chapter 2.2.2), PVDF-HFP (Chapter 2.2.2), or uncoated (positive control) glass coverslips were placed in duplicate (n=2) into a 24-well plate, then pre-adsorbed overnight at 4 °C with 1 mL of 3 mg/mL Fg (physiological concentration) (FIB3, human fibrinogen Pg/vWF/Fn depleted, Enzyme Research Laboratories, South Bend, IN) in carbonate buffer, pH 9.6. The following day, fresh human platelet rich plasma (PRP) was procured from Bloodworks Northwest (Seattle, WA), which was recovered from ACD-anticoagulated whole blood of n=2 healthy donors via centrifugation at 725 rpm (120xg) for 10 minutes. The number of platelets in an aliquot of PRP was counted, with an average platelet concentration of 2 x 10^8 platelets/mL. The FIB3-treated substrates were washed 3x with 0.1% PBS-T to remove bulk protein and incubated with 1 mL of the PRP for 2

hours at 37 °C. Following incubation, the spent PRP supernatant was recovered from each well into individual tubes for same-day assessment of platelet activation via release of soluble factors using a PF4 ELISA kit (ab189573, Abcam, Cambridge, MA). For determination of adherent platelet activation via morphology evaluation, samples were rinsed with 1x PBS to remove loosely bound platelets, then fixed for 2 hours at room temperature using Karnovsky solution. Following three 10-minute cacodylate buffer rinses, samples were stained for 30 minutes with osmium tetroxide, washed again with cacodylate buffer, and dehydrated using a 50/70/80/90/100% series of ethanol soaks. Finally, samples were critical point dried and stored with desiccant until ready for scanning electron microscopy (SEM) imaging.

The number and degree of activation of adherent platelets were assessed through SEM imaging. Samples were sputter coated with gold and imaged at an accelerating voltage of 5 kV. A final selection of five random images (collected at 1000x magnification) were selected for each duplicate substrate, and the degree of platelet activation was assessed based on cell morphology categorized into round (R), dendritic (D), spread dendritic (SD), spreading (S), or fully spread (FS) [12]. Counts for each morphology type were performed separately by n=2 counters, averaged, and divided by the overall platelet count per image to yield percentile values. The most favorable morphologies indicating low degree of long-term activation are R (resting; never activated) and FS (fully activated under 2 hours and strongly adhered to the underlying material to form a passivating layer). The most unfavorable morphologies are D/SD with extensive pseudopodia formation and unreleased granules. The statistical significance of the difference in average adherent platelet morphology between substrate types was determined via one-way analysis of variance (ANOVA) with Tukey HSD post-hoc multiple comparisons test. Differences satisfying the condition $p < 0.05$ were regarded as statistically significant.

6.4 Results

6.4.1 Platelet adhesion

Static platelet adhesion from PRP was assessed on samples preadsorbed with 3 mg/mL FIB3 through counting of randomly selected SEM images (n=5 images per n=2 counters). Final counts were scaled from a 1000x SEM image corresponding to a 175 x 125 μm image field to yield values in cells/cm^2. ppC_3F_6 demonstrated significantly more adherent platelets ($p<0.0001$) on its surface compared to PVDF and uncoated glass coverslips, and markedly more compared to PVDF-HFP, though the difference observed was not statistically significant at an $\alpha = 0.05$ or 0.1 level (**Figure 6.1**). The standard deviation in image counts between n=2 counters increased with increasing number of platelets observed on the surface, as borders between closely-packed or fully spread platelets became more difficult to distinguish. It is important to note that instances of large aggregate formation (as largely observed on PVDF) or dendritic platelets resting on top of spreading platelets (as laregly observed on PVDF-HFP) were not counted, as these accounted for platelet-platelet interactions and not platelet-protein/surface interactions that are being evaluated in this study. The occurrence of gradient platelet activation in this way (platelet-platelet signaling) is a sign of staggered and prolonged surface activation, with the formation of nonuniform unstable thrombi. Overall platelet adhesion at the monolayer level on surfaces preadsorbed with 3 mg/mL FIB3 increased in the order of glass → PVDF → PVDF-HFP → ppC_3F_6.

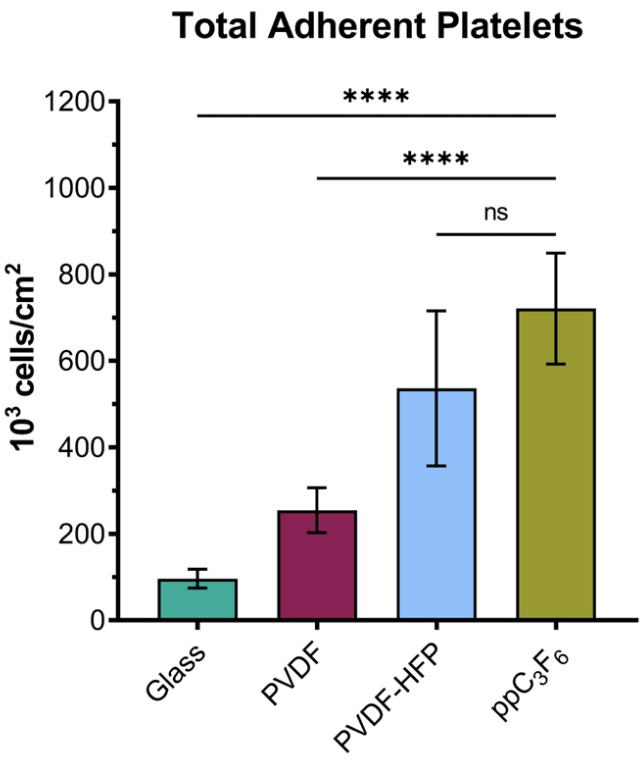

Figure 6.1. Total adherent platelets counted on PVDF, PVDF-HFP, ppC_3F_6, and uncoated glass via SEM imaging. PpC_3F_6 demonstrates significantly more adherent platelets ($p<0.0001$) on its surface compared to PVDF and uncoated glass coverslips, and markedly more compared to PVDF-HFP, though not to a statistically significant degree.

6.4.2 Platelet morphology

Evaluation of SEM images revealed a broad spectrum of platelet morphologies across the different material types. While each sample exhibited nonuniform platelet coverage, overall analyses indicated distinctly different morphological distributions unique to each material (**Figure 6.2**). Uncoated glass showed vast quantities of D and SD platelets that formed interconnected network structures. No R, S, or FS morphologies were observed on glass. The PVDF coating displayed the same spherulitic texture that was observed in AFM imaging (Chapter 2.3.2) due to semi-crystalline phase separation. The dominant platelet morphologies on PVDF were D/FS, which existed in distinct spatial populations. The D platelets were often clustered to form dense aggregates that were omitted from counting in

the total adherent platelet count but are depicted in the scanning electron micrograph as a representative image. Meanwhile, the FS morphology on PVDF was classified as such but displayed signs of trauma and spreading irregularity, with FS platelets 'splattered' on the surface and depicting folds in the membrane that appear poorly adherent to the underlying substrate. PVDF-HFP showed a slightly lower percentage of D/SD platelets than PVDF and a greater proportion of S/FS platelets, with overall platelet adhesion significantly higher than PVDF. The large D aggregates that were observed for PVDF are not observed as much for PVDF-HFP. The FS platelets appear relatively smooth and void of activating granules, though many bare substrate spots are still exposed and available for additional platelet binding. PpC_3F_6 yielded a near-confluent monolayer of S/FS platelets, with almost no exposed substrate. The spread platelets were fairly rounded in shape and formed a flat and uniform coating over the surface. Some cell and platelet fragments appear resting on top of this layer, but are not dendritic in nature.

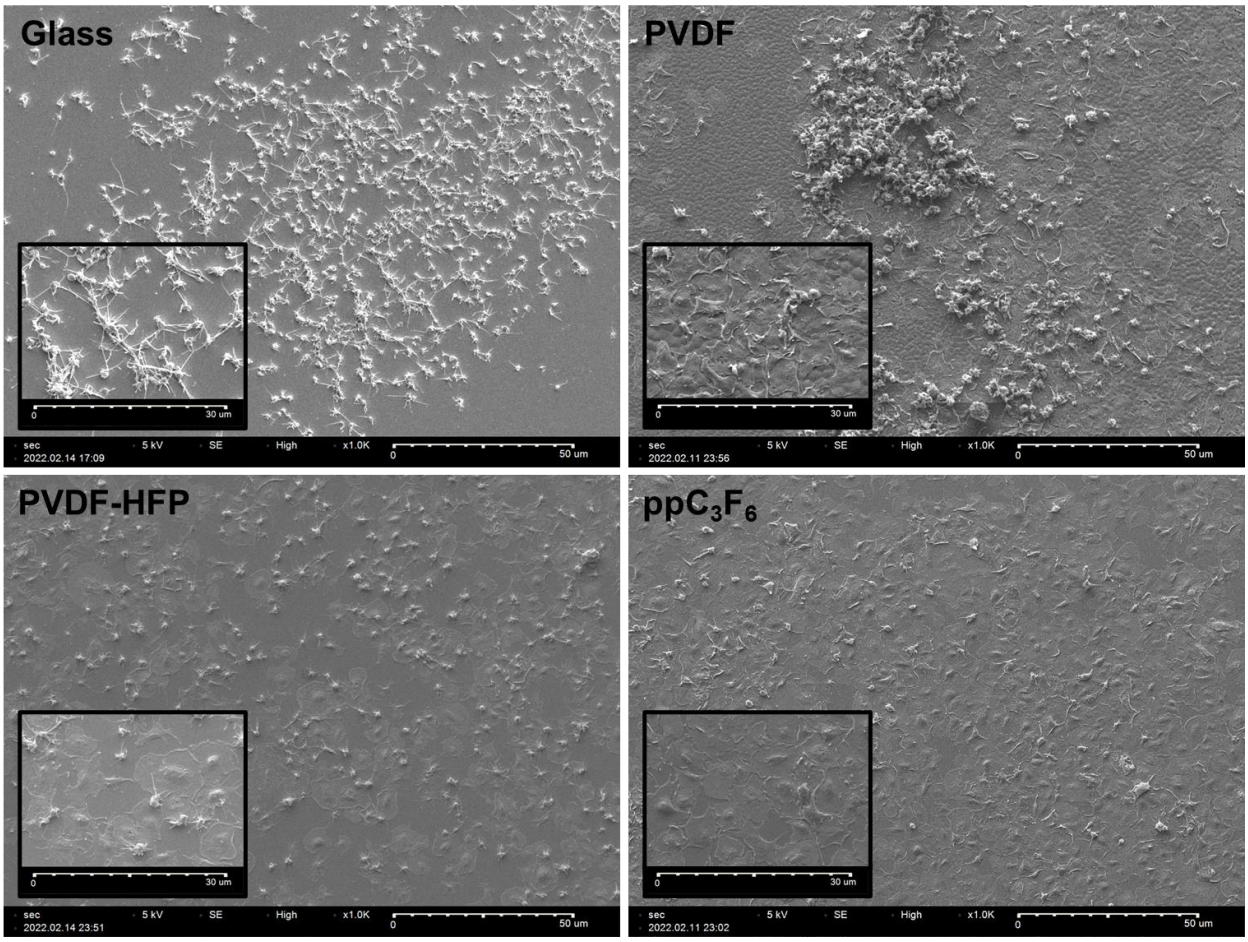

Figure 6.2. Representative scanning electron micrographs of platelets adhered to PVDF, PVDF-HFP, ppC_3F_6, and uncoated glass. SEM images are at 1000x magnification, while insets are at 2000x. Morphology abbreviations used are: round/resting (R), dendritic (D), spread dendritic (SD), spreading (S), or fully spread (FS). (Top left) Uncoated glass displayed a vast interconnected network of D/SD platelets. (Top right) The PVDF coating had a spherulitic rough texture with D/FS as the dominant morphologies. The FS platelets on PVDF, while classified as such, showed high degrees of trauma and irregularity unlike the archetypal FS platelet that has a mostly circular appearance Furthermore, large D aggregates were observed on the surface, but omitted from the final adherent platelet count as a representation of platelet-platelet (and not platelet-surface) interactions. (Bottom left) PVDF-HFP showed few D/SD platelets with a greater proportion of S/FS platelets compared to PVDF. However, the surface still possessed many bare exposed spots open for additional platelet binding. (Bottom right) PpC_3F_6 exhibited the greatest proportion of S/FS morophologies with high (near-confluent) surface coverage of flattened platelet membranes. All materials exhibited no (i.e. 0-2) platelets in the R morphology.

The distribution of morphologies by coating type is shown in **Figure 6.3**. All materials showed almost no presence of round (R) platelets (between 0-2 per

image), therefore the R morphology is not represented. There is no statistically significant difference in D or SD morphologies across any of the materials, with all materials showing some presence of these morphologies. Importantly, the number of D/SD platelets on PVDF appears to be reduced compared to the other materials. However, this value is vastly underestimated due to the formation of large D/SD aggregates on the surface that made it impossible to distinguish individual platelets, and were therefore not counted. Additionally, the large error bar on glass was due to the extreme nonuniformity of D/SD networks observed on the surface for the random sample of SEM images that were selected for this material. Thus the equal importance of evaluating both qualitative and quantitative data is highlighted.

PpC_3F_6 displays significantly more S morphology platelets of this morphology ($p < 0.0001$) than any of the other materials. Furthermore, it exhibits significantly more FS platelets than PVDF-HFP ($p < 0.05$), though the difference in this morphology with that of PVDF was not statistically different. However, from qualitative SEM image examination, the FS platelets on PVDF—though flat and void of localized granules—was highly irregular and appeared torn. Conversely, those on ppC_3F_6 were predominantly smooth and rounded in their circumference.

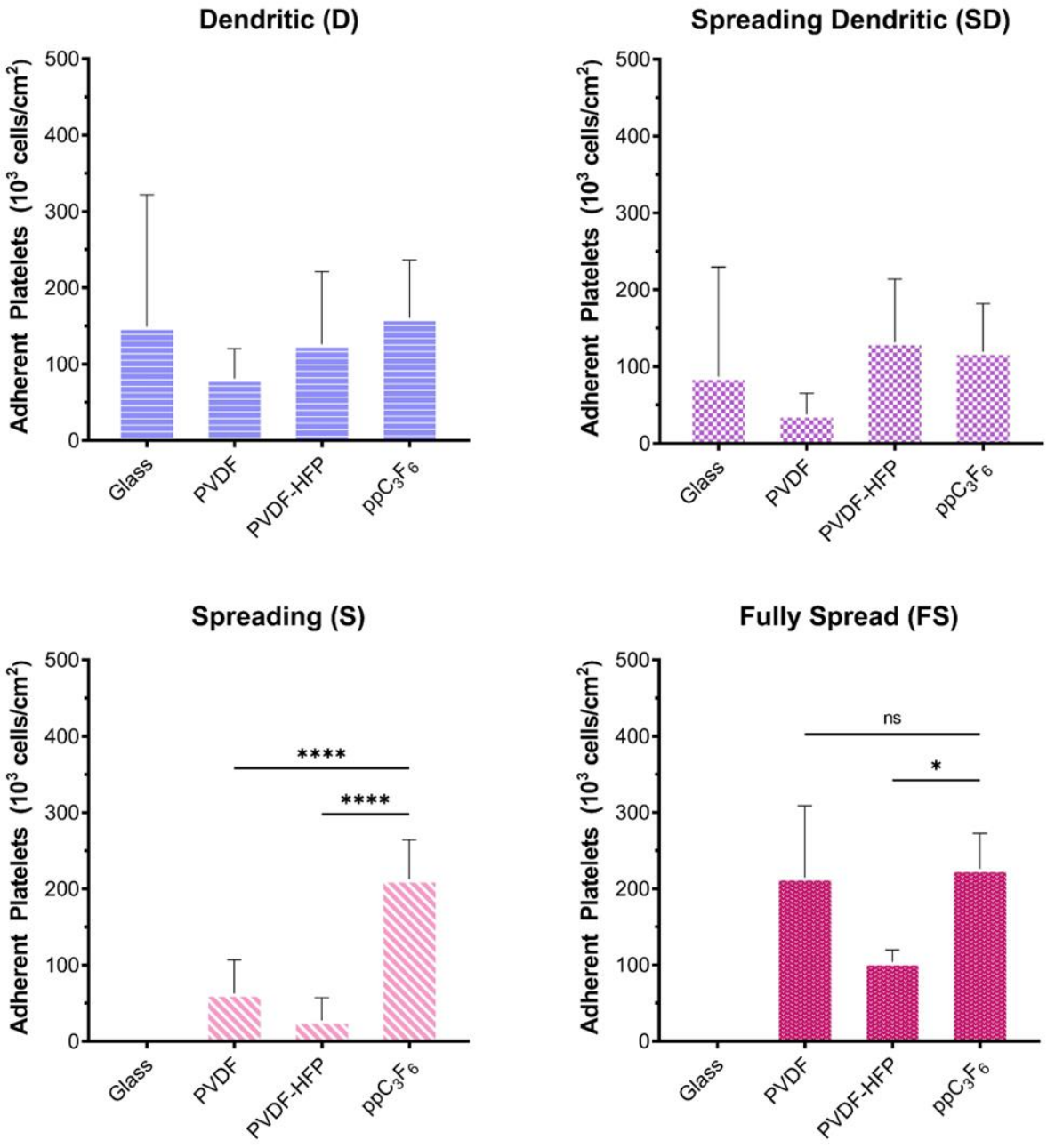

Figure 6.3. Platelet count by morphological assignment on PVDF, PVDF-HFP, ppC_3F_6, and uncoated glass. There is no statistically significant difference in D/SD morphologies across material types. PpC_3F_6 displays significantly more S platelets ($p < 0.0001$) than any of the other materials. Furthermore, it exhibits significantly more FS platelets than PVDF-HFP ($p < 0.05$), though the difference in this morphology with that of PVDF was not statistically different.

When viewing the distribution of morphologies holistically, we observe that

ppC_3F_6 not only adheres vastly more platelets than the other materials, but the majority of these platelets are in the S/FS morphology (**Figure 6.4**). Normalizing the morphology counts by the total number of counted platelets per material type shows this more clearly, where S/FS represents the greatest proportion of morphologies on ppC_3F_6 and D/SD the least.

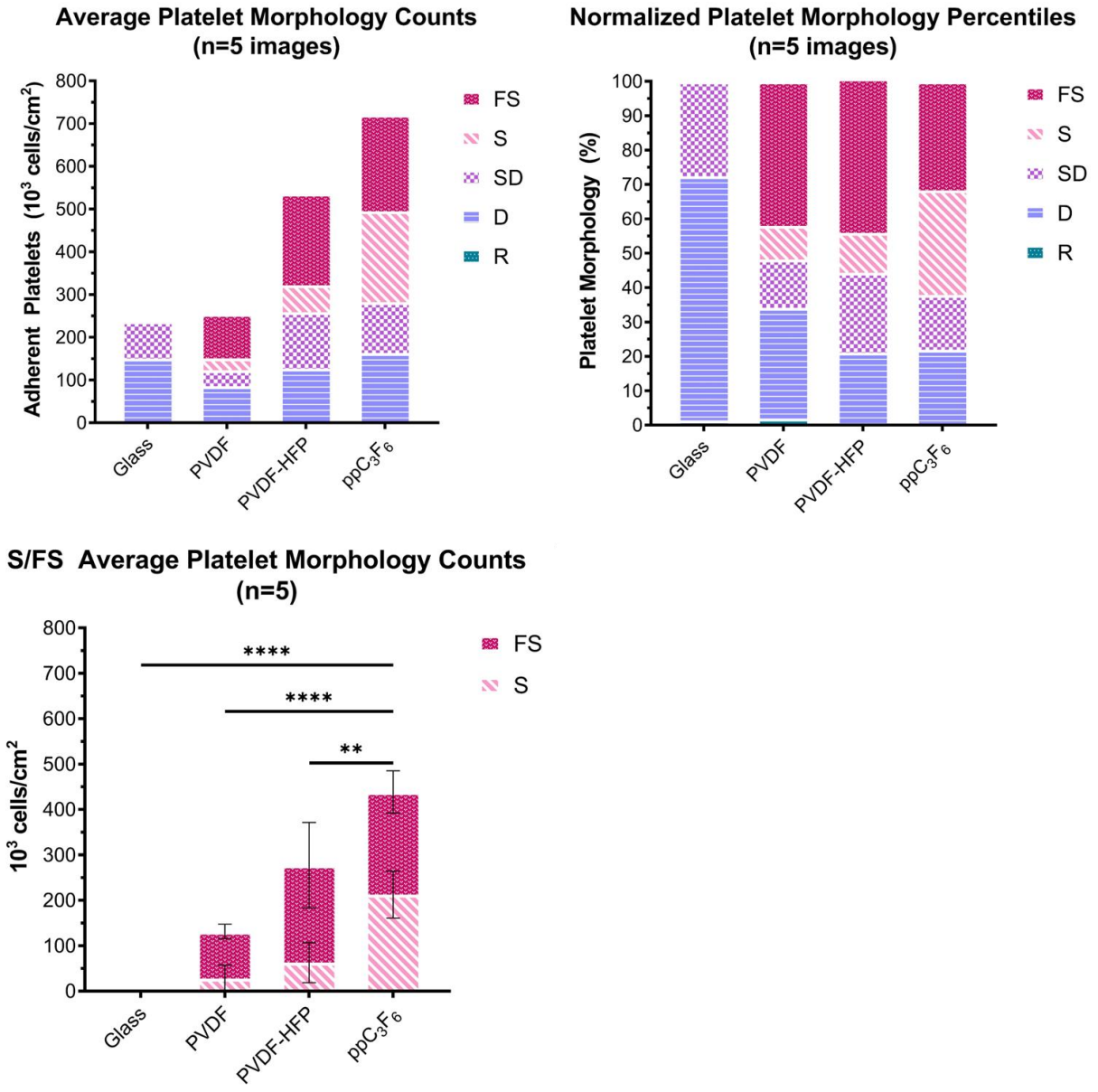

Figure 6.4. Summary plots of total adherent platelets by morphology and their percentiles on PVDF, PVDF-HFP, ppC_3F_6, and uncoated glass. PpC_3F_6 adheres the most platelets overall, and the majority of these platelets exhibit S/FS morphologies.

6.4.3 Release of PF4

Platelet activation was also assessed via α-granule release of the soluble protein marker, platelet factor 4 (PF4), following 2 hour incubation with our test materials. Final PRP concentrations were 0.5% plasma concentration. Fresh 0.5% PRP was also incubated with 20 mU/mL thrombin in the presence of 2 mM Ca^{2+} and 1 mM Mg^{2+} at 37 °C for 30 minutes prior to the assay as the positive control for maximum platelet activation. All samples showed significantly less PF4 release ($p<0.01$, not depicted on plot) than the positive control, though no statistically significant difference was observed among the four material types (glass, PVDF, PVDF-HFP, or ppC_3F_6) (**Figure 6.5**). On average, PVDF appeared to release the most PF4, possibly due to the mixture of FS platelets with large D aggregates. Given the vast quantity of platelets adhered to ppC_3F_6 in the S/FS morphology, the relatively minimal concentration of PF4 release on this material was somewhat surprising. This is perhaps explained by the significant proportion of S platelets, where the α-granules are still localized within the platelet and remain unreleased. This explanation is visually confirmed in the SEM images.

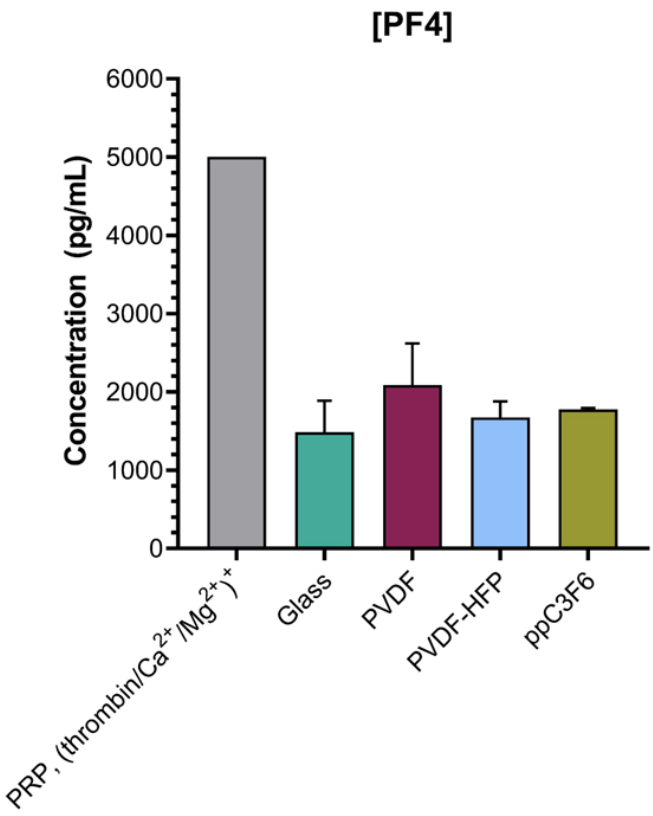

Figure 6.5. PF4 release from platelets adhered on PVDF, PVDF-HFP, ppC_3F_6, and uncoated glass preadsorbed with Fg. All samples showed significantly less PF4 release ($p<0.01$, not depicted on plot) than the positive control, though no statistically significant difference was observed among the four material types.

6.5 Discussion

Despite decades of intensive research, the issue of blood compatibility—or materials-induced activation of blood components (i.e. platelets) to form thrombi and/or emboli—has not yet been resolved. Platelets respond to soluble proteins and agonists including fibrinogen (Fg), von Willebrand factor (vWF), ADP, thrombin, and thromboxane A2 to initiate adhesion and activation. Taking cues from the physiological clotting process of hemostasis, a large percentage of efforts have focused on the development of low-fouling materials that resist nonspecific adsorption of proteins like Fg, which possess known platelet integrin-binding epitopes and are integral to the coagulation cascade. However, a material with

continuous “zero-fouling” capabilities that does not initiate clot formation remains to be identified.

An alternative strategy to achieving long-term blood compatibility seeks what appears to be the opposite of just that—rapid and abundant platelet adhesion and activation in the short term to passivate the surface with a nonthrombogenic monolayer of platelet membranes that remain resistant to further blood activation. This phenomenon has been observed for hydrophobic surfaces in a small body of reports to date [13-15, 19-20]. If supplemented with antiplatelet and anticoagulant pharmacological treatments during the acute phase of platelet activation upon initial exposure to blood, this mechanism could prove a viable strategy for endowing blood-contacting biomaterials with long-term hemocompatibility, where the patient’s own platelets form a protective and inert layer to shield the material surface from further activation.

Here, we observe strong evidence that ppC_3F_6 adsorbs the plasma protein Fg in a densely pro-adhesion structure that enables rapid and abundant platelet adhesion and spreading to enable this approach. Platelets adhered to ppC_3F_6 predominantly exhibited the S/FS morphologies at near-confluent coverage, with minimal additional platelets activated on top of this membrane monolayer. Szott et al. showed that PVDF-HFP preadsorbed with 0.03 mg/mL Fg exhibited a large number of flattened FS platelets; however, we have demonstrated that ppC_3F_6 far exceeds PVDF-HFP in platelet adhesion in the S/FS morphologies. We predict this is due in some part to ppC_3F_6’s highly crosslinked, low surface energy nature compared to other fluoropolymers, which encourages rapid and high surface-affinity binding of early-arrival proteins like the platelet-inert HSA and Fg. When Fg displaces HSA as part of the Vroman effect, we hypothesize that the hydrophobic CF_3-enriched surface of ppC_3F_6 promotes adsorption of the hydrophobic D-domains of Fg to the surface to form packed Fg biomolecules expressing the platelet binding γC dodecapeptide at the free end of the protein. This carpet of platelet-binding epitopes provides a bed of contact adhesion points

such that platelets—which express 50,000-100,000 copies of GPIIb-IIIa, the direct receptor for the Fg γC binding ligand—can rapidly spread across the surface and form strong surface contacts. After only 2 hour of incubation with PRP, the surface was mostly covered with minimal exposure of bare substrate.

The other two fluoropolymers (PVDF and PVDF-HFP) pursued in this project were selected as materials within the same chemical class as ppC_3F_6, yet their performance differed greatly from that of ppC_3F_6. PVDF is a partially fluorinated polymer used broadly in biotechnology and healthcare related applications including protein blotting and separation membranes, while PVDF-HFP is applied on cardiovascular stents such as the commercially available Abbott Vascular Xience V® DES. We observe that platelets incubated on PVDF preadsorbed with 3 mg/mL Fg showed large D aggregates and a subpopulation of FS platelets that appeared highly irregular and subjected to trauma (i.e. torn and folded edges). We note that PVDF's surface roughness, in addition to its surface chemistry, could be a contributing factor to this activated platelet morphology [22]. PVDF-HFP adhered more platelets than PVDF in total, and particularly in the S/FS morphologies. However, full surface coverage was not achieved, leaving surface sites exposed for further platelet binding and prolonged durations of thrombosis and blood activation.

6.6 Summary

In this chapter, we studied the effect of Fg-preadsorbed PVDF, PVDF-HFP, ppC_3F_6, and an uncoated glass control on platelet adhesion and activation under static conditions. Based on past reports of *ex vivo* shunt studies, we have strong reason to believe that rapid platelet adhesion to biomaterial surfaces to form a uniform monolayer of platelet membranes passivates the surface against further blood activation, and may be an effective strategy for long-term hemocompatibility. The total number of adherent platelets on surfaces after 2

hour incubation in platelet-rich plasma (PRP) in increasing order was glass → PVDF → PVDF-HFP → ppC_3F_6. When assessing morphology, the uncoated glass control displayed the highest proportion of activated dendritic (D) & spread dendritic (SD) platelets that formed interconnected networks. PVDF exhibited a rough textured surface with a large proportion of fully spread (FS) platelets that appeared highly irregular, torn, and poorly adhered to the surface, as well as massive formations of D/SD aggregates. Compared to the previous two materials, PVDF-HFP showed a marked progression towards platelets with the S/FS morphology. However, large regions of the surface remained uncovered, which are available surface sites for further platelet binding that only prolong the period of acute thrombosis. Finally, ppC_3F_6 demonstrated near-confluent coverage of the material surface, with platelets predominantly expressing the S/FS morphologies. Based on this data, we purport that ppC_3F_6 may ultimately serve as a candidate for use in long-term blood contacting medical devices by forming a uniform and stable initial passivating platelet membrane layer against chronic thrombosis and embolism.

6.7 Acknowledgments

The authors gratefully acknowledge Sharon Creason in assistance with procuring PRP from Bloodworks Northwest and training on the CPD instrument. Additionally, Irini Sotiri is thanked for their initial development of the static platelet adhesion and fixing protocol.

6.8 References

1. Brass, L. F., Tomaiuolo, M., and Stalker, T. J. Harnessing the platelet signaling network to produce an optimal hemostatic response. *Hematol. Oncol. Clin. North Am.* **27**, 381–409 (2013).
2. Frohlich, E. Action of nanoparticles on platelet activation and plasmatic

coagulation, *Curr. Med. Chem.* **23**, 408–430 (2016).

3. Golebiewska, E. M., and Poole, A. W. Platelet secretion: from haemostasis to wound healing and beyond. *Blood Rev.* **29**, 153–162 (2015).
4. Bennett, J.S. Platelet-fibrinogen interactions. *Ann N Y Acad Sci.* **936**, 340-354 (2001).
5. Springer, T.A., Zhu, J. & Xiao, T. Structural basis for distinctive recognition of fibrinogen γC peptide by the platelet integrin αIIbβ3. *J Cell Biol.* ***182***(4), 791-800 (2008).
6. Sivaraman, B. & Latour, R.A. The relationship between platelet adhesion on surfaces and the structure versus the amount of adsorbed fibrinogen. *Biomaterials*, **31**, 832-839 (2010).
7. Fitch-Tewfik, J. L., and Flaumenhaft, R. Platelet granule exocytosis: a comparison with chromaffin cells. *Front. Endocrinol. (Lausanne)* **4**, 77 (2013).
8. Brandt, E., Petersen, F., Ludwig, A., Ehlert, J. E., Bock, L. & Flad, H. D. The beta-thromboglobulins and platelet factor 4: blood platelet-derived CXC chemokines with divergent roles in early neutrophil regulation. *J. Leukoc. Biol.* **67**, 471–478 (2000).
9. Frenette, P. S., Denis, C. V., Weiss, L., Jurk, K., Subbarao, S., Kehrel, B., et al. P-Selectin glycoprotein ligand 1 (PSGL-1) is expressed on platelets and can mediate platelet-endothelial interactions in vivo. *J. Exp. Med.* **191**, 1413–22 (2000).
10. Sreeramkumar, V., Adrover, J. M., Ballesteros, I., Cuartero, M. I., Rossaint, J., Bilbao, I., et al. Neutrophils scan for activated platelets to initiate inflammation. *Science* **346**, 1234–1238 (2014).
11. Müller, F., Mutch, N. J., Schenk, W. A., Smith, S. A., Esterl, L., Spronk, H. M., et al. Platelet polyphosphates are proinflammatory and procoagulant mediators in vivo. *Cell* **139**, 1143–1156 (2009).
12. Goodman, S.L. Sheep, pig, and human platelet-materiral interactions with model cardiovascular biomaterials. *J Biomed Mater Res.* **45**(3), 240-250 (1999).
13. Dion, I., Baquey, C., Candelon, B. & Monties, J.R. Hemocompatibility of titanium nitride. *Int J Artif Organs.* **15**, 617 (1992).
14. Riederer, M.A., Ginsberg, M.H. & Steiner, B. Blockade of platelet GPIIB-IIIA (integrin alphaII(b)beta(3)) in flowing human blood leads to passivation of prothrombotic surfaces. *Thromb Haemost.* **88**(5), 858-64 (2002).
15. Szott, L.M., Irvin, C.A., Trollsas, M., Hossainy, S. & Ratner, B.D. Blood compatibility assessment of polymers used in drug eluting stent coatings.

Biointerphases, **11**, 029806 (2016).

16. Park, K., Mao, F.W. & Park, H. Morphological characterization of surface-induced platelet activation. *Biomaterials*, **11**, 24-31 (1990).
17. Kottke-Marchant, K., Anderson, J.M. & Rabinovitch, A. The platelet reactivity of vascular graft prostheses: an in vitro model to test the effect of preclotting. *Biomaterials*, **7**, 441-448 (1986).
18. De Mel, A., Chaloupka, K., Malam, Y., Darbyshire, A., Cousins, B. & Seifalian, A. M. A silver nanocomposite biomaterial for blood-contacting implants. *J Biomed Mater Res A*. **100**(9), 2348-2357 (2012).
19. Garfinkle, A.M., Hoffman, A.S., Ratner, B.D., Reynolds, L.O. & Hanson, S.R. Effects of a tetrafluoroethylene glow discharge on patency of small diameter dacron vascular grafts. *Trans Am Soc Artif Intern Organs*. **30,** 432-439 (1984).
20. Haycox, C. & Ratner, B.D. *In vitro* platelet interactions in whole human blood exposed to biomaterial surfaces: insights on blood compatibility. *J Biomed Mater Res*. **27**, 1181-1193 (1993).
21. Van Oeveren, W., Tielliu, I. F. & De Hart, J. Comparison of modified chandler, roller pump, and ball valve circulation models for in vitro testing in high blood flow conditions: application in thrombogenicity testing of different materials for vascular applications. *Int. J. Biomater.* **2012**, 673163 (2012).
22. Milleret, V., Hefti, T., Hall, H., Vogel, V. & Eberli, D. Influence of the fiber diameter and surface roughness of electrospun vascular grafts on blood activation. *Acta Biomaterialia*. **8**, 4349-4356 (2012).
23. Mehta *et al.* Hydrophilic Polymer Emboli: An under-recognized uatrogenic uause of ischemia and infarct. *Modern Pathology* **23**, 921-930 (2010).
24. Tsai, W.B., Grunkemeier, J.M., Horbett, T.A. Human plasma fibrinogen adsorption and platelet adhesion to polystyrene. *J. Biomed. Mater. Res.* **44**, 130-139 (1999).
25. Tsai, W.B., Grunkemeier, J.M., Horbett, T.A. Variations in the ability of adsorbed fibrinogen to mediate platelet adhesion to polystyrene-based materials: a multivariate statistical analysis of antibody binding to the platelet binding sites of fibrinogen. *J Biomed Mater Res. A.* **67**(4), 1255-1268 (2003).
26. Tsai, W.B., Grunkemeier, J.M., McFarland, C.D., Horbett, T.A. Platelet adhesion to PS-based surfaces preadsorbed with plasmas selectively depleted in fibrinogen, fibronectin, vitronectin, or von Willebrand's factor. *J Biomed Mater Res.* **60**(3), 348-359 (2002).

27. Hylton, D.M., Shalaby, W.S., Latour, R.A. Direct correlation between adsorption-induced changes in protein structure and platelet adhesion. *J. Biomed. Mater. Res.* **73A**, 349-358 (2005).

28. Sivaraman, B., Latour, R.A. The adherence of platelets to adsorbed albumin by receptor-mediated recognition of binding sites exposed by adsorption-induced unfolding. *Biomaterials*. **31**, 1036-1044 (2010).

29. Tsai, W.B., Shi, Q., Grunkemeier, J.M., McFarland, C. & Horbett, T.A. Platelet adhesion to radiofrequency glow-discharge-deposited fluorocarbon polymers preadsorbed with selectively depleted plasmas show the primary role of fibrinogen. *J Biomater Sci Polym.* **15**(7), 817-840 (2012).

30. D'Souza, S.E., Ginsberg, M.H., Matsueda, G.R., Plow, E.F. A Discrete Sequence in a Platelet Integrin is Involved in Ligand Recognition. *Nature*. **350**, 66-68 (1991).

31. Shattil, S.J., Hoxie, J.A., Cunningham, M., Brass, L.F. Changes in the Platelet Membrane Glycoprotein IIb.IIIa Complex During Platelet Activation. *J. Biol. Chem.* **260**, 11107 (1985).

32. Savage, B., Ruggeri, Z.M. Selective Recognition of Adhesive Sites in Surface-Bound Fibrinogen by Glycoprotein IIb-IIIa on Nonactivated Platelets. *J. Biol. Chem.* **266**(17), 11227-33 (1991).

33. Weisel, J.W., Nagaswami, C., Vilaire, G., & Bennett, J.S. Examination of the platelet membrane glycoprotein IIb-IIIa complex and its interaction with fibrinogen and other ligands by electron microscopy. *J. Biol. Chem.* **267**, 16637-16643 (1992).

Chapter 7

Summary and concluding remarks

7.1 Summary

The aim of this dissertation was to investigate the adsorption mechanism and structural/orientational properties of the blood coagulation protein, fibrinogen (Fg), on hydrophobic fluoropolymers for the development of thromboresistant hemodialyzer surfaces. We were particularly interested in radiofrequency glow-discharge deposited (plasma-polymerized) fluoropolymers, which were previously shown by our group and collaborators to exhibit remarkably high graft patency, high blood flow rates, and low embolization rates compared to untreated controls in *ex vivo* baboon femoral shunt models. *In vitro* analysis for these materials in select studies showed a flattened monolayer of fully spread platelets long past degranulation, therefore leading to the theory that rapid platelet adhesion and spreading to form a passivating platelet membrane layer may be beneficial for long-term blood contacting applications. We hypothesized that the highly crosslinked and CF_3-enriched films produced via this method adsorbed and retained significantly higher quantities of the non-platelet activating protein, human serum albumin (HSA), through the hydrophobic effect. This in turn vastly reduces the surface adsorption sites for Fg. As a result, among the bulk Fg

ensemble of randomly oriented molecules at the peri-surface environment, Fg molecules oriented in the end-on position are more favored for occupying the smaller and dwindling number of surface sites due to their smaller surface footprint. This interaction is enhanced by the fact that the distal ends of the Fg molecule (D region) are hydrophobic in nature, providing a secure anchoring point. Thus, the final protein adlayer contains a dense forest of end-on oriented Fg molecules that are associated at one hydrophobic D region to the surface, while the opposite D region on the free end containing the γC dodecapeptide is available for platelet binding. This creates a bed of adhesion contacts for platelets to rapidly adhere and spread over, thus providing a possible explanation for the platelet membrane passivation mechanism.

In Chapter 1, we provide motivation for this work through the need for improved long-term blood-contacting biomaterials that resist prolonged platelet activation and reduce the need for risky anticoagulant and antiplatelet therapies. This particular project was fully funded by the Center for Dialysis Innovation (CDI), which seeks to develop a wearable hemodialysis device (AKTIV) for patients with renal failure. A major design requirement for developing this device was the minimal need for anticoagulation, which is a risky treatment that requires careful and continuous monitoring. We then delved into the molecular level interaction of blood proteins on biomaterial surfaces and how they mediate platelet adhesion and activation. Next, we discuss the broad use of fluoropolymers for medical and healthcare-related applications and describe the benefits and drawbacks observed for different materials that have been studied for these use cases. We then propose our platelet membrane passivation strategy, instigated from the observation that plasma-polymerized fluoropolymers perform exceptionally well in non-human primate *ex vivo* shunt models and exhibit a flattened layer of platelet membranes on their surface. To end, the goals and contribution for the present work are provided.

In Chapter 2, all the test materials (PVDF, PVDF-HFP, and ppC_3F_6) are prepared

and characterized. We discuss the preparation methods for each fluoropolymer in detail. We then employ electron spectroscopy for chemical analysis (ESCA) to verify chemical composition, atomic force microscopy (AFM) for surface roughness, profilometry for coating thickness, and water contact angle (WCA) measurements for surface energy. We confirmed that the ppC_3F_6 coating is a CF_3-enriched surface with a high degree of crosslinking within the film, and is purported to account for much of the material's unique properties as observed in past *in vitro* and *ex vivo* studies. It was also highly smooth, thick (though thickness is easily adjustable via change in deposition time), and possessed a significantly lower surface free energy compared to the other polymers. PVDF and PVDF-HFP also exhibited the expected chemical compositions, and were significantly thinner than the ppC_3F_6 coating from the spincoating process. PVDF also demonstrated a rougher texture than the other two materials owing to its semi-crystallinity.

In Chapter 3, we employ quartz crystal microbalance with dissipation (QCM-D) to monitor competitive HSA:Fg adsorption on PVDF, PVDF-HFP, and ppC_3F_6. We showed that ppC_3F_6 demonstrates the highest and lowest surface affinities for HSA and Fg, respectively, with the overall greatest preference for HSA:Fg adsorption. We have also verified some basic principles regarding competitive protein adsorption on hydrophobic fluoropolymers using various protein buffer conditions to compare the effects of binary competitive adsorption and sequential non-competitive adsorption against HSA or Fg single protein solutions. The hypothesis that HSA unpacks and spreads upon prolonged surface exposure—particularly to ppC_3F_6—to yield greater resistance to Fg displacement was confirmed. Finally, the unique fluorochemistries and highly hydrophobic properties created by the plasma polymerization process for ppC_3F_6 are suspected to entropically drive rapid adsorption of HSA and free the energetically unfavorable association of surface-adjacent water molecules back into the bulk continuum. This causes a conformational change in the HSA to strongly associate hydrophobic residues with the surface while reorienting hydrophilic residues to

the bulk aqueous phase, thereby creating a partially coupled interfacial water network above the adsorbed protein layer that delays Fg adsorption.

In Chapter 4, bioactivity of Fg was explored using a series of immunoassays employing structurally sensitive monoclonal antibody probes to investigate how proteins activate and deactivate depending on adsorption-induced structural changes. These surface-denatured Fg were compared to thermally denatured Fg to determine if loss in bioactive sites was similar across denaturation mechanisms. In addition, we employed atomic force microscopy (AFM), quartz crystal microbalance with dissipation (QCM-D), and electron spectroscopy for chemical analysis (ESCA) to determine Fg surface orientation and adsorbate layer thickness. We first demonstrated the importance of bulk protein solution concentration in determining the adsorption orientation of elongated proteins, where below a threshold concentration, molecules adsorb in a side-on orientation and are susceptible to further surface-induced spreading and unfolding; however, above this threshold when molecular diffusion to the surface is no longer limited, fewer molecules are able to adsorb in the side-on orientation due to competitive occupation of surface sites by adjacent molecules. Thus, we observe a loss in monoclonal antibody binding with further increasing bulk protein solution concentration all the way to physiological levels. Conversely, bulk protein solution concentration does not appear to affect the antibody binding recognition of small globular proteins like HSA, confirming the importance of surface orientation and packing for high aspect ratio proteins in providing access to binding epitopes. Then, through a combination of immunoassays targeting the α-chain (FGA) and γ-chain (FGG) of Fg, we determined that ppC_3F_6 encourages rapid Fg adsorption in a configuration that limits FGA binding—in agreement with the end-on adsorbed interpretation where the FGA binding epitope is packed into the center of the adlayer 'forest'—and increases FGG binding at intermediate bulk solution concentrations before decreasing again due to the binding-inhibitory effects of surface crowding. Thermally denaturing Fg prior to adsorption on the

fluoropolymers increased FGA/FGG mAb for all materials, indicating that loss in structural integrity of Fg eliminates orientational preference of the protein and increases mAb binding accessibility, and by extension, platelet binding accessibility. The high-packing ability of end-on adsorbed Fg was also demonstrated through adsorbed-state circular dichroism (CD) to assist in preserving the protein's native structure by preventing surface spreading and unfolding. While it is true that the native Fg protein is non-platelet activating, we believe that the dense surface packing of Fg on ppC_3F_6 creates a carpet of end-on adsorbed Fg molecules that encourage rapid uniform platelet adhesion and spreading to form a passivating surface layer of platelet membranes after the initial phase of activation is past.

In Chapter 5, we identified three pathogenic variants of the platelet-binding γC-domain of fibrinogen obtained from clinical cases presenting with thrombotic (R275H), hemorrhagic (M310T), and combined (G292V) phenotypes. By performing molecular dynamics (MD) simulations on each of the mutants along with the wild-type structure, we sought to highlight structural differences and elucidate the molecular underpinnings that cause the different blood disorders to arise. To this end, conformations unique to thrombotic phenotypes may shape design criteria for blood compatible materials. Our results demonstrated that three critical loop regions (γ214-229, γ292-298, and γ357-362) are highly sensitive to perturbations in surrounding water organization or steric clashes that affected ensemble structural flexibility or ligand binding. Decreasing mobility in these loop regions was associated with increasingly thrombotic genotype/phenotypes. Ultimately, we purported that surfaces that adsorb fibrinogen in a conformation that preserves the flexibility of these loop regions will yield reduced thrombogenicity.

In Chapter 6, we determine the ultimate effect of fluoropolymer surface chemistry and resultant Fg surface structure on blood component interactions. Fresh platelet-rich plasma (PRP) was exposed to Fg-preadsorbed PVDF, PVDF-HFP,

and ppC_3F_6 under static *in vitro* conditions to assess platelet adhesion and activation. Adhered platelets were imaged via SEM, counted, and characterized by morphology based on activation state. The total number of adherent platelets on surfaces after 2 hour incubation in platelet-rich plasma (PRP) in increasing order was glass → PVDF → PVDF-HFP → ppC_3F_6. When assessing morphology, the uncoated glass control displayed the highest proportion of activated dendritic (D) & spread dendritic (SD) platelets that formed interconnected networks. PVDF exhibited a rough textured surface with a large proportion of fully spread (FS) platelets that appeared highly irregular, torn, and poorly adhered to the surface, as well as massive formations of D/SD aggregates. Compared to the previous two materials, PVDF-HFP showed a marked progression towards platelets with the S/FS morphology. However, large regions of the surface remained uncovered, which are available surface sites for further platelet binding that only prolong the period of acute thrombosis. Finally, ppC_3F_6 demonstrated near-confluent coverage of the material surface, with platelets predominantly expressing the S/FS morphologies. Based on past reports of *ex vivo* shunt studies, we have strong reason to believe that rapid platelet adhesion to biomaterial surfaces to form a uniform monolayer of platelet membranes passivates the surface against further blood activation and may be an effective strategy for long-term hemocompatibility.

7.2 Future work

For Ch 3. Selective Plasma Protein Adsorption.

Employing multiple analytical techniques enables us to draw better-informed conclusions on surface-level molecular events. The QCM-D provides excellent information on time-resolved adsorption kinetics and adlayer properties, but does not elucidate the final protein layer composition (HSA:Fg). These will be quantitively investigated with existing ^{125}I-radiolabeling methods used within our

lab to assess Fg adsorption and degree of HSA retention. Surface plasmon resonance (SPR) will also be employed as an optical technique for total protein adsorption that will provide a clearer value of the protein 'dry mass' compared to QCM-D, as the method does not accommodate coupled water layers. Finally, for a better understanding of water structure over each HSA/Fg adsorbed FP, injecting solutions containing the Hofmeister ion series combined with QCM-D will serve to perturb the overlying bulk water network, enabling us to measure changes in adlayer viscosity that can provide insights into the FP's ability to organize water. The Hofmeister ion series is a well-established effect observed when the addition of ions organizes (kosmotropic) or breaks (chaotropic) the 3D water structure. The order of the anion series from kosmotropic to chaotropic is CO_3^{2-} > SO_4^{2-}> $S_2O_3^{2-}$ > $H_2PO_4^-$ > F^-> Cl^-> Br^- ~ NO_3^- > I^-> ClO_4^- > SCN^-, but a smaller grouping will be selected for sequential injection into the QCM-D to observe the change in viscoelastic mass attributed to water coupling.

For Ch 4. Fg Surface Structure

Fg Surface Orientation (AFM). AFM imaging of Fg surface orientation adsorbed on FPs is an ongoing project. PVDF and PVDF-HFP remain to be imaged in air before progressing to imaging in fluid mode for all FPs. We hope to capture images in fluid at varying timepoints post-adsorption to visualize Fg unfolding and relaxation over a longer duration of time. This will provide us with a better understanding of the denaturing effects of different FP surface chemistries on Fg that enhance or inhibit its platelet binding capabilities.

Fg Surface Structure Using Adsorbed-State Circular Dichroism (CD). Circular dichroism is a method usually restricted to analyzing protein secondary structure in soluble forms. However, Dr. Robert Latour and colleagues at Clemson University have developed a method for assessing protein secondary structure in an adsorbed state (Thyparambil, Wei & Latour, 2015). In summary, six fused-quartz slides are modified with the desired coating and loaded into a standard cuvette separated by vinyl spacers, between which the desired protein

for adsorption-induced conformational studies is injected. By stacking multiple slides, a strong enough signal from the protein can be detected while accommodating background absorbance from the slides themselves. While we have initiated studies with this group to analyze physiological concentrations (3 mg/mL) of Fg adsorbed on ppC_3F_6, we have not yet tested this method on other fluoropolymers (e.g. PVDF and PVDF-HFP) to verify that the end-on adsorption effect ppC_3F_6 has on Fg is due to its unique surface chemistry among other materials in its class. We would also like to verify that at lower (sub-physiological and submonolayer) surface concentrations, the reduction in surface density permits protein unfolding and changes in accessibility of its bioactive sites.

Covalent Labeling Mass Spectrometry (CL/MS) of Adsorbed State Fg. Covalent labeling (CL) of protein side chains combined with standard proteomic methods (e.g. MS) can provide information on a protein's surface structure and enable rapid identification of modified sites (Limpikirati, Liu, Vachet, 2018). Compared to amino acid specific labeling reagents, CL-MS is a nonspecific technique capable of modifying a greater variety of residue side chains in one experiment and therefore providing a more global view of the protein's surface topography. A common CL reagent is diazirine derivatives, which serve as carbene precursors. Carbenes are highly reactive species that can insert into any X-H bond (X=C, O, N, S) and therefore hypothetically label any accessible protein residue, and the labeling process is irreversible (no back exchange as seen in HDX), rapid (nanonsecond time scale, which is more rapid than protein unfolding), independent of concentration, and does not require quenching agents. Manzi et al. reported a custom, high-efficiency aryl diazirine developed for carbene footprinting of proteins that is presently commercially available (Manzi et al. 2016). Thus, CL-MS will be pursued as another characterization method of Fg adsorbed to ppC_3F_6 to coarsely investigate its solvent-accessible surface area.

For Ch 6. Platelet Adhesion & Activation

The platelet adhesion and activation studies on FPs will be expanded to include

substrates pre-adsorbed with both thermally and chemically denatured Fg (in addition to nondenatured Fg) to provide a benchmark comparison for the effects of surface-induced denaturation on platelet binding. Additionally, for a more holistic understanding of platelet activation to supplement the platelet morphology assessments, we hope to expand the analysis of platelet activation markers to include PAC-1, a murine monoclonal antibody that binds only to an epitope on the GPIIbIIIa complex of activated platelets near the platelet-Fg receptor. This will serve to capture any suspended activated platelets in the spent PRP that experienced a nonadhesive encounter with the surface that initiated activation. Ultimately, This will provide an indicator for surfaces that are activating but produce weakly adhesive interactions that are susceptible to platelet shedding and embolus formation. Finally, *ex vivo* shunt models are clearly lacking for this study, and are the best metric for determining long-term effects of blood exposure on ppC_3F_6 under shear flow conditions. Including animal studies with continuous blood exposure to ppC_3F_6—combined with repeated imaging of the surface to monitor adhesive platelet formation, morphology, and surface coverage—will ultimately allow us to assess the validity of the platelet passivation hypothesis.

7.3 Concluding remarks on blood compatibility

Achieving true hemocompatibility of biomaterials is a challenge that has confounded the biomedical research community for decades, but is of critical importance to ensuring long-term safety and efficacy of blood-contacting medical devices. Based on the body of research produced to date on this topic, and through our own experimental efforts and data analysis, we would like to offer a few final thoughts on blood compatibility and its directions for the future:

1. It is likely impossible to fully prevent protein adsorption on any synthetic material (i.e. 100% nonfouling coating), and even low-fouling surfaces

induce platelet reactivity under whole blood conditions over time.

2. Slow adhesion and accumulation of platelets on surfaces delays formation of a smooth and stable thrombus layer. This leads to a negative feedback loop of thrombus detachment (and high risk for embolism), continued exposure of artificial surfaces to circulating blood components, platelet activation and initiation of the coagulation and inflammation cascades (intrinsic, complement, leukocyte, etc.), and repeat.
3. Adsorbed Fg is the primary mediator of platelet activation on biomaterial surfaces, and its surface orientation (and therefore bioactivity) is strongly dependent on the surface concentration attained, which ultimately influences platelet adhesion outcomes.
4. Platelet adhesion and blood incompatibility should not be conflated. Platelet membranes themselves are nonreactive, and if formed properly with tight adhesion to the underlying substrate, can serve as a passivating layer against further blood activation.
5. *In vitro* tests are necessary but overly simplistic, and are often incomparable with *ex vivo* or *in vivo models*. Furthermore, single protein solutions, and even blood fractions (PRP, serum, etc.), are not representative of whole blood outcomes.
6. Due to the differences in coagulation initiation across different blood shear regimes, different biomaterials may be needed to meet the flow requirements of complex blood-contacting devices with intricate geometries like hemodialysis circuits. Therefore, exceptionally low-fouling materials like certain hydrophilic or zwitterionic coatings may perform better in regions of low hemodynamic shear to combat the contact protein fouling triggers of the intrinsic pathway, while hydrophobic materials may perform better in regions of high hemodynamic shear to moderate platelet aggregation through control of Fg and vWF adsorption.

Chapter 8

Appendix

8.1 QCM-D kinetic derivation of the Langmuir adsorption concentration isotherm

The Langmuir adsorption model predicts adsorbate kinetics through the assumption of the following:

1. Adsorbate binding is fully reversible.
2. Adsorbent has a finite number of discrete binding sites (no multilayers).
3. All binding sites on adsorbent are equivalent.

$$A + S \underset{k_{off}}{\overset{k_{on}}{\rightleftharpoons}} AS$$

Association Constant $K_A = \frac{[AS]}{[A][S]} = \frac{k_{on}}{k_{off}}$

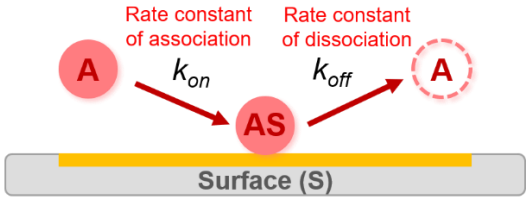

The response R can be any measured parameter; for QCM-D this can be Δf, ΔD, areal mass, thickness, etc. Kinetic derivation of the Langmuir adsorption concentration isotherm is as follows:

Rate of change of free binding sites

$$\frac{dR}{dt} = k_{on}C(R_{max} - R_t) - k_{off}R_t \quad \text{EQN 1}$$

Rate of adsorption — Rate of desorption

- Boundary Conditions:
  1. $R_{t=0} = 0$
  2. $R_{t\to\infty} = R_{eq} = R_{max}\frac{K_A C}{K_A C + 1}$ EQN 2

Set $\frac{dR}{dt} = 0$ and solve for R_t (R_{eq})

- Integrate and solve for the rate equation:

$$R(t) = R_{eq}(1 - e^{-(k_{on}C + k_{off})t}) \quad \text{EQN 3}$$

- During the dissociation phase, $k_{on}C = 0$:

$$R(t) = R_{eq}e^{-k_{off}t}$$

Determine K_A and R_{max}:

Linearization of the Adsorption Rate Equation

$$\frac{C}{R_{eq}} = \frac{1}{R_{max}}C + \frac{1}{K_A R_{max}}$$

y = m x + b

Plot $\frac{C}{R_{eq}}$ vs. C → least squares fit to obtain R_{max} (slope) and K_A (intercept)

8.2 QCM-D Raw Data (Δf, ΔD vs. time)

Raw Δf and ΔD QCM-D plots are shown here for all results presented in Chapter 3. Frequency (Δf) are in hertz (Hz) while dissipation (ΔD, 1E-6) is unitless. Figure legends depict frequency and dissipation at each harmonic overtone (n=3, 5, 7, 9, 11, 13). The higher harmonic overtones (e.g. n=13) are sometimes excluded from Voigt viscoelastic modeling due to their high surface sensitivity and therefore high degree of noise.

3.4.1. Sauerbrey vs. Voigt modeling for HSA and Fg monolayers:

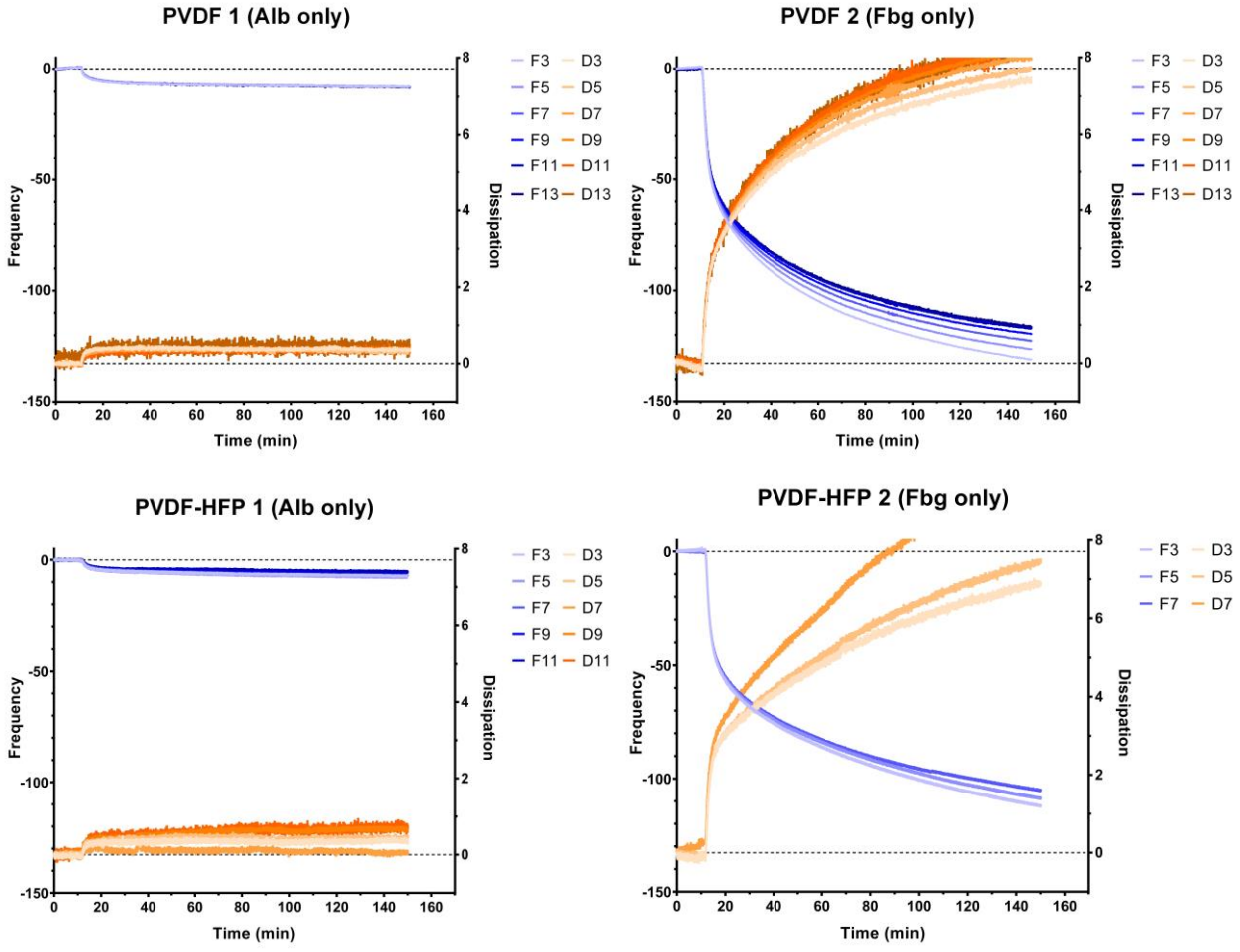

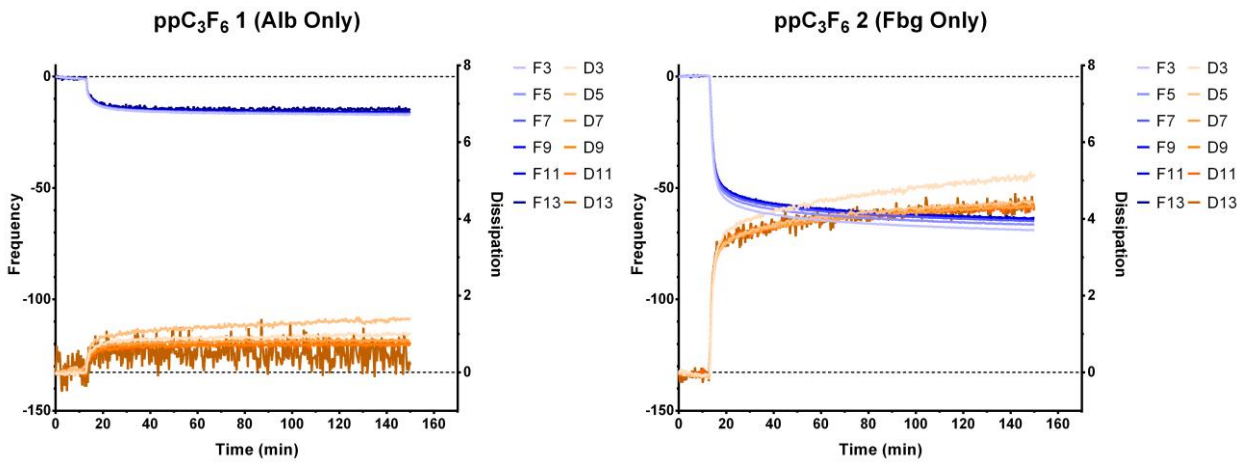

3.4.2. HSA/Fg concentration isotherms and kinetic analysis

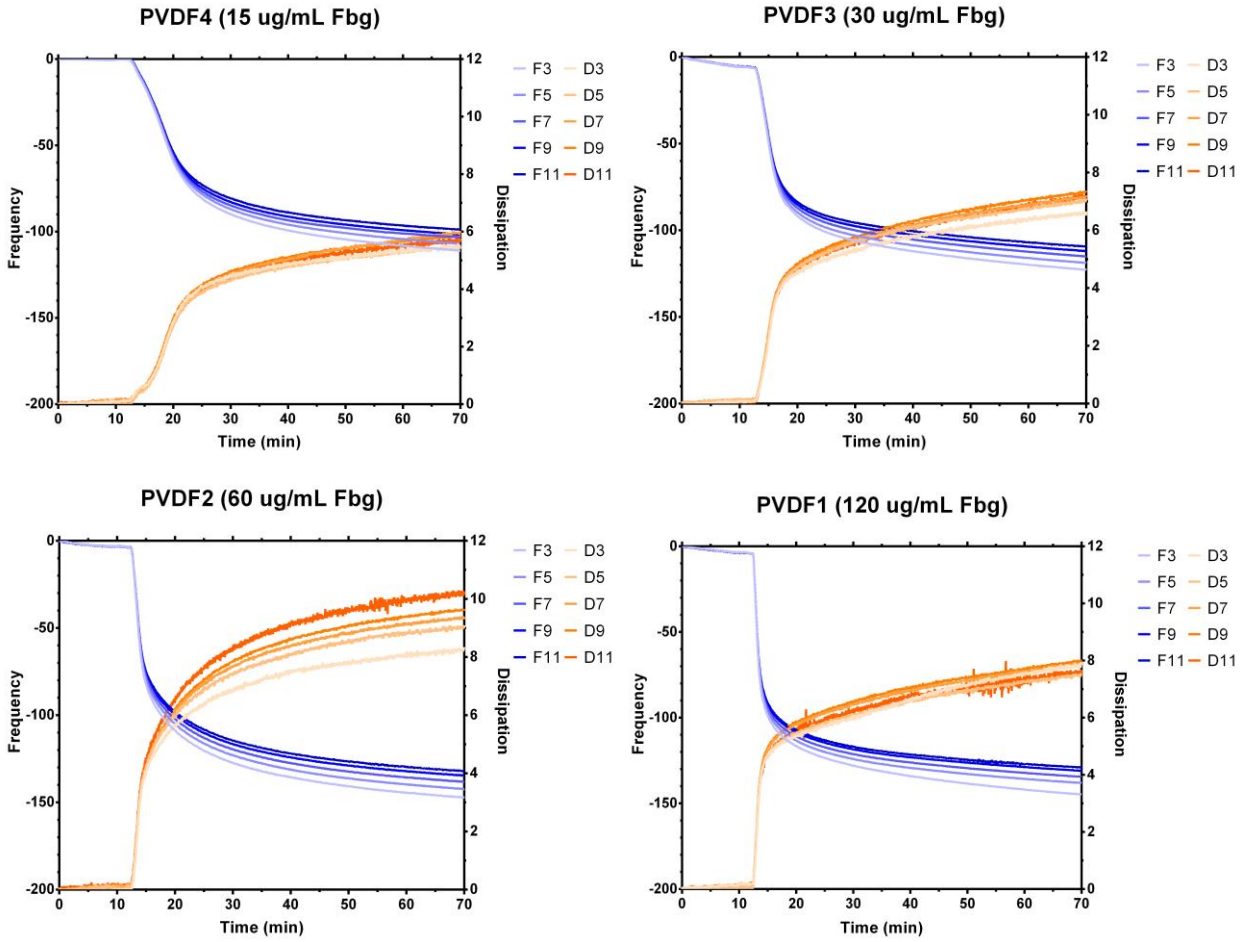

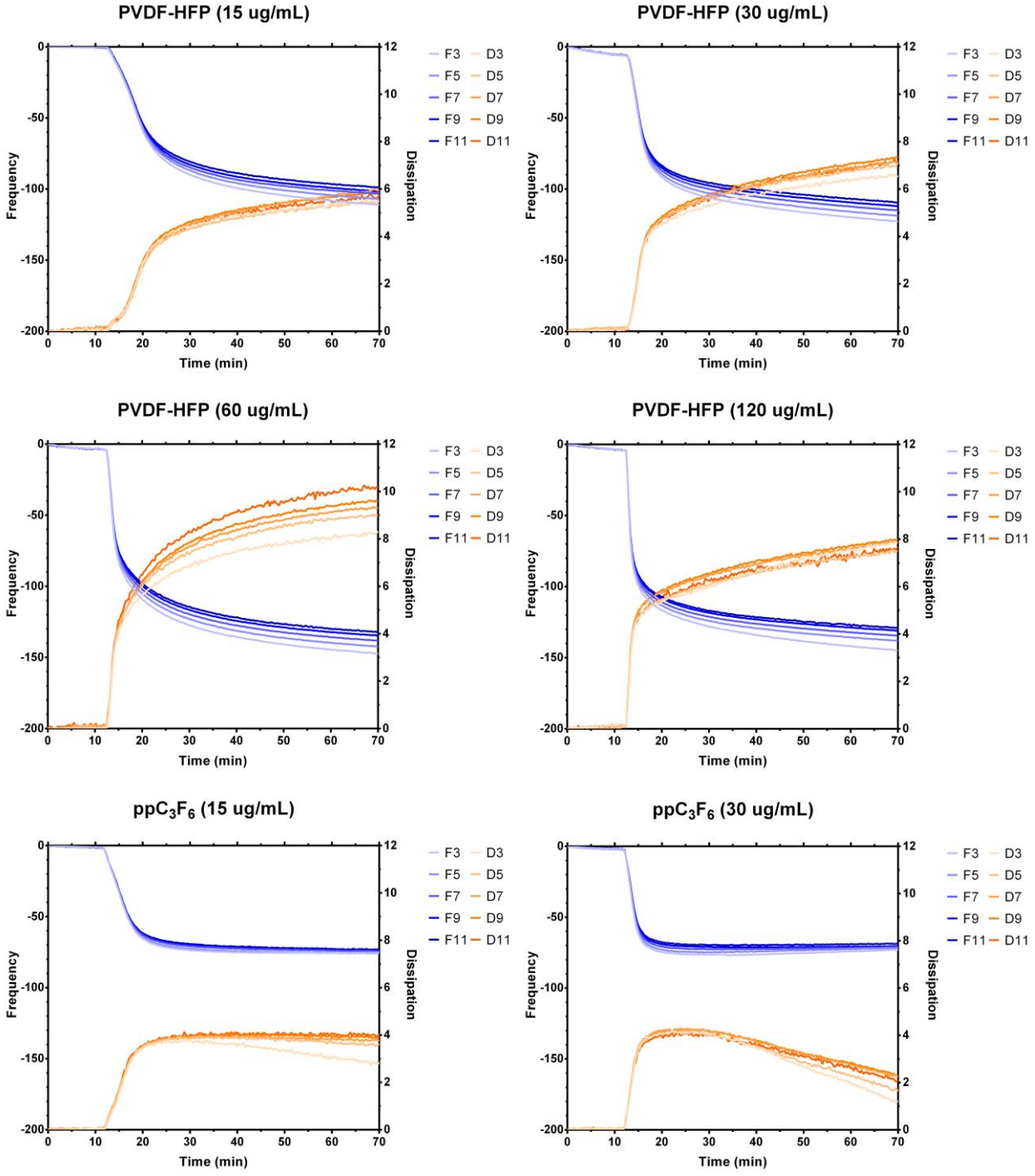
PVDF-HFP (15 ug/mL)
PVDF-HFP (30 ug/mL)
PVDF-HFP (60 ug/mL)
PVDF-HFP (120 ug/mL)
ppC3F6 (15 ug/mL)
ppC3F6 (30 ug/mL)
Frequency
Dissipation
Time (min)
F3 D3
F5 D5
F7 D7
F9 D9
F11 D11

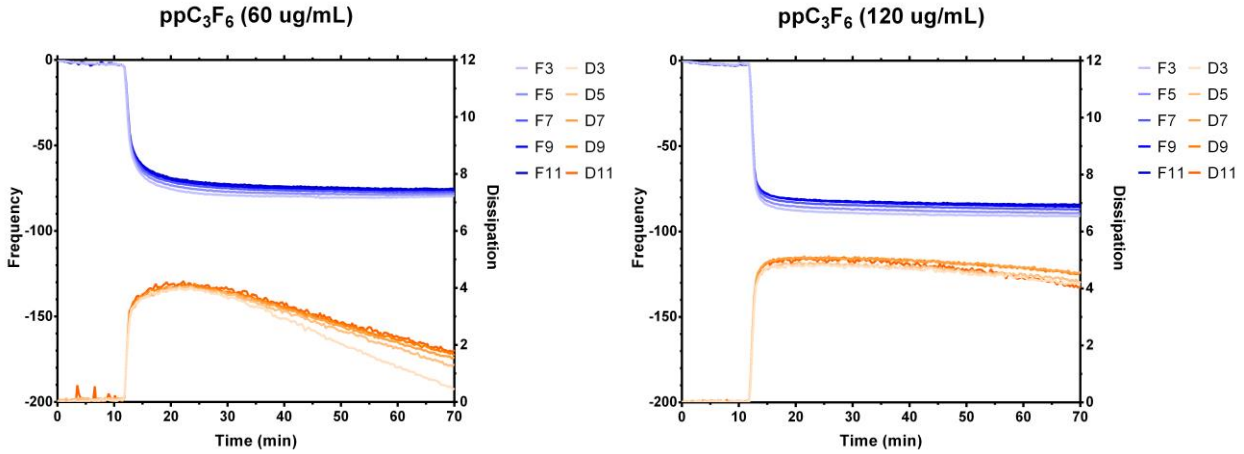

3.4.3. HSA vs. Fg total adsorption from single-protein solutions

Same as 3.4.1, but modeled using Sauerbrey for HSA and Voigt for Fg only.

3.4.4. Protein sequence: exploring the Vroman Effect

(Left) HSA → Fg; (Right) Fg → HSA (reverse Vroman Effect)

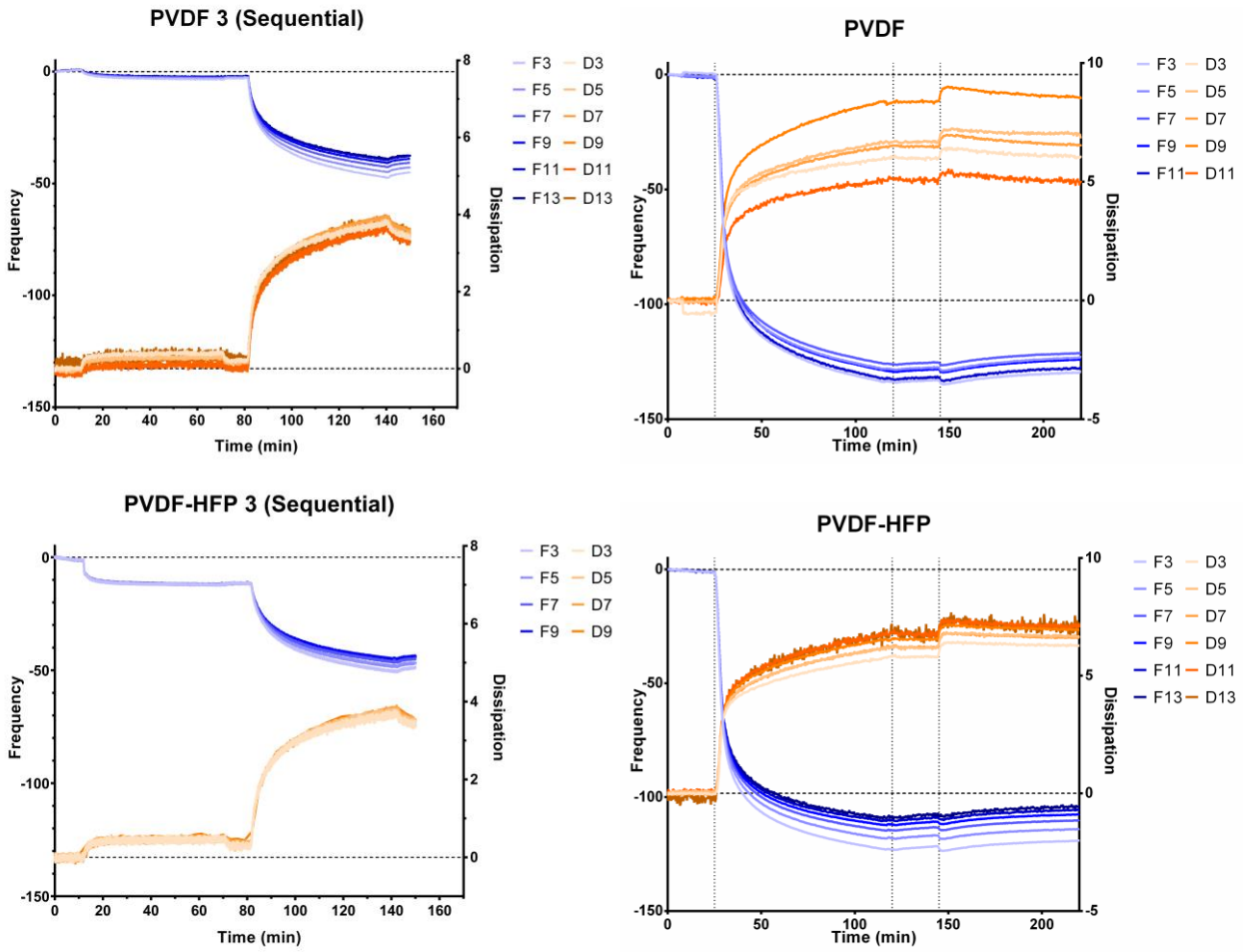

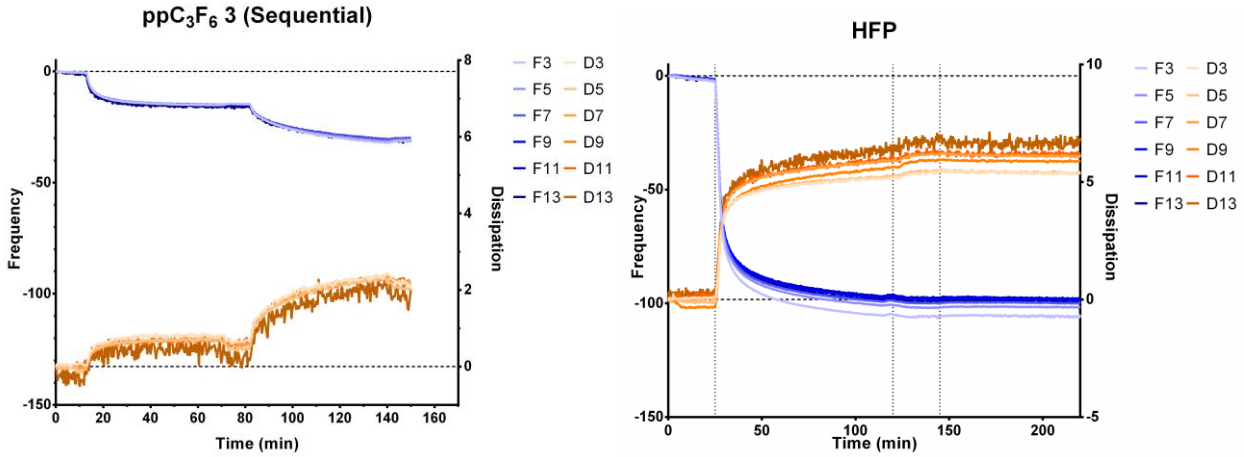

3.4.5. HSA and Fg protein solution variations

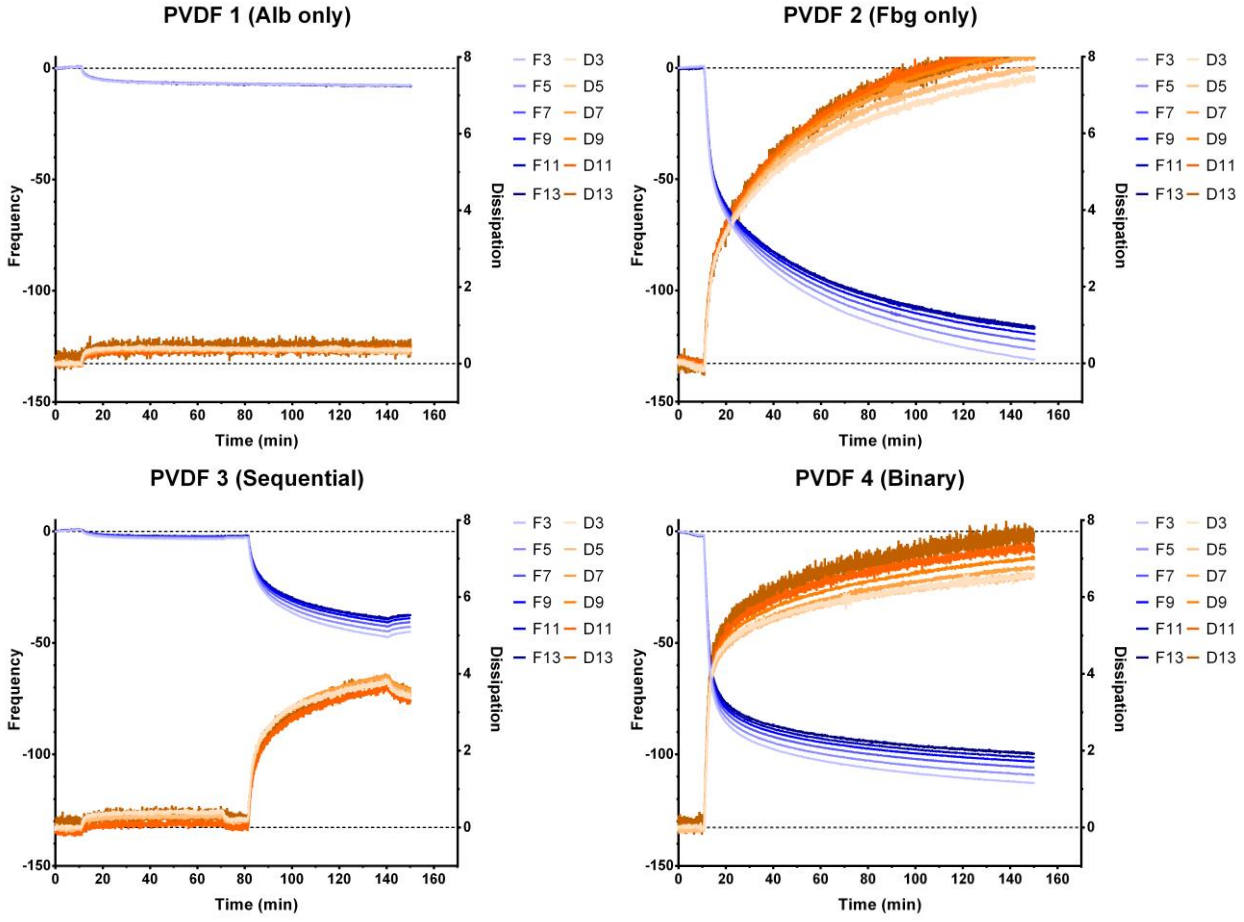

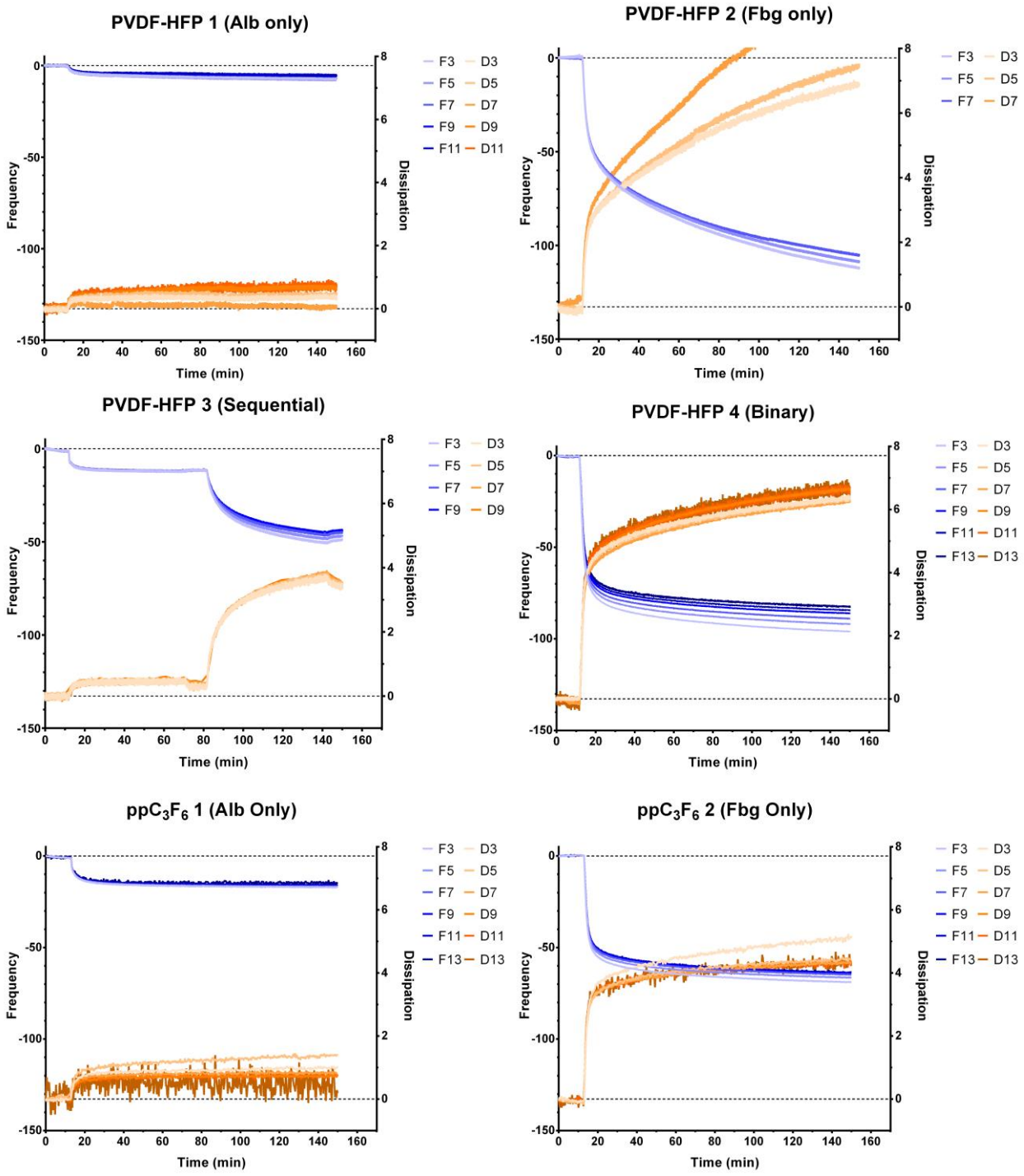
PVDF-HFP 1 (Alb only)
PVDF-HFP 2 (Fbg only)
PVDF-HFP 3 (Sequential)
PVDF-HFP 4 (Binary)
ppC3F6 1 (Alb Only)
ppC3F6 2 (Fbg Only)
Frequency
Dissipation
Time (min)
F3 D3
F5 D5
F7 D7
F9 D9
F11 D11
F13 D13

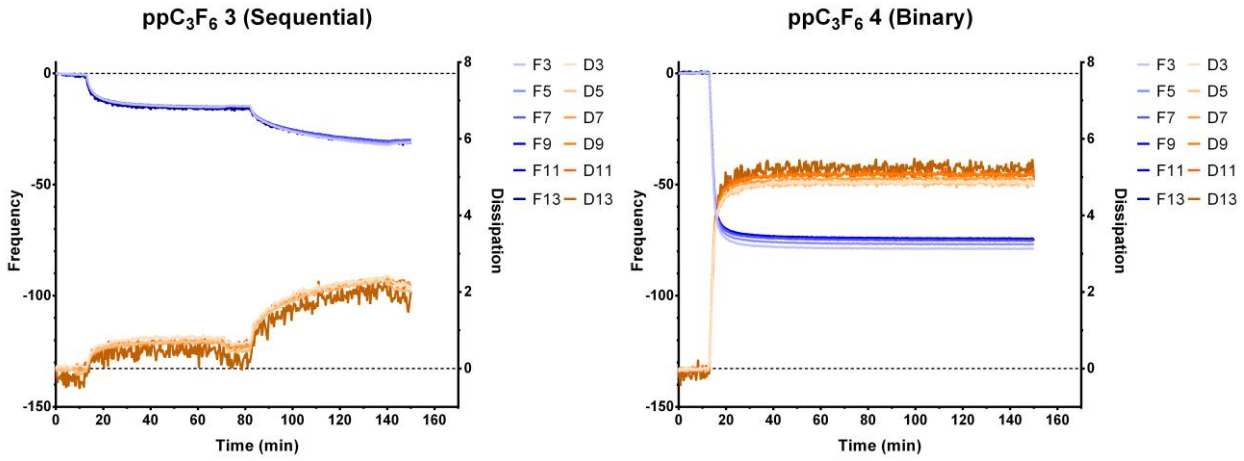

3.4.6. HSA residence time on sequential Fg adsorption

The Sauerbrey relation was used to convert frequency (n=5) to mass of HSA on ppC_3F_6 (both n=3 and n=5 are depicted).

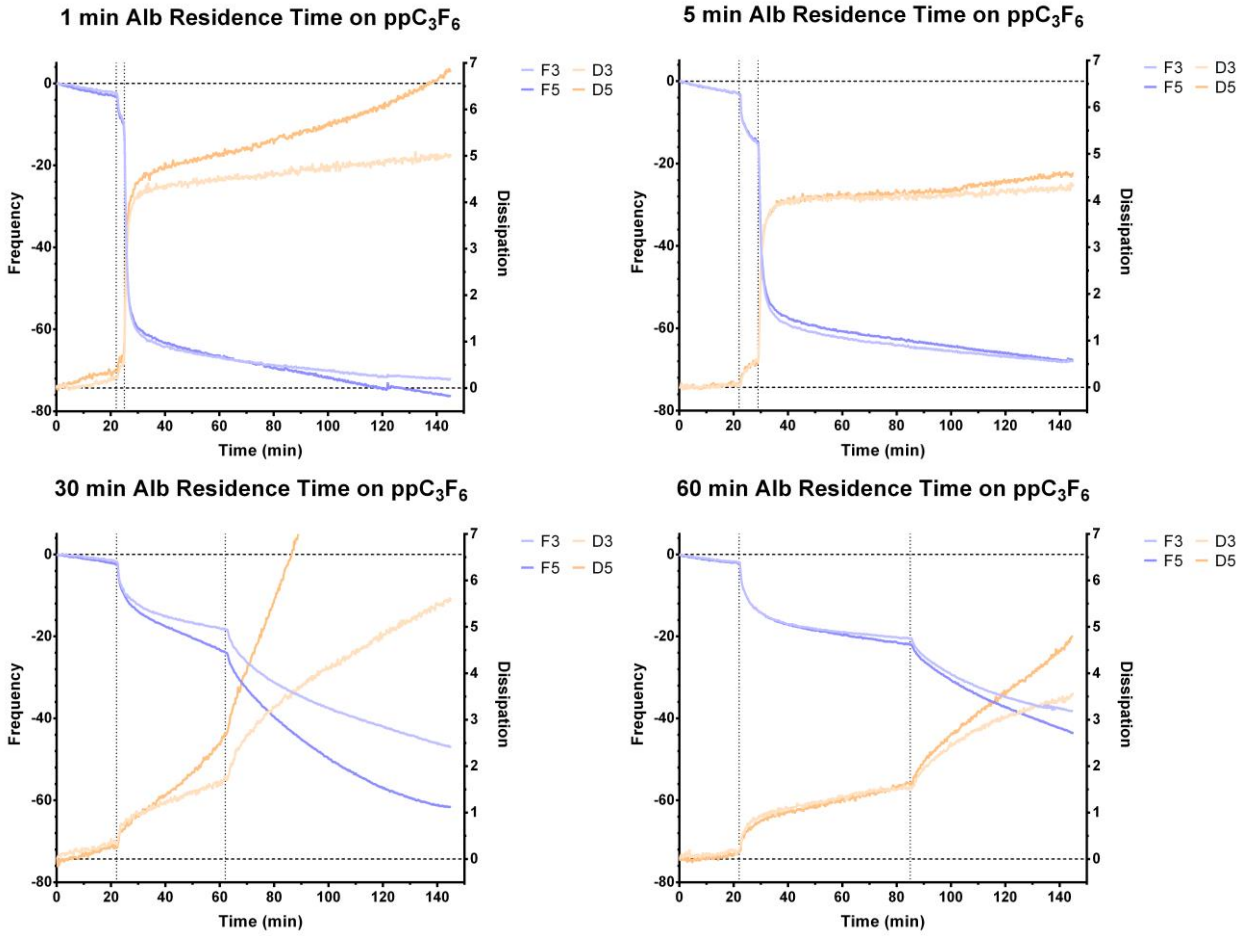

3.4.7. D vs. F plots

D vs. F plots were obtained from the raw data from Chapter 3.4.5. (protein solution variations).

8.3 Adjustments to ppC3F6 deposition for adsorbed-state CD measurements

The standard process for depositing ppC_3F_6 films was found to absorb the CD beam too strongly in the 190-300 nm range and was therefore incompatible with this analysis method. The following modifications were made to the coating and were deemed successful in maintaining the surface composition of the original ppC_3F_6 films (as determined via ESCA) while also passing delamination testing and falling below the CD high tension voltage (HTV) limit of 500 V. The authors' collaborators, Latour and coworkers, were thus able to take CD measurements of Fg adsorbed on the modified ppC_3F_6 to characterize adsorbed-state secondary structure.

In summary:

- The underlying CH_4 adhesion layer was omitted;
- The total deposition time for ppC_3F_6 was reduced from the standard 20 minutes down to 5 minutes. This was determined to be the shortest duration acceptable for maintaining the original surface chemistry while still adhering to the quartz slide (sans CH_4 adhesion layer) after a 24-hour delamination test in 10 mM phosphate buffer;
- To compensate for omitting the CH_4 adhesion layer, the Ar etching time of the substrate prior to deposition was doubled from 5 to 10 minutes to improve surface activation.

Angle-dependent ESCA analysis demonstrated that the 5-minute deposition was at least 10 nm thick (no Si peaks from the quartz detected, pre- or post-delamination test) (Fig. 1 & 2). Preliminary absorbance testing was also performed using a Jasco J-720 CD instrument (Jasco, Inc., Easton, MD), from which we determined that the high tension voltage was below the 500 V threshold for the CH_4-free slides (1 coated slide tested per condition) (Fig. 3 & 4). Based on

these results, the high absorbance was attributed to the CH_4 adhesion layer.

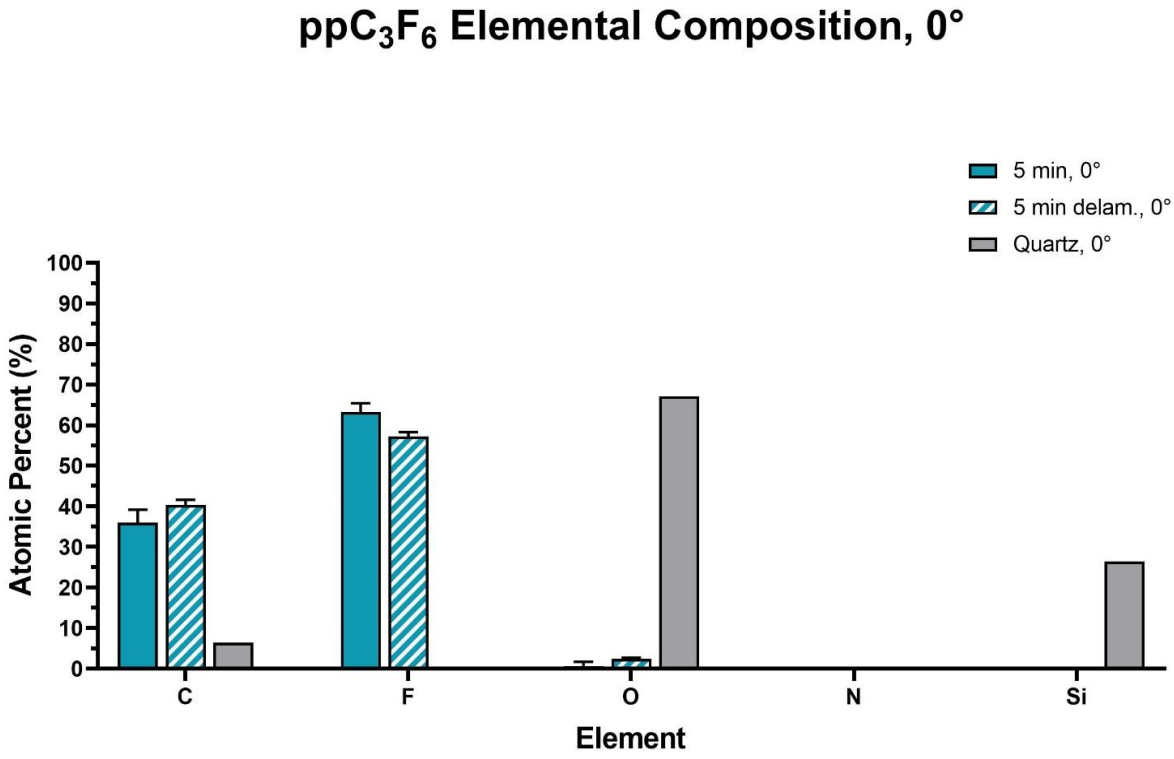

	C	F	O	N	Si
ppC_3F_6, 5 min	36.0	63.3	0.7	-	-
ppC_3F_6, 5 min, delam. test	40.3	57.2	2.5	-	-
Quartz	10.9	-	63.2	-	25.9

*All values were derived from angle-dependent ESCA/XPS analysis (0°; ~10 nm sampling depth) and averaged across 3 spots.

Figure 8.3.1. Elemental composition of the 5-minute ppC_3F_6 layer (sans CH_4 adhesion layer) from the 0° angle-dependent XPS survey scan. No Si was detected pre- or post-delamination test, indicating the film is at least 10 nm thick.

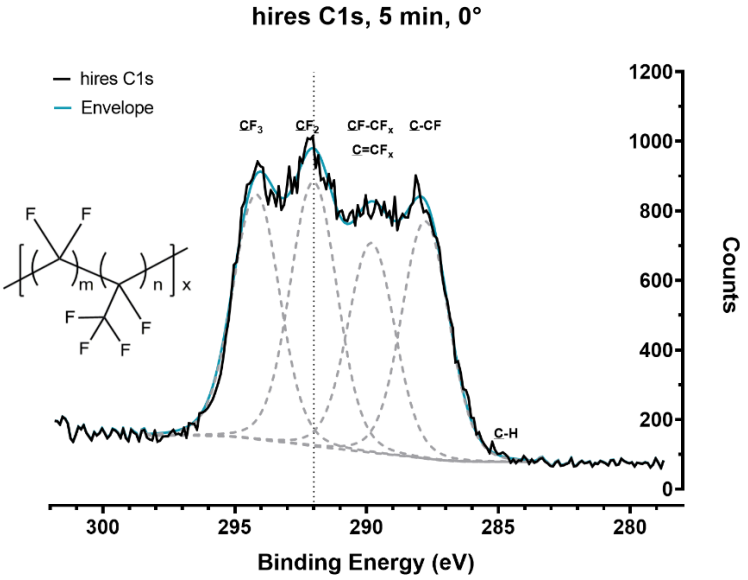

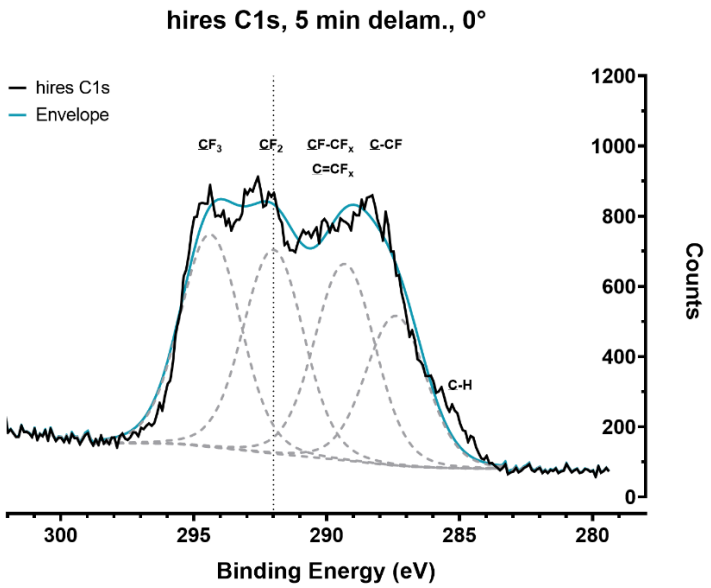

	CF3	CF2	CF-CFx, C=CFx	C-CF
ppC3F6, 5 min	27.7%	24.8%	25.6%	21.9%
ppC3F6, 5 min, delam. test	26.7%	19.6%	27.9%	25.8%

*All values were derived from angle-dependent ESCA/XPS analysis (0°; ~10 nm sampling depth) and CasaXPS peak fitting software. Spectral binding energies are referenced to the CF_2 peak assigned to 292.0 eV.

Figure 8.3.2. High resolution C1s XPS scan of the 5-minute ppC_3F_6 layer (sans CH_4 adhesion layer) pre- and post-delamination test (top and bottom, respectively). There is minimal difference between the two spectra, indicating that the film is durable enough to retain the critical surface chemistries for at least 24 hours in 10 mM PB.

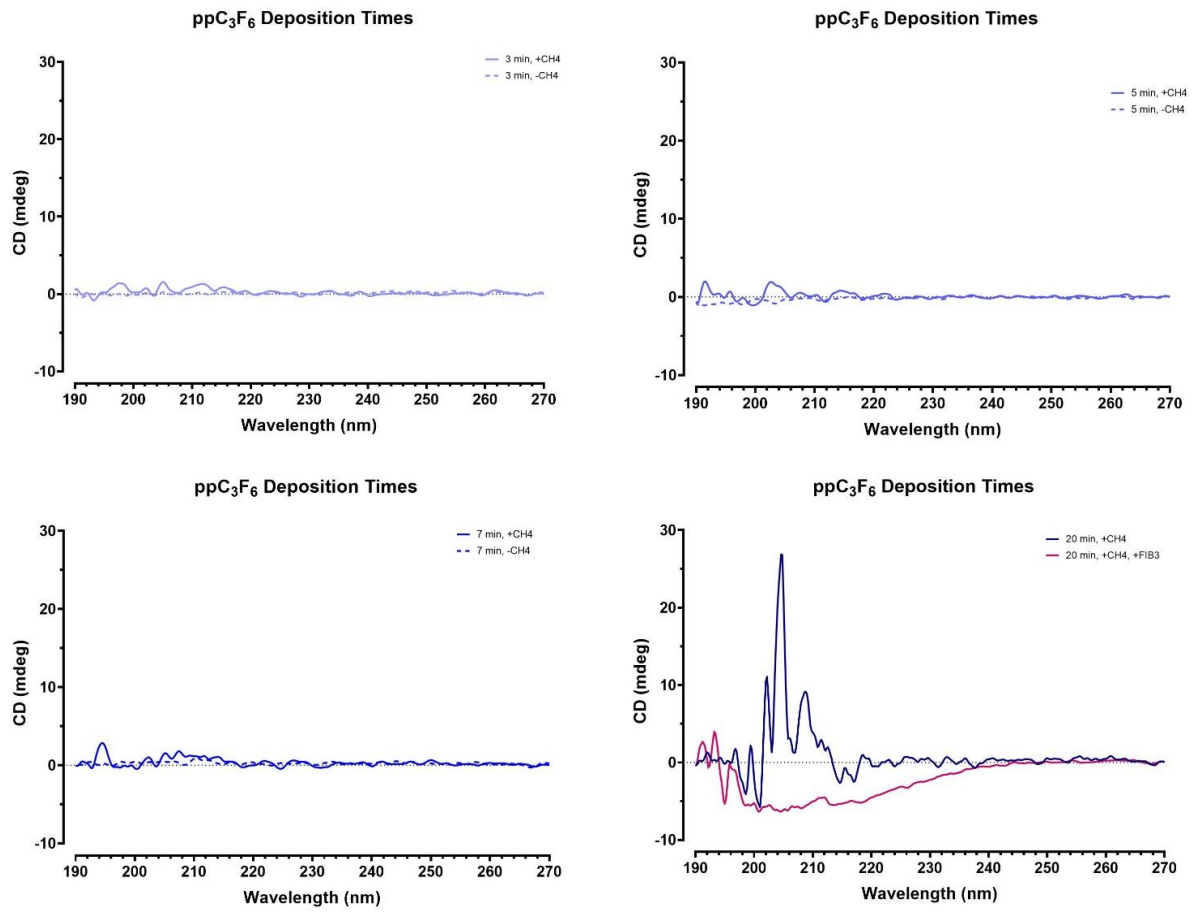

Figure 8.3.3. CD (mdeg) spectra for all tested deposition times (3, 5, 7, and the standard 20 minutes, with and without the CH_4 adhesion layer). The 20 minute samples that were tested here (bottom right) were received back from Clemson University after the initial unsuccessful CD experiment (one pristine, one with FIB3 adsorbed to it).

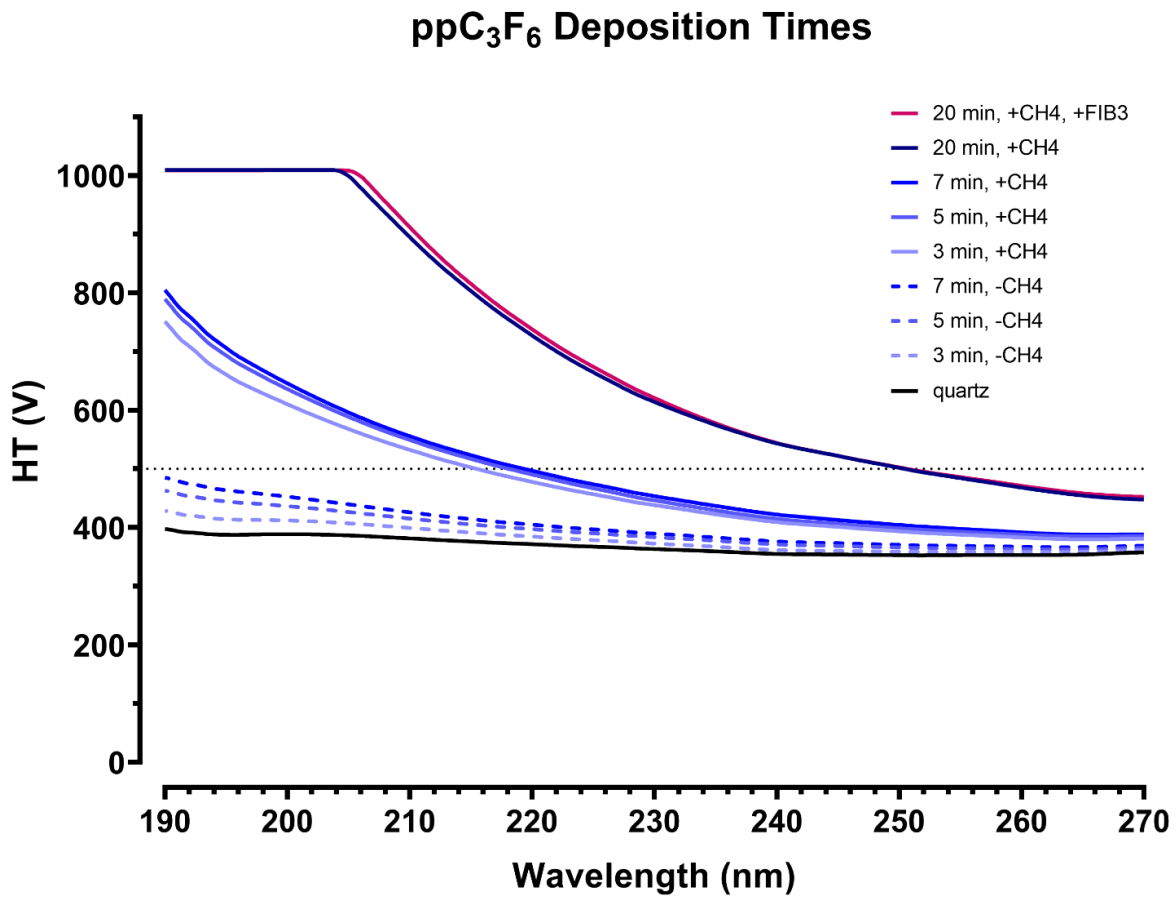

Figure 8.3.4. Corresponding high tension voltage for samples from Figure 3. The top two traces are the standard 20 minute ppC_3F_6 samples (received back from Clemson University after unsuccessful testing), showing the high absorbance issue. The middle cluster of traces represent 3/5/7 minute deposition times with the underlying CH_4 adhesion layer, showing the HTV surpassing the 500 V cutoff below 220 nm. The lower cluster of traces represent 3/5/7 minute deposition times without the underlying CH_4 adhesion layer, which all remained below the 500 V cutoff. An uncoated quartz slide is shown at the bottom.The ppC_3F_6 layer itself shows a small absorbance increase with longer deposition time, but the most dramatic increase in absorbance appears to be caused by the CH_4 adhesion layer.

8.4 Adsorbed-state CD 6 vs. 4 slides

Due to elevated absorbance in the far-UV CD measurement range and consequent high-tension voltage (HTV) experienced with the ppC_3F_6-modified quartz slides that made it impossible to measure Fg adsorption-induced secondary structure changes with the usual 6 slides, CD measurements were run with serially reduced slide quantities to determine the HTV threshold that would maintain <600 V at 190 nm. CD was performed in 5 mM potassium phosphate buffer (PPB) in a 1.0 cm quartz cuvette and HTV was recorded at wavelengths of 300, 200, and 190 nm (**Table 8.4.1**). Based on these results, and considering the anticipated additional absorbance from an adsorbed layer of Fg, it was decided that the CD experiments could be conducted with a maximum of 4 of the ppC_3F_6-modified quartz slides.

Table 8.4.1. Measured HTV at specific wavelengths for different numbers of ppC_3F_6-coated slides in sets. To leave room for some anticipated absorbance of the Fg layer, a maximum of 4 ppC_3F_6-modified slides was selected for subsequent CD measurements taken with the protein in buffer.

Slide Quantity	HTV (V)		
	300 nm	200 nm	190 nm
6	247	532	616
5	244	488	589
4	240	446	563
3	237	400	524

Next, to ensure the reduced number of slides did not affect measurement of adsorbed Fg signal, two control datasets (6 vs. 4 slides) were generated for unmodified quartz slides. No significant difference (Student's t-test, $p > 0.05$) was found between these two datasets for any of the secondary structural elements of Fg (**Table 8.4.2**). Thus using only a set of 4 slides (as required for the ppC_3F_6 surface-modified slides) provides results that are not statistically different from using a set of 6 slides.

Table 8.4.2. Comparison between CD measurements for 4 vs. 6 slides for Fg adsorbed on quartz slides. There was no significant difference (Student's t-test, $p > 0.05$) in secondary structure percentages obtained for 4 or 6 slides. For each set of slides, each of the utilized algorithms (DichroWeb and CD Pro) provide four independent estimates for each % content, which were averaged to provide the estimated % structural content.

	Fg on Set of 4 Plain Slides				Fg on Set of 6 Plain Slides				t value (dof = 2)	Sig. (p value)
Secondary Structure Elements	**CD Pro**	**Dichro Web**	**Mean**	**St Dev**	**CD Pro**	**Dichro Web**	**Mean**	**St Dev**		
% Helix	48.8	46.3	47.6	1.80	47.5	43.9	45.7	2.58	0.831	0.502
% Sheet	15.1	13.8	14.4	0.90	11.2	8.1	9.6	2.21	2.844	0.163
% Turns	19.9	20.0	19.9	0.04	18.0	20.1	19.0	1.52	0.837	0.556
% Unordered	17.4	20.2	18.8	2.00	25.1	27.5	26.3	1.68	4.037	0.0590
Total %	101.2	100.3	100.7		101.8	99.5	99.5		**t.crit= 4.303**	

Vita

Sherry Liu grew up in Rockville, MD and earned her B.S. in materials science and engineering with a focus on biomaterials. Her undergraduate research was based at Cornell's Comparative Orthopaedics Laboratory, where she investigated synovial glycoproteins critical to joint tribology to characterize the progression of degenerative joint diseases. After graduation, she worked for 2 years as a materials and manufacturing engineer at Nordson Medical in Huntington Beach, CA supporting technical operations in the development of advanced polymeric cannulae and catheter solutions for minimally invasive surgical applications. In 2017, she joined the UW Bioengineering community where she studies blood-compatible biomaterials at the Center for Dialysis Innovation (CDI). Her research focus areas are in surface science and the study of molecular interactions at the solid-liquid interface from both experimental and computational perspectives. Her project involves the study of blood protein adsorption on fluoropolymers and their structural or orientational properties that promote long-term thromboresistance. This work is part of a concerted effort to develop a low-cost, wearable hemodialyzer requiring minimal systemic anticoagulation to transform the healthcare and quality of life of patients with renal disease. Sherry is passionate about high-quality dissemination of scientific discovery and driven to translate materials-enabled biomedical technologies into commercialized products to improve health and reduce environmental impact. Outside of research, she enjoys hiking, cooking, puzzles, literature, film, and music.